NASA CR-175062
GARRETT 21-5723

TRANSITION MIXING STUDY FINAL REPORT

by
R. REYNOLDS
C. WHITE

Garrett Turbine Engine Company
A Division of the Garrett Corporation

October 1986

Prepared for

National Aeronautics and Space Administration
NASA-Lewis Research Center

Contract NAS3-24340

TABLE OF CONTENTS

LIST OF FIGURES

LIST OF FIGURES (Contd)

LIST OF FIGURES (Contd)

LIST OF FIGURES (Contd)

LIST OF FIGURES (Contd)

LIST OF FIGURES (Contd)

LIST OF FIGURES (Contd)

LIST OF TABLES

FINAL REPORT
FOR
TRANSITION MIXING STUDY
NASA CONTRACT NO. NAS3-24340

SUMMARY

The Transition Mixing Study (TMS) was a two year program to develop a computer model that can predict the flow field in the transition liner of small gas turbine engines. A Fortran code that meets all of the program requirements has been assembled and used to analyze several flow situations that contain characteristics similar to actual transition liners and for which reasonably accurate experimental data were available in the literature.

Based on the comparisons between measurements and predictions, it can be concluded that the model produces good qualitative results for all aspects of the flow. The results obtained from some of the computations show that the turbulence models, both k-ε and Algebraic Reynolds Stress, significantly underestimate the cross-stream diffusion.

The Transition Mixing Model (TMM) has also been used to perform a numerical experiment that examined the effect of a variety of parameters on the mixing process in transition liners. Comparisons between different cases have illustrated that geometries with significant curvature show a jet trajectory drift toward the inner wall and weaker wake region vortices for jets injected from the inner boundary rather than the outer. These geometries also show decreased penetration for jets injected along the inner boundary within the turning portion of the liner. Also shown were the approximate equivalency of angled slots and round holes and a technique by which jet mixing correlations derived for rectangular ducts can be applied to pipe geometries.

1.0 INTRODUCTION

This report documents the NASA TMS, Contract No. NAS3-24340, and presents the portion of the work undertaken by the Garrett Turbine Engine Company (GTEC). The goals of the program (described in Section 2.0) were to develop and assess a computer program capable of analyzing the mixing process of dilution jets and combustor mainstream gas within transition liners. In Section 3.0, the various physical submodels are described while in Section 4.0, the assessment of the model against experiment data is presented. The program was then used to perform a numerical experiment (described in Section 5.0) to determine the effect of several geometry and operating condition parameters on transition liner mixing rates. Finally, Section 6.0 provides the conclusions derived from the assessment procedure and the numerical experiment and offers recommendations.

2.0 BACKGROUND AND OBJECTIVES

2.1 Background

In recent years, due to improvements in the manufacturing technology of high temperature materials, emphasis has been directed towards increasing the power-to-weight ratio and lowering the specific fuel consumption (SFC) of aircraft gas turbine engines. To accomplish this, higher pressure and temperature levels in the engine cycles are employed. As a result, the hot section components, the combustor, transition liner and turbine, are required to operate in an increasingly hostile environment.

The resulting high thermal loads have caused increased durability problems for these components to the point that they account for over 50 percent of all engine maintenance items. Therefore, industry and government agencies have initiated several efforts which aim to improve the capability of designing hot section components with extended life -- among these is the TMS.

The transition liner, found on engines using a reverse-flow combustor configuration, is the duct which connects the exit of the combustor to the inlet of the first stage turbine stator. With the current trend toward shorter engines and therefore shorter combustors, the transition liner not only must turn the flow direction by 180 degrees, but also efficiently mix the dilution air with the hot mainstream gas. Detailed understanding of the flow field in the transition liner is essential to eliminate hot streaks from entering the stator, thereby extending the stator durability.

Experimental investigations to characterize the mixing in transition liners are becoming increasingly expensive. If a computer model could be generated which accurately simulated the transition liner flow, then various configurations could be evaluated on the computer at less expense and with much greater speed.

2.2 Objectives

The purpose of the TMS was to develop a computer model which was capable of predicting the flow in transition liners used on small reverse flow gas turbines. The model was to be assembled from existing submodels which represented the best available techniques and physical modeling. Minor improvements in the submodels could be performed, however, it was not within the scope of this study to develop substantially different modeling techniques.

Several requirements on the capabilities of the resulting model were imposed.

The model must:

- Be assembled from currently available codes with no operational difficulties
- Solve the steady-state imcompressible flow equations
- Calculate 3-D isothermal turbulent, recirculating subsonic flow fields
- Be capable of calculating density variation due to temperature differences
- Have the geometric flexibility to analyze planer, axisymmetric and annular flow fields, including arbitrary turn section shapes
- Be capable of calculating flow fields in both straight and turn section, with and without dilution air injection and flow area convergence
- Have the flexibility in the specification of the axial location of the inlet boundary condition, such that they may be in either a straight or converging section, either upstream or downstream of the dilution zone
- Allow the independent specification of the dilution jet inlet boundary conditions at each injection location
- Provide a fully elliptic flow calculation
- Include a two-equation (k-ε), or better, turbulence model
- Have the capability to calculate swirl velocity and boundary layer effects
- Include the capability to calculate film cooling and backside cooling, with temperature or heat transfer coefficient boundary conditions
- Include the capability to analyze radiation effects
- Be extendable to the calculation of reacting flows

A model which would meet the above requirements was to be assembled and tested against experimental data taken for flows that exhibit similar characteristics as transition liners. Based on the results of the calculations, an assessment of the model's capabilities would be made. The resulting model would then be used to perform a numerical experiment that would identify the differences in the mixing process in the curved transition liner as compared to straight constant area or straight converging ducts.

3.0 ANALYTICAL MODEL DESCRIPTION

In the following sections, a description of the physical submodels contained within the program is provided. While it is hoped that the text will provide insight into the operation of the submodels, it is emphasized that more detailed descriptions are provided in the references. Therefore, it is recommended that they also be consulted for a complete understanding of the subject.

3.1 Introduction

The Transition Mixing Model (TMM) is based on the GTEC 3-D elliptic code developed in the USARTL Program [Reference (1)]. This original code contained the same numerics and physical submodels as the well known "TEACH" series of codes. Since then, the code has undergone considerable modifications to tailor it to gas turbine combustor and transition liner analysis. As part of the TMS, several additional features were added and are discussed below.

The features dealing with the coordinate system are derived from the methods described in References (2) and (3). The numerical scheme and the pressure-velocity solution algorithms are adopted from the techniques described in References (4), (5), and (6). The algebraic stress turbulence model is the result of in-house development based on Reference (7). The radiation model is an extension of the 2-D version described in Reference (8).

3.2 Coordinate System

The complex geometrical shape of typical transition liners could not be handled within the framework of the cylindrical coordinate system used in the original 3-D program. The common practice of "stair stepping" curved boundaries would have resulted in an excessive number of grid nodes outside the calculation domain. Another consideration was that the basic numerical scheme required the use of an orthogonal system, thus skewed or otherwise arbitrarily shaped control volumes were undesirable.

It was therefore decided to convert the original program to a general orthogonal curvilinear coordinate system. Since transition liners are invariably of an axisymmetric geometry, a significant simplification in the coordinate system was possible. If a global coordinate system is considered where X is coincident with the engine centerline, R is the radial distance from the centerline and Z is the circumferential angle around the centerline, it is obvious that the transition liner curvature is confined to the X-R plane and that in the Z or circumferential direction, the liner is merely a

body of rotation. This observation allows the general orthogonal coordinate system to be confined to the X-R plane. This restriction greatly simplified the geometry package required by the TMM.

The governing equations are solved in the local system X_1, X_2, and X_3, as illustrated in Figure 3-1, where X_1 and X_2 are a general orthogonal curvilinear system while X_3 is identical to the Z coordinate of the global cylindrical system.

3.3 Numerical Scheme

The numerical scheme used in the TMM is basically the same as that used in the "TEACH" series of codes, namely, upwind hybrid differencing. This procedure is widely used for a variety of numerical calculations and flow conditions.

The fundamental characteristic of the upwind hybrid differencing scheme is that the numerical technique used to compute the convective coefficients, depends on the relative strength of the convective and diffusive terms in the governing equation. For low Peclet number situations, second order accurate central differencing is used. As the Peclet number is increased beyond 2, the hybrid technique switches to first order upwind differencing to ensure numerical stability. Central differencing is always used for the diffusion terms.

The scheme can be described by referring to Figure 3-2 which shows a 1-D grid network over which some variable ϕ is to be calculated. The convection and diffusion terms in the governing equation are discretized using central differencing techniques as follows:

$$\rho U \frac{\partial \phi}{\partial X} = (\rho AU)_+ \left(\frac{\phi_P+\phi_E}{2}\right) - (\rho AU)_- \left(\frac{\phi_P+\phi_W}{2}\right)$$

$$\frac{\partial}{\partial X}\left(\Gamma \frac{\partial \phi}{\partial X}\right) = (\Gamma A)_+ \left(\frac{\phi_E-\phi_P}{\Delta X}\right) - (\Gamma A)_- \left(\frac{\phi_P-\phi_W}{\Delta X}\right)$$

If source terms are ignored (they have no effect on the current discussion), the above expressions can be combined into the following results,

$$\phi_P = \frac{(T_+ - L_+)\,\phi_E + (T_- + L_-)\,\phi_W}{(L_+ - L_- + T_+ + T_-)}$$

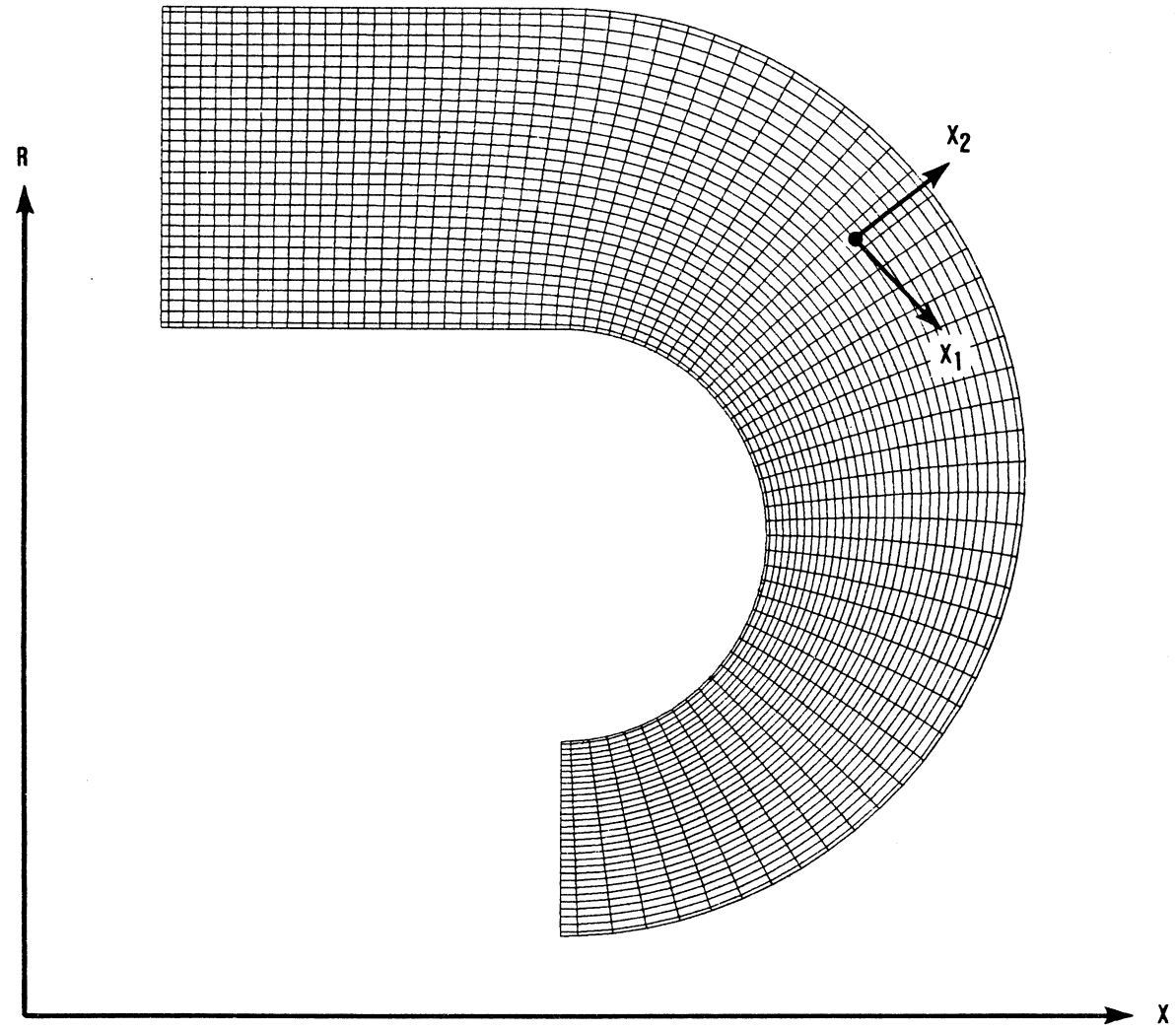

Figure 3-1. Transition Mixing Model Coordinate System.

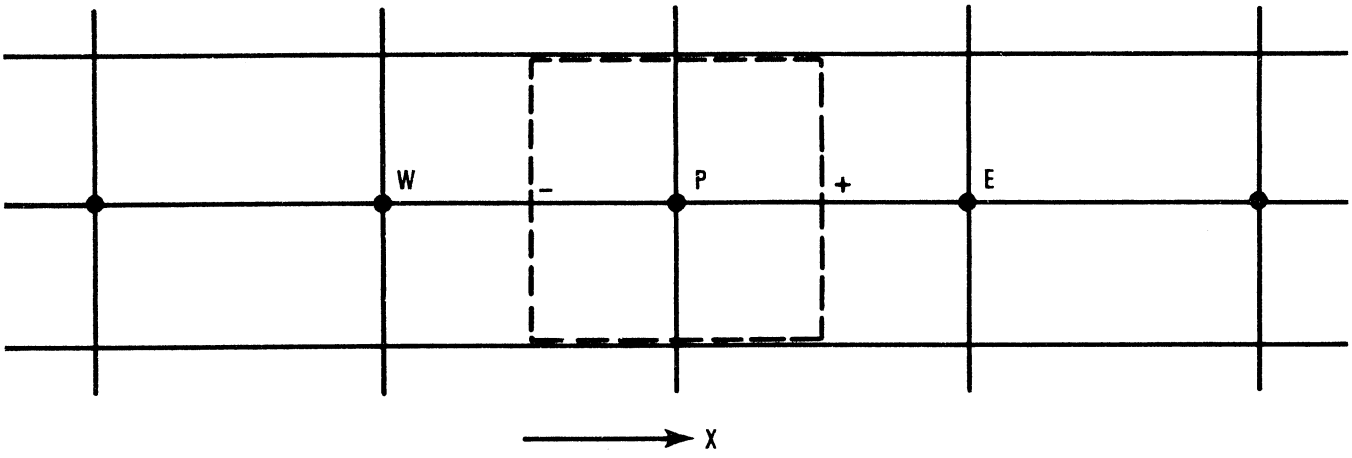

Figure 3-2. One-Dimensional Finite-Difference Grid.

Where:

$$L_+ = (1/2\rho AU)_+ \qquad L_- = (1/2\rho AU)_- \qquad T_+ = \left(\frac{\Gamma A}{\Delta X}\right)_+ \qquad T_- = \left(\frac{\Gamma A}{\Delta X}\right)_-$$

Using these definitions, the expression for ϕ_p becomes,

$$\phi_p = A_W \phi_W + A_E \phi_E$$

where,

$$A_W = \frac{(T_- + L_-)}{(L_+ - L_- + T_+ + T_-)}$$

$$A_E = \frac{(T_+ - L_+)}{(L_+ - L_- + T_+ + T_-)}$$

If the convective influence, denoted by the L's is sufficiently low, each of the coefficients will be positive, which is desirable from the standpoint of numerical stability. However, under higher convective situations, the L's begin to dominate the diffusion terms which are represented by the T's and, if no action were taken, would drive the coefficients negative. In such a situation, numerical divergence is likely.

As an illustration of how the hybrid scheme avoids this difficulty, consider the upwind differencing for the convective terms as shown below.

$$\rho U \frac{\partial \phi}{\partial X} = \left(\frac{\rho U}{\Delta X}\right)_- (\phi_p - \phi_W)$$

If the coefficients of the neighbor points are computed using the above discretization method, the following expression results:

$$A_W = \frac{T_- + L_-}{(L_- + T_+ + T_-)}$$

$$A_E = \frac{T_+}{(L_-{}_+ + T_+ + T_-)}$$

Where:

$$L_- = \left(\frac{\rho U}{\Delta X}\right)_- \quad T_+ = \left(\frac{\Gamma A}{\Delta X}\right)_+ \quad T_- = \left(\frac{\Delta A}{\Delta X}\right)_-$$

It can be seen that these coefficients will always be positive regardless of how large the value of the convective term L becomes. For large negative convective terms, a similar situation of positive coefficients would be generated when the proper upwind discretization term is used.

One slight modification to the hybrid scheme has been incorporated and is referred to as the Power Law Formulation of Patankar. It allows the variation in the finite difference coefficients needed to promote numerical stability to mimic the exact solution more closely. The justification for the use of the hybrid scheme results from the fact that under highly convective situations, the value of some variable ϕ at an upstream node is swept downstream unchanged toward its neighbor. Thus the value of ϕ at the interface of the control volumes surrounding the two nodes is best represented by the upstream value. Under low convective situations, however, a linear profile assumption is made between nodes that corresponds to the central differencing technique. The Peclet number at which the transformation occurs is 2.

The variation of the difference coefficient relating a node to its upstream neighbor is shown in Figure 3-3 for the hybrid scheme. The coefficient variation can also be derived based on the exact solution of the ϕ profile under convection and diffusion with constant convective velocity and diffusion coefficients. An exponential variation is the result. However it is time consuming to compute, so a power law approximation is used. The variation of the exact and power law coefficients are also shown in Figure 3-3.

3.4 Pressure-Velocity Solution Algorithm

In the TEACH series of codes, the solution of the continuity and momentum equations was obtained through the use of the SIMPLE (Semi-Implicit Method for Pressure Linked Equations) algorithm. In this method, a guessed pressure field (usually the values from the previous iteration) was used to solve the momentum equations. A correction equation was then formulated from continuity considerations and solved to yield a pressure correction p'. Finally, the p' values were used to correct the velocity and pressure fields in preparation for the next iteration.

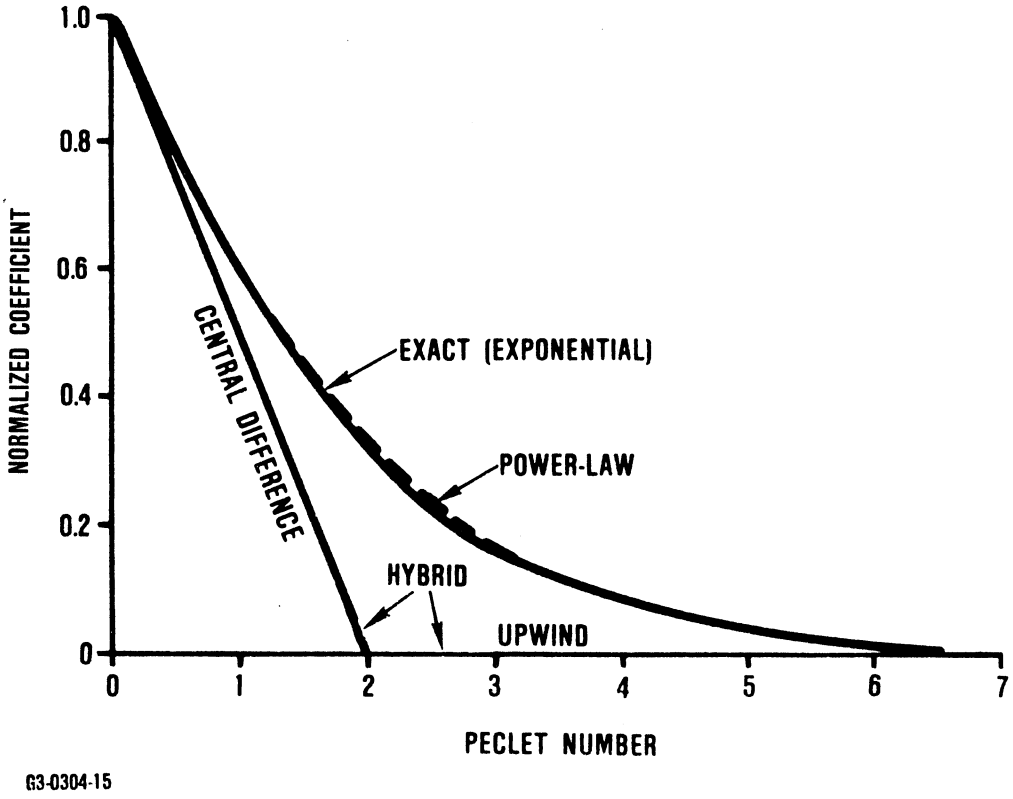

Figure 3-3. Finite-Difference Coefficient Variation With Peclet Number.

The convergence rate using SIMPLE suffered from the fact that although p' corrected the velocity field reasonably well, it did a poor job for pressure. The SIMPLER (Semi-Implicit Method for Pressure Linked Equations Revised) method of Patankar, which is used in the TMM, corrects this deficiency since p' is used only to correct the velocity field while the pressure is obtained from the solution of an addition equation.

Consider the 2-D grid network shown in Figure 3-4. A 2-D example is used simply because of the ease of pictorial representation and because the extension to 3-D is quite straight forward. The grid point labeled P has four neighbors N,S,E and W. Velocities are computed at locations n, s, e and w for the staggered control volumes shown by the dashed lines. The continuity equation can be expressed for the control volume surrounding P as,

$$(\rho AU)_w - (\rho AU)_e + (\rho AV)_s - (\rho AV)_n = 0$$

Each of the four velocities used in the above equation are obtained from the appropriate momentum equation such as the X-component example shown in the following equation.

$$U_w = \frac{\sum_{i=1}^{N_b} A_i U_i + D_w (P_p - P_W)}{\sum_{i=1}^{N_b} A_i}$$

N_b = Number of neighbors

It is assumed that a correction for the velocities will be made through the use of a variable p' and the following expressions:

$$U_W = U'_w + D_W (P'_P - P'_W)$$

$$V_S = V'_S + D_S (P'_P - P'_S)$$

If these expressions, and the ones corresponding to the other velocities involved, are substituted into the continuity equation, an equation for p' is generated which has the same form as the general momentum expression,

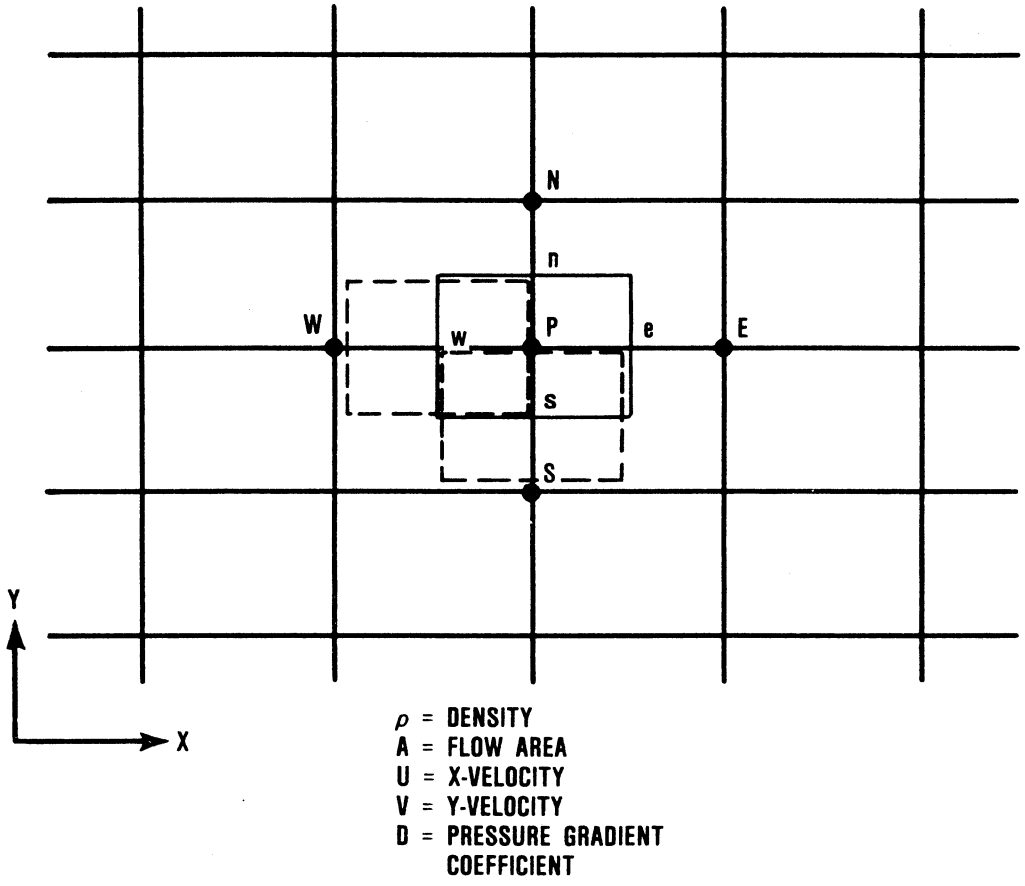

Figure 3-4. Two-Dimensional Finite-Difference Grid.

$$P'_P = \frac{\sum_{i=1}^{N_b} A_i P'_i + S_u}{\sum_{i=1}^{N_b} A_i}$$

The coefficients A_i contain the velocities generated from the guessed pressure field, the density and cell flow areas. The source term S_u, contains the continuity mass error as determined from the existing velocity field. Solving this equation yields values for P' which are used to update the velocity field and thus satisfy continuity. Pressure is also updated via P' by the expression shown below where R is a relaxation factor.

$$P_P = P_P + RP'_P$$

The previous description is a general summary of the SIMPLE algorithm. A similar expression can be derived for the SIMPLER algorithm by noting that the previous momentum equation can be rewritten as follows:

$$U_W = U^*_W + \frac{D_W}{\sum_{i=1}^{N_b} A_i}(P_P - P_W)$$

where U* is a pseudo-velocity which can be computed directly from the existing velocity field and coefficients. If the above equation and the Y-momentum counterpart are substituted into the continuity equation, the result is an equation for pressure of the form,

$$P_P = \frac{\sum_{i=1}^{N_b} A_i P_i + S_u}{\sum_{i=1}^{N_b} A_i}$$

The solution of this equation will produce a pressure field which, when coupled with the existing velocity field, will satisfy continuity. Thus, a consistent, mass-conserving pressure field is used in the solution of the momentum equations rather than guessed values which are later corrected. In addition, the correction to the pressure field used by SIMPLE omits terms involving the velocity corrections at the four neighbor points but which are included with the SIMPLER formulation.

With the pressure field established, the momentum equations are then solved. This velocity field is then substituted into the continuity equation in an identical manner as described for SIMPLE. The p' equation is solved and the velocity field is corrected as before. A summary of the steps in the SIMPLER algorithm is presented in the following:

- Compute the coefficients for the U, V, and W momentum equations and the pseudo-velocities U*, V* and W*
- Compute the coefficients for the pressure equation which involve the pseudo-velocities, density and flow areas of the control volumes
- Solve for the pressure field
- Using this pressure field, add the pressure gradient terms to the source terms of the momentum equations and solve each in turn
- Using this velocity field, compute the coefficients for the p' equation in an identical manner as was done for the SIMPLE method
- Solve the p' equation and update the velocity field

3.5 Turbulence Model

Contained within the TMM are two turbulence models. The first is the widely used two-equation k-ε model. For computing turbulent flows, this model is a reasonable compromise between accuracy and computational effort. The turbulent or effective viscosity is determined from the solution of two additional differential equations, one for k, the turbulent kinetic energy and the other for ε the turbulent dissipation rate.

The second turbulence model is an Algebraic Reynolds Stress Model (ARSM) wherein algebraic expressions for the individual Reynolds stresses are solved to obtain an anisotropic viscosity model. The fundamental assumption in this or

any ARS model is that the transport of turbulence via convection and diffusion is proportional to the transport of turbulent kinetic energy. By using the transport information from the k-equation, the necessity of solving a differential equation for each Reynolds stress, as is done in full Reynolds Stress Models, is eliminated which greatly decreases computational time and computer memory requirements.

The development of the ARSM starts with the general equation for a Reynolds Stress $\overline{u_i u_j}$ given below.

$$\underbrace{\frac{D}{Dt}\left(\overline{\rho u_i u_j}\right)}_{\text{Convection}} - \underbrace{\rho D_{ij}}_{\text{Diffusion}} = \underbrace{\rho P_{ij}}_{\text{Production}} + \underbrace{\rho \Pi_{ij}}_{\text{Redistribution}} - \underbrace{\rho \varepsilon_{ij}}_{\text{Dissipation}}$$

The transport or convection plus diffustion of $\overline{u_i u_j}$ is, as mentioned above, taken to be proportional to the transport of k, thus,

$$\frac{D}{Dt}\left(\left(\overline{\rho u_i u_j}\right)\right) - \rho D_{ij} = C_{u_{ij}} \rho \frac{\overline{u_i u_j}}{k} (P-\varepsilon)$$

Where P and ε are the production and dissipation rate of turbulent kinetic energy and $C_{u_{ij}}$ is an emperical constant.

The Reynolds stress production term does not require any modeling and is written as,

$$P_{ij} = -\left[\overline{u_i u_k} \frac{\partial U_j}{\partial X_k} + \overline{u_j u_k} \frac{\partial U_i}{\partial X_k}\right]$$

Different researchers have modeled the pressure redistribution term in different ways. It is usually considered to possess two distinct parts, the first attributed to the interaction of the turbulence field and the second, due to the interaction of the turbulence and mean velocity field.

$$\Pi_{ij} = \Pi_{ij,\,1} + \Pi_{ij,\,2}$$

The first part is almost universally modeled by the following expression,

$$\Pi_{ij,1} = C_1 \left(\frac{\varepsilon}{k}\right)\left(\overline{u_i u_j}\right) - 2/3\ k\delta_{ij}$$

The second part has had many representations, however the one adopted for the TMM is due to Launder, Reece and Rodi and is shown below.

$$\Pi_{ij,\,2} = -\alpha\ (P_{ij} - 2/3P\delta_{ij}) - \beta(D_{ij} - 2/3P\delta_{ij}) - \gamma k \left[\frac{\partial U_i}{\partial X_i} + \frac{\partial U_j}{\partial X_i}\right]$$

Where,

$$D_{ij} = -\left[\overline{u_i u_k}\ \frac{\partial U_k}{\partial X_i} + \overline{u_j u_k}\ \frac{\partial U_k}{\partial X_j}\right]$$

and, α, β, and γ are emperical constants
δ_{ij} is the Kronecker delta

For the final term, the dissipation, it is the usual practice to adopt the following expression:

$$\varepsilon_{ij} = 2/3\ \delta_{ij}\varepsilon$$

Assembling all these terms, the general expression for the Reynolds stresses $u_i u_j$ is obtained and is given below.

$$\left(C_{\mu ij}\rho\ \frac{\overline{u_i u_j}}{k}\right)(P-\varepsilon) = -\rho\left[\overline{u_i u_K}\ \frac{\partial U_i}{\partial X_K} + \overline{u_j u_K}\ \frac{\partial U_i}{\partial X_k}\right] -$$

$$\rho C_1 \left(\frac{\varepsilon}{K}\right) \left[\overline{u_i u_j} - 2/3 k\delta_{ij}\right] - \alpha\rho(P_{ij} - 2/3\ P\delta_{ij}) -$$

$$\rho\beta(D_{ij} - 2/3 P\delta_{ij}) - \gamma k\rho \left[\frac{\partial U_i}{\partial X_j} + \frac{\partial U_j}{\partial X_i}\right] - 2/3\rho\delta_{ij}\varepsilon$$

To compute each Reynolds stress would normally require the simultaneous solution of a six-equation set for each grid point for each iteration, a task which would consume a considerable amount of computational time. An alternate approach used in the TMM is an approximate solution which proceeds along with the main flow field iteration.

Since each normal Reynolds stress involves only the shear stresses and no other normal stresses, arrays are provided to store the equivalent of the shear components. At each iteration, the shear stress information is recovered from these arrays and used to compute the normal stresses. Then the shear stresses are updated using the new normal stresses and the values of the shear stresses from the previous iteration. When the solution converges and the stress components do not change from iteration to iteration, this iterative technique is equivalent to the simultaneous solution of all six Reynolds stress equations.

The anisotropy of the Reynolds stresses needs to be introduced into the momentum equations which is accomplished through the use of different components for the effective viscosity. Usually the fluid stress tensor is related to the strain rate tensor by a single scalar effective viscosity. In the TMM ARS model however, the stress and strains are related as follows:

$$\begin{bmatrix} \sigma_{11} & \sigma_{12} & \sigma_{13} \\ & \sigma_{22} & \sigma_{23} \\ & & \sigma_{33} \end{bmatrix} = \begin{bmatrix} \mu e_{11} & \mu_{12} e_{12} & \mu_{13} e_{13} \\ & \mu e_{22} & \mu_{23} e_{23} \\ & & \mu e_{33} \end{bmatrix}$$

There are now four components of effective viscosity, one for the normal stresses and three others connected with the shear stresses. These four viscosity components are then used in the momentum equations, however, it is necessary to first relate the effective viscosities to the Reynolds stresses mentioned above.

The viscosity component associated with the normal stresses is taken to be the isotropic value as determined from the normal k-ε model.

$$\mu = \rho C_\mu \frac{k^2}{\varepsilon}$$

For the shear stress components, it would be possible to relate the viscosities to the corresponding Reynolds stress via a mean gradient. However, this approach would only account for the anisotropy in the turbulence velocity fluctuations and not the anisotropy in the length scales. To address the latter, the solution of the dissipation stress tensor, ε_{ij}, is required. The governing equations for ε_{ij} are extremely complicated and require phenomenological modeling, therefore a simpler algebraic model of the dissipation tensor was used,

$$\varepsilon_{ij} = \frac{2}{3} \varepsilon \delta_{ij} - \gamma \varepsilon \left(\frac{2}{3} \delta_{ij} - \frac{|\overline{u_i u_j}|}{k} \right)$$

where, γ is an empirical constant. The previous equation is a simplified dissipation rate tensor, and automatically reduces to the isotropic value when the degree of anisotropy is small.

From the values of ε_{ij} obtained, the components of the diffusion coefficients are computed from the following expression,

$$\mu_{ij} = \rho C_\mu \frac{\overline{u_i u_j}}{\varepsilon_{ij}}, \quad i \neq j$$

This model accounts for anisotropic distributions in both turbulent velocity and length scales without prescribing arbitrary bounds on the values of diffusion coefficients.

3.6 Radiation Model

The radiation algorithm examined during TMS is called the Discrete Flux Radiation (DFR) model. It involves the solution of a number of predetermined radiation rays between the boundaries. This model offers the advantage of improved accuracy since more directions (usually about 25) are included in the solution of the radiation flux reaching a boundary point as opposed to only six directions in the commonly used six-flux model. The disadvantage of the model is the geometric complexity involved in solving each radiation ray.

The solution procedure used by the DFR model is illustrated in Figure 3-5, which shows a boundary point P upon which several radiation rays converge. Obviously, in the TMS the situation is 3-dimensional, however, for the purposes of explanation, a 2-D example will suffice. If the radiation intensity leaving point E_1, for example, were known, the intensity after crossing the first control volume would be given by the following expression:

$$I = I_{E_1} e^{-\delta s} + \frac{E}{\Pi} (1-e^{-\delta s})$$

Where:

δ_s - Optical path length (related to Δ_s)

E - Modified emissive power of gas

This simple relation is derived by assuming that the emissive power of the gas and the absorption coefficient in a given control volume are constant. By successive application of the same relation through each control volume crossed by the E_1 ray, the intensity incident on point P can be calculated. If a similar operation were performed for each of the other rays, the total intensity arriving at point P would be the sum of each individual ray, weighted by the cosine of the angle of incidence and the solid angle which the emitting area represents as viewed from point P.

If the calculation domain walls were divided into a number of "plates", where each plate represented some fraction of the wall area and existed at some wall temperature, then the radiation impinging on each plate from every other plate could be calculated by the above procedure. One difficulty is that for grey surfaces, the radiation intensity leaving the wall is partially a function of the incident radiation. This fact requires that the radiation solution be iterative, however since the flow field solution is also iterative, they can proceed simultaneously.

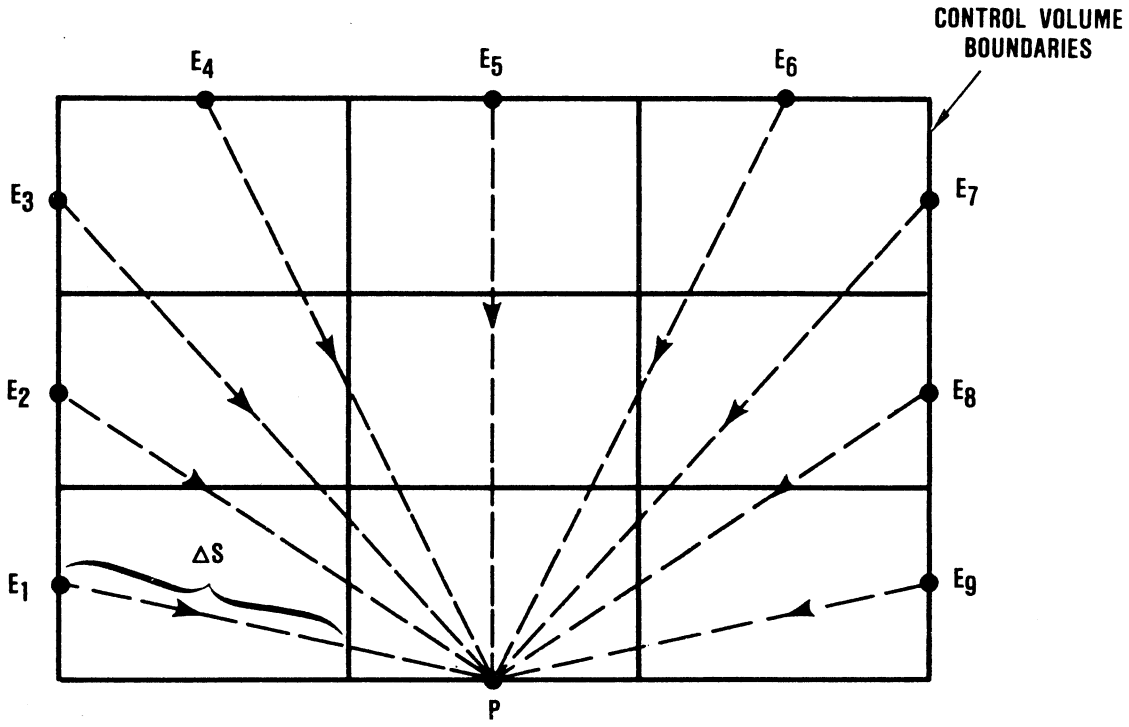

Figure 3-5. Solution Grid for Discrete Flux Radiation Model.

The above described procedure is deceptively simple because in the 2-D example, the calculation of the travel distances through each control volumes is relatively easy. When this model is extended to 3-D, the determination of these distances is significantly more complicated. The rays are traveling through 3-Dimensional six-sided control volumes which can be oriented arbitrarily in 3-D space. The difficulty of these calculations is indicated by the fact that 90 percent of the coding associated with the radiation model is connected with the travel distance computation.

4.0 MODEL ASSESSMENT

A crucial portion of any model development is the comparison of the predictions with experimental data. In the TMS, this was accomplished in two phases. The first was a verification of the model against a few test cases conducted as the code was being assembled. Once the complete program had been generated, a more extensive assessment was performed using data which contained the essential characteristics of transition liner flows. In the following paragraphs, the verification and assessment procedures and the results will be discussed.

4.1 Verification

The verification consisted of comparing the model predictions against two cases of flow over a backward facing step, one laminar[9] and one turbulent[10]. These cases were selected because they were relatively complex flows yet retained a simple geometry and provided accurate benchmark-quality data.

The test geometry for the laminar flow can be inferred from the X-Y computational grid that was used for the case and is shown in Figure 4-1. The fluid was water which entered from the left, passed over the backward facing step and exited to the right.

An X-Y grid of 79 x 23 was selected for this case. To simulate the step, coding was added to properly modify the coefficients of the grid nodes next to the shaded blockage also shown in Figure 4-1. In the Z direction, 7 nodes spaced uniformly at 2.2 mm were used.

The lowest Reynolds Number (Re) for which data were obtained was 73 (based on the step height of 1.5 cm and the mean velocity upstream of the step). This was also the flow condition chosen for the first test case. For the initial velocity profile, the measured values taken 2.0 cm upstream of the step were used. Comparisons between the predicted axial velocity profiles (solid lines) and the measurements (symbols) at several stations are shown in Figure 4-2.

The good comparison between measurements and predictions was attributed to the low numerical and false diffusion in this test problem. Though the X-direction Peclet numbers in the mainstream region were in the 10 to 20 range, the flow was approximately aligned with the grid lines and only small axial gradients existed. In the recirculation zone, where the flow was not aligned and larger gradients occurred, the X and Y-direction Peclet numbers were under two indicating that the second order accurate differencing mode of the numerical scheme was used.

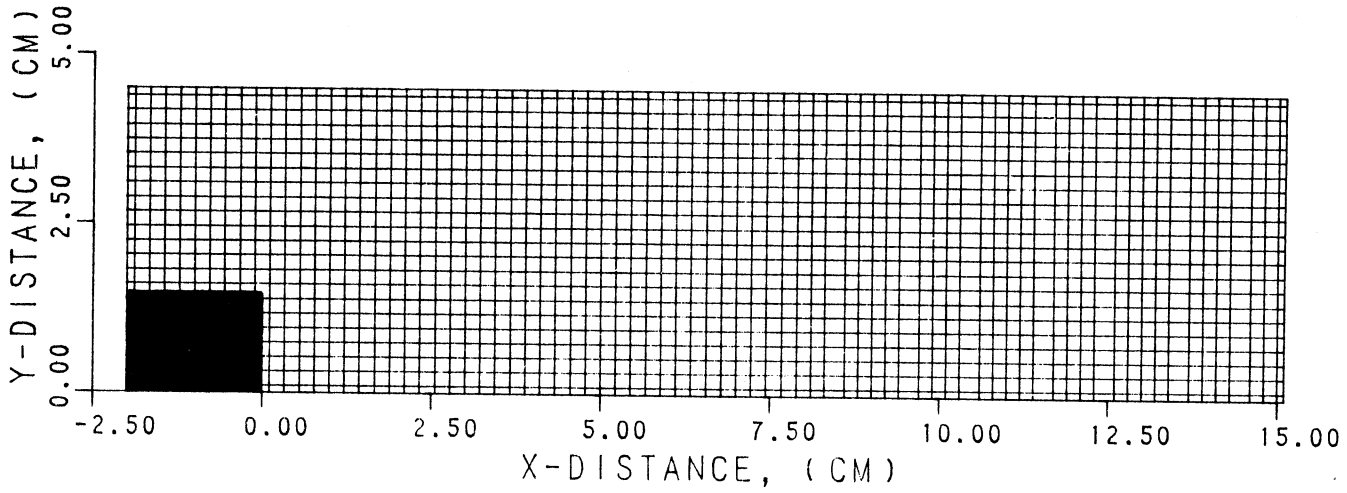

Figure 4-1. Computational Grid for Laminar Flow Over a Step.

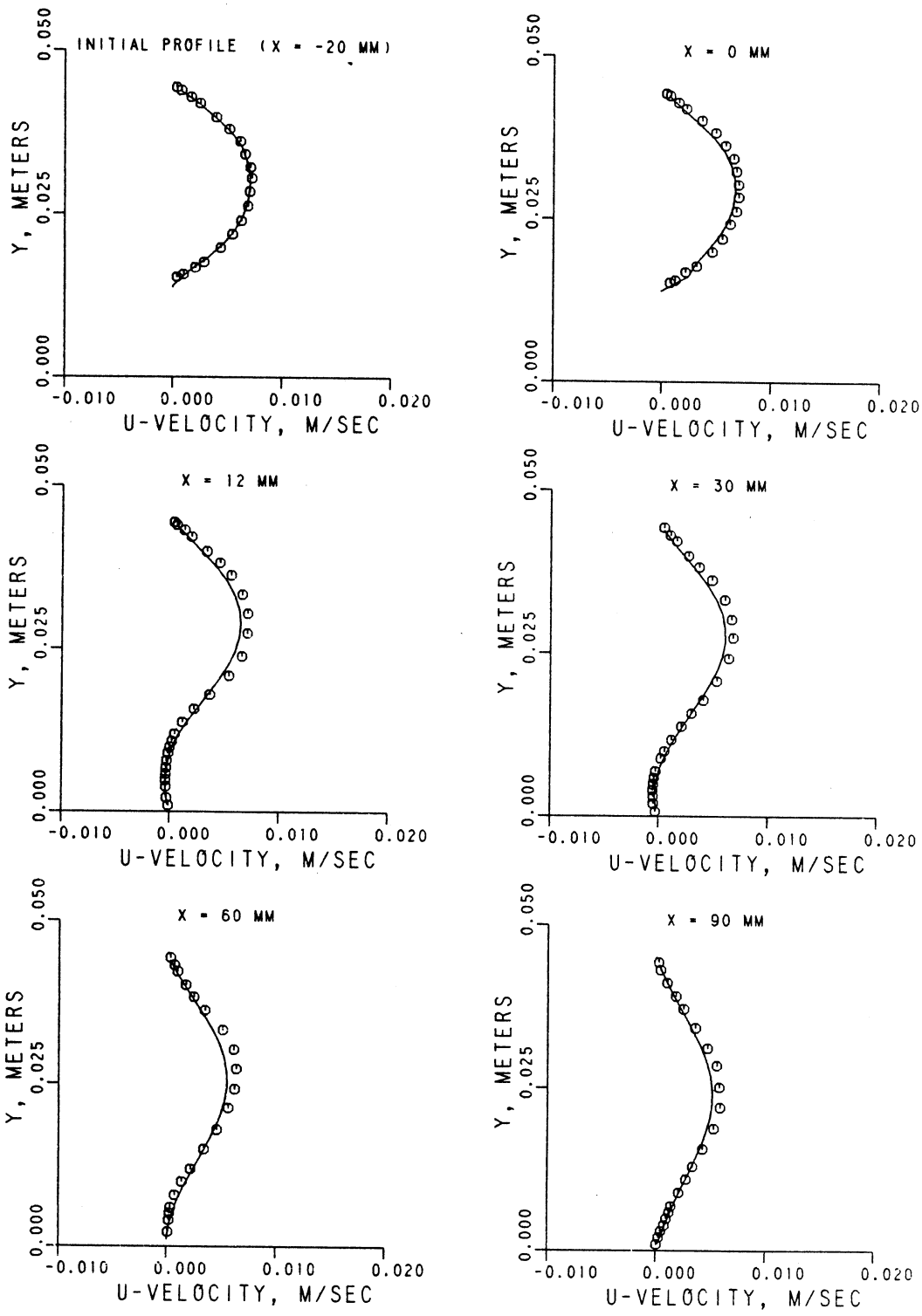

Figure 4-2. Axial Velocity Comparison for Laminar Flow, Re=73.

A second laminar flow case, for Re = 191 was also analyzed. A grid network identical to the previous example was used but with different inlet velocity profiles, again taken as the measured values 2.0 cm upstream of the step. The results for this case are shown in Figure 4-3. Again the comparison is quite good for all stations.

The computational X-Y grid used for the turbulent step flow is shown in Figure 4-4. The network was 54 x 37 with 5 uniformly spaced grid nodes in the Z direction. Again, modified coding in the TMM was used to properly account for the shaded blockage which simulated the backward facing step.

Initial profiles for axial velocity, turbulent kinetic energy and length scale at X = -2.31 cm had been previously calculated using a 2-D program. The actual measurement domain extended 15.24 cm upstream of the step but since there was little interest in this portion of the flow, the TMM calculations were begun at the X = -2.31 station to conserve grid nodes. As there were no intermediate stations between X = -15.24 cm and the beginning of the step for which both the mean velocity and turbulent kinetic energy were measured, the calculated values were used so that there would be a consistency in the initial velocity and turbulence profiles.

Data for two different step heights were provided with the 3.81 cm step chosen for these calculations. Comparisons of the mean velocity at several axial stations are shown in Figure 4-5. The agreement would appear reasonable. Similar plots for turbulent kinetic energy are shown in Figure 4-6 and, as can be seen, the TMM over predicts the kinetic energy level in the initial regions of the step flow and shows too high a decay rate in the downstream regions.

4.2 Description of the Assessment Procedure

The purpose of the model assessment was to determine the accuracy with which the TMM could predict flow field situations that exhibit the characteristics of turbulence, curvature, jet mixing and radiation usually found in transition liners. In order that each characteristic could be examined as independently as possible, a series of five separate classes were selected. They range from very simple flows which were used to test the basic numerical procedure in the TMM without additional physical submodel complication, to ones containing nearly all of the characteristics of transition liners:

- Laminar flow in a curved duct[11]
- Turbulent flow in a curved duct[12,13]

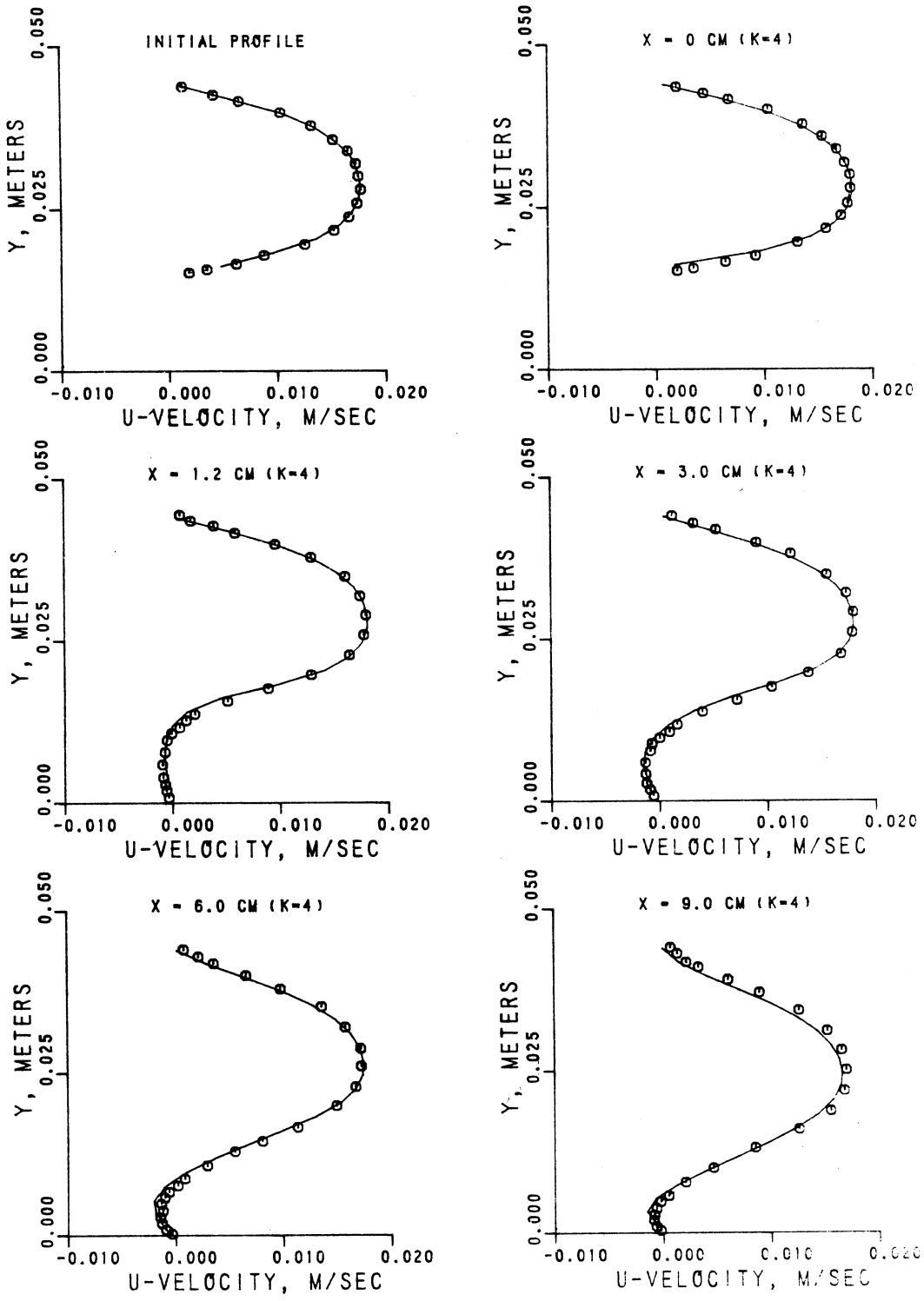

Figure 4-3. Axial Velocity Comparison for Laminar Flow, Re=191.

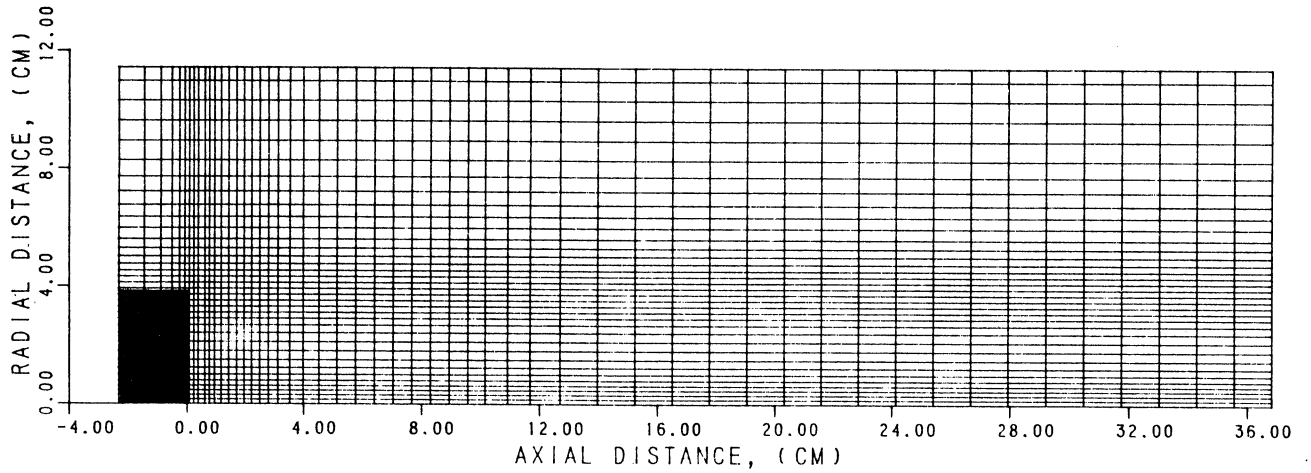

Figure 4-4. Computational Grid for Turbulent Flow Over a Step.

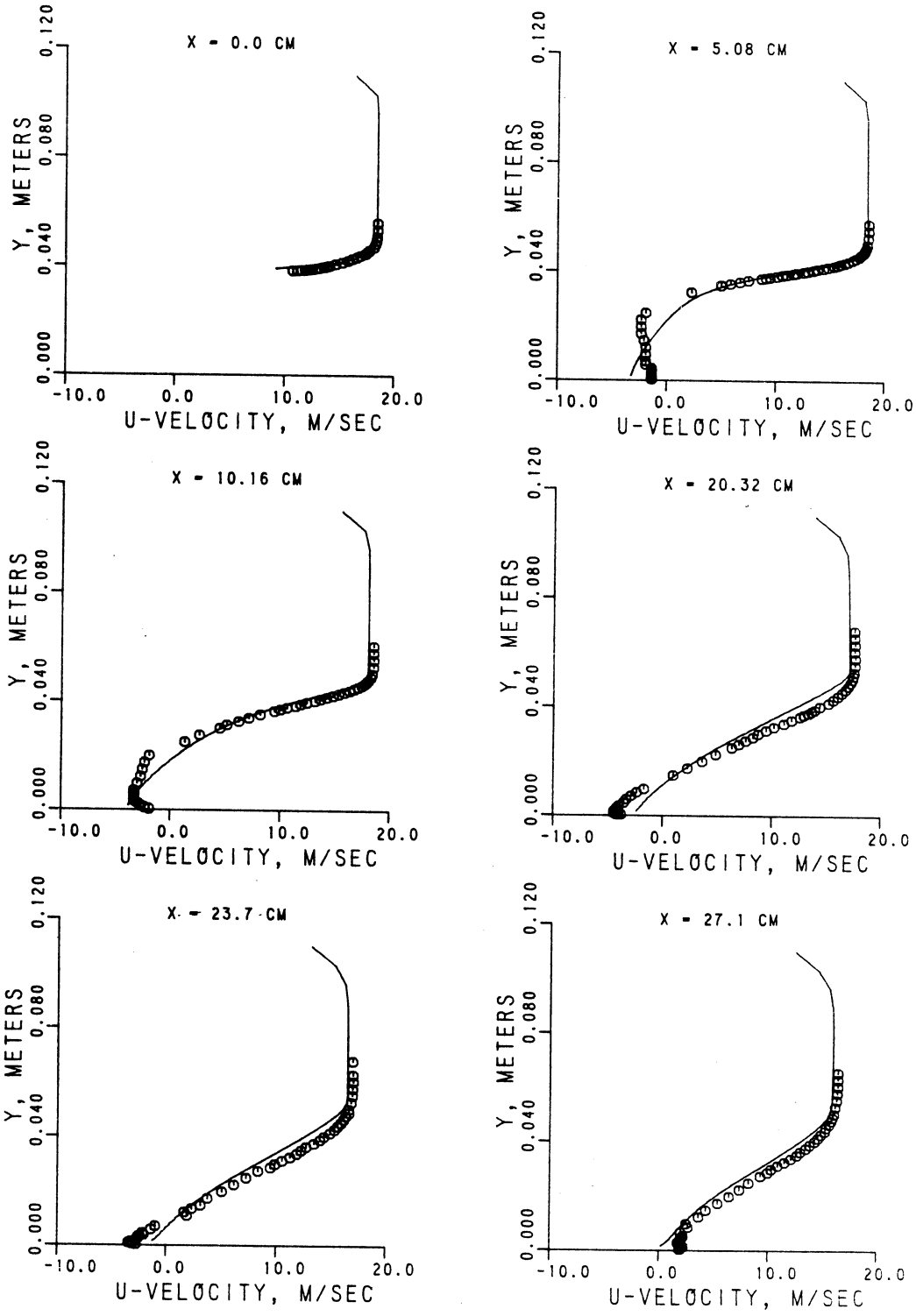

Figure 4-5. Axial Velocity Comparison for Turbulent Flow, 1.5 Inch Step.

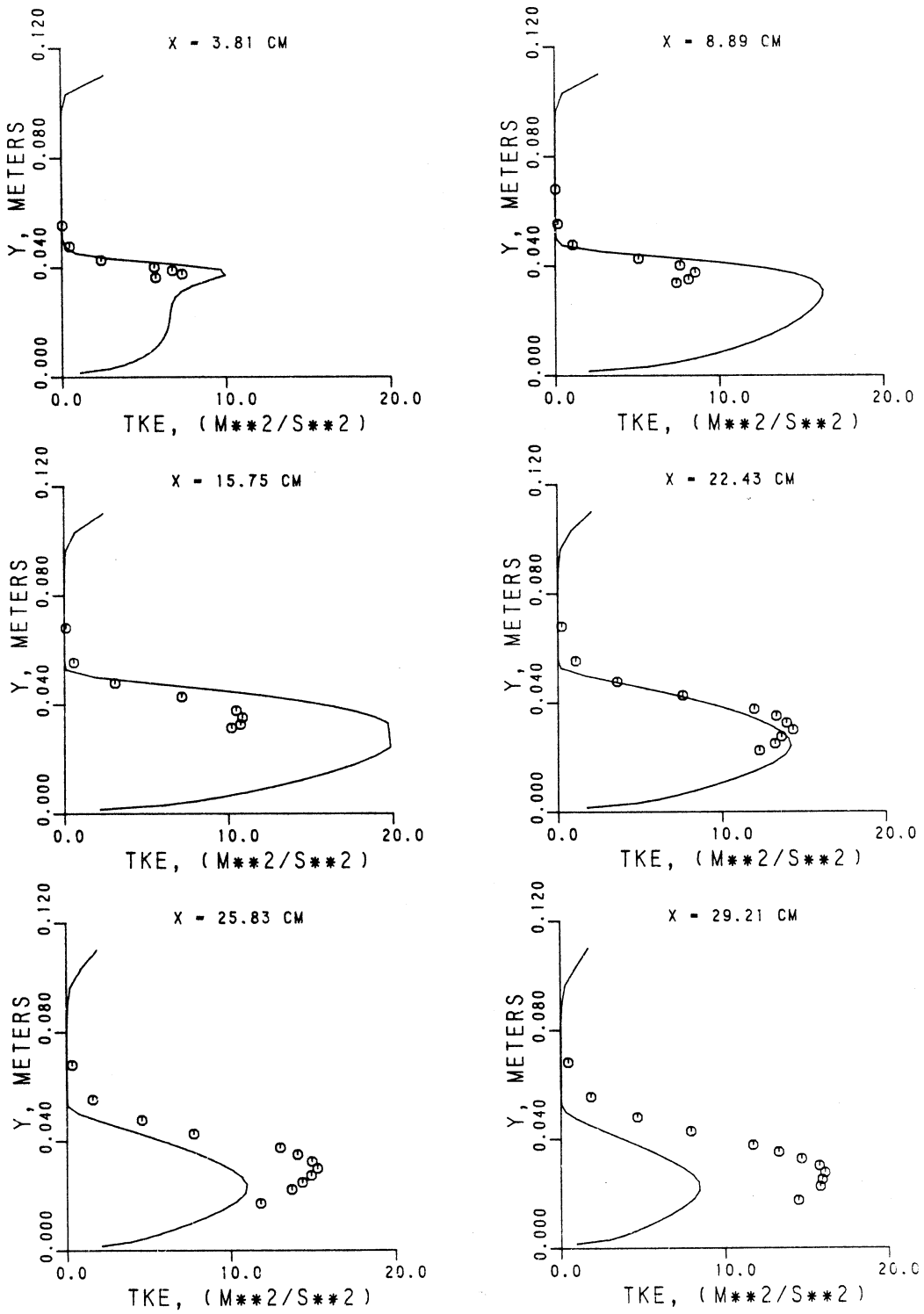

Figure 4-6. Turbulent Kinetic Energy Comparison for Turbulent Flow, 1.5 Inch Step.

- Jet mixing in a symmetrically converging straight duct[14,15]
- Jet mixing in a curved duct[16]
- Radiation in an enclosed cavity[8]

4.3 Results

The first assessment test case was a laminar flow in a 40 x 40 mm square duct containing a 90 degree bend with a mean radius of curvature of 92 mm. To analyze this case, the grid network shown in Figure 4-7a was used. The X-Y system consisted of 79 by 27 nodes in the streamwise and radial directions respectively. Water entered from the left, passed through the 90 degree curved duct and exited at the bottom of the figure. The nodes were equally spaced in the radial direction, but were concentrated toward the exit in the streamwise dimension since the curvature induced flow distortion would be greatest in this area. The Y-Z grid network is shown in Figure 4-7b and used 14 equally spaced nodes in the cross-stream direction. Since the flow exhibits a symmetry about the cross-stream centerline , only half of the duct was actually modeled.

The boundary condition for streamwise velocity at the inlet to the duct was determined by performing a bicubic spline interpolation on the measured values 20 mm upstream from the start of the curved section. The radial and cross-stream velocities were assumed to be zero since there were no measurements of these velocities provided at the 20 mm upstream station. At the exit of the duct, zero gradients in the streamwise direction were used thus allowing the exit profile to be determined by the solution process. In the Y-Z plane, the Z = 0.0 boundary was treated as a plane of symmetry, whereas all other boundaries were walls.

The comparison between measurements and predictions for the streamwise and radial velocity for Theta (or the angular position within the curved section) of 60 degrees is shown in Figure 4-8. The velocities have been normalized by the mean streamwise velocity of 0.0198 m/sec and have been plotted against the cross-stream distance, z, normalized by the duct half width of 20 mm. Five different radial positions are shown where y in the figure is measured from the outer wall. Thus Y/YM = 0.1 is next to the outer or concave wall while Y/YM = 0.9 is next to the inner or convex one. YM is the duct height, or 40 mm.

In general, the comparison is reasonable. All measurement stations exhibited similar or better levels of agreement. The most significant deviation occurs at Y/YM = 0.9

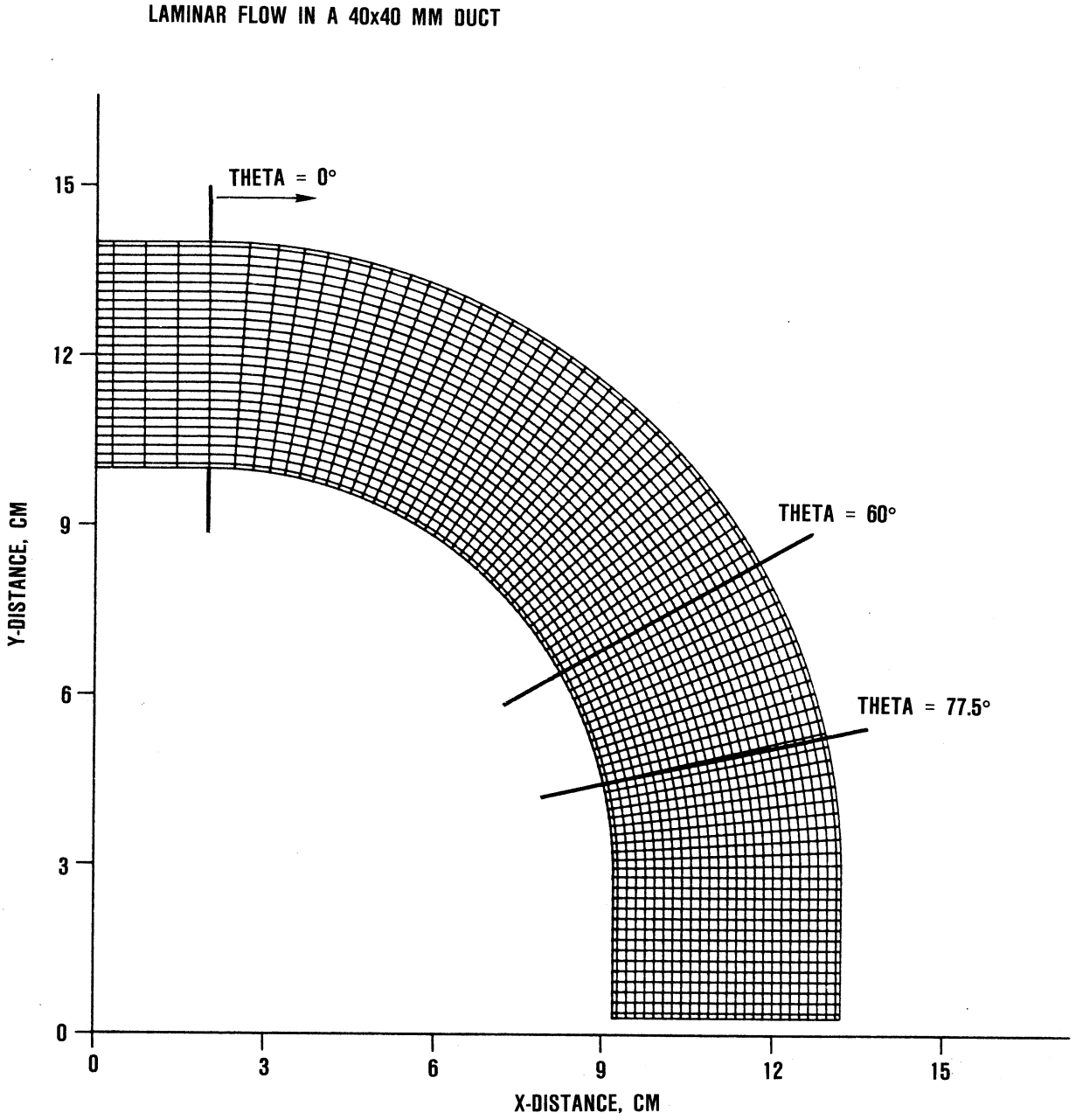

Figure 4-7a. Computational Grid for Laminar Curved Duct Flow, X-Y Plane.

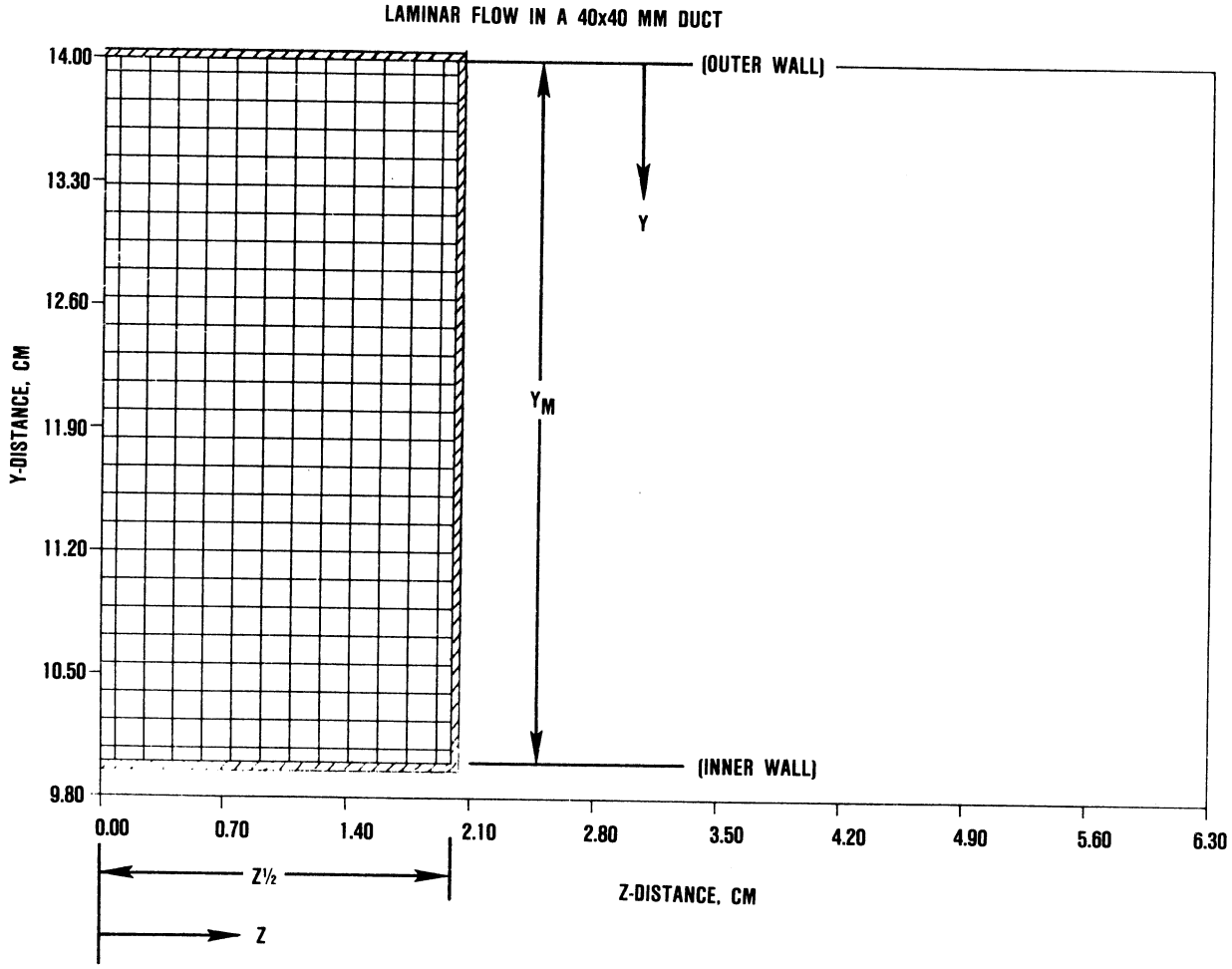

Figure 4-7b. Computational Grid for Laminar Curved Duct Flow, Y-Z Plane.

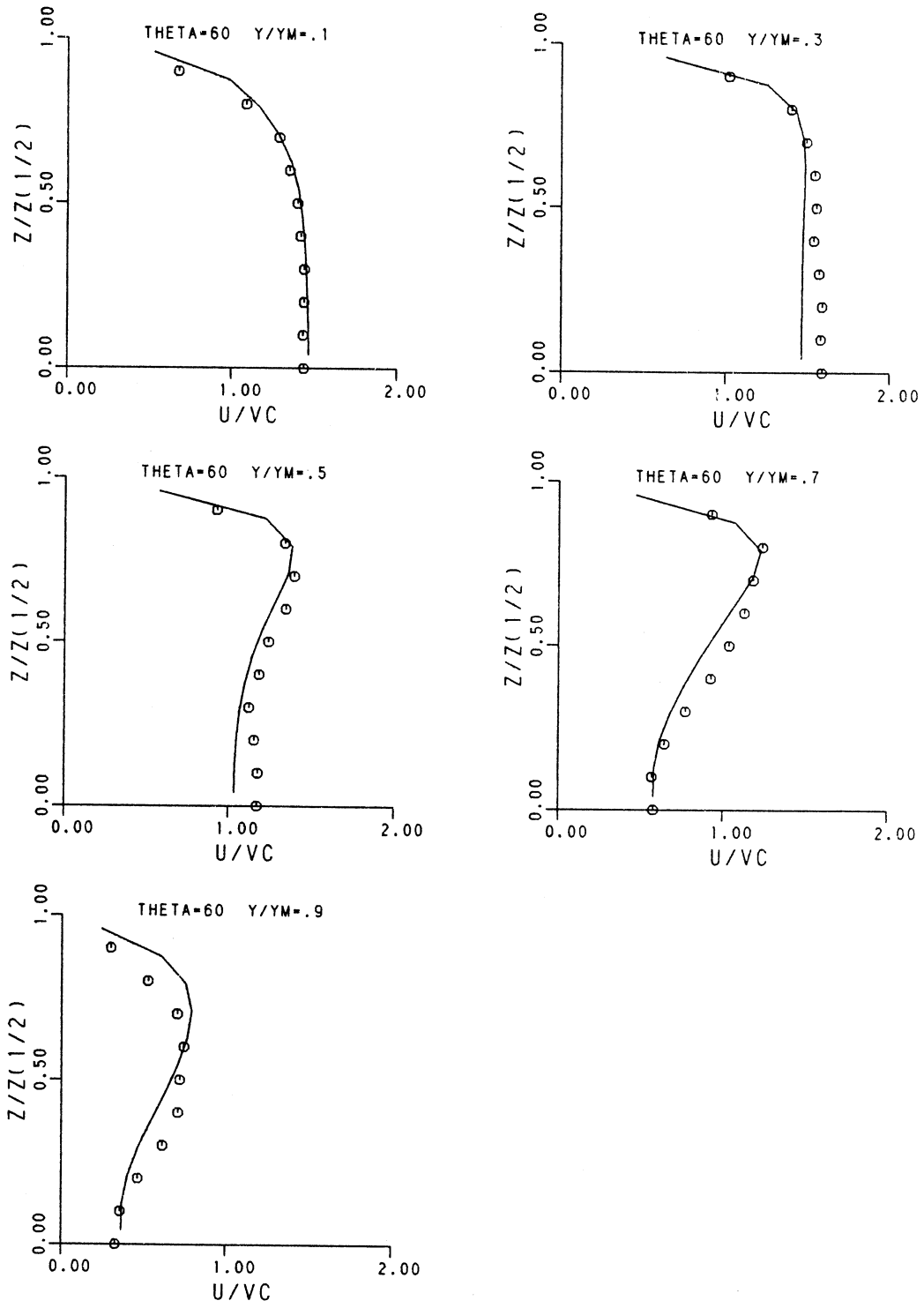

Figure 4-8. Axial Velocity Comparison for Laminar Curved Duct Flow, Theta = 60 Degrees.

where the calculated velocity profile peaks at a larger cross-stream position than the measurements show. At the next measurement station of Theta = 77.5 degrees, shown in Figure 4-9, the comparison at Y/YM = 0.9 has deteriorated.

To determine if these discrepancies were the result of a lack of grid resolution, a portion of the duct was re-analyzed, starting at 30 degrees in the bend and ending at 90 degrees thus allowing a much finer grid mesh than was possible for the entire duct. This region was selected because the 30 degree station was a measurement plane from which initial profiles could be obtained and the 60 degree arc would include the station of interest which was located at 77.5 degrees.

Shown in Figure 4-10 is the X-Y grid network used consisting of 60 x 31 nodes while 16 nodes were used in the Z-direction. By restricting the analyses to this smaller domain, the average X, Y and Z grid spacing in the 77.5 degree region was reduced to 1.08, 0.857 and 1.33 mm respectively compared to 2.26, 1.65 and 1.82 mm for the complete duct analysis. Initial profiles were obtained from the measurements by interpolation as was done for the complete duct analysis with the addition that an inlet radial velocity component was also specified.

Comparisons between measurements and predictions at theta = 77.5 degrees are shown in Figure 4-11. Improvements in the calculated profiles are evident although at Y/YM = 0.9 some disparity between measurements and predictions remains.

The second assessment case was turbulent flow in a 180 degree bend, 44.5 x 44.5 mm duct with a 126.8 mm inner radius of curvature. Since some difficulties attributed to grid resolution had been encountered in the laminar flow case, the analysis of the entire 180 degree duct was not considered since the larger geometry would necessitate the use of a coarser grid compared to the laminar case. Therefore, only a portion of this flow, consisting of the entrance section and the first 60 degrees of the bend, was analyzed. Measurement stations had been provided in the bend at angles of 3 and 45 degrees and the initial profiles were available at 44.5 mm upstream of the entrance to the curved section. The computational grid used is shown in Figure 4-12, which also identifies the two measurement planes. The flow is again from left to right and the fluid was water.

The initial profiles were determined in a similar manner as for the laminar case. Bicubic spline fits to the data at the first measurement plane were used for both streamwise and radial velocity with the cross-stream component again taken to be zero. Profiles of turbulent kinetic energy and length

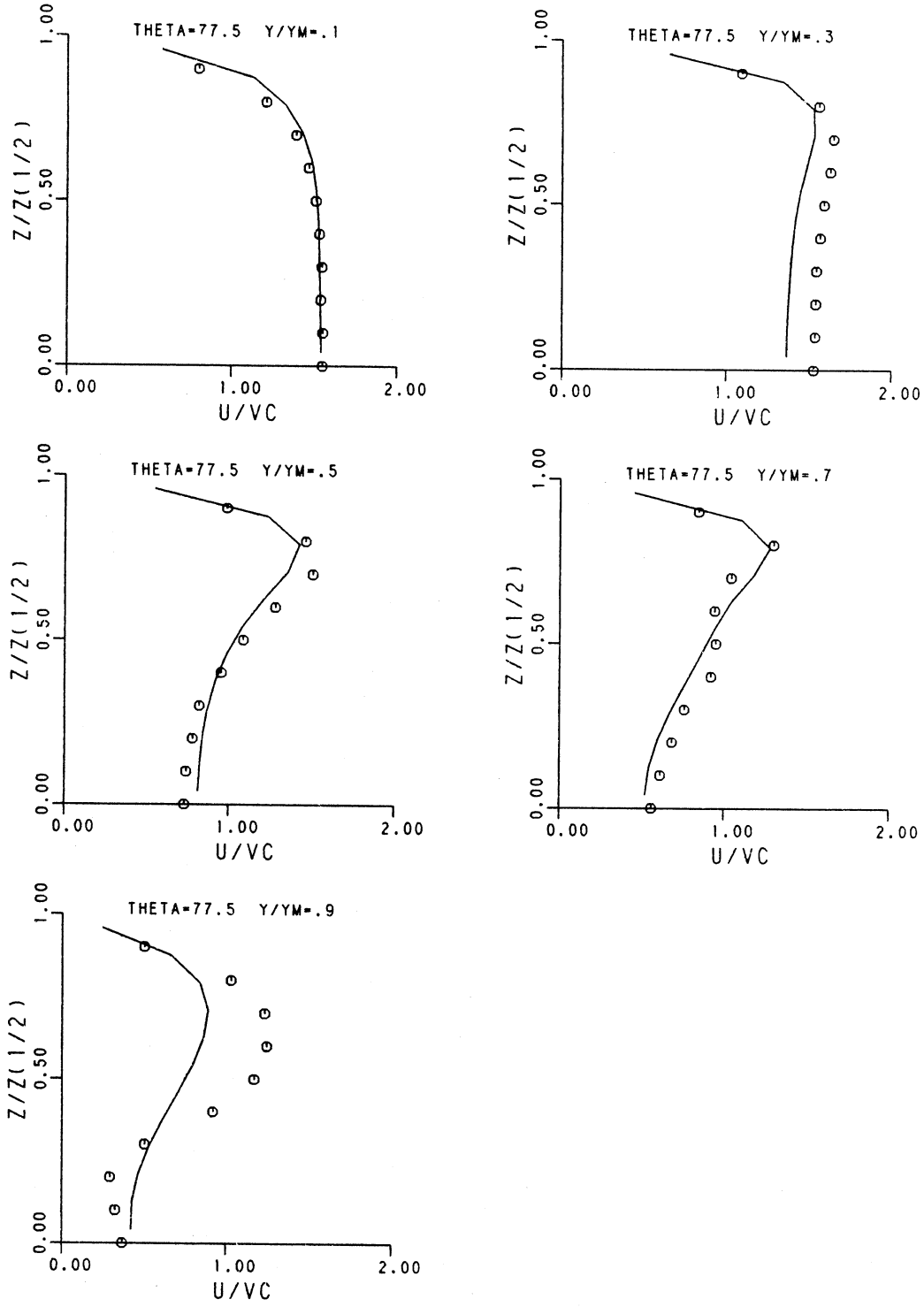

Figure 4-9. Axial Velocity Comparison for Laminar Curved Duct Flow, Theta = 77.5 Degrees.

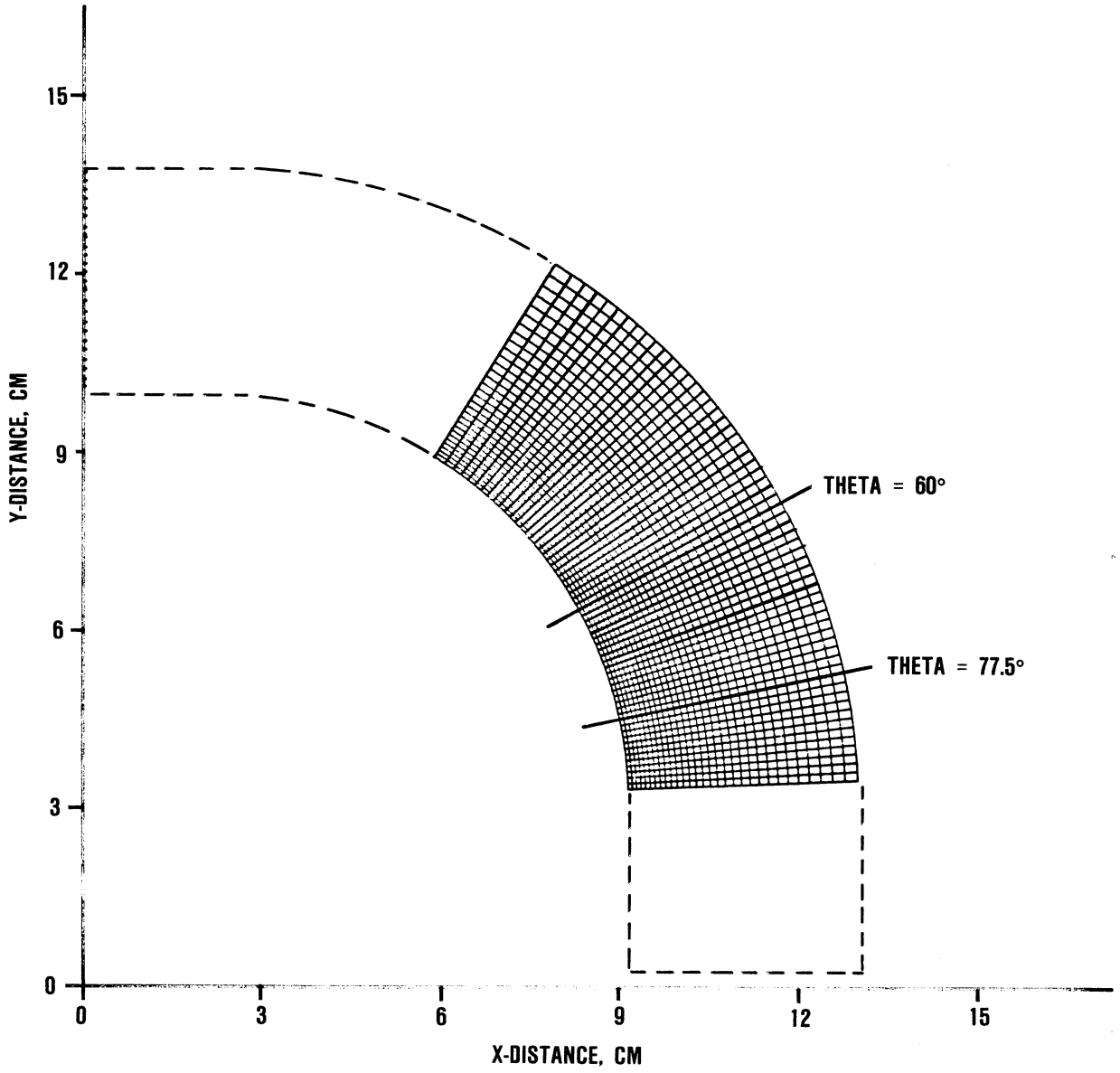

Figure 4-10. Computational Grid for Partial Duct Laminar Flow.

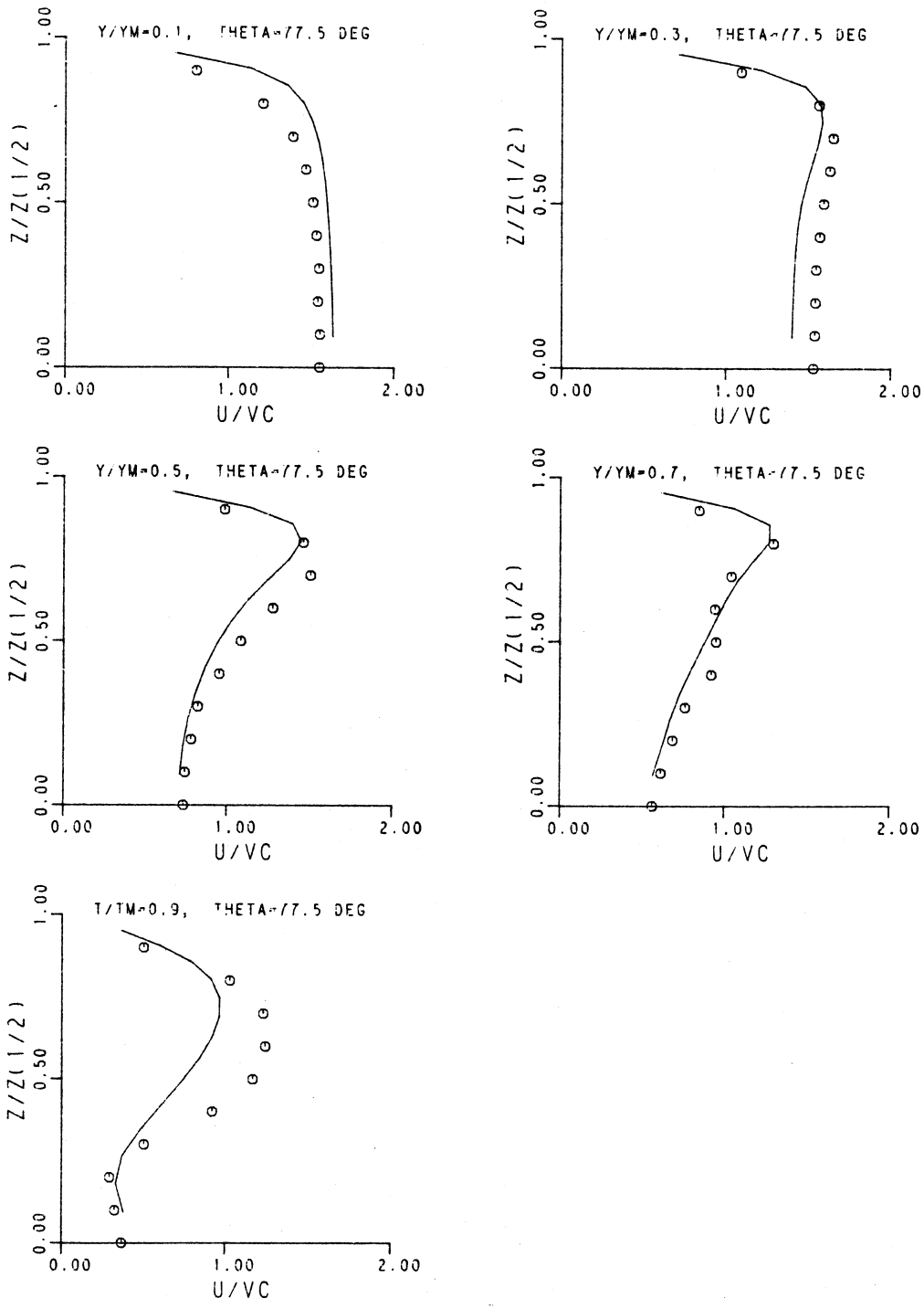

Figure 4-11. Comparison of Axial Velocities for Partial Duct Laminar Flow.

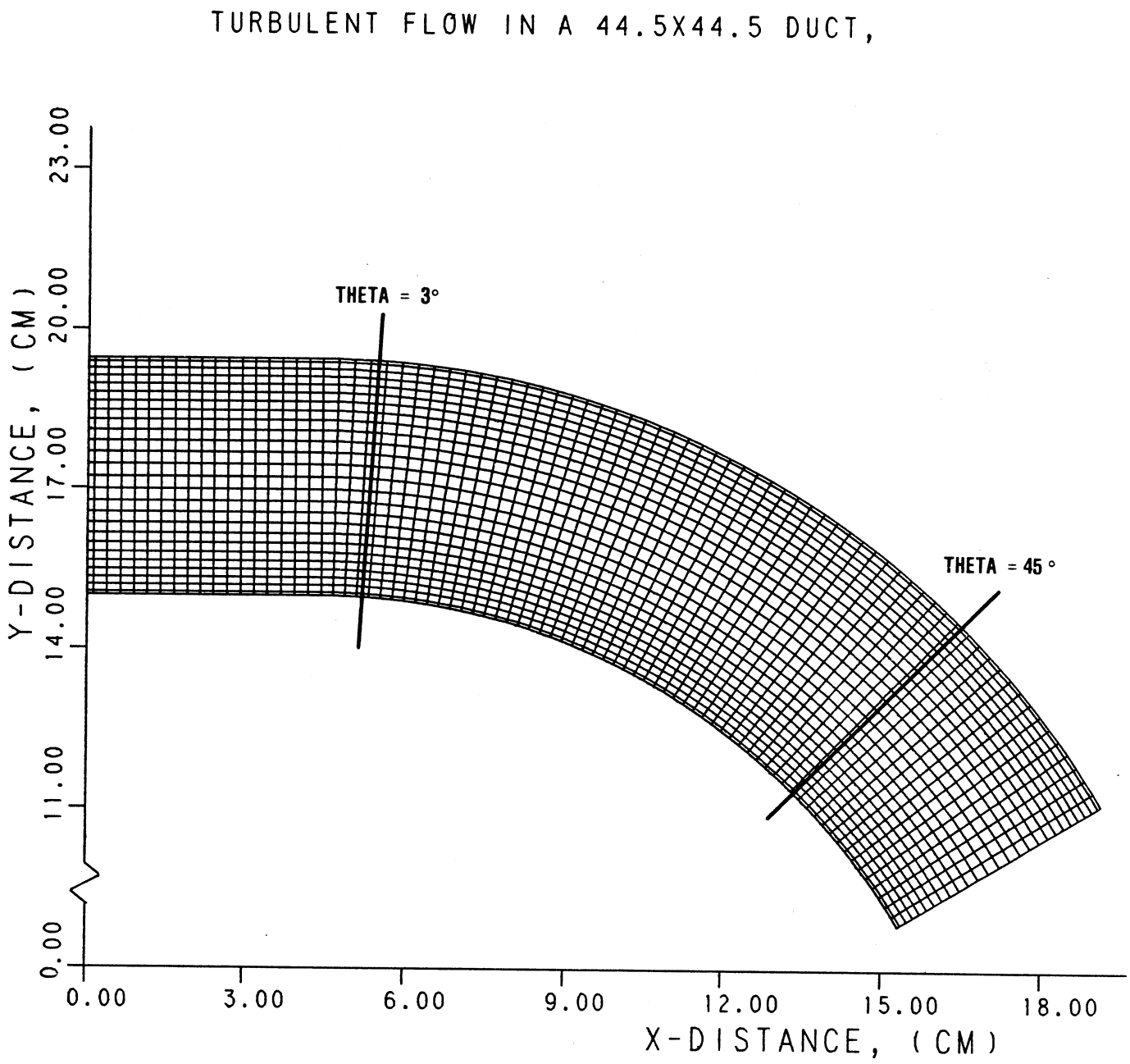

Figure 4-12. Computational Grid for 60 Degree Turbulent Duct Flow.

scale were also required for this case. Since u' and v', the fluctuating components in the streamwise and radial directions were measured, the kinetic energy was easily calculated from its definition,

$$k = \frac{\overline{(u')^2}+\overline{(v')^2}+\overline{(w')^2}}{2}$$

where w' was assumed to be equal to v'. Also needed was turbulent length scale, however, it was not provided. Rather than assume a value based on other experimental data for similar flows, a profile that was compatible with the mean velocity and turbulent kinetic energy fields was calculated.

It was assumed that upstream of the entrance to the curved duct, cross-stream and radial variations in the flow are much greater than streamwise ones and that diffusion was small. Under these assumptions the equation for turbulent kinetic energy reduces to simply production equals dissipation or,

$$\mu_t P = \rho\varepsilon$$

For the flow conditions stated above, the production term is given by,

$$\mu_t P = \mu_t \left[2 \left(\frac{\partial U}{\partial Y}\right)^2 + \left(\frac{\partial U}{\partial z}\right)^2 \right]$$

where the mean streamwise velocity gradients in the radial and cross-stream directions were determined from bicubic spline fits of the experimental data. Since the dissipation is related to the length scale through,

$$\varepsilon = \frac{C\mu k^{3/2}}{l_s}$$

and,

$$\mu_t = \rho C_\mu \frac{k^2}{\varepsilon}$$

the length scale was calculated from the following expression:

$$l_s = \sqrt{\frac{C\mu k}{2\left(\frac{\partial U}{\partial Y}\right)^2 + \left(\frac{\partial U}{\partial Z}\right)^2}}$$

This case was first analyzed using the k-ε model. Comparisons of the mean streamwise velocity at the 3 and 45 degree measurement stations are shown in Figures 4-13a and 4-13b. The velocities have also been normalized by the bulk velocity but are plotted against the normalized radial coordinate which is measured from the inner wall rather than from the outer as was done for the laminar case. The profiles are for different transverse locations ranging from Z/(DH/2) = 0.0 which is the duct centerline to Z/(DH/2) = 0.75 which is close to a side wall. DH is the duct height (and width) and is equal to 44.5mm. The agreement is poorer than for the laminar flow, because of the added complexity of turbulent flow.

Running the same flow situation with the same grid network but using the ARSM produced the comparison shown in Figures 4-14a and 4-14b. An item of particular significance in these plots is the virtually identical predicted mean velocity profiles compared to the standard k-ε model, despite the non-isotropic nature of the ARSM. This behavior can be partially attributed to the dominance of the convective terms. Over a majority of the flow field, the net convective terms are from 2 to 10 times the value of the net diffusion, thus changes in the viscosity must be large to impact the velocity field.

Another factor is the estimated truncation error that is the same order as the net physical diffusion. The numerical diffusion may be dominating changes in the effective viscosity which result from the ARSM.

To assess the program in a turbulent flow situation with more than 60 degrees of curvature, a second curved duct flow was analyzed. This was a turbulent counterpart of the laminar flow discussed above and was of an identical geometry. The complete 90 degree bend with entrance and exit sections was analyzed using both the k-ε and ARSM.

Figures 4-15a and 4-15b show comparisons of mean velocity at selected stations for the k-ε model. As with the laminar flow the velocities have been normalized with respect

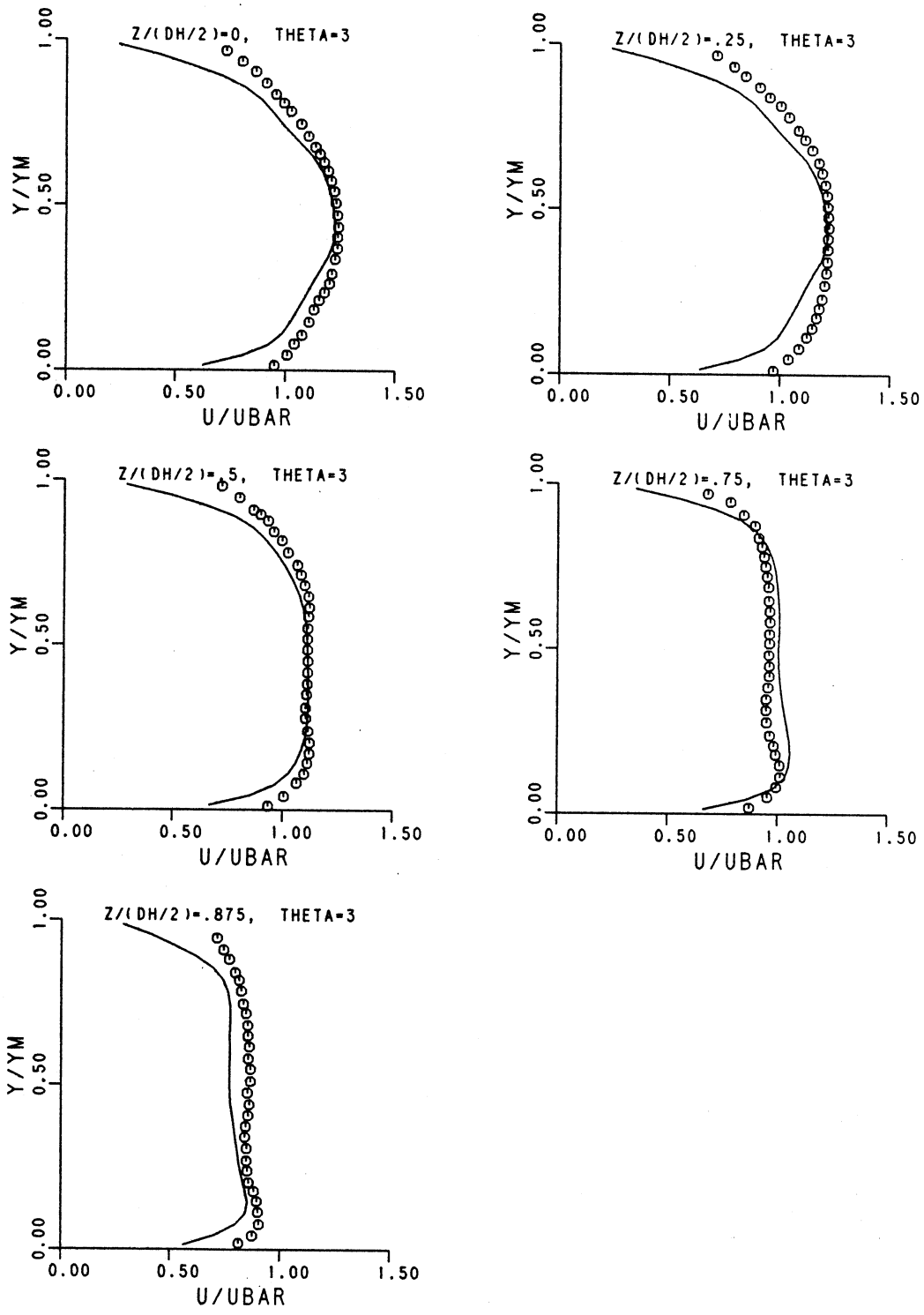

Figure 4-13a. Axial Velocity Comparison for 60 Degree Turbulent Duct Flow, K-ε Model, Theta=3 Degrees.

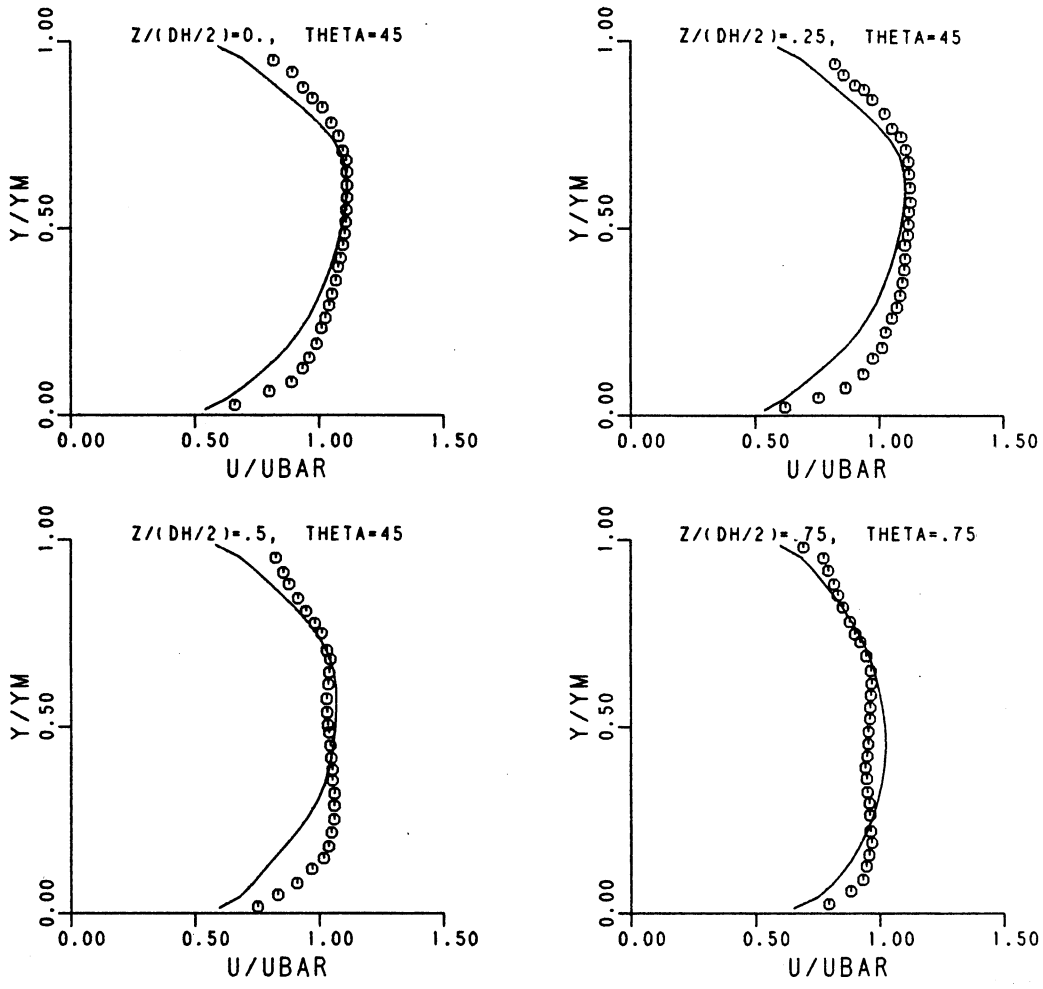

Figure 4-13b. Axial Velocity Comparison for 60 Degree Turbulent Duct Flow, K-ε Model, Theta=45 Degrees.

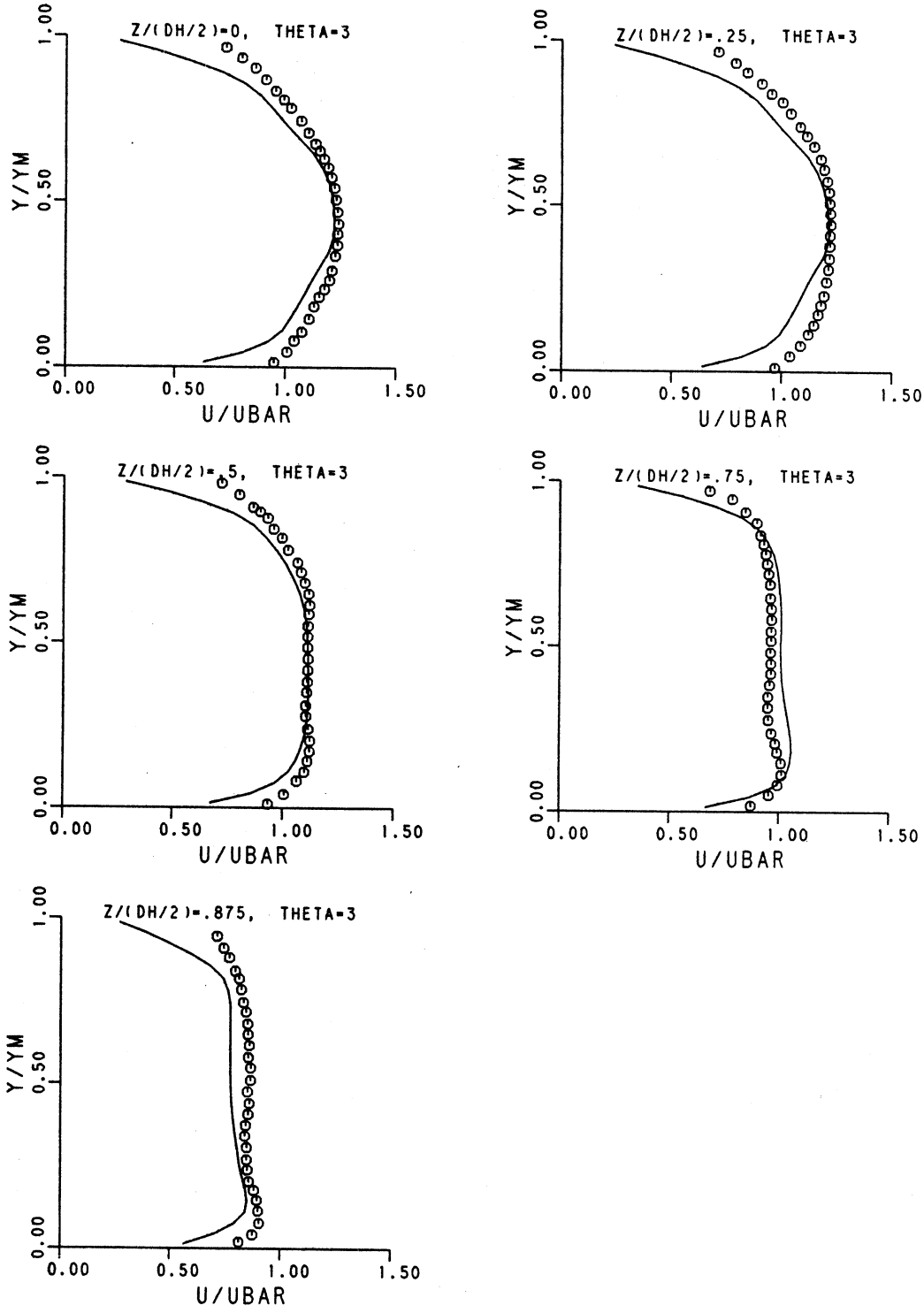

Figure 4-14a. Axial Velocity Comparison for 60 Degree Turbulent Duct Flow, ARS Model, Theta=3 Degrees.

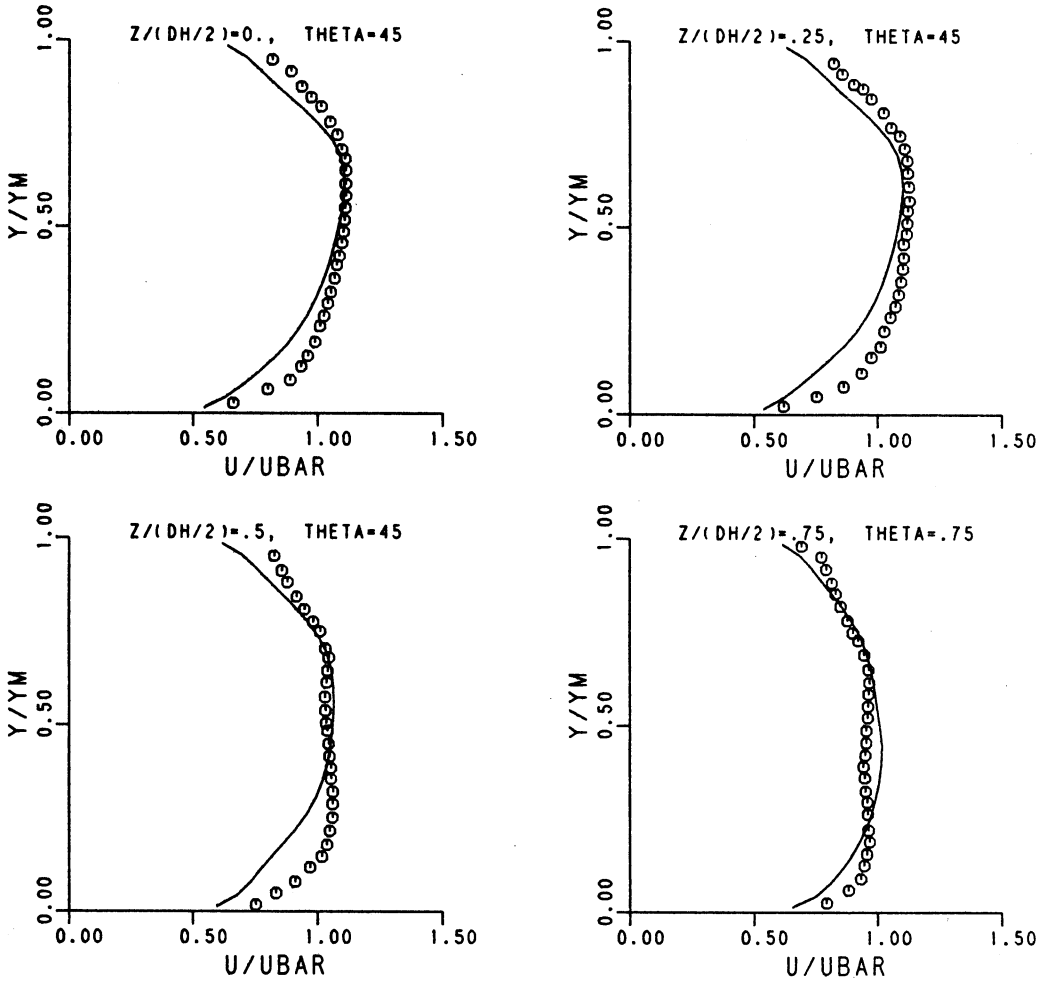

Figure 4-14b. Axial Velocity Comparison for 60 Degree Turbulent Duct Flow, ARS Model, Theta=45 Degrees.

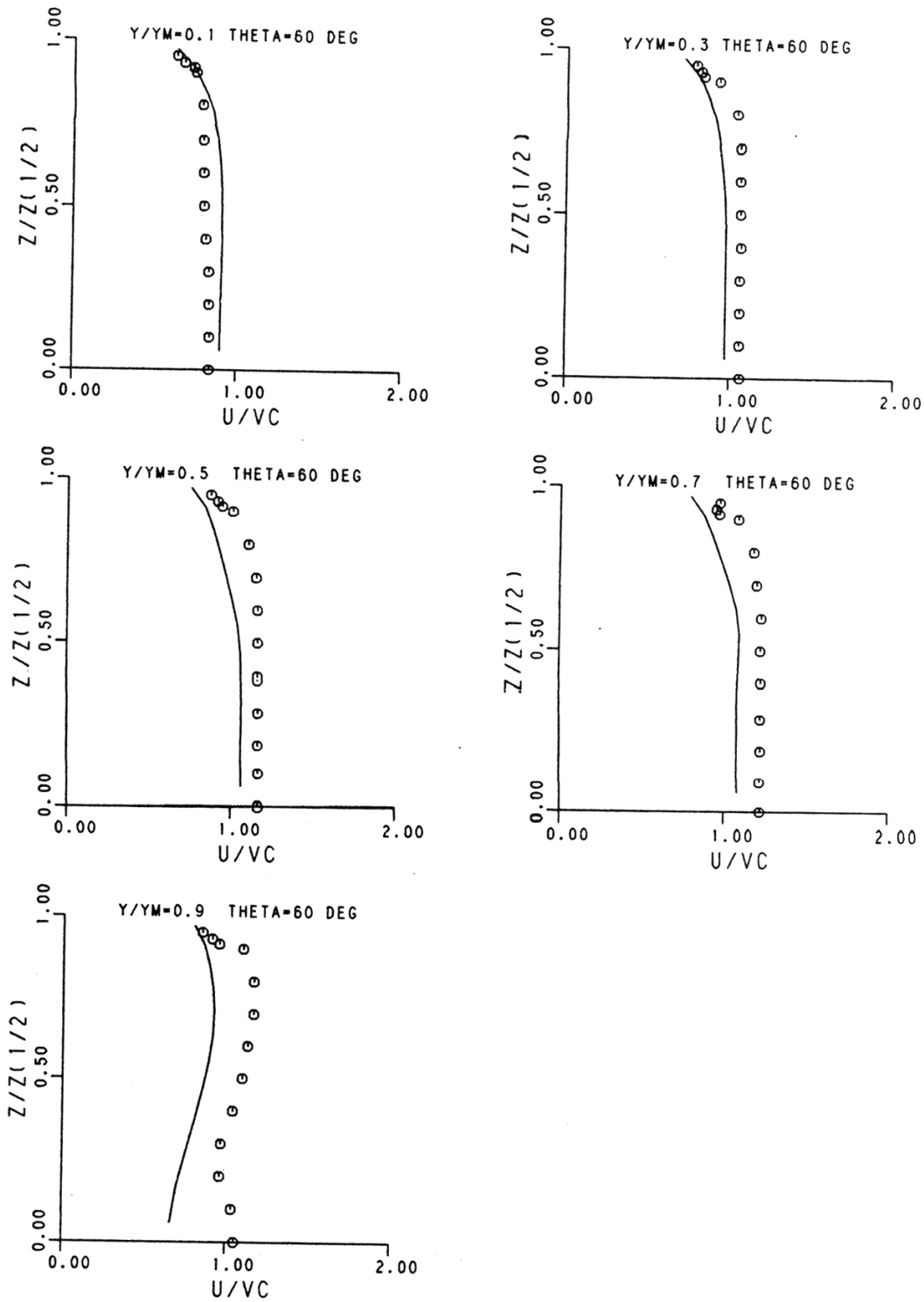

Figure 4-15a. Comparison of Axial Velocity for 90 Degree Turbulent Duct Flow, K-ε Model, Theta=60 Degrees.

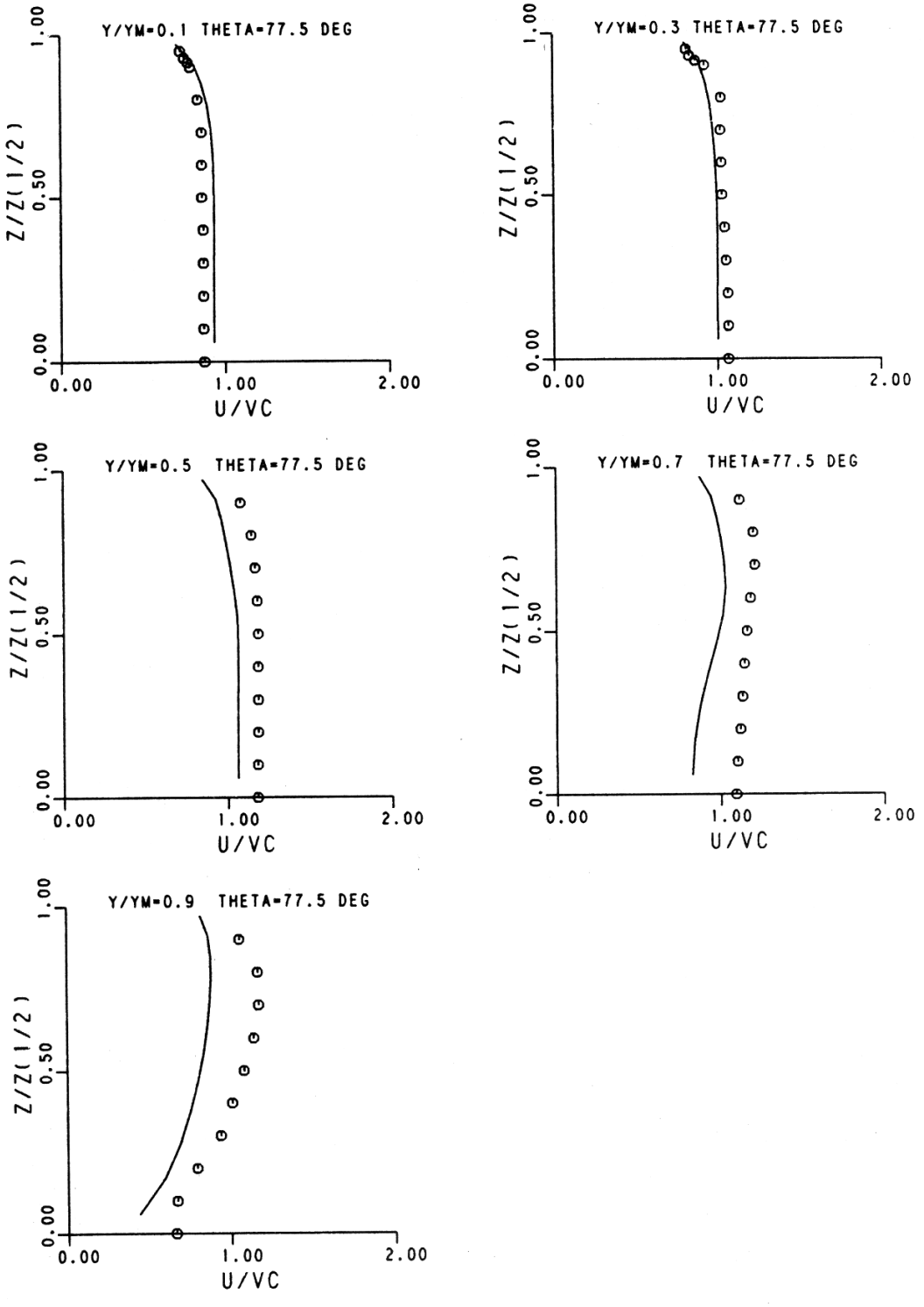

Figure 4-15b. Comparison of Axial Velocity for 90 Degree Turbulent Duct Flow, K-ε Model, Theta=77.5 Degrees.

to the bulk velocity and they are plotted against a normalized transverse coordinate. Figures 4-16a and 4-16b show the ARSM counterpart at the same stations. Again, there is almost no difference in the predicted mean velocity profiles for similar reasons as mentioned above. Plots of turbulent quantities from the ARSM are shown in Figures 4-17a and 4-17b and are typical of comparisons throughout the duct.

The first jet mixing test case selected was an opposed injection into an accelerating symmetric duct with a momentum flux ratio of 6.68. This particular momentum flux ratio was chosen because it is representative of values found in actual transition liner dilution zones. The orifice diameters were 25.4mm with a spacing of 50.8mm for both upper and lower orifice rows. The plane geometry duct had an initial height of 152.4mm and converged to a height of 50.8mm. At the orifice location, the height was 101.6mm, giving an orifice spacing-to-height ratio of 0.25.

Figures 4-18a and 4-18b show the computed grid which is a 53 x 29 X-Y system while 19 nodes were distributed in the Z-direction. The orifices located in the upper and lower walls were each represented by 69 grid nodes. Inlet profiles for the mainstream and the dilution jets were taken to be uniform. In the Z-direction, cyclic boundary conditions were employed, but because of the symmetry of the flow they reduced to symmetry planes when the solution converged.

The comparison of temperature measurements and predictions is presented in terms of theta, which here represents a nondimensional temperature based on the average upstream temperature (T_{main}), the jet temperature (T_{jet}) and is defined as,

$$\text{Theta} = \frac{T_{main} - T}{T_{main} - T_{jet}}$$

Profiles at various Z or transverse stations for two different axial locations are shown in Figures 4-19a and 4-19b for a case using the k-ε turbulence model. Theta is plotted against the vertical distance as measured from the upper wall normalized by the local duct height. The Z location is normalized by the spacing (S = 50.8 mm, Z/S = 0.0 corresponds to the centerline of the jets) and the axial position downstream from the jets is normalized by the duct height (H_o = 101.6mm) at X = 0.0.

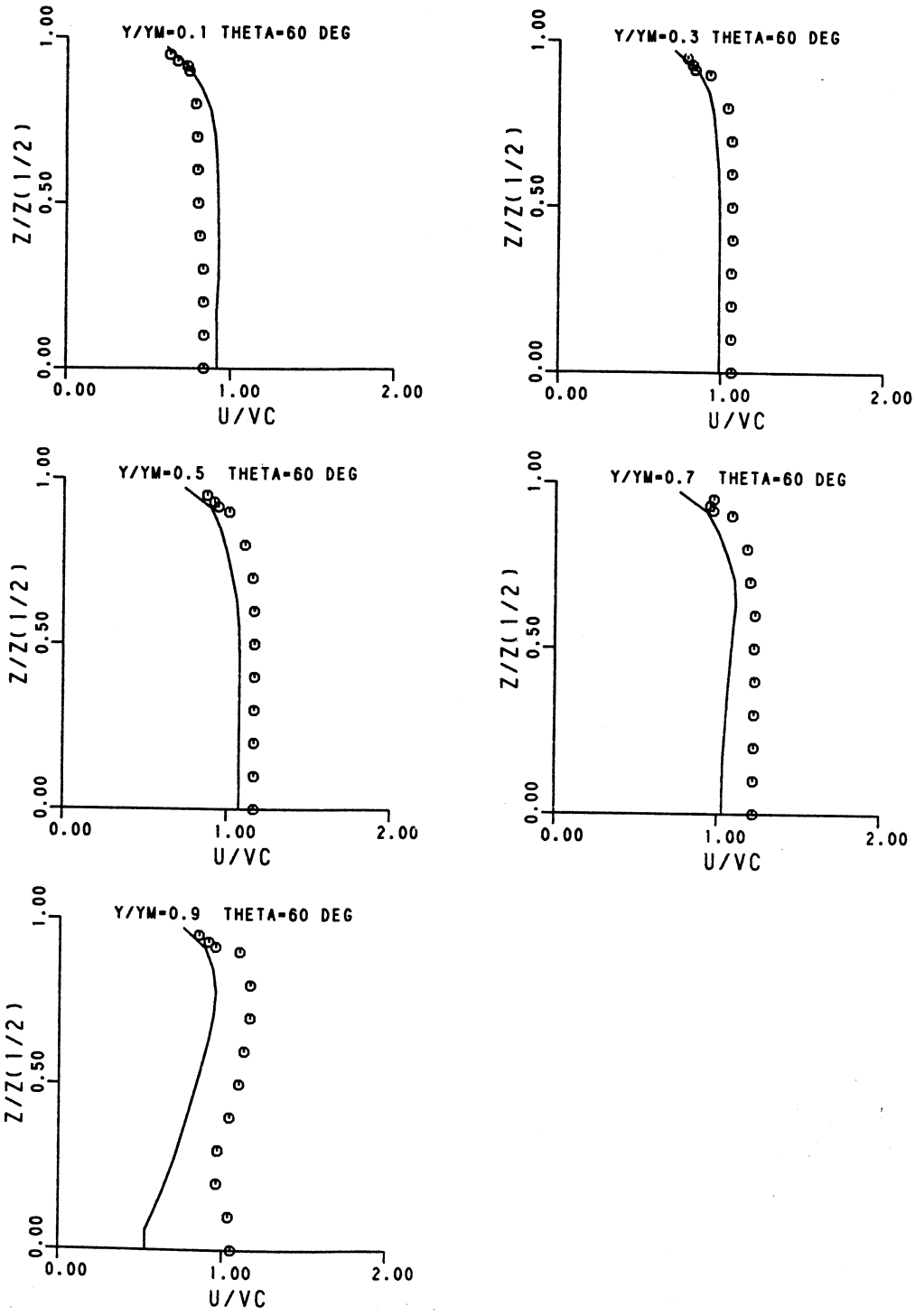

Figure 4-16a. Comparison of Axial Velocity for 90 Degree Turbulent Duct Flow, ARS Model, Theta=60 Degrees.

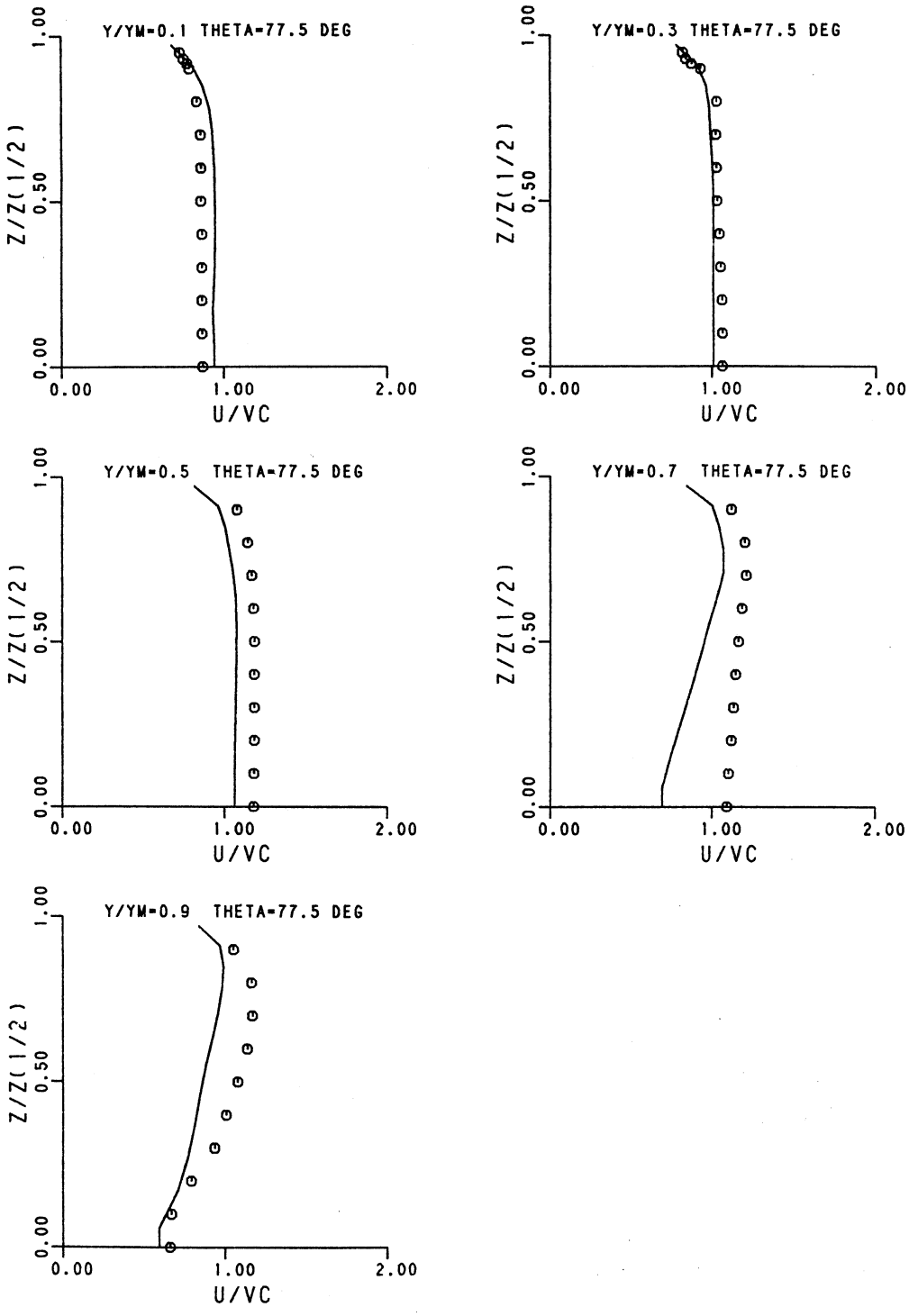

Figure 4-16b. Comparison of Axial Velocity for 90 Degree Turbulent Duct Flow, ARS Model, Theta=77.5 Degrees.

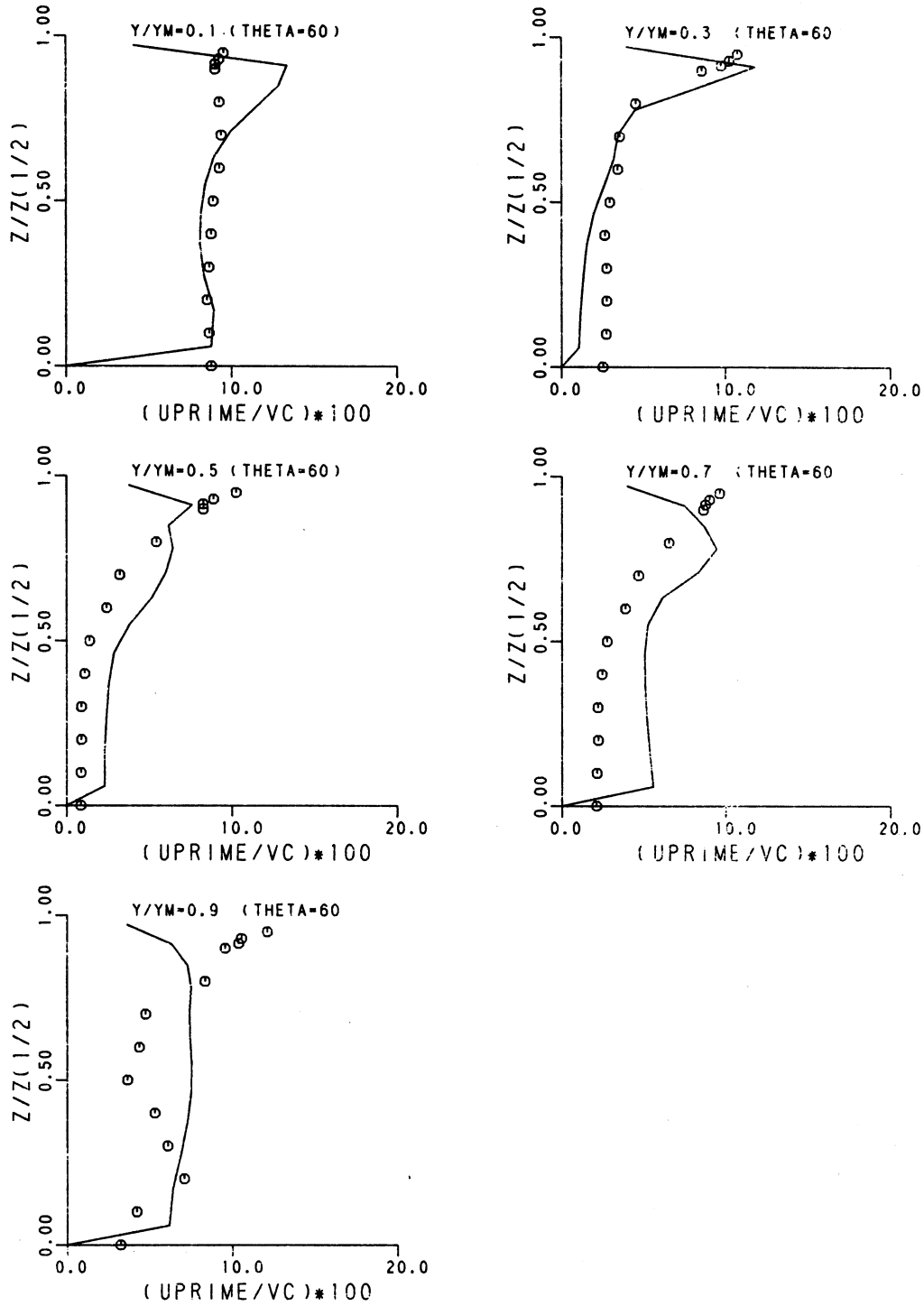

Figure 4-17a. Comparison of u-Prime for 90 Degree Transient Duct Flow, ARS Model, Theta=60 Degrees.

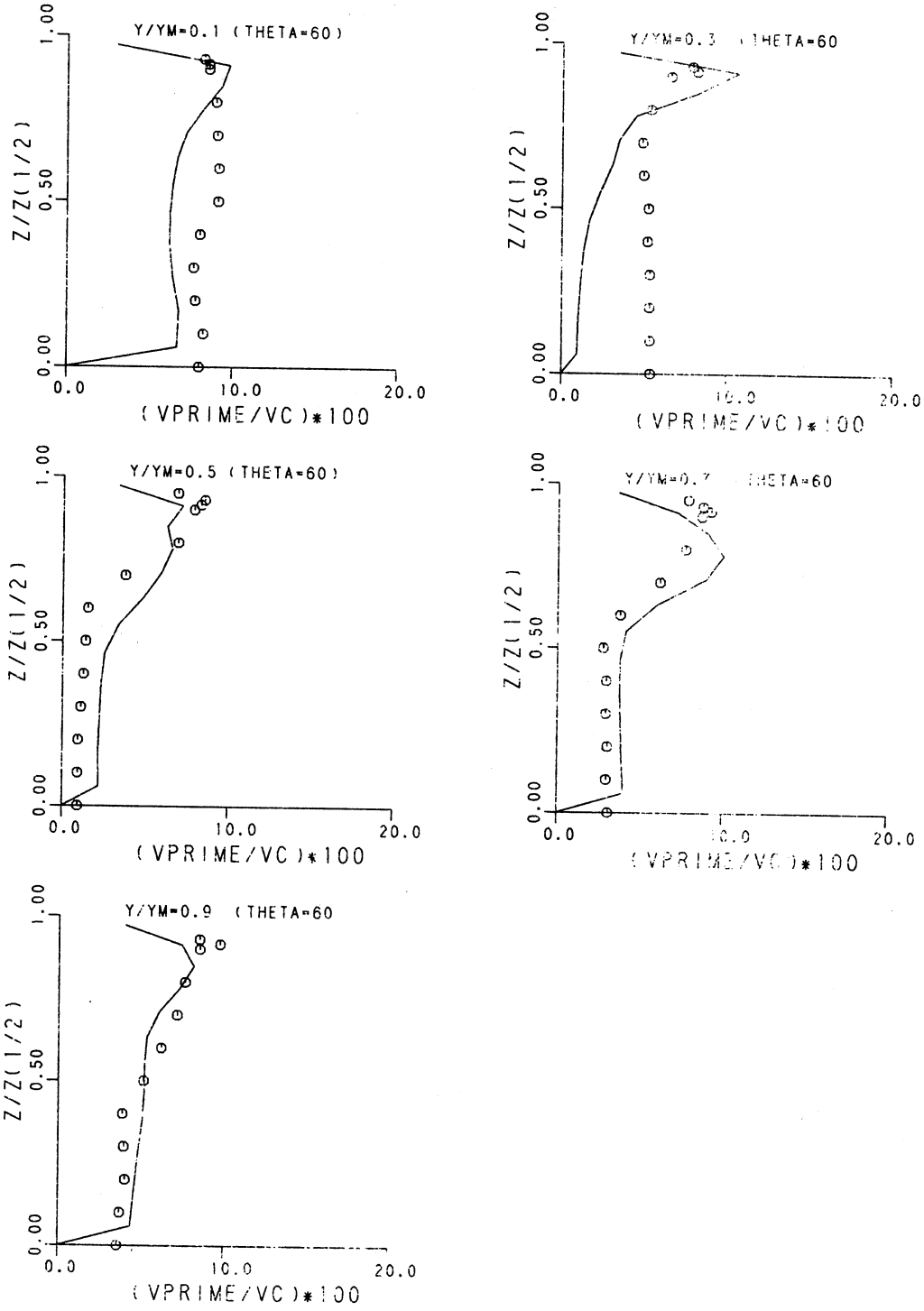

Figure 4-17b. Comparison of v-Prime for 90 Degree Turbulent Duct Flow, ARS Model, Theta=60 Degrees.

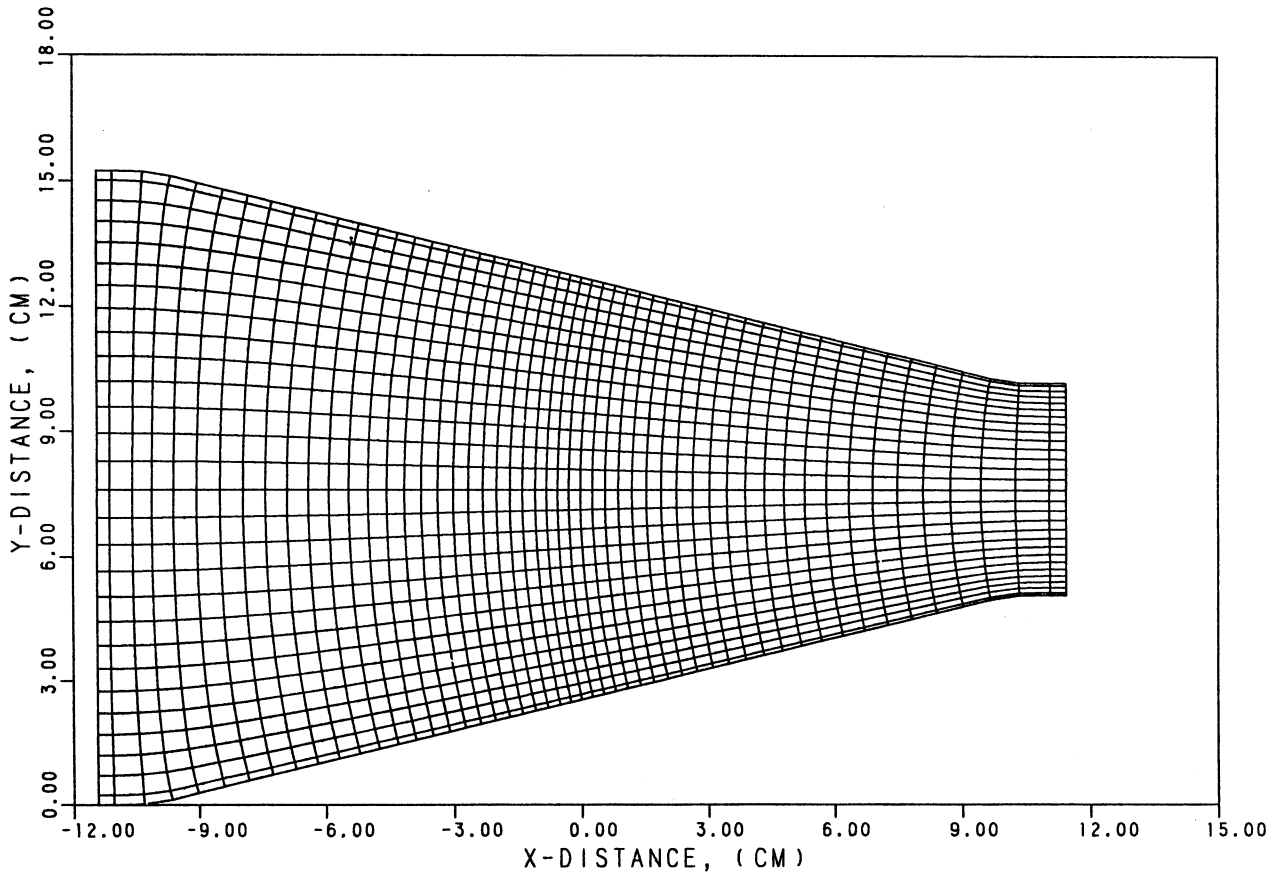

Figure 4-18a. Computational Grid for Converging Duct Double Sided Injection, X-Y Plane.

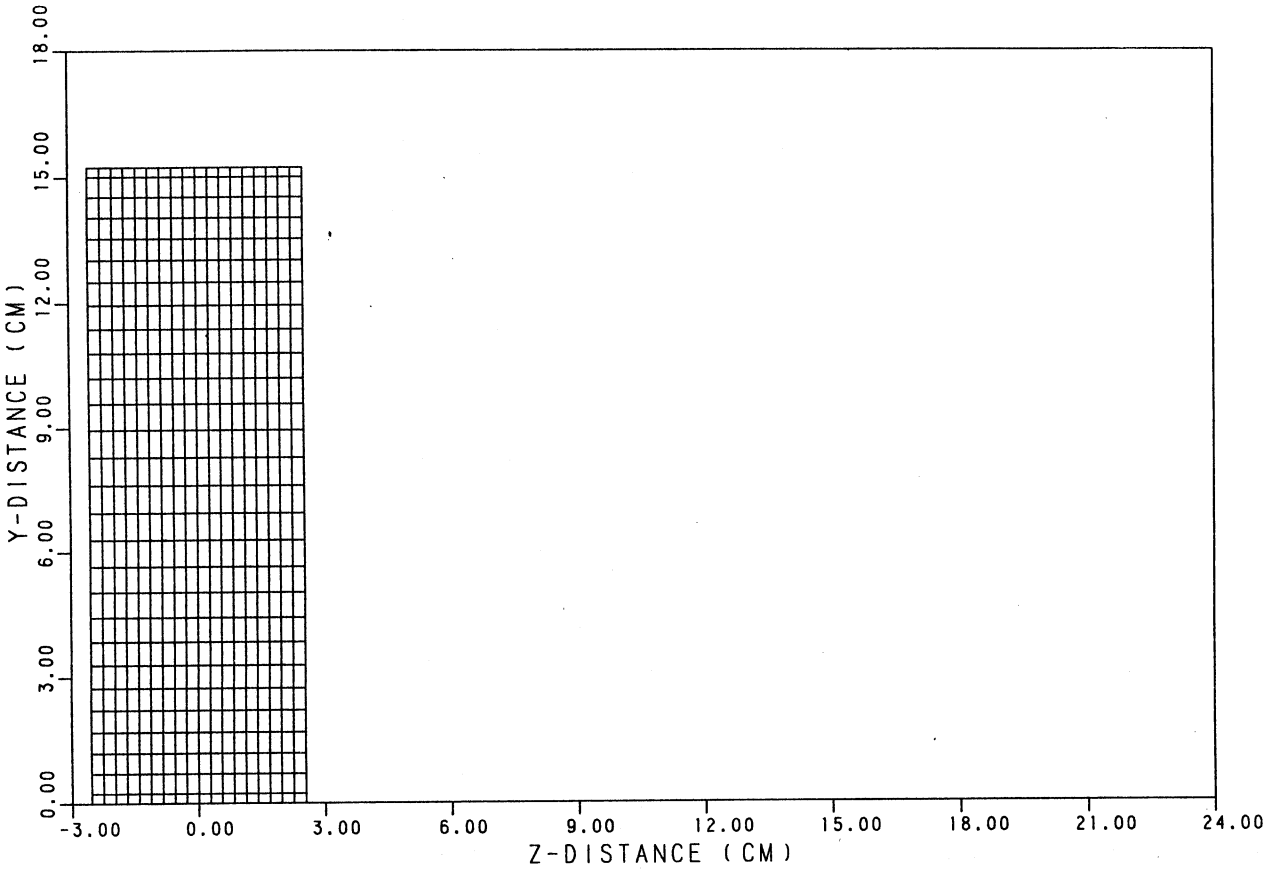

Figure 4-18b. Computational Grid for Converging Duct Double Sided Injection, X-Y Plane.

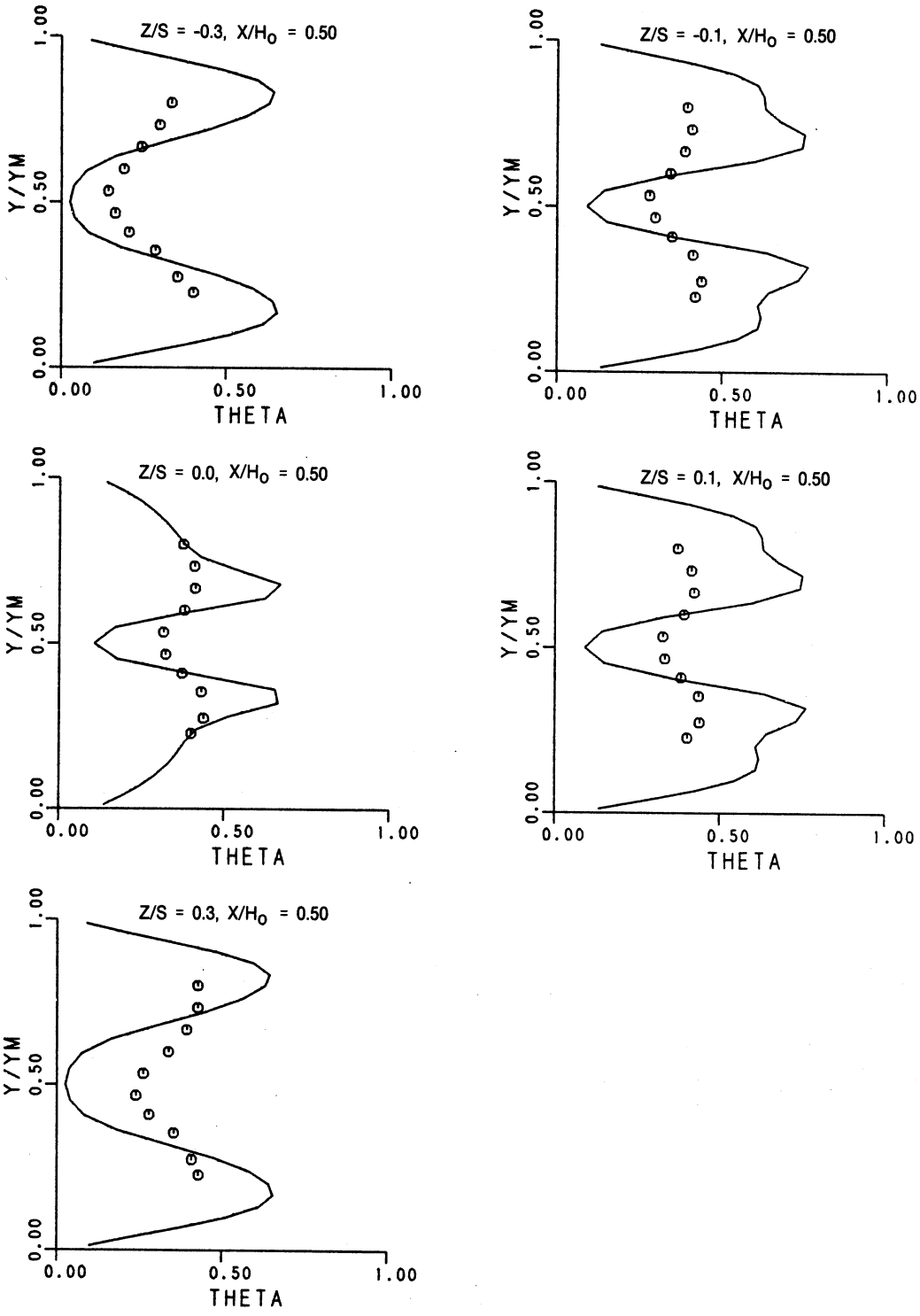

Figure 4-19a. Comparison of Theta for Double Sided Injection in Converging Duct, K-ε Model, X/H_O=0.5.

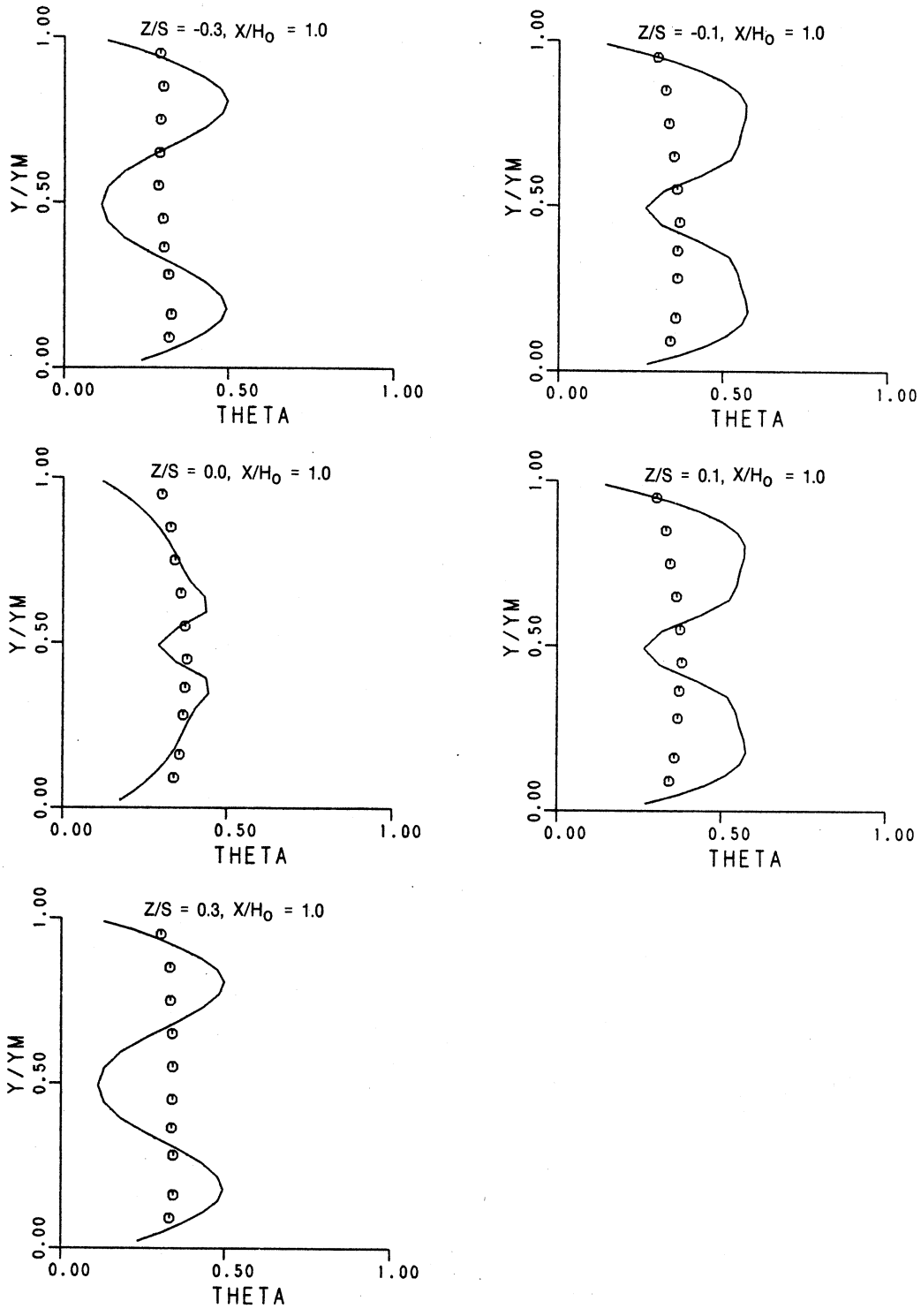

Figure 4-19b. Comparison of Theta for Double Sided Injection in Converging Duct, K-ε Model, X/H_O=1.0.

Figures 4-20a and 4-20b show the corresponding velocity profiles at the same locations for which theta was presented. The agreement is reasonable although it tends to deteriorate at the last axial station.

Assessment Case 3 was rerun using the ARSM. Examples of temperature and mean axial velocity compared to the measured data are shown in Figures 4-21a and 4-21b. Slight improvements in the theta profiles can be discerned, however the overall characteristic of under predicting the mixing rate remains.

Further assessments of the TMM were made by analyzing another jet mixing case which used the same accelerating duct geometry but only single sided injection with a momentum flux ratio of 26.7. Comparisons of theta and velocity for the k-ε model are shown in Figures 4-22a and 4-22b. Again the lower predicted mixing rate is apparent. When the ARSM is used for this case, the results are as shown in Figures 4-23a and 4-23b. The influence of the ARSM is somewhat stronger than observed for the double sided injection, however it is insufficient to produce good correlation with the data.

The reasons for the poor comparison between the measurements and predictions that have been seen for the single and double sided jet mixing cases need to be identified. Errors in numerical predictions for turbulent flows have been historically attributed to either the numerical scheme which introduces numerical diffusion or inadequacies in the particular turbulence model used. If numerical diffusion is present in a solution, it is usually manifested as an enhancement to the total diffusion resulting in a smearing or smoothing of the predicted profiles. In the TMM analysis of the jet mixing cases, steeper profiles were consistently seen in the predicted results as compared to the data. From this observation, it was concluded that any numerical diffusion present in the solution is not dominating the flow field and that deficiencies in the turbulence model must be the primary source of measurement-prediction anomalies.

As an exercise to test the sensitivity of the predicted profiles to cross-stream diffusion, the single sided injection case was rerun using the k-ε model but with the program code altered so that the cross-stream viscosity components were multiplied by a factor of 10. The results of this exercise are shown in Figure 4-24, where it can be seen that the predicted profiles assume the more two dimensional character seen in the data, further indicating that the turbulence model is the primary source of error in the TMM.

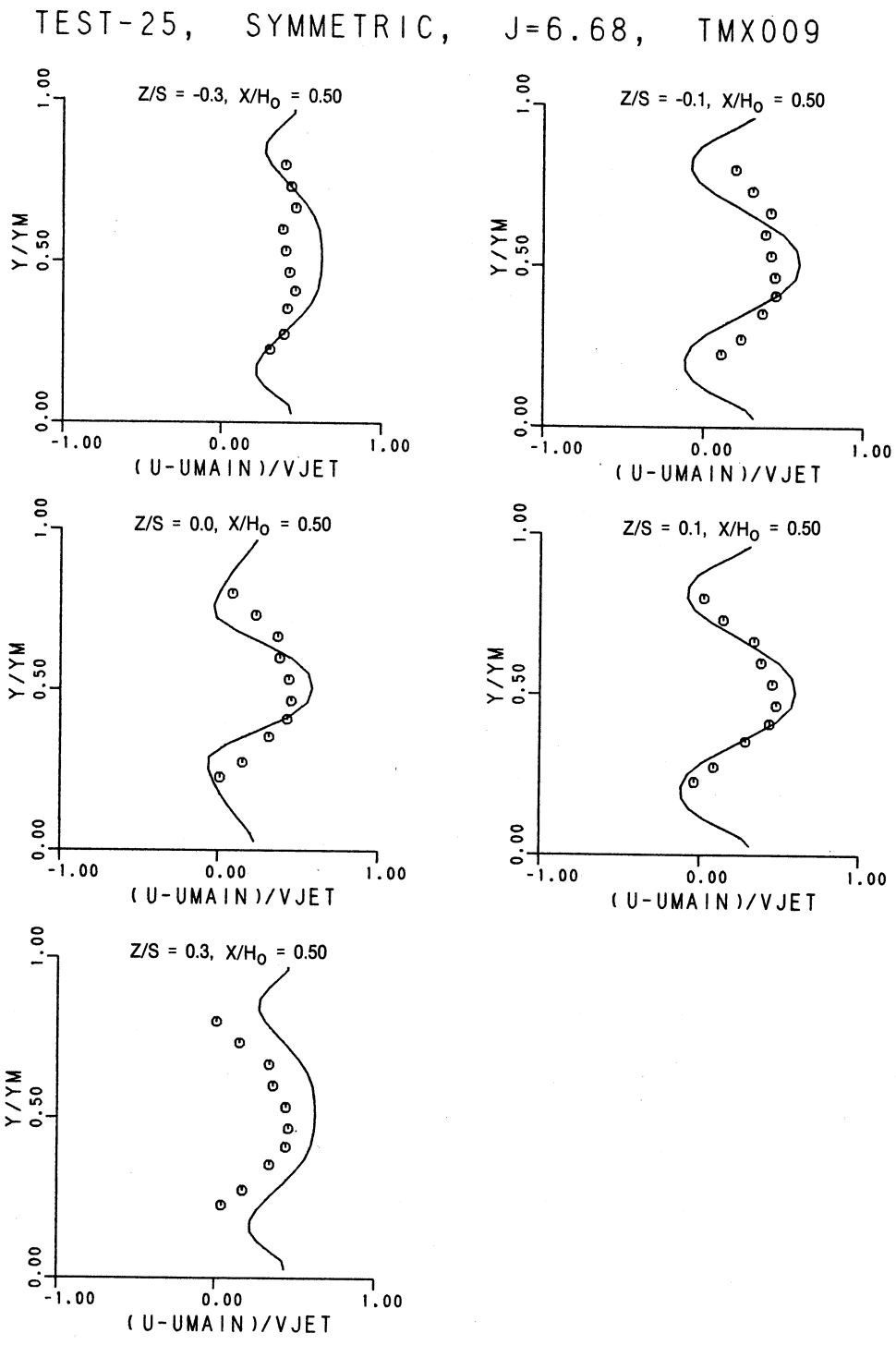

Figure 4-20a. Comparison of Axial Velocity for Double Sided Injection in Converging Duct, K-ε Model, X/H_O=0.5.

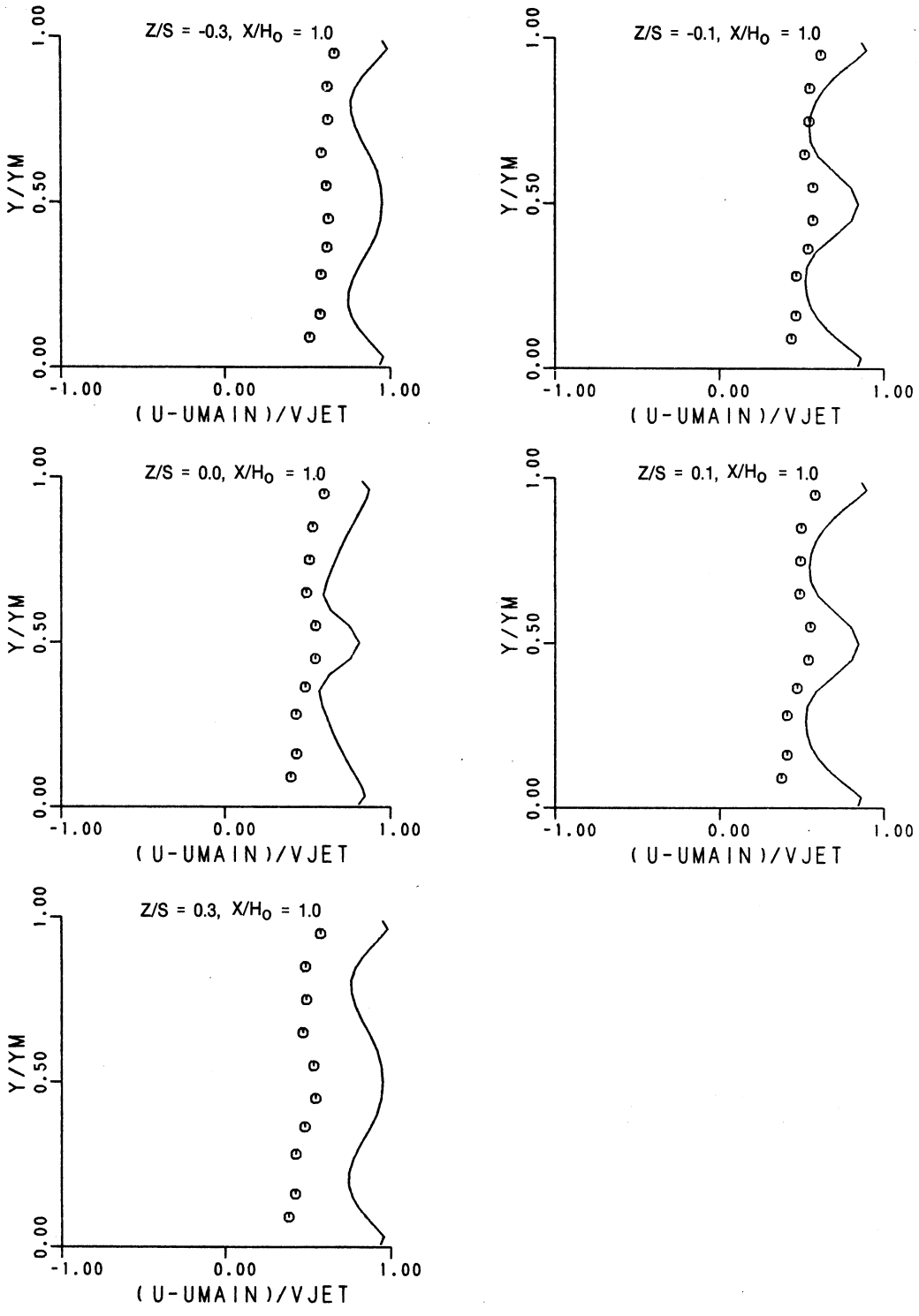

Figure 4-20b. Comparison of Axial Velocity for Double Sided Injection in Converging Duct, K-ε Model, X/H_O=1.0.

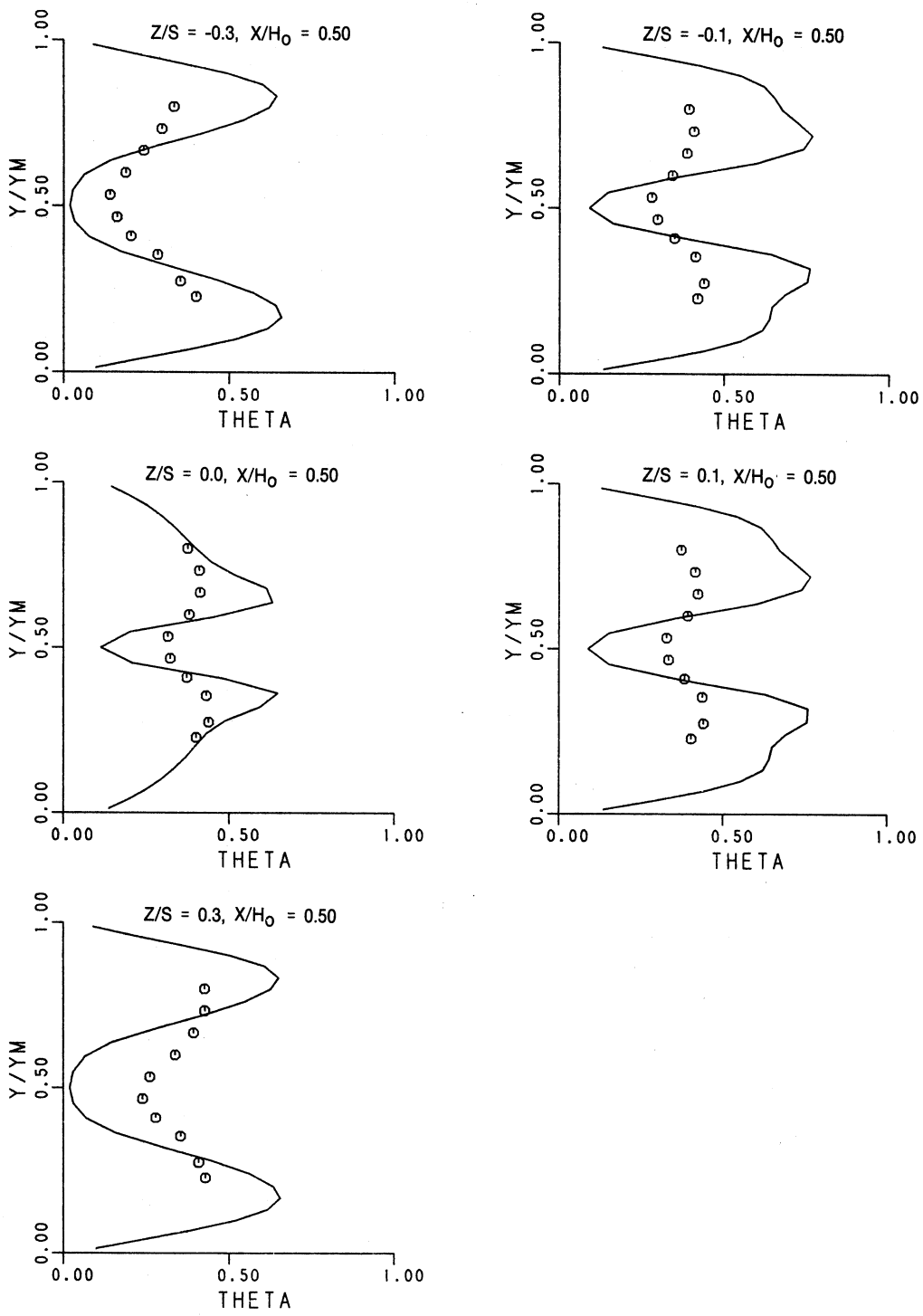

Figure 4-21a. Comparison of Theta for Double Sided Injection in Converging Duct, ARS Model, X/H_O=0.5.

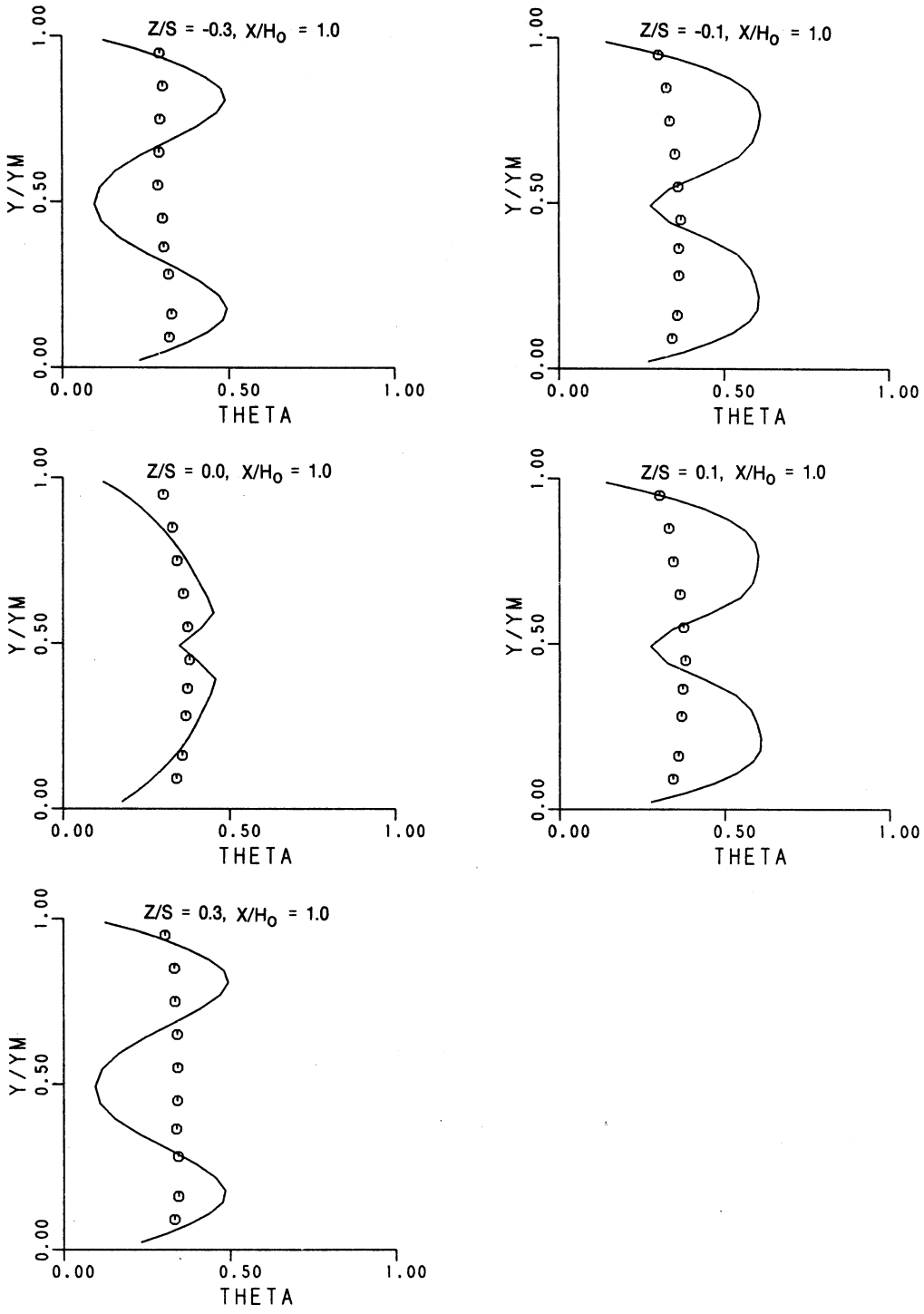

Figure 4-21b. Comparison of Theta for Double Sided Injection in Converging Duct, ARS Model, X/H_O=1.0.

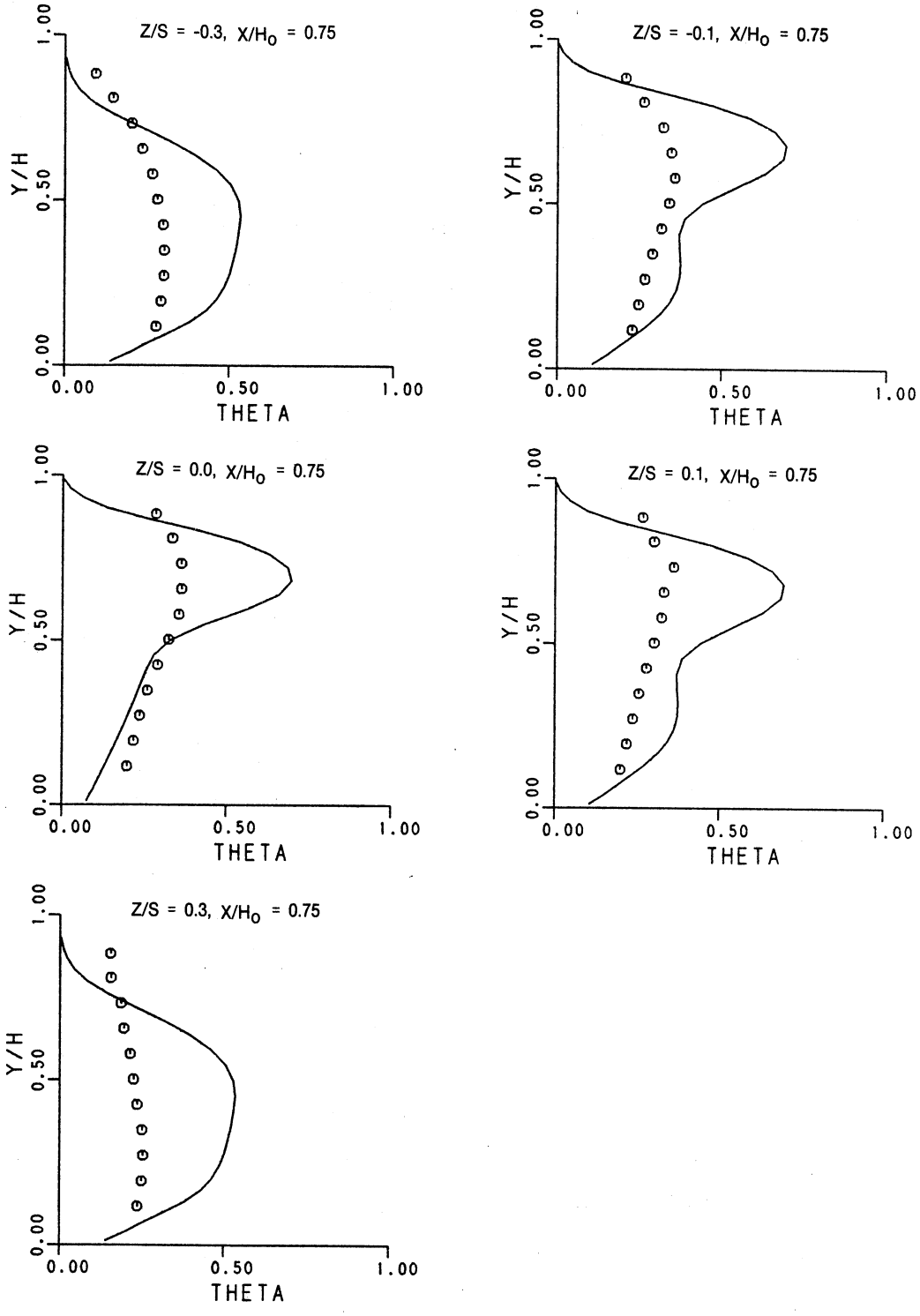

Figure 4-22a. Comparison of Theta for Single Sided Injection in Converging Duct, K-ε Model, X/H_O=0.75.

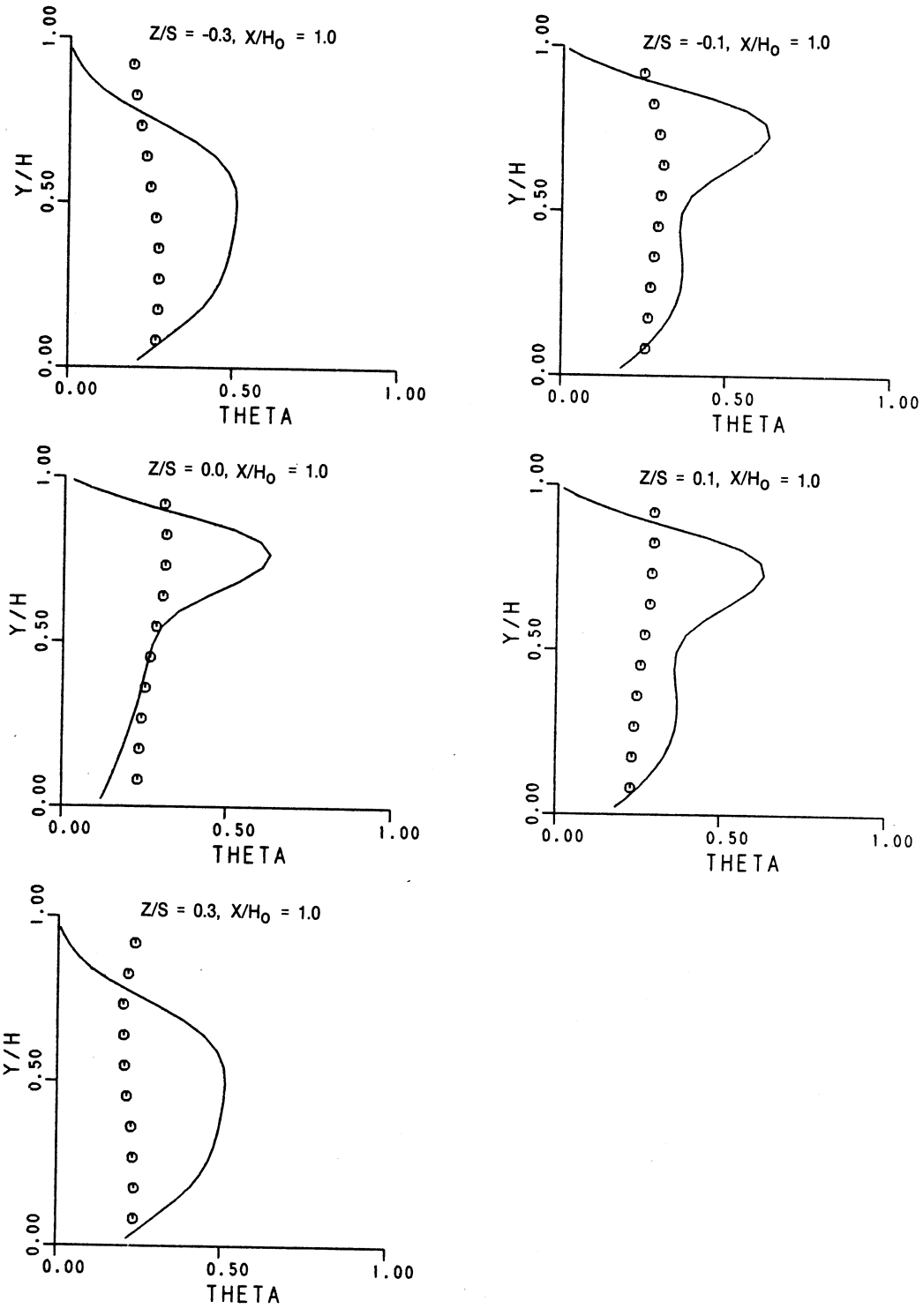

Figure 4-22b. Comparison of Theta for Single Sided Injection in Converging Duct, K-ε Model, X/H_O=1.0.

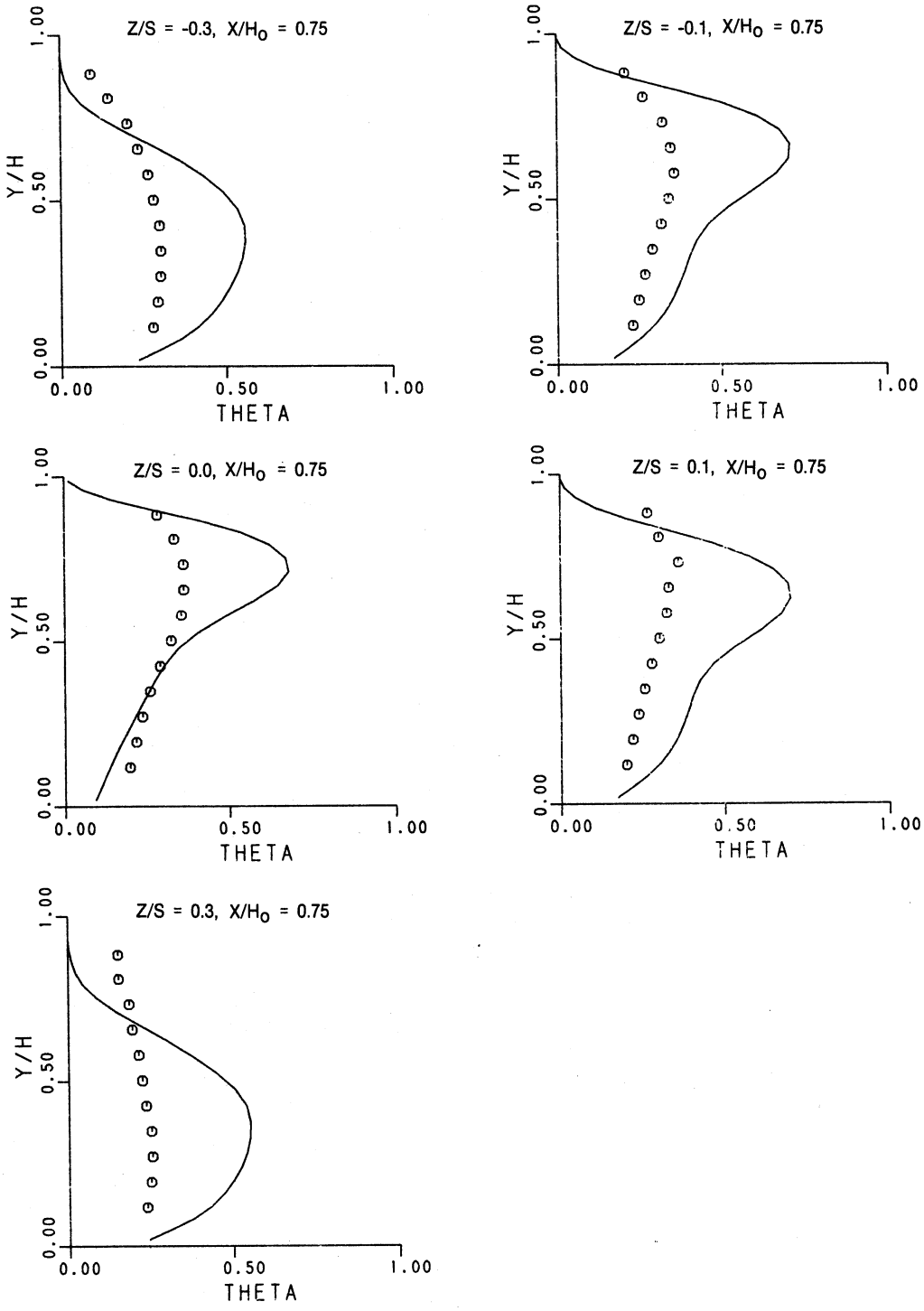

Figure 4-23a. Comparison of Theta for Single Sided Injection in Converging Duct, ARS Model, X/H_O=0.75.

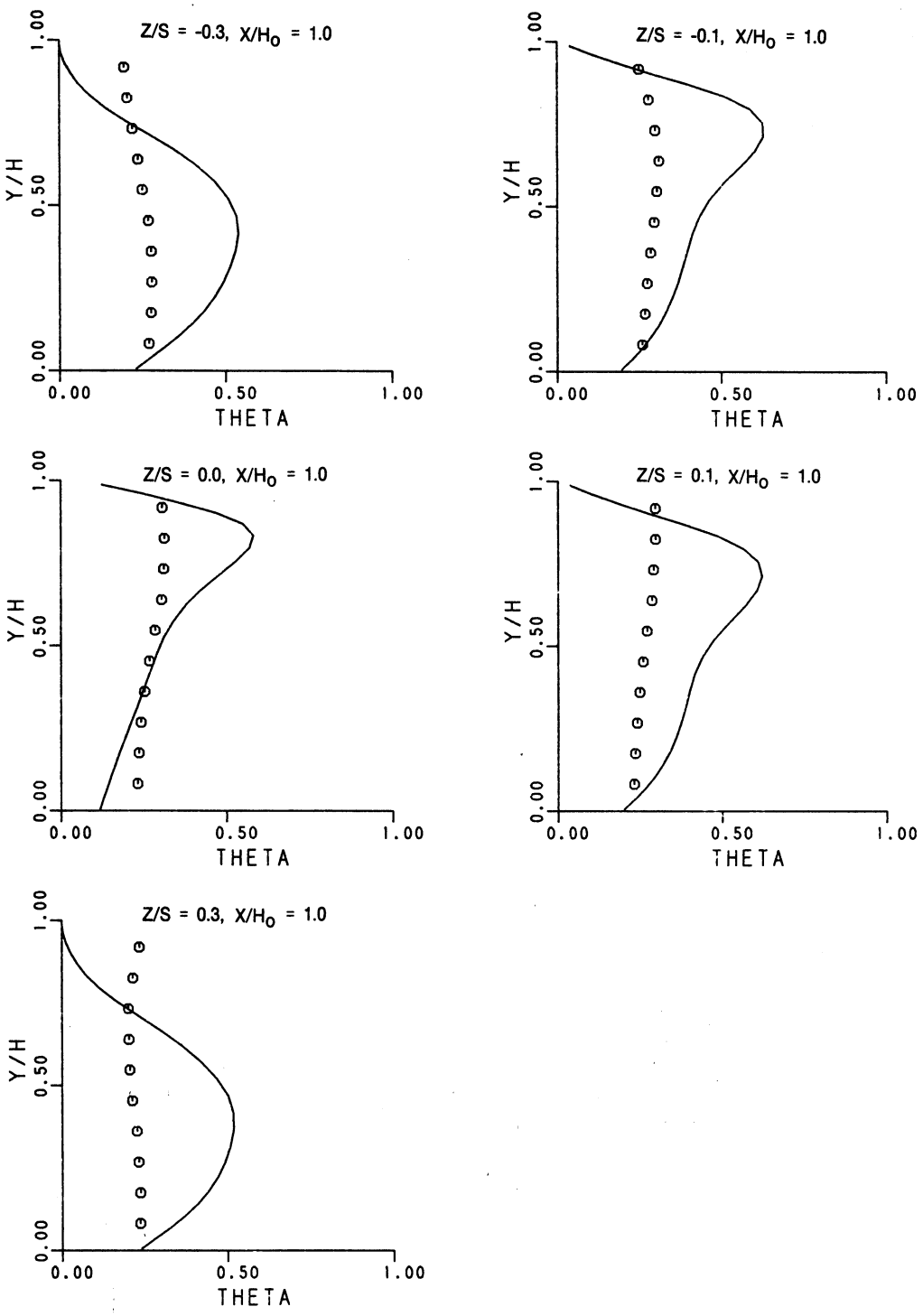

Figure 4-23b. Comparison of Theta for Single Sided Injection in Converging Duct, ARS Model, X/H_O=1.0.

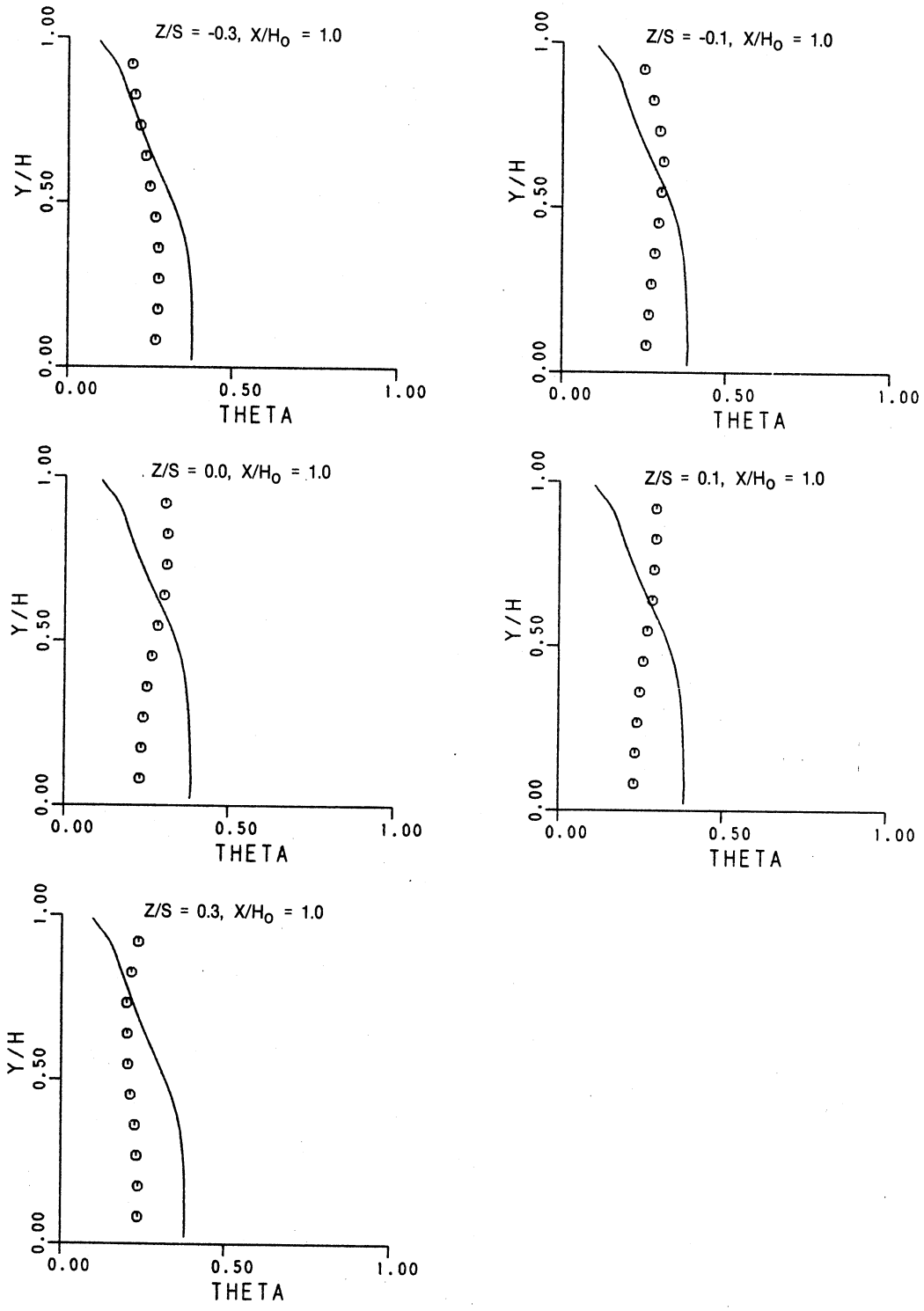

Figure 4-24. Comparison of Theta for Single Sided Injection Duct, K-ε Model with 10x Cross-Stream Diffusion, X/H_O=1.0.

The next series of assessment cases for the TMM was concerned with the injection of radial jets into a curved duct which simulated a typical transition liner. The geometry for this case, (References 16 and 17), is illustrated by the computational grid which is shown in Figure 4-25a and 4-25b. The X-Y plane used 72 x 32 nodes respectively while 13 nodes were used in the circumferential direction. Heated air entered the transition section from the upper left, was turned 180 degrees and exited at the lower right.

The first case analyzed had a radial jet with a momentum flux ratio of 9.8 located along the outer wall. Figure 4-26 shows contours of temperature for a plane through the centerline of the jet. Superimposed on this plot is the location of the minimum temperature at several stations as measured by a thermocouple probe and thus defines the jet centerline. A second case was also run wherein the radial jet was located along the inner wall. A comparison of the predicted temperature contours and the measured jet centerline are shown in Figure 4-27.

The final assessment case involved the calculation of the radiation flux within a square 2-dimensional cavity using the DFR model. The walls were black and cold and the cavity contained a gas of constant temperature and absorption coefficient. Since the DFR model, as formulated for the TMS, is 3-dimensional, the analysis of a true 2-D configuration was not possible, however it was simulated by using a geometry with a width 10 times the other two dimensions.

The results of the calculations are shown in Figures 4-28a, 4-28b, and 4-28c. Plotted in each figure is the radiation flux incident on the wall as a function of distance along the wall. The abscissa (X/L) of the figures is the wall distance divided by the total wall length L, while the ordinate (QNOR) is the incident radiation flux normalized by the emissive power of the gas (Sigma*T^4gas). The three figures correspond to three different levels of gas absorption with Kg*L being equal to 0.1, 1.0 and 10 respectively for the three figures where Kg is the gas absorption coefficient.

It is easily seen that the DFR model reproduces the exact solution quite accurately for this test case. While the geometry and conditions of this case are quite idealized, it does illustrate the most significant advantage the DFR model has over the more commonly used six-Flux models. In this example, the DFR model considered radiation fluxes from approximately twenty different directions within the cavity as opposed to the six directions that would have been used by a six-Flux model. This extra resolution allowed the DFR model to accurately predict the attenuation of the radiation flux near the cavity corners which the six-Flux model cannot do.

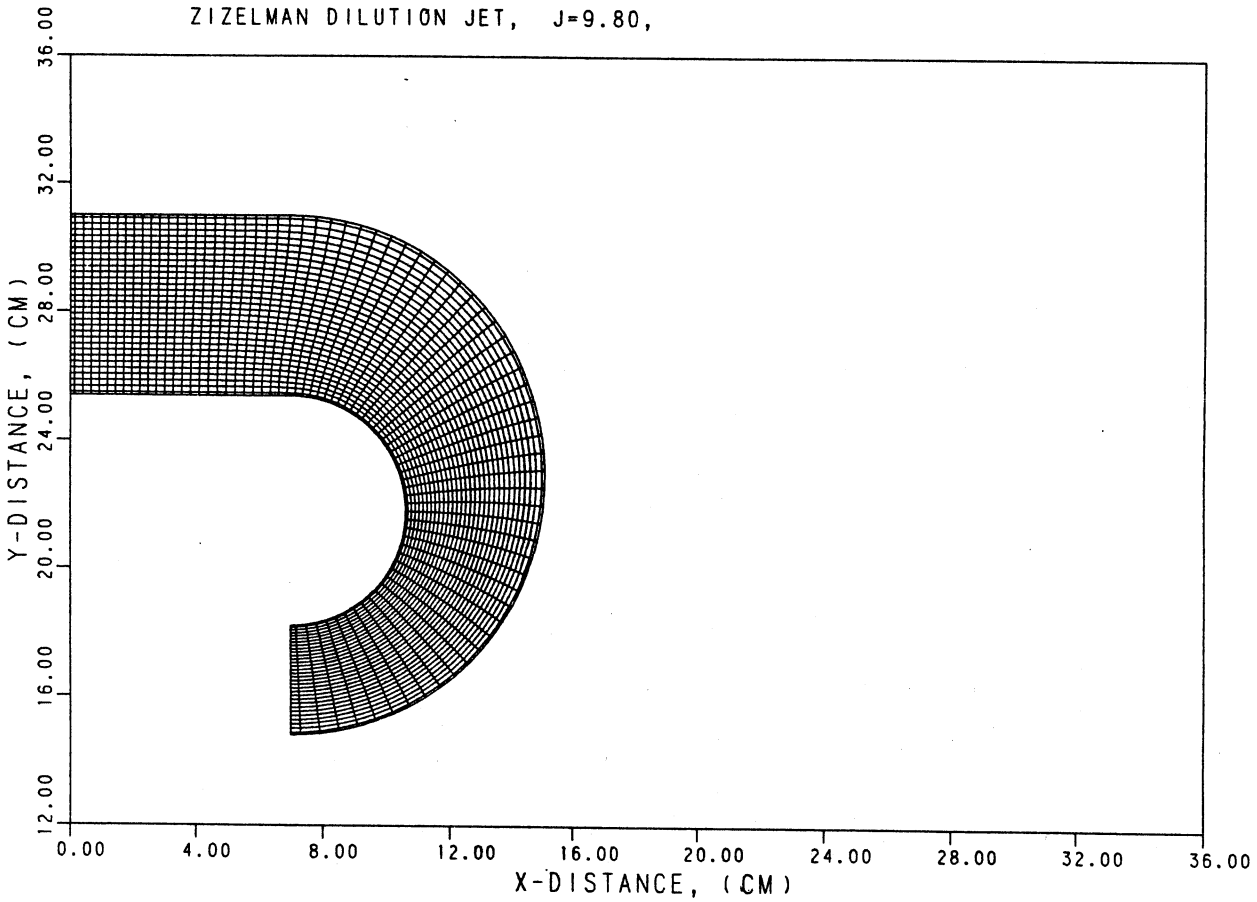

Figure 4-25a. Computational Grid for Curved Duct Jet Mixing, X-Y Plane.

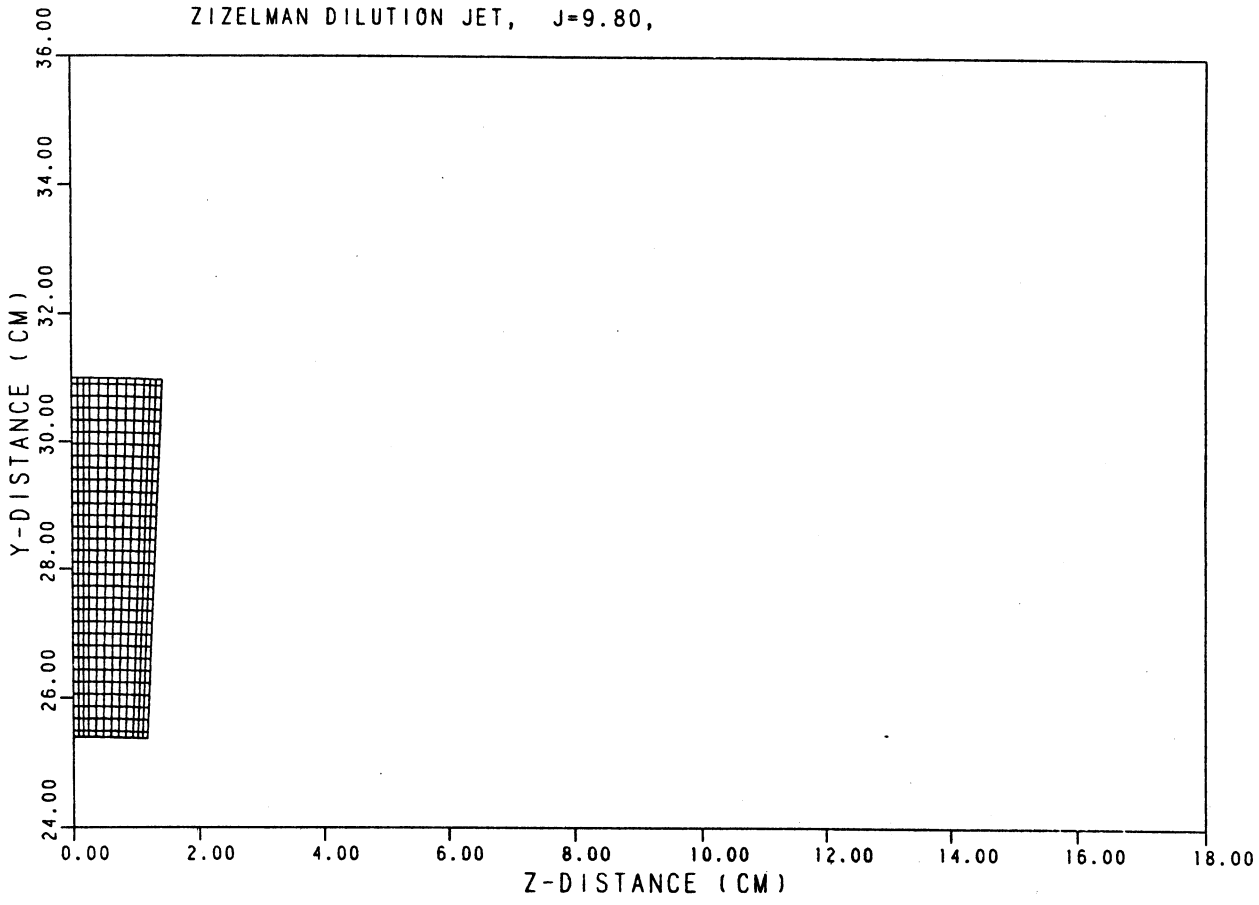

Figure 4-25b. Computational Grid for Curved Duct Jet Mixing, Y-Z Plane.

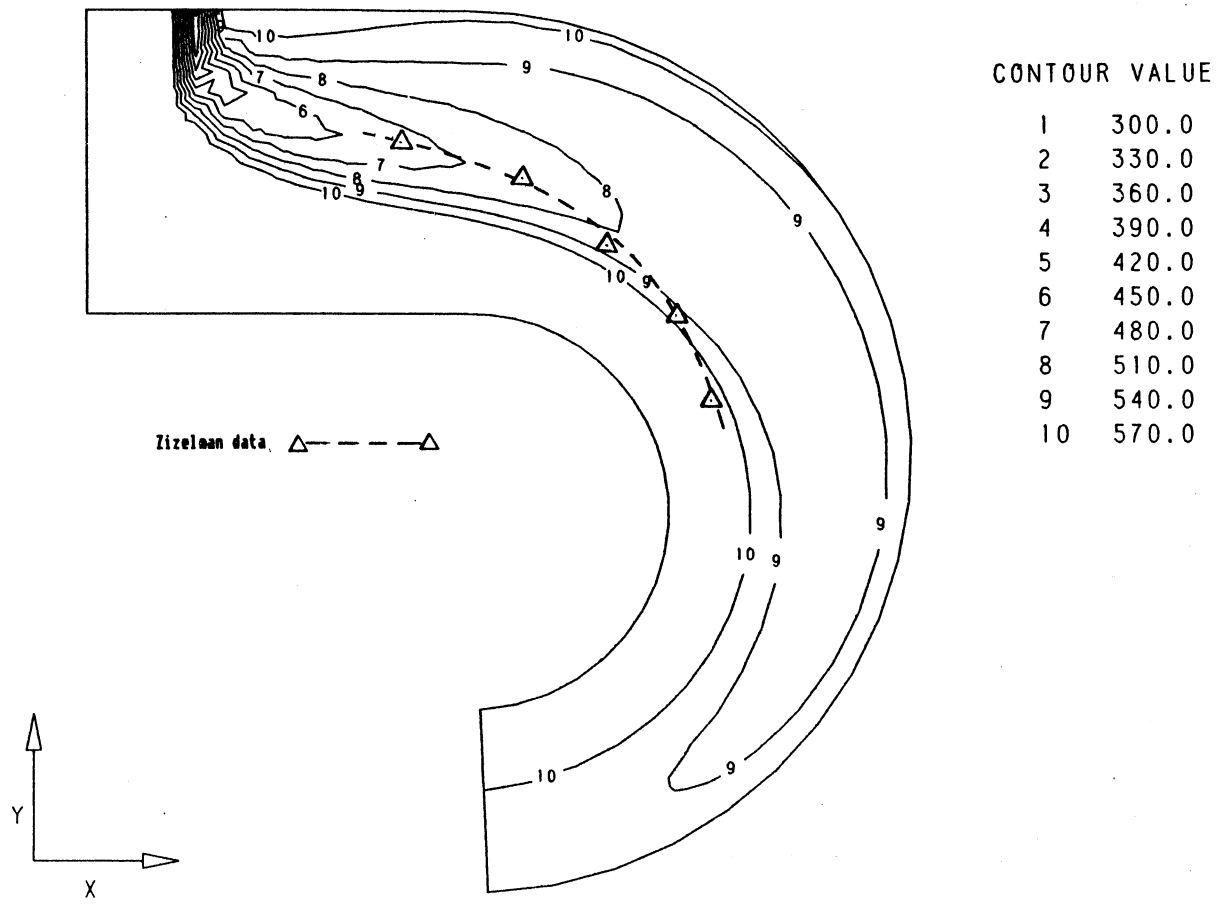

Figure 4-26. Comparison of Jet Trajectory for Jet Injection from OD Wall, J=9.8.

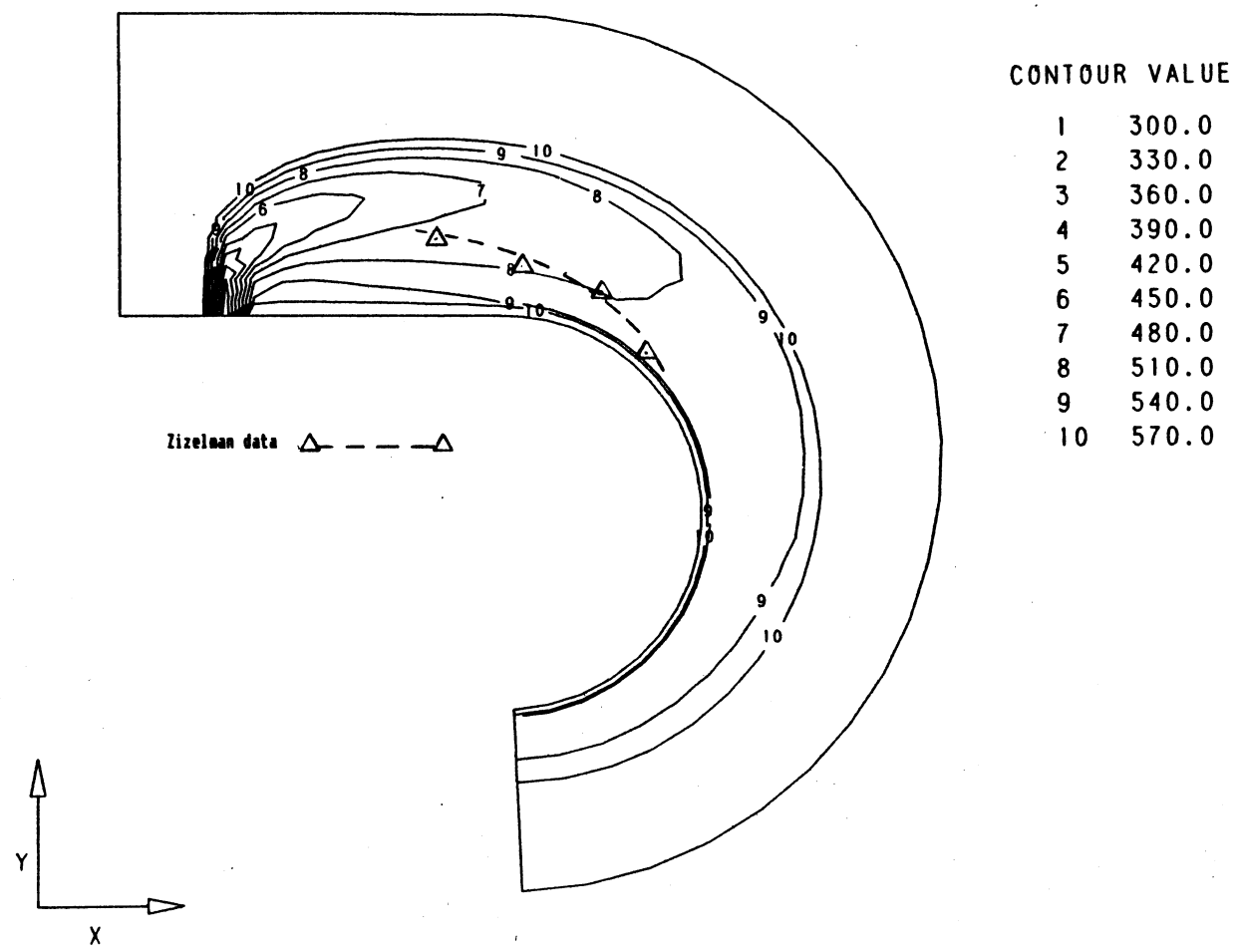

Figure 4-27. Comparison of Jet Trajectory for Jet Injection from ID Wall, J=9.73.

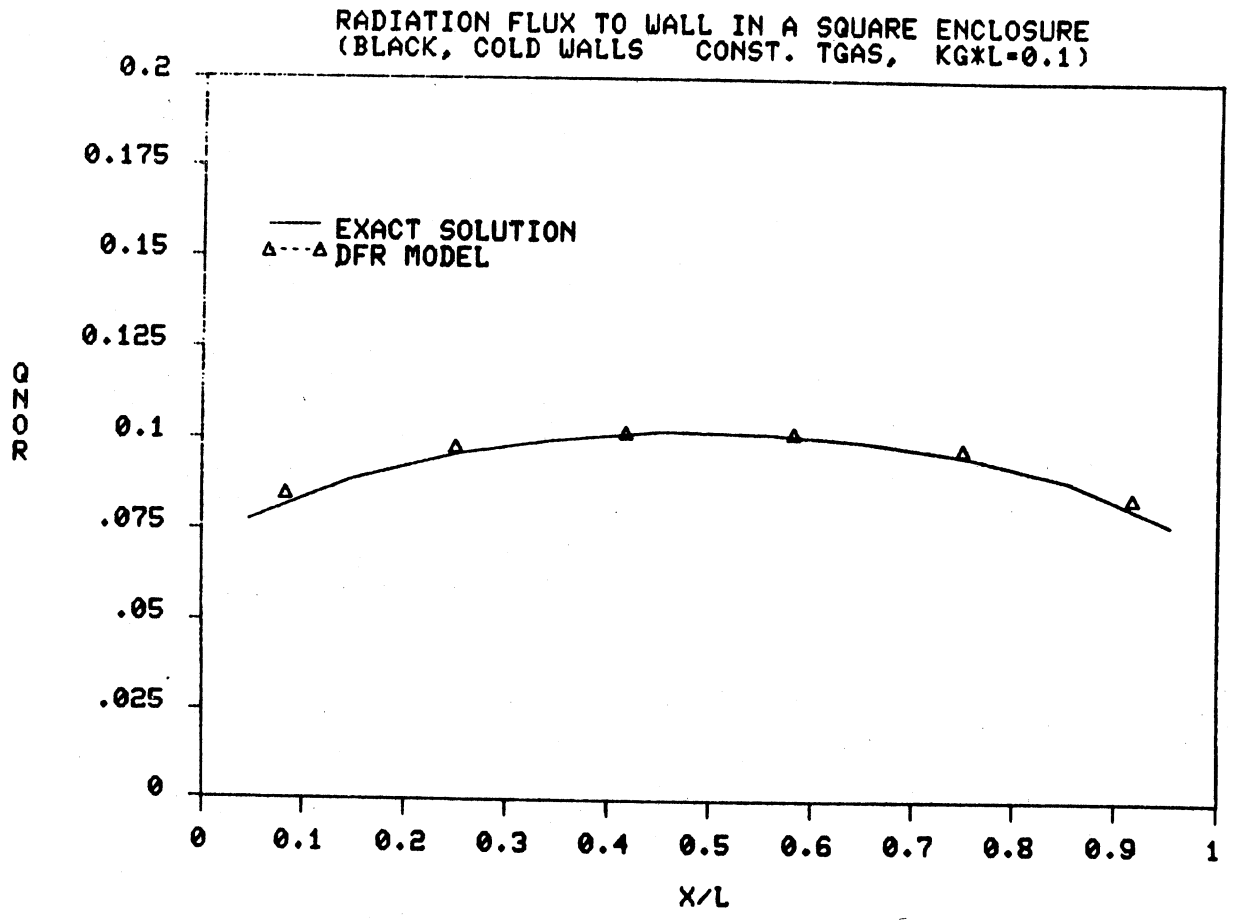

Figure 4-28a. Comparison of Radiation Flux to Walls of Square Enclosure, Kg*L=0.1.

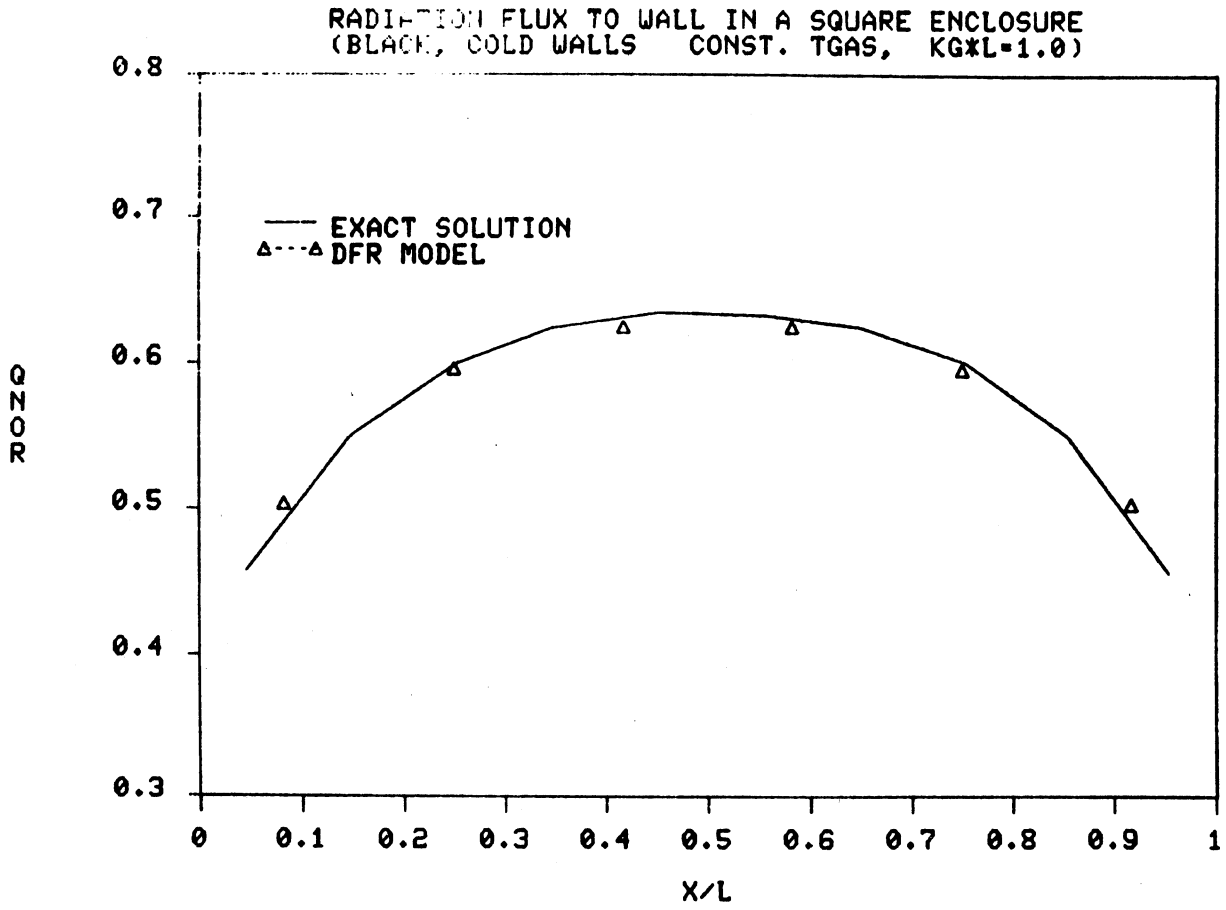

Figure 4-28b. Comparison of Radiation Flux to Walls of Square Enclosure, Kg*L=1.0.

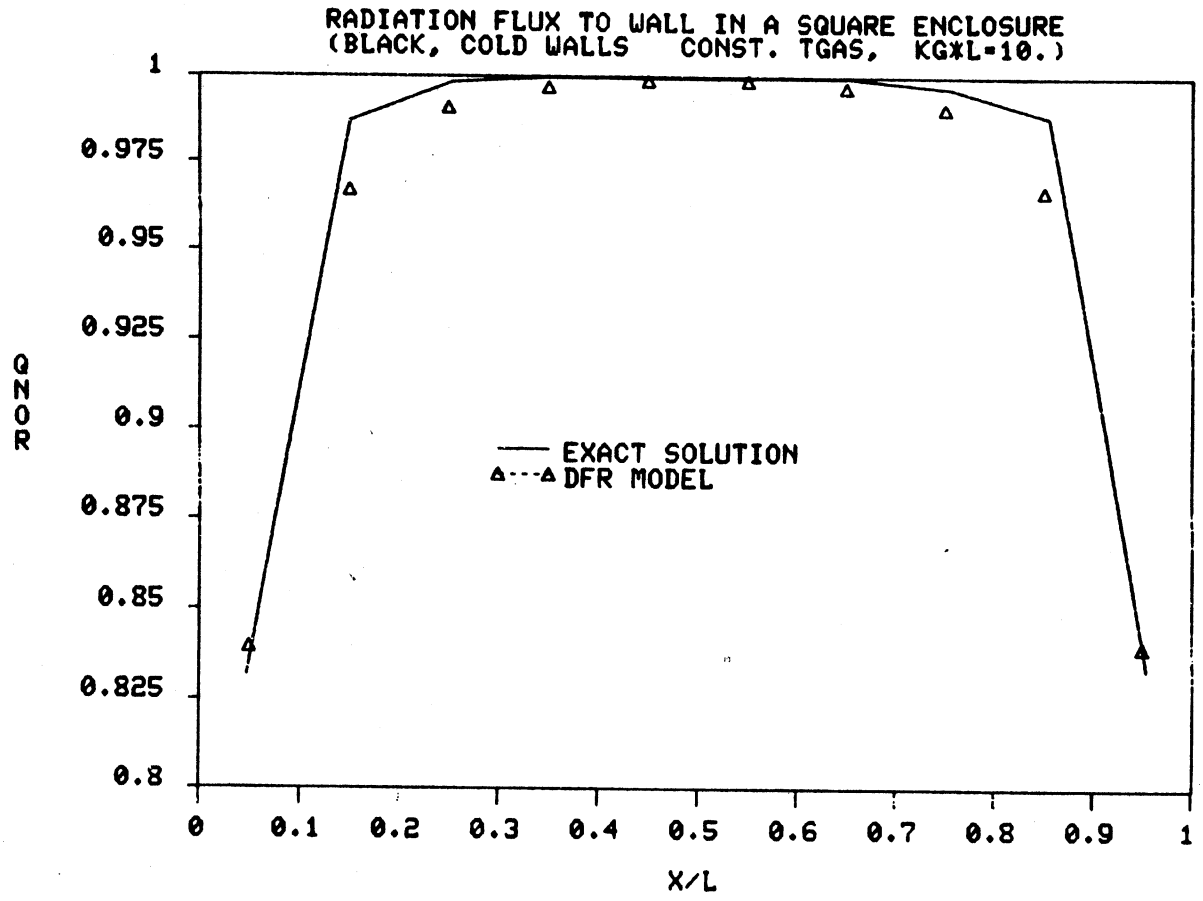

Figure 4-28c. Comparison of Radiation Flux to Walls of Square Enclosure, Kg*L=10.0.

5.0 NUMERICAL EXPERIMENT

The Transition Mixing Model (TMM), generated and evaluated during Phases I to V, was used to conduct a numerical experiment to determine the effects of several important parameters on the mixing process of dilution jets and hot mainstream gas in transition liners. Forty-two different geometry and flow rate configurations were analyzed and the resulting contours of nondimensionalized temperature were compared. In the following paragraphs, the description of the geometries and flow conditions, the procedures for running the cases and the results will be discussed.

5.1 Introduction

The purpose of this task was to perform the numerical equivalent of an experimental test series to illustrate the effect of various parameters on the mixing process in typical transition liner geometries. Each of the selected configurations was to be analyzed by the TMM and the predicted results compared. However, before beginning a discussion of the cases, the limitations of the computational procedure need to be considered.

From the assessment task, it was apparent that the model tended to underpredict the mixing process in straight ducts and would likely do the same for transition liners. Therefore, the prediction of absolute temperature levels was not deemed possible without further work on the turbulence model and possible use of advanced numerical schemes. However, in each of the assessment cases the trends were certainly reproduced. This would indicate that a relative comparison of the various cases would provide a worthwhile technique and it is in this manner that the results are presented. Cases will be compared that differ from each other by only a single parameter so that the effect of that parameter can be examined.

Because of the limited time involved and the large number of cases to be analyzed, it was not possible to perform detailed evaluations of numerical diffusion by running larger and larger grid networks or by rerunning the cases many times with restructured grids to minimize numerical effects. Most cases employed a 76x28x14 grid network of 29,792 nodes as this was approximately the largest number which could be run practically on the available computer. (Three special cases were run with a smaller grid and will be identified in the text).

Since the task was limited to making relative comparisons about mixing behavior, in each case efforts were made to minimize the numerical differences by using approximately the same node spacings. In many situations, the same grid was

re-used. The 42 test configurations required a total of only 12 different grid systems. Therefore, whatever numerical effects exist, should be present in similar amounts in all cases making the relative comparison of the resulting output valid.

5.2 Description of Geometry and Test Parameters

The basic geometry for the transition liners used in the numerical experiment is shown in Figure 5-1.* The curved sections were generated using circular arcs, thus the curvature parameter was specified as the inner boundary radius of curvature, Rci, normalized by the inlet duct height, H_o. The baseline value for H_o (10.16 cm), was selected because this number was used in previous experimental programs for jet mixing in rectangular ducts (14, 15, 17) and it was felt that certain commonality with these previous experiments would be advantageous if comparisons between the predicted curved duct and measured straight duct mixing were ever to be made.

Within this framework, the following 11 parameters were selected for evaluation during the numerical experiment. A description and a listing of the values each assumed is given below.

- Rci/H_o - Radius of curvature of the inner duct wall divided by the inlet duct height
  - 0.25
  - 0.50
  - Infinite, (straight duct)
- AR - Reference duct area ratio. It was actually the same average pressure gradient through the duct that was maintained rather than the same area ratio, since it was the pressure gradient that effects the flow. However, it was more convenient to refer to the area ratio. An explanation of the different values below is given in paragraph 5.6.
  - 1:1
  - 3:1 (radial)
  - 3:1 (circumferential)
  - 3:1 (mixture)
- J - Jet momentum flux ratio
  - 6.6
  - 26.4
  - 105.6

*All figures will be found at the end of this section for convenience.

- D/H_o - Jet diameter divided by the inlet duct height
  - 0.125
  - 0.1768
  - 0.25
  - Slots (equivalent in geometric area to D/H_o = 0.25 round holes)
- S/H_o - Spacing ratio, jet spacing divided by the inlet duct height
  - 0.125
  - 0.25
  - 0.3536
  - 0.50
  - 0.707
  - 1.00
- Iside - Injection side
  - OD duct wall
  - ID duct wall
  - ID and ID duct wall
- Type - Injection Type
  - Single row
  - Opposed OD/ID rows
  - Double row
  - Staggered OD/ID rows
  - Double row, offset
  - Opposed OD/ID, aligned (slots only)
  - Opposed OD/ID, crossed (slots only)
- Tprof - Upstream temperature profile
  - Uniform
  - Temperature OD peaked
- Rt - Radius of the inner duct wall at the inlet of the curved section.
  - 0.0 cm
  - 10.16 cm
  - 22.08 cm
  - 28.21 cm
  - 36.23 cm
  - Infinite (Plane geometry)
- Phi - Injection position measured as the angle from the start of the curved portion of the liner

- 0.0 degrees
- 20 degrees
- 60 degrees

o H_o - Inlet duct height

- 10.16 cm
- 14.37 cm
- 20.32 cm

5.3 Description of Test Cases

Table 5-I provides a listing of the values of each of the 11 previously mentioned parameters for each of the 42 test cases. Case 1 was chosen to be the nominal baseline from which deviations in the parameters would be made. Cases are listed in the order the calculations were run and the order is of no particular significance as several changes to the case list were made during the course of the task.

For all cases, certain inlet parameters were held constant so that exact momentum flux ratios and equilibrium temperature levels could be obtained. These include the mainstream flow conditions and certain jet conditions. A summary of these is provided below.

Mainstream Axial Velocity	15 M/sec
Mainstream Temperature	650 degrees K
Mainstream Pressure	101,325 Pascals
Mainstream Turbulence Intensity	7.5 percent
Mainstream Length Scale	2.03 mm (.02* H_o)
Jet Temperature	300 degrees K
Jet Turbulence Intensity	7.5 percent
Jet Length Scale	0.02* jet diameter
Jet Discharge Coefficient	0.6
Jet Velocity (6.6 Mom. flux ratio)	26.18 M/sec
(26.4 Mom. flux ratio)	52.36 M/sec
(105.6 Mom. flux ratio)	104.72 M/sec

5.4 Analysis Procedure

The specification of the radius of curvature, the area ratio and the liner radius, along with the known inlet duct height was all the data required to completely define the boundary shape of a typical transition liner. This information was supplied to a program that computed an orthogonal curvilinear grid network over the calculation domain. A typical mesh, such as the one used for Case 1, has been drawn in Figures 5-2a and 5-2b that shows the X-Y and Y-Z (at the initial X-station) views respectively.

Table 5-I. Numerical Experiment Test Cases

PARAMETER	DESCRIPTION	UNITS	CASE 1	CASE 2	CASE 3	CASE 4	CASE 5	CASE 6	CASE 7	CASE 8
Rci/Ho	Curvature Ratio	---	0.5	0.25	0.5	0.5	0.5	0.5	0.5	0.5
AR	Ref. Area Ratio	---	1	1	1	1	3	3 (Cir)	1	3
J	Mom. Flux Ratio	---	26.4	26.4	26.4	26.4	26.4	26.4	6.6	6.6
S/Ho	Spacing Ratio	---	0.5	0.5	0.5	0.5	0.5	0.5	0.5	0.5
D/Ho	Jet Dia. Ratio	---	0.25	0.25	0.125	0.125	0.25	0.25	0.25	0.25
Iside	Injection Side	---	OD	OD	OD	ID	OD	OD	OD	OD
Type	Injection Type	---	Single	Single	Single	Single	Single	Single	Single	Single
Tprof	Inlet Profile	---	Uniform	Uniform	Uniform	Uniform	Uniform	Uniform	Uniform	Uniform
Rt	Liner Radius	Meters	Inf.	Inf.	Inf.	Inf.	Inf.	0.2821	Inf.	Inf.
Phi	Inj. Position	Deg's	0	0	0	0	0	0	0	0
Ho	Duct Height	Meters	0.1016	0.1016	0.1016	0.1016	0.1016	0.1016	0.1016	0.1016

PARAMETER	DESCRIPTION	UNITS	CASE 9	CASE 10	CASE 11	CASE 12	CASE 13	CASE 14	CASE 15	CASE 16
Rci/Ho	Curvature Ratio	---	0.5	0.5	0.5	Inf	0.5	0.5	0.5	0.5
AR	Ref. Area Ratio	---	1	1	3	1	1	1	1	1
J	Mom. Flux Ratio	---	26.4	6.6	6.6	26.4	26.4	---	6.6	6.6
S/Ho	Spacing Ratio	---	0.5	0.5	0.5	0.5	0.5	---	0.5	0.5
D/Ho	Jet Dia. Ratio	---	0.25	0.25	0.25	0.25	0.25	---	0.25	0.25
Iside	Injection Side	---	ID	OD/ID	OD/ID	OD	OD	---	ID	OD
Type	Injection Type	---	Single	Opposed	Opposed	Single	Single	---	Single	Single
Tprof	Inlet Profile	---	Uniform	Uniform	Uniform	Uniform	Uniform	OD Peak.	Uniform	OD Peak.
Rt	Liner Radius	Meters	Inf.	Inf.	Inf.	Inf.	Inf.	Inf.	Inf.	Inf.
Phi	Inj. Position	Deg's	0	0	0	---	20	---	0	0
Ho	Duct Height	Meters	0.1016	0.1016	0.1016	0.1016	0.1016	0.1016	0.1016	0.1016

PARAMETER	DESCRIPTION	UNITS	CASE 17	CASE 18	CASE 19	CASE 20	CASE 21	CASE 22	CASE 23	CASE 24
Rci/Ho	Curvature Ratio	---	0.5	0.5	0.5	0.5	Inf	Inf	Inf	0.5
AR	Ref. Area Ratio	---	1	1	1	1	1	1	1	1
J	Mom. Flux Ratio	---	26.4	26.4	26.4	105.6	6.6	26.4	26.4	26.4
S/Ho	Spacing Ratio	---	0.5	1	0.25	0.5	0.5	0.3535	0.25	0.5
D/Ho	Jet Dia. Ratio	---	0.1768	0.25	0.125	0.125	0.25	0.1768	0.125	0.125
Iside	Injection Side	---	OD	OD/ID	OD	ID	OD/ID	OD	OD	ID
Type	Injection Type	---	Double	Staggard	Single	Single	Double	Single	Single	Single
Tprof	Inlet Profile	---	Uniform	Uniform	Uniform	Uniform	Uniform	Uniform	Uniform	Uniform
Rt	Liner Radius	Meters	Inf.	Inf.	Inf.	Inf	0.1016	0.1016	0	Inf.
Phi	Inj. Position	Deg's	0/20	0	0	0	---	---	---	60
Ho	Duct Height	Meters	0.1016	0.1016	0.1016	0.1016	0.1016	0.1437	0.2032	0.1016

Table 5-I. Numerical Experiment Test Cases (Contd)

PARAMETER	DESCRIPTION	UNITS	CASE 25	CASE 26	CASE 27	CASE 28	CASE 29	CASE 30	CASE 31	CASE 32
Rci/Ho	Curvature Ratio	---	0.5	0.25	0.25	0.25	0.25	Inf	Inf	0.25
AR	Ref. Area Ratio	---	1	1	1	1	1	1	3	3
J	Mom. Flux Ratio	---	26.4	26.4	6.6	6.6	6.6	6.6	6.6	6.6
S/Ho	Spacing Ratio	---	0.5	0.5	0.5	0.5	0.5	0.5	0.5	0.5
D/Ho	Jet Dia. Ratio	---	0.1768	0.25	0.25	0.25	0.25	0.25	0.25	0.25
Iside	Injection Side	---	OD	ID	ID	OD	OD/ID	OD/ID	OD/ID	OD
Type	Injection Type	---	Dou/Off	Single	Single	Single	Opposed	Opposed	Opposed	Single
Tprof	Inlet Profile	---	Uniform	Uniform	Uniform	Uniform	Uniform	Uniform	Uniform	Uniform
Rt	Liner Radius	Meters	Inf.	Inf.	Inf.	Inf.	Inf.	Inf.	Inf.	Inf.
Phi	Inj. Position	Deg's	0/20	0	0	0	0	---	---	0
Ho	Duct Height	Meters	0.1016	0.1016	0.1016	0.1016	0.1016	0.1016	0.1016	0.1016

PARAMETER	DESCRIPTION	UNITS	CASE 33	CASE 34	CASE 35	CASE 36	CASE 37	CASE 38	CASE 39	CASE 40
Rci/Ho	Curvature Ratio	---	0.25	0.25	0.25	0.25	0.5	Inf	Inf	Inf
AR	Ref. Area Ratio	---	3	3	3 (Cir)	3 (Mix.)	1	1	1	1
J	Mom. Flux Ratio	---	6.6	6.6	6.6	6.6	26.4	6.6	6.6	26.4
S/Ho	Spacing Ratio	---	0.5	0.5	0.5	0.5	0.25	0.5	0.5	1
D/Ho	Jet Dia. Ratio	---	0.25	0.25	0.25	0.25	0.125	Slot	Slot	0.25
Iside	Injection Side	---	OD/ID	ID	OD/ID	OD/ID	OD/ID	OD/ID	OD/ID	OD
Type	Injection Type	---	Opposed	Single	Opposed	Opposed	Opposed	Opp/Algn	Opp/Cross	Single
Tprof	Inlet Profile	---	Uniform	Uniform	Uniform	Uniform	Uniform	Uniform	Uniform	Uniform
Rt	Liner Radius	Meters	Inf.	Inf.	0.2208	0.3623	Inf.	Inf	Inf	0
Phi	Inj. Position	Deg's	0	0	0	0	0	---	---	---
Ho	Duct Height	Meters	0.1016	0.1016	0.1016	0.1016	0.1016	0.1016	0.1016	0.1016

PARAMETER	DESCRIPTION	UNITS	CASE 41	CASE 42
Rci/Ho	Curvature Ratio	---	Inf	Inf
AR	Ref. Area Ratio	---	1	1
J	Mom. Flux Ratio	---	26.4	6.6
S/Ho	Spacing Ratio	---	0.707	0.5
D/Ho	Jet Dia. Ratio	---	0.25	0.25
Iside	Injection Side	---	OD	OD
Type	Injection Type	---	Single	Single
Tprof	Inlet Profile	---	Uniform	Uniform
Rt	Liner Radius	Meters	0	Inf.
Phi	Inj. Position	Deg's	---	---
Ho	Duct Height	Meters	0.1016	0.1016

Each orifice was simulated by a number of grid nodes, ranging from approximately 15 to 100 points, depending on the orifice size and location. A typical orifice grid pattern, used for the OD jet in Case-1 is shown in Figure 5-3. Profiles of velocity, temperature, turbulent kinetic energy and dissipation rate within the jet were assumed to be uniform. The jet mass flow was computed using the effective orifice area based on the above listed discharge coefficient that was a typical value for the type of orifices being simulated. The physical size of the orifice was always based on geometric area, however, since the round orifice shape could only be specified by "stairsteps", and was therefore approximate at best. The TMM automatically adjusted the boundary point density to compensate for any mismatch between the specified area, velocity and mass flow rate.

This boundary condition information, along with the grid geometry, was then supplied to the TMM where each case was run with the Algebraic Reynolds Stress model for 450 to 550 iterations. A case was considered converged when two criteria were met. First, the sum of the mass errors of all of the individual control volumes in the calculation domain had to be less than 0.1 percent of the total inlet flow rate. Secondly, the maximum change in the temperature at any grid node for a 25 iteration period had to be less than 10 degrees Kelvin.

The resulting temperature field was then transferred to a contour plotting program were the values were converted to a non-dimensional parameter called, Theta, whose definition is given below.

$$\mathbf{Theta} = \frac{\mathbf{T_{main} - T}}{\mathbf{T_{main} - T_{jet}}}$$

where,

T_{main} - Initial mainstream temperature
T - Local temperature
T_{jet} - Initial jet temperature

In viewing the results, it should be remembered that high values of Theta correspond to cooler regions.

Contour plots of Theta, shown in Figures 5-4 to 5-45, were then made and will be used as the basis of comparison for the various cases in the following paragraphs. It should be noted that each of the contour plots that show a stream-

wise or side view of the jet and its resultant trajectory in the mainstream flow are plotted to the same scale so direct comparisons between plots can be made. All contour plots that show a cross-stream view are also plotted to the same scale, however it is larger than that used for the side views so that more detail can be shown.

In each case the same contour values are used to assist in the comparison of different cases. The 11 contour values are shown in the following.

Contour Number	Theta Value
1	0.05
2	0.10
3	0.15
4	0.20
5	0.25
6	0.30
7	0.35
8	0.40
9	0.50
10	0.60
11	0.70

In the following paragraphs, each of the 42 cases run will be presented, and when a phenomenon of some significance occurs, an interpretation will be noted in the text. However, there will be no attempt to analyze each and every bend in the contour lines and from them make a corresponding deduction. The authors are well aware that there are limitations in the computational accuracy of the model and that it would be ill advised to draw too fine of a conclusion based on these results.

5.5 Effect of Curvature Ratio

In this section, those cases which illustrate the effect of changing the curvature ratio of the duct will be discussed. To aid in this process, Table 5-II has been generated that lists each of the relevant cases to this section, the relationship between the cases and the values of the defining parameters.

The first triad of Cases are 1, 2 and 12 whose contour plots of Theta are shown in Figures 5-4a, 5-5 and 5-15a respectively. Each is a side view for a longitudinal plane through the center of the jet and clearly shows the trajectory. The maximum jet penetration for each of the three cases

Table 5-II. Test Cases Comparing Curvature Ratio Effects

			Comparison 1			Comparison 2			Comparison 3	
PARAMETER	DESCRIPTION	UNITS	CASE 1	CASE 2	CASE 12	CASE 7	CASE 28	CASE 42	CASE 8	CASE 32
Rci/Ho	Curvature Ratio	---	0.5	0.25	Inf	0.5	0.25	Inf	0.5	0.25
AR	Ref. Area Ratio	---	1	1	1	1	1	1	3	3
J	Mom. Flux Ratio	---	26.4	26.4	26.4	6.6	6.6	6.6	6.6	6.6
S/Ho	Spacing Ratio	---	0.5	0.5	0.5	0.5	0.5	0.5	0.5	0.5
D/Ho	Jet Dia. Ratio	---	0.25	0.25	0.25	0.25	0.25	0.25	0.25	0.25
Iside	Injection Side	---	OD	OD	OD	OD	OD	OD	OD	OD
Type	Injection Type	---	Single	Single	Single	Single	Single	Single	Single	Single
Tprof	Inlet Profile	---	Uniform	Uniform	Uniform	Uniform	Uniform	Uniform	Uniform	Uniform
Rt	Liner Radius	Meters	Inf.	Inf.	Inf.	Inf.	Inf.	Inf.	Inf.	Inf.
Phi	Inj. Position	Deg's	0	0	---	0	0	---	0	0
Ho	Duct Height	Meters	0.1016	0.1016	0.1016	0.1016	0.1016	0.1016	0.1016	0.1016
	Figure Number	---	5-4	5-5	5-15	5-10	5-31	5-45	5-11	5-35

			Comparison 4			Comparison 5		
PARAMETER	DESCRIPTION	UNITS	CASE 9	CASE 26	CASE 12	CASE 10	CASE 29	CASE 30
Rci/Ho	Curvature Ratio	---	0.5	0.25	Inf	0.5	0.25	Inf
AR	Ref. Area Ratio	---	1	1	1	1	1	1
J	Mom. Flux Ratio	---	26.4	26.4	26.4	6.6	6.6	6.6
S/Ho	Spacing Ratio	---	0.5	0.5	0.5	0.5	0.5	0.5
D/Ho	Jet Dia. Ratio	---	0.25	0.25	0.25	0.25	0.25	0.25
Iside	Injection Side	---	ID	ID	OD	OD/ID	OD/ID	OD/ID
Type	Injection Type	---	Single	Single	Single	Opposed	Opposed	Opposed
Tprof	Inlet Profile	---	Uniform	Uniform	Uniform	Uniform	Uniform	Uniform
Rt	Liner Radius	Meters	Inf.	Inf.	Inf.	Inf.	Inf.	Inf.
Phi	Inj. Position	Deg's	0	0	---	0	0	---
Ho	Duct Height	Meters	0.1016	0.1016	0.1016	0.1016	0.1016	0.1016
	Figure Number	---	5-12	5-29	5-15	5-13	5-32	5-33

			Comparison 6			Comparison 7		
PARAMETER	DESCRIPTION	UNITS	CASE 11	CASE 33	CASE 31	CASE 15	CASE 27	CASE 42
Rci/Ho	Curvature Ratio	---	0.5	0.25	Inf	0.5	0.25	Inf
AR	Ref. Area Ratio	---	3	3	3	1	1	1
J	Mom. Flux Ratio	---	6.6	6.6	6.6	6.6	6.6	6.6
S/Ho	Spacing Ratio	---	0.5	0.5	0.5	0.5	0.5	0.5
D/Ho	Jet Dia. Ratio	---	0.25	0.25	0.25	0.25	0.25	0.25
Iside	Injection Side	---	OD/ID	OD/ID	OD/ID	ID	ID	OD
Type	Injection Type	---	Opposed	Opposed	Opposed	Single	Single	Single
Tprof	Inlet Profile	---	Uniform	Uniform	Uniform	Uniform	Uniform	Uniform
Rt	Liner Radius	Meters	Inf.	Inf.	Inf.	Inf.	Inf.	Inf.
Phi	Inj. Position	Deg's	0	0	---	0	0	0
Ho	Duct Height	Meters	0.1016	0.1016	0.1016	0.1016	0.1016	0.1016
	Figure Number	---	5-14	5-36	5-34	5-18	5-30	5-45

with their differing curvature ratios, is approximately the same at 80 percent of the duct height although, for the 26.4 momentum flux ratio used, the limiting factor to the penetration was probably the presence of the opposing wall.

The mixing rate of the jet is slightly increased by decreasing the curvature ratio. If the distance from the injection point to the apex of the Theta=0.4 contour island measured along the jet path is used as an inverse indicator of the mixing rate, one finds for the straight channel (or infinite radius), that the distance is 15.6 cm; for the 0.5 curvature ratio, the distance is 10.8 cm; and for the 0.25, curvature ratio it is 9.7 cm.

The second triad of cases involving varying curvature ratio is 7, 28 and 42. These differ from the previous three cases in that a momentum flux ratio of 6.6 was used for the jets. The contour plots can be seen in Figures 5-10a, 5-31 and 5-45 respectively. In this situation, the opposing wall can have only minimal effect on the ultimate jet penetration. For the straight duct in Case 42, the penetration is approximately 33 percent of the duct height, in Case 7, which has the 0.5 curvature ratio, it is about 50 percent and in Case 28, with the 0.25 ratio, it is greater than 50 percent. The radially inward drift of the jets in Cases 7 and 28 is the result of the curvature induced pressure gradient.

Cases 8 and 32 also differ from each other by only the curvature ratio and are related to 7 and 28 in that a 3:1 area ratio has been applied to the duct. Contours for 8 and 32 can been seen in Figures 5-11 and 5-35. The same conclusion regarding the effect of curvature is reached from the comparison of these two cases as from the comparison of 7 and 28.

The next set of cases under consideration are 9, 26 and 12. Here the momentum flux ratio of 26.4 (same as in Case 1) is used but with the injection from the inner wall of the duct. (Since Case 12 is a straight duct, it is included in the comparison because OD and ID injections would be equivalent.) Inspection of the contour plots for these cases, which are shown in Figures 5-12a, 5-29 and 5-15a, indicates approximately the same ultimate jet penetration of 80 percent of the duct height as was seen for the OD in injection cases.

Opposed jets with a momentum flux ratio of 6.6 are used in the next series of Cases 10, 29 and 30. Here the curvature ratio varies from infinite for Case 30 to 0.5 for Case 10 to 0.25 for Case 29. Contour plots of the predicted Theta values are shown in Figures 5-13, 5-32 and 5-33a. For the straight duct, both the inner and outer jets penetrate approximately the same amount, 30 percent of the duct. For

the 0.5 curvature ratio however, the symmetry plane between the inner and outer jets is no longer coincident with the duct centerline, as the outer jet penetrates to 50 percent of the duct while the inner jet appears to adhere to the inner wall with almost no penetration. A similar effect is also observed for the 0.25 curvature ratio.

To the opposed injection of the previous three cases, a 3:1 area ratio was added and the result was Cases 11, 33 and 31. Here again, the curvature ratio varies from infinite for Case 31 to 0.5 for Case 11 to 0.25 for Case 33. Contour plots of the predicted Theta values are shown in Figures 5-14, 5-36 and 5-34. As was seen earlier, both jets penetrate equal amounts for the straight duct but when curvature exists, the ID jet adheres closely to it's wall while the OD jet penetrates to approximately the duct centerline.

The characteristics of OD jets in the absence of ID jets was given in Cases 7, 28 and 42 described above. The behavior of ID jets in the absence of OD jets for differing curvature ratios can be seen in Cases 15, 27 and 42. (Case 42 is included here since, like Case 12, it is a straight duct and OD and ID injections are equivalent). The 6.6 momentum flux ratio jets were used in these cases and the corresponding contour plots are shown in Figures 5-18a, 5-30 and 5-45. Clearly, the characteristic of the ID jets adhering to the wall with almost no penetration is retained, even without the OD jets being present. Here also, it is the curvature induced radial pressure gradient which causes this phenomenon.

The ID jets of Case 9, however, do not show this effect as they penetrate almost to the same point as its OD counterpart, Case 1. At low momentum flux ratios, the jet's outward momentum is countered by the radial pressure gradient and the jet is forced against the inner wall. For higher jet momentum flux ratios, the pressure gradient lacks the strength to significantly effect the ultimate jet penetration.

5.6 Effect of Area Ratio

The next parameter studied was the area ratio of the duct and in this section those cases which illustrate this parameter will be discussed. Table 5-III lists each of the relevant cases and the values of the defining parameters.

The first set of Cases are 1, 5 and 6. Case 1, shown in Figure 5-4a represented the baseline geometry in which the duct inlet to outlet area ratio was 1:1. There were two methods by which the 3:1 area ratio could be achieved. The height of the duct could be decreased while maintaining the same depth, as in a plane geometry situation. This has been

Table 5-III. Test Cases Comparing Area Ratio Effects

TABLE 5-III, Test Cases Comparing Area Ratio Effects

			Comparison 1			Comparison 2		Comparison 3	
PARAMETER	DESCRIPTION	UNITS	CASE 1	CASE 5	CASE 6	CASE 7	CASE 8	CASE 10	CASE 11
AR	Ref. Area Ratio	---	1	3	3 (Cir)	1	3	1	3
Rci/Ho	Curvature Ratio	---	0.5	0.5	0.5	0.5	0.5	0.5	0.5
J	Mom. Flux Ratio	---	26.4	26.4	26.4	6.6	6.6	6.6	6.6
S/Ho	Spacing Ratio	---	0.5	0.5	0.5	0.5	0.5	0.5	0.5
D/Ho	Jet Dia. Ratio	---	0.25	0.25	0.25	0.25	0.25	0.25	0.25
Iside	Injection Side	---	OD	OD	OD	OD	OD	OD/ID	OD/ID
Type	Injection Type	---	Single	Single	Single	Single	Single	Opposed	Opposed
Tprof	Inlet Profile	---	Uniform	Uniform	Uniform	Uniform	Uniform	Uniform	Uniform
Rt	Liner Radius	Meters	Inf.	Inf.	0.2821	Inf.	Inf.	Inf.	Inf.
Phi	Inj. Position	Deg's	0	0	0	0	0	0	0
Ho	Duct Height	Meters	0.1016	0.1016	0.1016	0.1016	0.1016	0.1016	0.1016
	Figure Number	---	5-5	5-8	5-9	5-10	5-11	5-13	5-14

			Comparison 4		Comparison 5				Comparison 6	
PARAMETER	DESCRIPTION	UNITS	CASE 27	CASE 34	CASE 29	CASE 33	CASE 35	CASE 36	CASE 30	CASE 31
AR	Ref. Area Ratio	---	1	3	1	3	3 (Cir)	3 (Mix.)	1	3
Rci/Ho	Curvature Ratio	---	0.25	0.25	0.25	0.25	0.25	0.25	Inf	Inf
J	Mom. Flux Ratio	---	6.6	6.6	6.6	6.6	6.6	6.6	6.6	6.6
S/Ho	Spacing Ratio	---	0.5	0.5	0.5	0.5	0.5	0.5	0.5	0.5
D/Ho	Jet Dia. Ratio	---	0.25	0.25	0.25	0.25	0.25	0.25	0.25	0.25
Iside	Injection Side	---	ID	ID	OD/ID	OD/ID	OD/ID	OD/ID	OD/ID	OD/ID
Type	Injection Type	---	Single	Single	Opposed	Opposed	Opposed	Opposed	Opposed	Opposed
Tprof	Inlet Profile	---	Uniform	Uniform	Uniform	Uniform	Uniform	Uniform	Uniform	Uniform
Rt	Liner Radius	Meters	Inf.	Inf.	Inf.	Inf.	0.2208	0.3623	Inf.	Inf.
Phi	Inj. Position	Deg's	0	0	0	0	0	0	---	---
Ho	Duct Height	Meters	0.1016	0.1016	0.1016	0.1016	0.1016	0.1016	0.1016	0.1016
	Figure Number	---	5-30	5-37	5-32	5-36	5-38	5-39	5-33	5-34

termed a radial contraction. Alternately, the duct could have a constant height in an axisymmetric geometry, wherein the area ratio would have been achieved because the outlet was at a smaller radius. Thus it would be the circumferential extent of the duct which would have been decreased. The third possibility, of course, would have been a mixture of the two methods.

Case 5, shown in Figure 5-8a, represents the former of the two situations while Case 6, shown in Figure 5-9a represents the latter. In comparing Case 5 and Case 1, there would seem to be little difference in the jet characteristics or the mixing as the distance to the apex of the Theta=0.4 contour island is similar. The circumferential contraction, Case 6, does show some effect especially in the Theta=0.4 contour line. That island has been compressed circumferentially and appears much broader when viewed in the jet centerplane.

Cross-stream contours at a position 90 degrees through the curved portion of the duct in Case 6 can be seen in Figure 5-9b. In this, as in all cross stream plots, the OD wall is at the top of the figure. The jet, in this situation, was located at the vertical centerline. This can be compared with the corresponding plots from Case 1 and Case 5 in Figures 5-4c and 5-8b. It would appear that there is a slight degradation in mixing when circumferential contraction is used.

The next pair of cases which represent changes in the area ratio are 7 and 8. In 7 the 1:1 ratio is used along with the 6.6 momentum flux ratio jet and the resulting contour plot was presented in Figure 5-10a. Case 8, shown in Figure 5-11, uses the same jet but has a 3:1 area ratio with radial contraction. In these cases both the ultimate penetration and the mixing rate appear little effected by the area ratio change. The jet characteristics have already been determined before a significant change in the duct area occurs since the jets are positioned at the start of the curved portion of the duct. This orientation was chosen because it represents the typical arrangement of dilution jets in reverse flow combustion systems.

Case 10 and 11 bear the same relationship in area ratio as 7 and 8 but opposed injection was used with the same 6.6 momentum flux ratio jets. Again, there would appear to be little effect of the area ratio change as evidenced by Figures 5-13 and 5-14.

If the opposed jet Cases 10 and 11 show little effect of area ratio, it would be reasonable that when the ID jets were used by themselves, there would also be little effect. That can be confirmed by observing the contour plots of Cases 27 and 34 which can been found in Figures 5-30 and 5-37.

A series of four cases, each with the 6.6 momentum flux ratio opposed injection used in Case 10 but with the 0.25 curvature ratio are used to further illustrate the effect of area ratio. These Cases are 29, shown in Figure 5-32 which used the 1:1 area ratio, 33, shown in Figure 5-36, which used the 3:1 radial contraction, 35, shown in Figure 5-38, which used the 3:1 circumferential contraction and finally, 36, shown in Figure 5-39, which used a 3:1 combination of radial and circumferential contraction such that the ratio of inlet to outlet duct height was approximately the same as the ratio of the inlet to outlet sector arc length. There would again appear to be minimal effect of area ratio.

Finally, two straight duct cases, 30 and 31, shown in Figure 5-33 and 5-34 show the effect of area ratio without any radius curvature influences. As with the curved duct cases, there appears to be very little effect due to the Area Ratio.

5.7 Effect of Momentum Flux Ratio

Table 5-IV lists the values of the defining parameters for those cases which deal with the effect of differing momentum flux ratio.

The first pair of Cases 1 and 7 have been shown in Figures 5-4a and 5-10a and they compare the 26.4 and 6.6 momentum flux ratio jets respectively for identical orifice and duct configurations. The expected result of lower penetration with lower momentum flux ratio is observed.

Table 5-IV. Test Cases Comparing Momentum Flux Ratio Effects

			Comparison 1		Comparison 2		Comparison 3		Comparison 4	
PARAMETER	DESCRIPTION	UNITS	CASE 1	CASE 7	CASE 2	CASE 28	CASE 4	CASE 20	CASE 5	CASE 8
J	Mom. Flux Ratio	---	26.4	6.6	26.4	6.6	26.4	105.6	26.4	6.6
Rci/Ho	Curvature Ratio	---	0.5	0.5	0.25	0.25	0.5	0.5	0.5	0.5
AR	Ref. Area Ratio	---	1	1	1	1	1	1	3	3
S/Ho	Spacing Ratio	---	0.5	0.5	0.5	0.5	0.5	0.5	0.5	0.5
D/Ho	Jet Dia. Ratio	---	0.25	0.25	0.25	0.25	0.125	0.125	0.25	0.25
Iside	Injection Side	---	OD	OD	OD	OD	ID	ID	OD	OD
Type	Injection Type	---	Single	Single	Single	Single	Single	Single	Single	Single
Tprof	Inlet Profile	---	Uniform	Uniform	Uniform	Uniform	Uniform	Uniform	Uniform	Uniform
Rt	Liner Radius	Meters	Inf.	Inf.	Inf.	Inf.	Inf.	Inf	Inf.	Inf.
Phi	Inj. Position	Deg's	0	0	0	0	0	0	0	0
Ho	Duct Height	Meters	0.1016	0.1016	0.1016	0.1016	0.1016	0.1016	0.1016	0.1016
	Figure Number	---	5-4	5-10	5-5	5-31	5-7	5-23	5-8	5-11

Reducing the curvature ratio from the baseline 0.50 to 0.25 for Cases 2 and 28 produced the same result. As the contour plots in Figures 5-5 and 5-31 show, the 6.6 momentum flux ratio jet penetrated to only 55 percent of the duct height while the 26.4 jet reached 80 percent.

ID injection and 0.125-diameter ratio jets are used in Cases 4 and 20 with momentum flux ratios of 26.4 and 105.6 respectively. Figure 5-7a shows the contours for Case 4 from which the penetration at a position 90 degrees into the bend was 65 percent of the duct height. However, the jet in Case 20 penetrates almost immediately to the opposite duct wall as shown in Figure 5-23.

With a 3:1 area ratio duct, the results are again as would be expected. Case 5, shown in Figure 5-8a and Case 8, shown in Figure 5-11, have the 26.4 and 6.6 momentum flux ratio jets respectively. Again the penetration for the lower momentum flux ratio is 55 percent while the higher ratio reaches 75 percent.

5.8 Effect of Jet Diameter Ratio

Four cases were used to address the effect of varying the jet diameter ratio. Table 5-V lists those cases and their associated parameters.

Case 1 and 3 are OD injection with 0.25- and 0.125-diameter ratio jets respectively with the same orifice spacing (S/H_O). Contours for Case 1 were presented in Figure 5-4a and show a jet penetration of about 80 percent of the duct height. Case 3, shown in Figure 6a, exhibits approximately the same penetration as Case 1, even though smaller diameter ratio jets are used.

When the jets are moved to the ID wall, the penetration results are similar. In Case 9, shown in Figure 5-12a, the penetration reached 77 percent of the duct height at a position 90 degrees through the bend. It's counter part, Case 4, shown in Figure 5-7a, reached 65 percent of the duct height at the same position, however the overall character of the two jets is very similar.

5.9 Effect of Spacing Ratio

Five cases were used to address the effect of varying the jet spacing ratio. They are listed in Table 5-VI along with their associated parameters. It should be noted that throughout this report, the term spacing ratio refers to the jet spacing to duct height ratio.

Table 5-V. Test Cases Comparing Jet Diameter Ratio Effects.

			Comparison 1		Comparison 2	
PARAMETER	DESCRIPTION	UNITS	CASE 1	CASE 3	CASE 4	CASE 9
D/Ho	Jet Dia. Ratio	---	0.25	0.125	0.125	0.25
Rci/Ho	Curvature Ratio	---	0.5	0.5	0.5	0.5
AR	Ref. Area Ratio	---	1	1	1	1
J	Mom. Flux Ratio	---	26.4	26.4	26.4	26.4
S/Ho	Spacing Ratio	---	0.5	0.5	0.5	0.5
Iside	Injection Side	---	OD	OD	ID	ID
Type	Injection Type	---	Single	Single	Single	Single
Tprof	Inlet Profile	---	Uniform	Uniform	Uniform	Uniform
Rt	Liner Radius	Meters	Inf.	Inf.	Inf.	Inf.
Phi	Inj. Position	Deg's	0	0	0	0
Ho	Duct Height	Meters	0.1016	0.1016	0.1016	0.1016
	Figure Number	---	5-4	5-6	5-7	5-12

Table 5-VI. Test Cases Comparing Spacing Ratio Effects.

			Comparison 1			Comparison 2	
PARAMETER	DESCRIPTION	UNITS	CASE 3	CASE 19	CASE 7	CASE 10	CASE 37
S/Ho	Spacing Ratio	---	0.5	0.25	0.5	0.5	0.25
Rci/Ho	Curvature Ratio	---	0.5	0.5	0.5	0.5	0.5
AR	Ref. Area Ratio	---	1	1	1	1	1
J	Mom. Flux Ratio	---	26.4	26.4	6.6	6.6	26.4
D/Ho	Jet Dia. Ratio	---	0.125	0.125	0.25	0.25	0.125
Iside	Injection Side	---	OD	OD	OD	OD/ID	OD/ID
Type	Injection Type	---	Single	Single	Single	Opposed	Opposed
Tprof	Inlet Profile	---	Uniform	Uniform	Uniform	Uniform	Uniform
Rt	Liner Radius	Meters	Inf.	Inf.	Inf.	Inf.	Inf.
Phi	Inj. Position	Deg's	0	0	0	0	0
Ho	Duct Height	Meters	0.1016	0.1016	0.1016	0.1016	0.1016
	Figure Number	---	5-6	5-22	5-10	5-13	5-40

In Case 3, shown in Figure 5-6a, a spacing to height ratio of 0.5 was used while in 19, shown in Figure 5-22, the spacing ratio was 0.25. As expected, decreasing the spacing decreases the penetration of the jets. It is also interesting to compare Case 19 (0.25 spacing ratio and 26.4 momentum flux ratio) with Case 7, shown in Figure 5-10a, (0.5 spacing ratio and 6.6 momentum flux ratio) as the higher momentum flux ratio in 19 offsets the effect of the larger spacing ratio in 7 resulting in jet characteristics which are very similar.

The coupling of spacing ratio and momentum flux ratio can also be observed for opposed injection by considering Cases 37, shown in Figure 5-40 (0.25 spacing ratio and 26.4 momentum flux ratio) and 10 shown in Figure 5-13 (0.5 spacing ratio and 6.6 momentum flux ratio).

Both Case 19 and 37 used a smaller 76x28x10 grid network since, in each case, the physical spacing was half of the normal value and although more nodes were available than were used, it was decided to use approximately the same cross stream node spacing so that any numerical effects present would be similar to the other cases.

5.10 Effect of Injection Side

The effect of injection side will be discussed in this section. Table 5-VII lists each of the relevant cases and the values of the defining parameters.

Table 5-VII. Test Cases Comparing Injection Side Effects.

			Comparison 1			Comparison 2		Comparison 3	
PARAMETER	DESCRIPTION	UNITS	CASE 1	CASE 9	CASE 18	CASE 3	CASE 4	CASE 7	CASE 15
Iside	Injection Side	---	OD	ID	OD/ID	OD	ID	OD	ID
Rci/Ho	Curvature Ratio	---	0.5	0.5	0.5	0.5	0.5	0.5	0.5
AR	Ref. Area Ratio	---	1	1	1	1	1	1	1
J	Mom. Flux Ratio	---	26.4	26.4	26.4	26.4	26.4	6.6	6.6
S/Ho	Spacing Ratio	---	0.5	0.5	1	0.5	0.5	0.5	0.5
D/Ho	Jet Dia. Ratio	---	0.25	0.25	0.25	0.125	0.125	0.25	0.25
Type	Injection Type	---	Single	Single	Staggard	Single	Single	Single	Single
Tprof	Inlet Profile	---	Uniform	Uniform	Uniform	Uniform	Uniform	Uniform	Uniform
Rt	Liner Radius	Meters	Inf.	Inf.	Inf.	Inf.	Inf.	Inf.	Inf.
Phi	Inj. Position	Deg's	0	0	0	0	0	0	0
Ho	Duct Height	Meters	0.1016	0.1016	0.1016	0.1016	0.1016	0.1016	0.1016
	Figure Number	---	5-4	5-12	5-21	5-6	5-7	5-10	5-18

The first triad of Cases to be compared are 1, 9 and 18. The baseline, Case 1, was presented in Figure 5-4a. Case 9 is the ID injection counterpart and was shown in Figure 5-12a while 18 is shown in Figures 5-21a and 5-21b and represents a configuration in which every other OD orifice in Case 1 was moved to the ID wall, thus the spacing ratio in Case 18 is double of that of Case 1.

A clearer perspective of these three cases can be seen from the cross stream contour plots generated at a position 30 degrees into the turning section of the duct. These are shown in Figures 5-4b, 5-12b and 5-21c respectively. In Figure 5-4c (Case 1), the classic horse shoe shape in the jet wake has developed as expected. In contrast, the contour islands in Figure 5-12b (Case 9) are significantly different as the wake development has been inhibited, while Figure 5-21c (Case 18) shows both types of characteristics.

Computations for Case 18 were performed for only half of the region shown which was then reflected by the plot program provide a clearer illustration of the jet development.

The radially inward (or downward in the figures) pressure gradient generated by the duct curvature opposes the roll-up of the wake vortices behind the ID jets and slows the mixing rate but enhances the vortex development for OD jets.

Cases 3 and 4 represent the same OD/ID comparison as Cases 1 and 9 above except that the smaller 0.125-diameter ratio jets were used. Streamwise contours for Case 3 have been presented in Figure 5-6a while Case 4 was shown in Figure 5-7a. Cross-stream contours were generated for these cases, again at a position 30 degrees into the turning section of the duct, and are shown in Figures 5-6b and 5-7b. As with the previous cases, when the jet is located on the OD wall a horseshoe wake region develops but when an ID location is used, the character of the wake is markedly different.

Differences in the character of OD and ID injection are also present when the 6.6 momentum flux ratio jets are used. Case 7, shown in Figure 5-10a, used an OD injection while Case 15, shown in 5-18a employed ID injection. Cross-stream plots at the 30-degree position are provided in Figures 5-10b and 5-18b.

5.11 Effect of Inlet Profile

The effect of the inlet temperature profile will be discussed in this section. Table 5-VIII lists each of the relevant cases and the values of the defining parameters.

For most of the cases analyzed, the inlet temperature profile was taken to be uniform, however, Cases 14 and 16 were run with the profile shown in Figure 5-46, which peaked at 80 percent of the inlet duct height but had the same mass average inlet temperature as the uniform cases. In Case 14, shown in Figure 5-17a, no jets were used so that little temperature changes occur in the duct. This case also provided an indication of the radial pressure gradient isolated from jet effects. Contours of relative pressure can be seen in Figure 5-17b and clearly show the radial gradient. The relative values were obtained by subtracting the centerline exit pressure value for the rest of the field.

In Case 16 (shown in Figure 5-19), the same OD peaked inlet temperature profile was used but a 6.6 momentum flux ratio OD jet was added. Also, Figure 5-10a (Case 7), should be considered as this case uses the same orifice conditions as 16, but with a uniform inlet temperature profile.

These three cases provide an opportunity to test the principle of superposition. Contour plots of Theta, shown in Figure 5-47, have been generated in which the inlet Theta distribution used in Case 14 was superimposed on the profiles of Case 7 which had a uniform inlet. If this figure is compared to Case 16, reasonable agreement is seen.

5.12 Effect of Injection Type

The effect of injection type will be discussed in this section. Table 5-IX lists each of the relevant cases and the values of the defining parameters.

The effect of multiple row injection was examined in a series of three Cases, 1, 17 and 25. Case 1 has been presented earlier in Figure 5-4a and was the baseline configuration with a single row of 0.25 diameter ratio OD orifices. In Case 17, shown in Figure 5-20a, the single row was replaced with a double row of 0.1768 diameter ratio orifices whose combined geometric area was the same as the single row. The orientation of the second row is such that the holes were inline with the leading row and positioned at 20 degrees into the turning section of the duct as opposed to 0 degrees for the leading row or the single row of Case 1. It is apparent that the leading row in Figure 5-20a acts as a shield allowing the second row to penetrate further than either the leading row or the single row case.

Table 5-VIII. Test Cases Comparing Inlet Profile Effects.

PARAMETER	DESCRIPTION	UNITS	Comparison 1		
			CASE 7	CASE 14	CASE 16
Tprof	Inlet Profile	---	Uniform	OD Peak.	OD Peak.
Rci/Ho	Curvature Ratio	---	0.5	0.5	0.5
AR	Ref. Area Ratio	---	1	1	1
J	Mom. Flux Ratio	---	6.6	---	6.6
S/Ho	Spacing Ratio	---	0.5	---	0.5
D/Ho	Jet Dia. Ratio	---	0.25	---	0.25
Iside	Injection Side	---	OD	---	OD
Type	Injection Type	---	Single	---	Single
Rt	Liner Radius	Meters	Inf.	Inf.	Inf.
Phi	Inj. Position	Deg's	0	---	0
Ho	Duct Height	Meters	0.1016	0.1016	0.1016
	Figure Number	---	5-10	5-17	5-19

Table 5-IX. Test Cases Comparing Injection Type Effects.

PARAMETER	DESCRIPTION	UNITS	Comparison 1			Comparison 2		
			CASE 1	CASE 17	CASE 25	CASE 38	CASE 39	CASE 30
Type	Injection Type	---	Single (Row)	Double (Row)	Dou/Off (Row)	Opp/Aign (Slots)	Opp/Cross (Slots)	Opposed (Holes)
Rci/Ho	Curvature Ratio	---	0.5	0.5	0.5	Inf	Inf	Inf
AR	Ref. Area Ratio	---	1	1	1	1	1	1
J	Mom. Flux Ratio	---	26.4	26.4	26.4	6.6	6.6	6.6
S/Ho	Spacing Ratio	---	0.5	0.5	0.5	0.5	0.5	0.5
D/Ho	Jet Dia. Ratio	---	0.25	0.1768	0.1768	Slot	Slot	0.25
Iside	Injection Side	---	OD	OD	OD	OD/ID	OD/ID	OD/ID
Tprof	Inlet Profile	---	Uniform	Uniform	Uniform	Uniform	Uniform	Uniform
Rt	Liner Radius	Meters	Inf.	Inf.	Inf.	Inf	Inf	Inf
Phi	Inj. Position	Deg's	0	0/20	0/20	---	---	---
Ho	Duct Height	Meters	0.1016	0.1016	0.1016	0.1016	0.1016	0.1016
	Figure Number	---	5-4	5-20	5-28	5-41	5-42	5-33

In Case 25, the same double row orifice pattern is used as 17 but the second row was staggered from the leading by one-half of the spacing. The resulting contours through the leading and trailing rows can be found in Figures 5-28a and 5-28b respectively. The penetration of the trailing row is now significantly less than the single row case rather than greater. Other views of Case 17 and 25 can be seen in the cross stream contours for the 30 degree station shown in Figures 5-20b and 5-28c.

Case 25 used a smaller 76x28x10 grid network in order to obtain the correct circumferential boundary conditions while maintaining node spacings similar to other cases. The actual computations were performed for only the center third of the region shown in Figure 5-28c and the results were then reflected both right and left by the plot program to obtain the figure shown.

Two opposed injection Cases, 38 and 39, were run which used slots rather than the round holes employed for all other Cases in this study. Figure 5-48 is a drawing of the slots which have the same geometric area as a 0.25 diameter ratio hole. The major axis øf each slot was orientated at a 45 degree angle with respect to the incoming mainstream flow. In Case 38, the 45 degree orientation was the same for the upper and lower jet rows while in 39 the lower orientation was opposite the upper so that the slots appeared to be crossed when viewed for above.

The streamwise contours for these cases are shown in Figures 5-41a and 5-42a respectively and can be compared to Case 30, shown in Figure 5-33a, which used the normal round holes. A better perspective of the characteristics can be seen in Figures 5-41b, 5-42b and 5-33b. Each figure shows cross-stream contours at three distances, X/H of 0.5, 1.0 and 2.0, downstream from the center of the orifice. Also shown are oblique plots at the same stations. The calculations were performed for only half of the region shown in the figures and was then duplicated by the plot program to produce the figures shown.

5.13 Effect of Injection Position

The effect of injection position will be discussed in this section. Table 5-X lists each of the relevant cases and the values of the defining parameters.

In the baseline, Case 1, the injection position was 0 degrees or at the start of the turning section of the duct. The contours for this case have been shown in Figure 5-4a previously. Case 13 is identical in every aspect except that the injection position was specified as 20 degrees into the

Table 5-X. Test Cases Comparing Injection Position Effects.

			Comparison 1		Comparison 2	
PARAMETER	DESCRIPTION	UNITS	CASE 1	CASE 13	CASE 4	CASE 24
Phi	Inj. Position	Deg's	0	20	0	60
Rci/Ho	Curvature Ratio	---	0.5	0.5	0.5	0.5
AR	Ref. Area Ratio	---	1	1	1	1
J	Mom. Flux Ratio	---	26.4	26.4	26.4	26.4
S/Ho	Spacing Ratio	---	0.5	0.5	0.5	0.5
D/Ho	Jet Dia. Ratio	---	0.25	0.25	0.125	0.125
Iside	Injection Side	---	OD	OD	ID	ID
Type	Injection Type	---	Single	Single	Single	Single
Tprof	Inlet Profile	---	Uniform	Uniform	Uniform	Uniform
Rt	Liner Radius	Meters	Inf.	Inf.	Inf.	Inf.
Ho	Duct Height	Meters	0.1016	0.1016	0.1016	0.1016
	Figure Number	---	5-4	5-17	5-7	5-27

turning section. This position was selected since it corresponds to the trailing orifice row of Cases 17 and 25. Contours for this case can be seen in Figure 5-16 which shows nearly identical jet characteristics as Case 1 except for a slight elongation of some of the contour islands. Obviously the conditions in the mainstream which control the jet trajectory and penetration have changed little in the first 20 degrees of the duct turn.

The second pair of Cases is 4, shown in Figure 5-7a and 24, shown in Figure 5-27. A 0 degree injection position was used in Case 4 which has a penetration of 65 percent of the duct height. For Case 24, however, a 60 degree position was used resulting in very different jet characteristics with the penetration being only 35 percent. Clearly, the radial pressure gradient has developed further by the 60 degree position and is opposing the movement of the jet into the mainstream. It should be remembered that in these cases the duct area ratio is 1:1 so that the average velocity upstream of the jet is the same in both cases.

5.14 Comparison of Can, Channel and Annular Characteristics

As part of the numerical experiment, several cases were run that were used to investigate the relationship between mixing characteristics in rectangular, annular and can geometries. Table 5-XI lists the relevant cases and the values of the defining parameters.

Table 5-XI. Test Cases Comparing Can Annular/Channel Effects.

			Comparison 1			Comparison 2		Comparison 3		
PARAMETER	DESCRIPTION	UNITS	CASE 12	CASE 22	CASE 23	CASE 21	CASE 30	CASE 12	CASE 40	CASE 41
Rt	Liner Radius	Meters	Inf.	0.1016	0	0.1016	Inf.	Inf.	0	0
Rci/Ho	Curvature Ratio	---	Inf	Inf	Inf	Inf	Inf	Inf	Inf	Inf
AR	Ref. Area Ratio	---	1	1	1	1	1	1	1	1
J	Mom. Flux Ratio	---	26.4	26.4	26.4	6.6	6.6	26.4	26.4	26.4
S/Ho	Spacing Ratio	---	0.5	0.3535	0.25	0.5	0.5	0.5	1	0.707
D/Ho	Jet Dia. Ratio	---	0.25	0.1768	0.125	0.25	0.25	0.25	0.25	0.25
Iside	Injection Side	---	OD	OD	OD	OD/ID	OD/ID	OD	OD	OD
Type	Injection Type	---	Single	Single	Single	Double	Opposed	Single	Single	Single
Tprof	Inlet Profile	---	Uniform	Uniform	Uniform	Uniform	Uniform	Uniform	Uniform	Uniform
Phi	Inj. Position	Deg's	---	---	---	---	---	---	---	---
Ho	Duct Height	Meters	0.1016	0.1437	0.2032	0.1016	0.1016	0.1016	0.1016	0.1016
	Figure Number	---	5-15	5-25	5-26	5-24	5-33	5-15	5-43	5-44

The first set of Cases are 12, 22 and 23. Case 12 represents a straight rectangular duct with single sided injection with a momentum flux ratio of 26.4 and has been shown in Figure 5-15a. Case 22 has the same jet configuration and jet physical spacing but is an annular geometry, while Case 23 also used the same jet and spacing but was a straight can. The height of the annulus in Case 22 and the radius of the can in Case 23 were selected such that the volume into which each orifice discharged was the same as the volume of the rectangular duct in Case 12. This criteria resulted in an annulus height of 14.37 cm and a can radius of 20.32 cm. The relative cross stream shapes for these three cases is illustrated in Figure 5-49.

If the Case 12 results are compared to those of Case 22, shown in Figure 5-25 and Case 23, shown in Figure 5-26, it can be seen that the jet trajectories are almost identical even though the ratios of the orifice spacing to duct height are quite different. As the jet penetrates toward the centerline in an annular or can geometry configuration, the narrowing of the circumferential extent of the duct retards the jet movement. However, additional work with these configurations is recommended before any significant conclusions can be made.

The next pair of comparison Cases are 21 and 30. Streamwise contours of Case 30, that is the opposed injection in a straight rectangular duct, were shown in Figure 5-33a. These can be compared to Figure 5-24a that shows the same streamwise contour for Case 21 which is an opposed injection into an annular duct. The orifice spacing to height ratio in this case was selected such that the same 0.5 value was obtained at the annulus radius which divided the annulus into two equal areas. Cross-stream plots for these two cases can be seen in Figures 5-24b and 5-33c.

Finally, the equivalency between a can and a rectangular duct was investigated by Cases 12, 40 and 41. Case 12, present earlier in Figure 5-15a, was again used as a reference. In Case 40, a can with a radius equal to the duct height in Case 12 and with the same spacing ratio as Case 12, was used, but the spacing was based on the sector arc length at the can half radius, or 5.08 cm. In 41, also a can of the same radius and spacing, the spacing was based on the sector arc length at the radius which divided the cross sectional area of the can into two equal parts. Streamwise contours for these cases can be seen in Figures 5-43 and 5-44a. It is quite evident that the trajectory of the jet in Case 41 almost exactly duplicates that in Case 12 while 40 over penetrates. The equivalency of 12 and 41 can also be seen in the cross stream contours shown in Figures 5-15b and 5-44b.

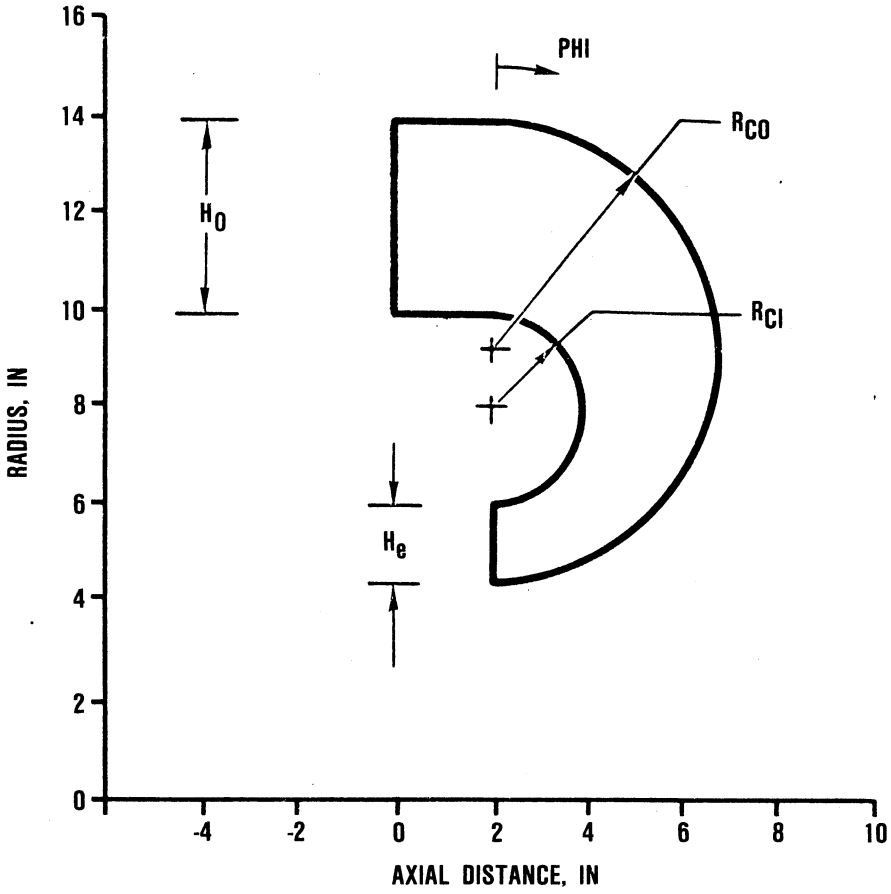

Figure 5-1. Numerical Experiment Geometry.

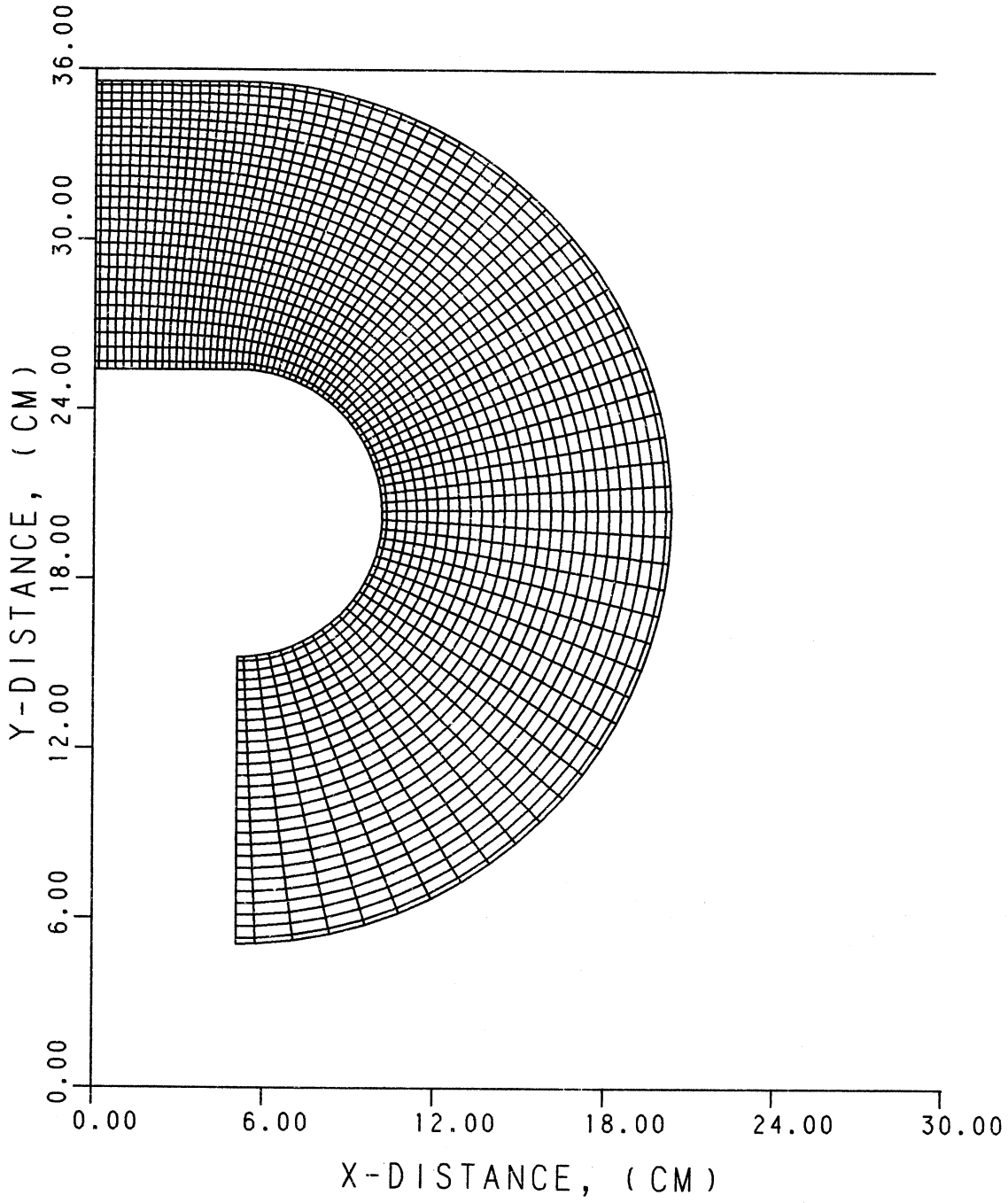

Figure 5-2a. X-Y Grid Network for Case 1.

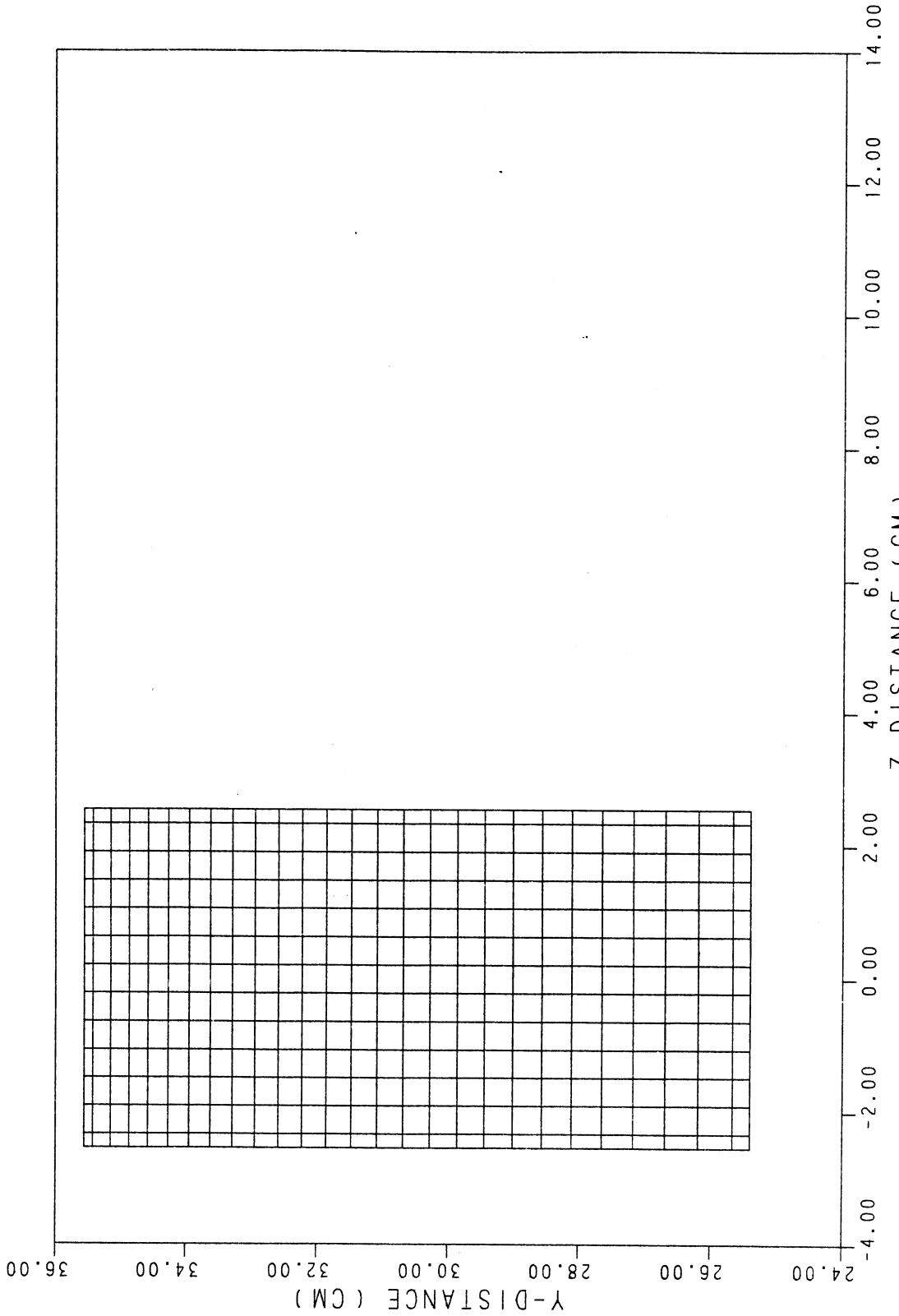

Figure 5-2b. Y-z Grid Network for Case 1.

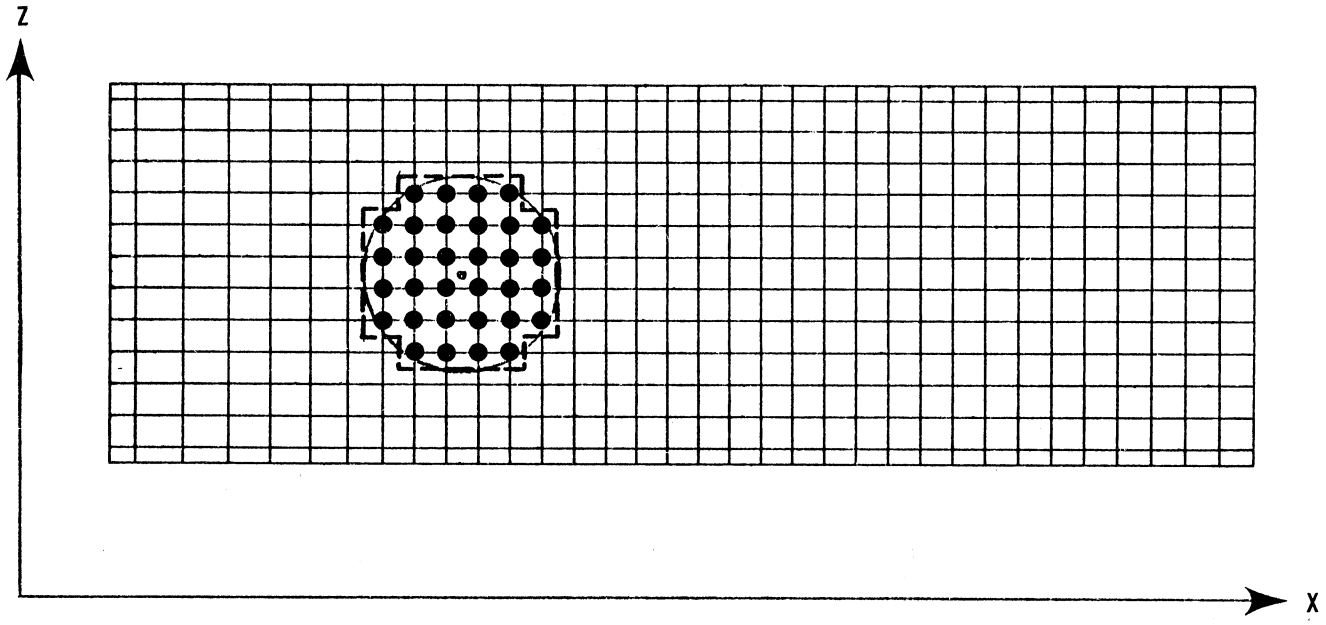

Figure 5-3. Orifice Simulation Pattern for Case 1.

CONTOUR	VALUE
1	0.0500
2	0.1000
3	0.1500
4	0.2000
5	0.2500
6	0.3000
7	0.3500
8	0.4000
9	0.5000
10	0.6000
11	0.7000

J = 26.4
S/H_0 = 0.5
D/H_0 = 0.25

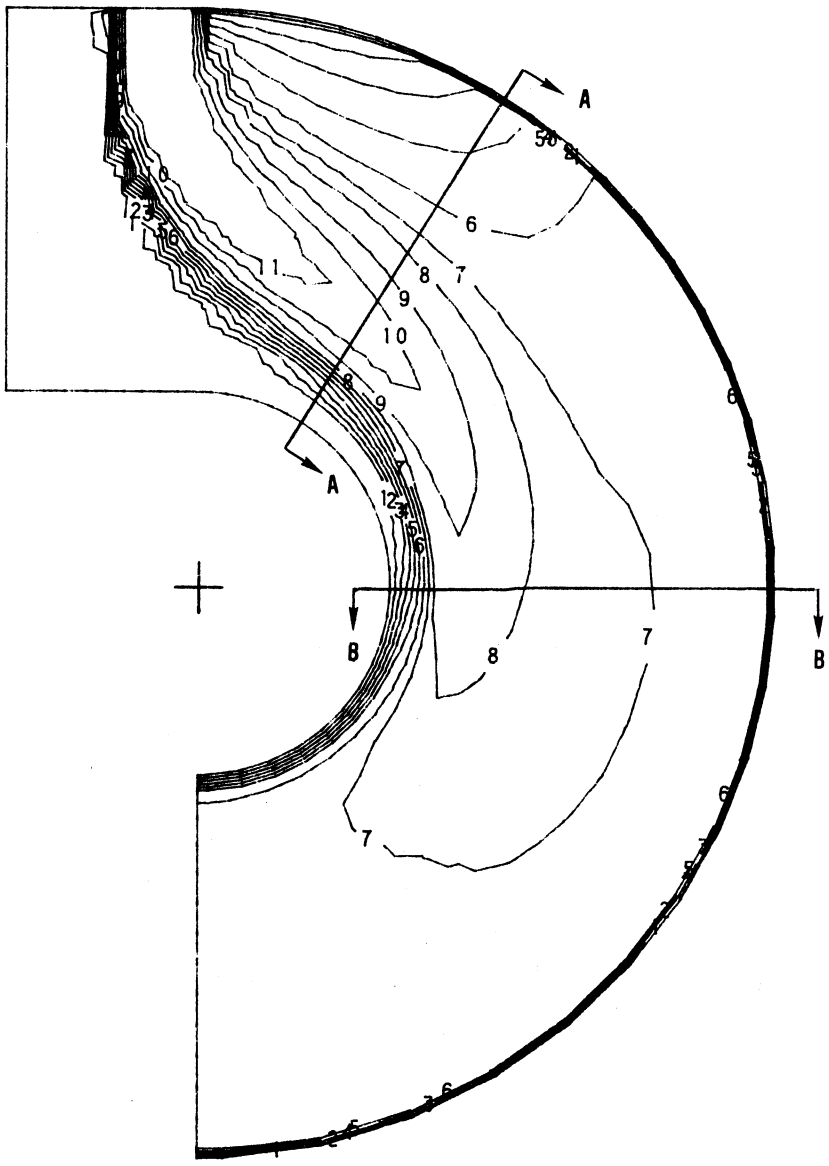

Figure 5-4a. Streamwise Theta Contours for Case 1.

J = 26.4
S/Ho = .5
Ho/D = 4
Ro = Ho/2

CONTOUR	VALUE
1	0.0500
2	0.1000
3	0.1500
4	0.2000
5	0.2500
6	0.3000
7	0.3500
8	0.4000
9	0.5000
10	0.6000
11	0.7000

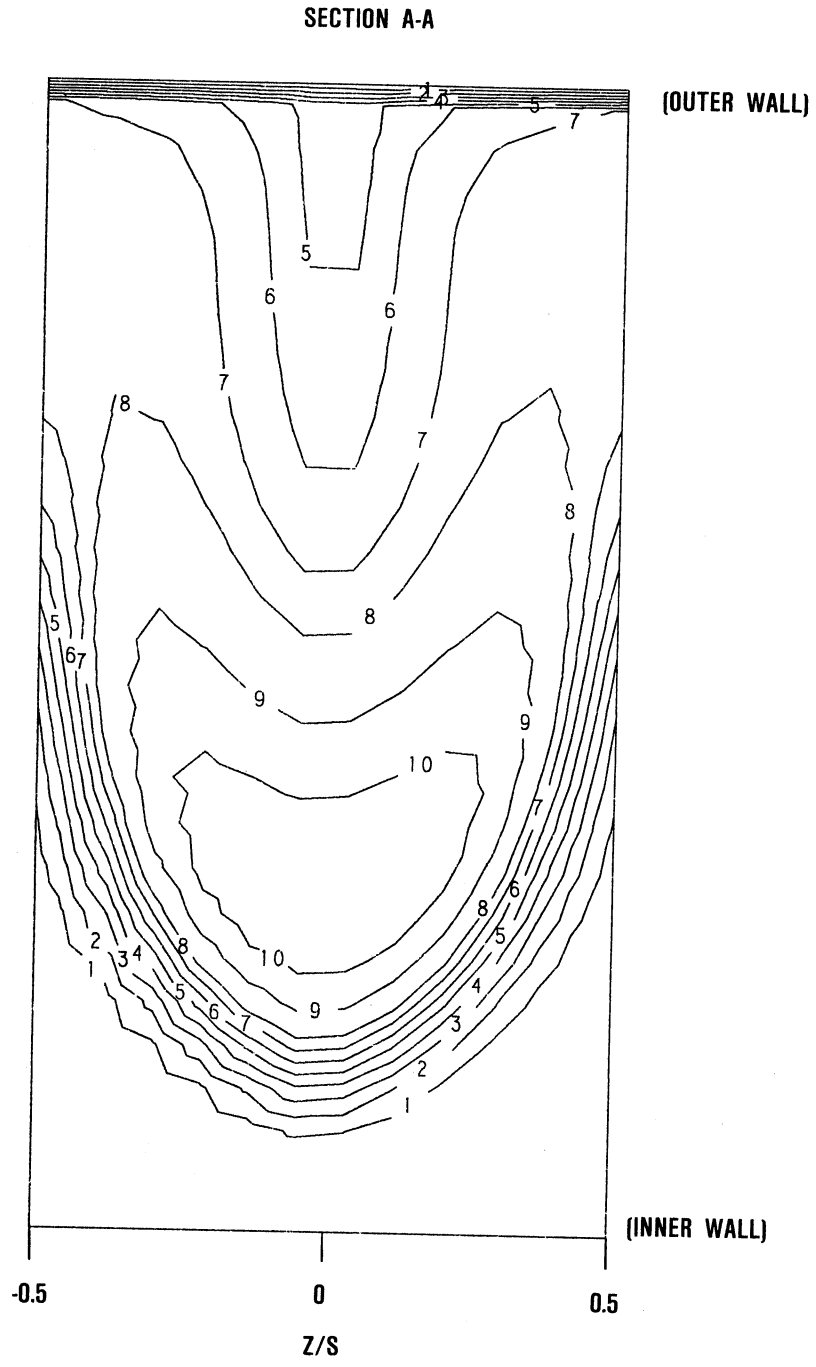

Figure 5-4b. Cross-Stream Theta Contours at Phi=30 Degrees for Case 1.

SECTION B-B

CONTOUR	VALUE
1	0.0500
2	0.1000
3	0.1500
4	0.2000
5	0.2500
6	0.3000
7	0.3500
8	0.4000
9	0.5000
10	0.6000
11	0.7000

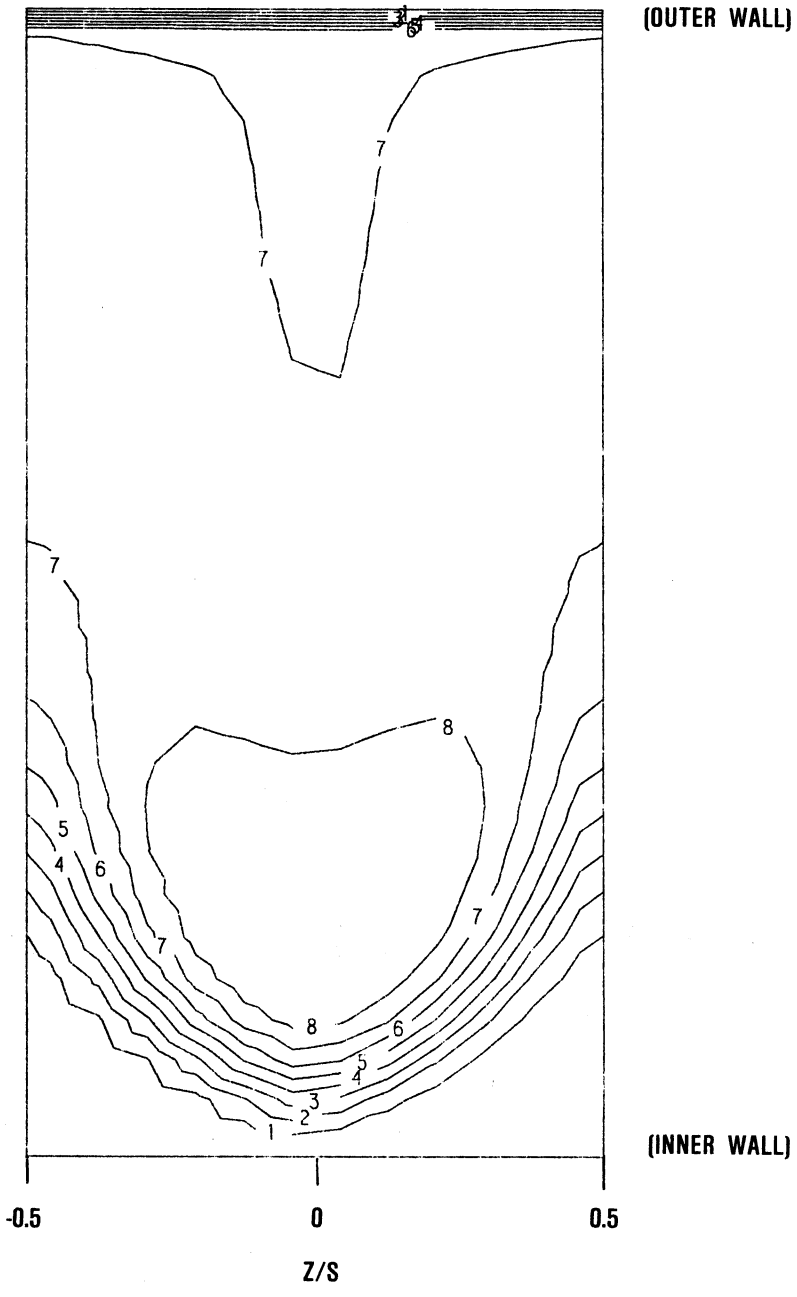

Figure 5-4c. Cross-Stream Theta Contours at Phi=90 Degrees for Case 1.

CONTOUR	VALUE
1	0.0500
2	0.1000
3	0.1500
4	0.2000
5	0.2500
6	0.3000
7	0.3500
8	0.4000
9	0.5000
10	0.6000
11	0.7000

J = 26.4
S/H_0 = 0.5
D/H_0 = 0.25

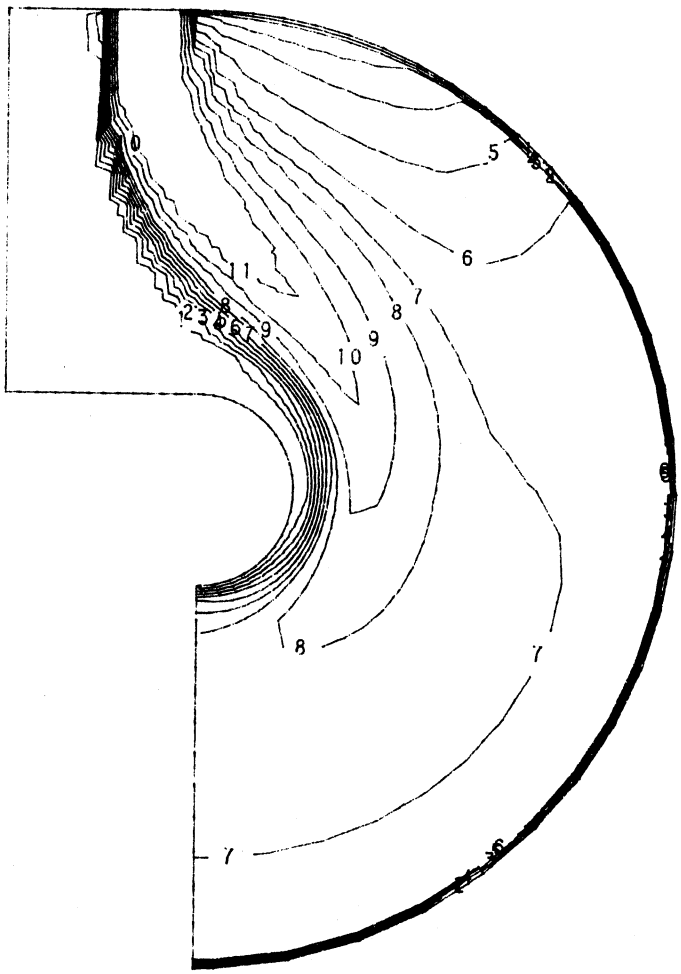

Figure 5-5. Streamwise Theta Contours for Case 2.

J= 26.4
S/Ho = .5
Ho/D = 4
Rci/Ho = .25

CONTOUR	VALUE
1	0.0500
2	0.1000
3	0.1500
4	0.2000
5	0.2500
6	0.3000
7	0.3500
8	0.4000
9	0.5000
10	0.6000
11	0.7000

J = 26.4
S/H_0 = 0.5
D/H_0 = 0.125

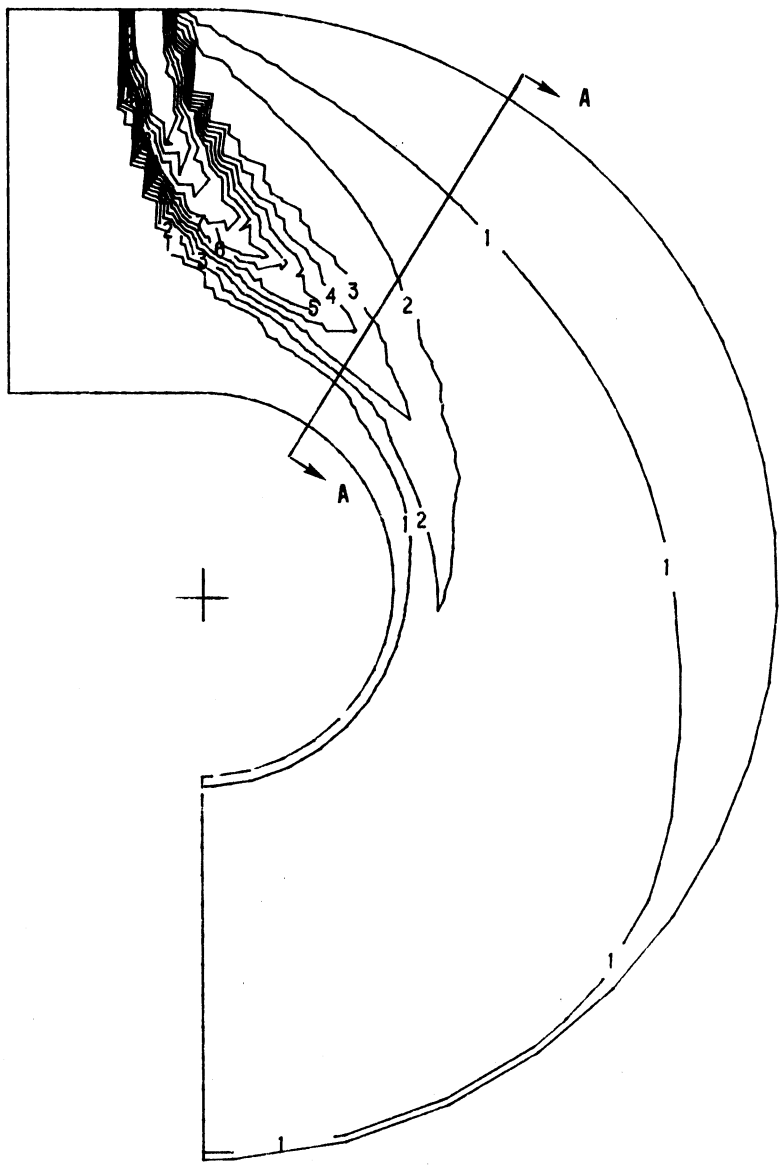

Figure 5-6a. Streamwise Theta Contours for Case 3.

J = 26.4
S/Ho = .5
Ho/D = 8
Rci/Ho = .5

CONTOUR	VALUE
1	0.0500
2	0.1000
3	0.1500
4	0.2000
5	0.2500
6	0.3000
7	0.3500
8	0.4000
9	0.5000
10	0.6000
11	0.7000

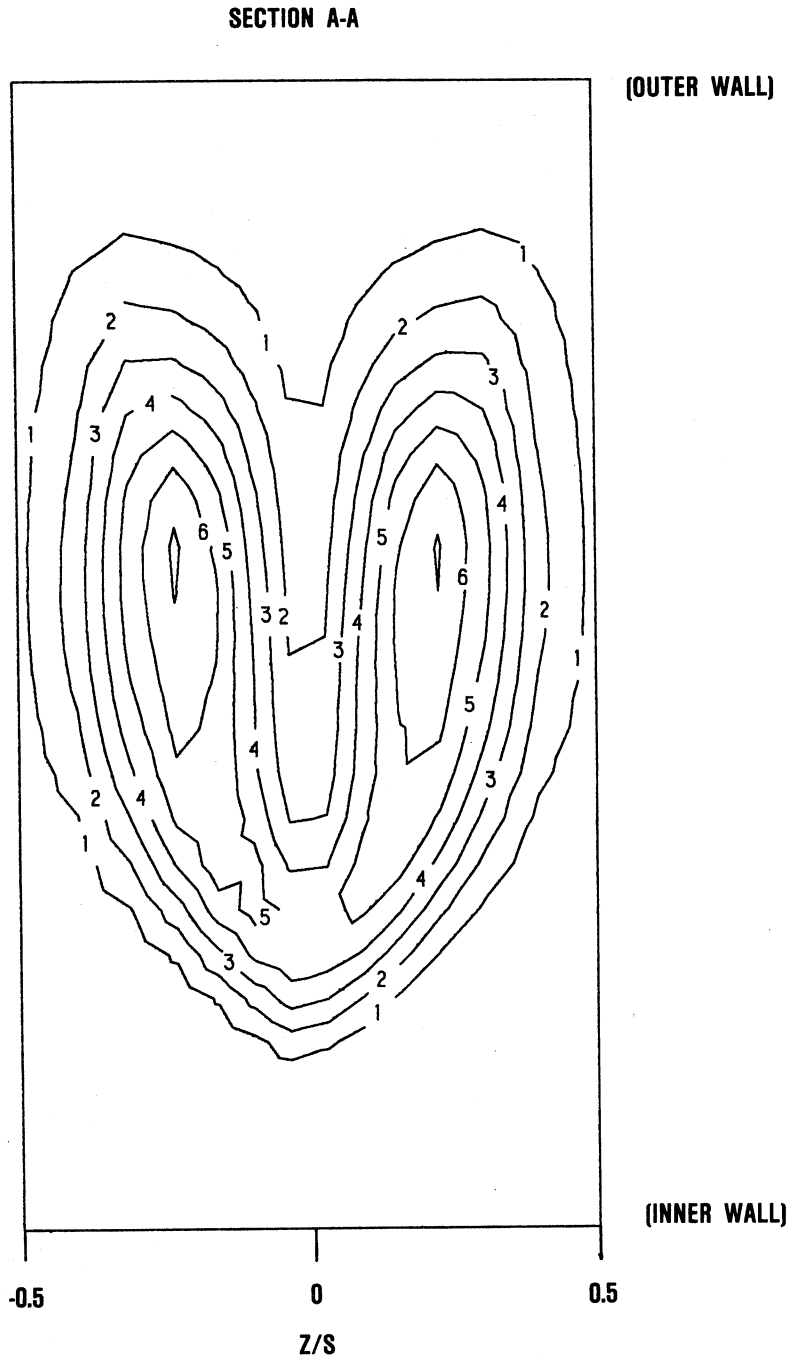

Figure 5-6b. Cross-Stream Theta Contours at Phi=30 Degrees for Case 3.

CONTOUR	VALUE
1	0.0500
2	0.1000
3	0.1500
4	0.2000
5	0.2500
6	0.3000
7	0.3500
8	0.4000
9	0.5000
10	0.6000
11	0.7000

J = 26.4

S/H_0 = 0.5

D/H_0 = 0.125

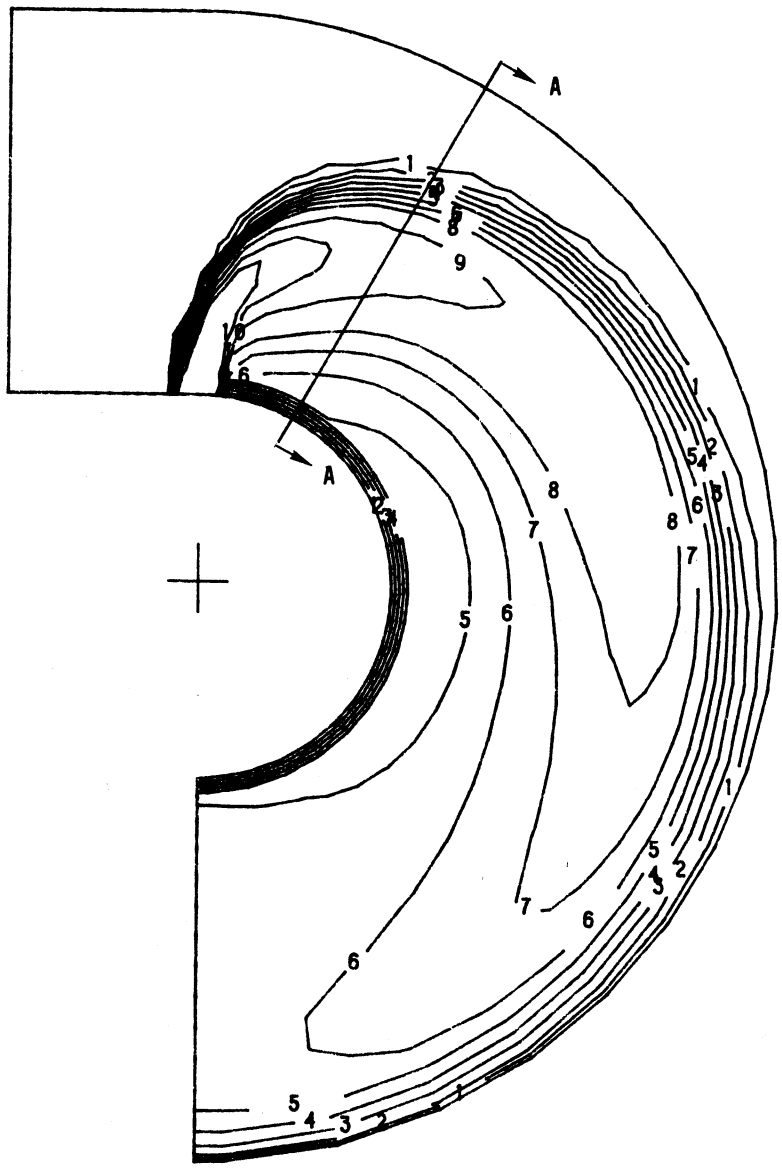

Figure 5-7a. Streamwise Theta Contours for Case 4.

J = 26.4
$H_0/D = 8$
$S/H_0 = .5$
$R_{ci}/H_0 = .5$

CONTOUR	VALUE
1	0.0500
2	0.1000
3	0.1500
4	0.2000
5	0.2500
6	0.3000
7	0.3500
8	0.4000
9	0.5000
10	0.6000
11	0.7000

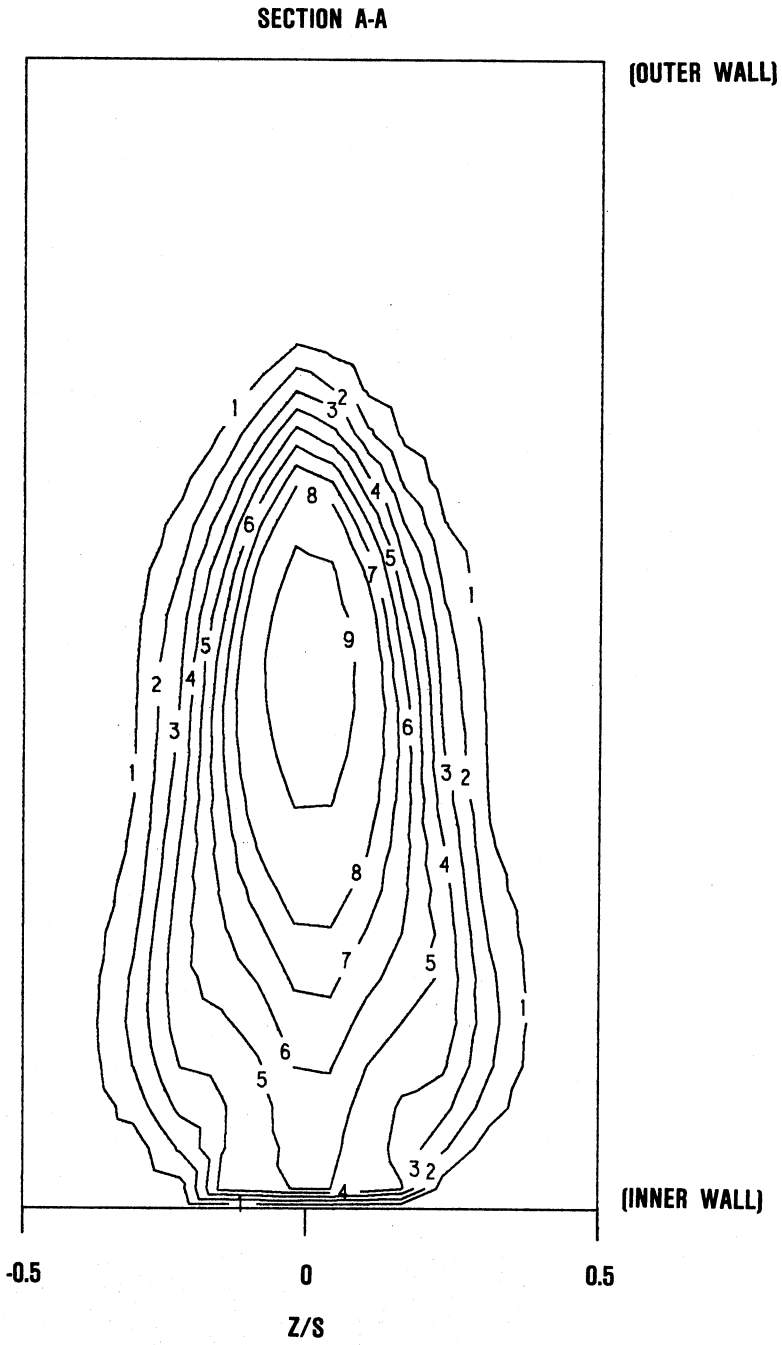

Figure 5-7b. Cross-Stream Theta Contours at Phi=30 Degrees for Case 4.

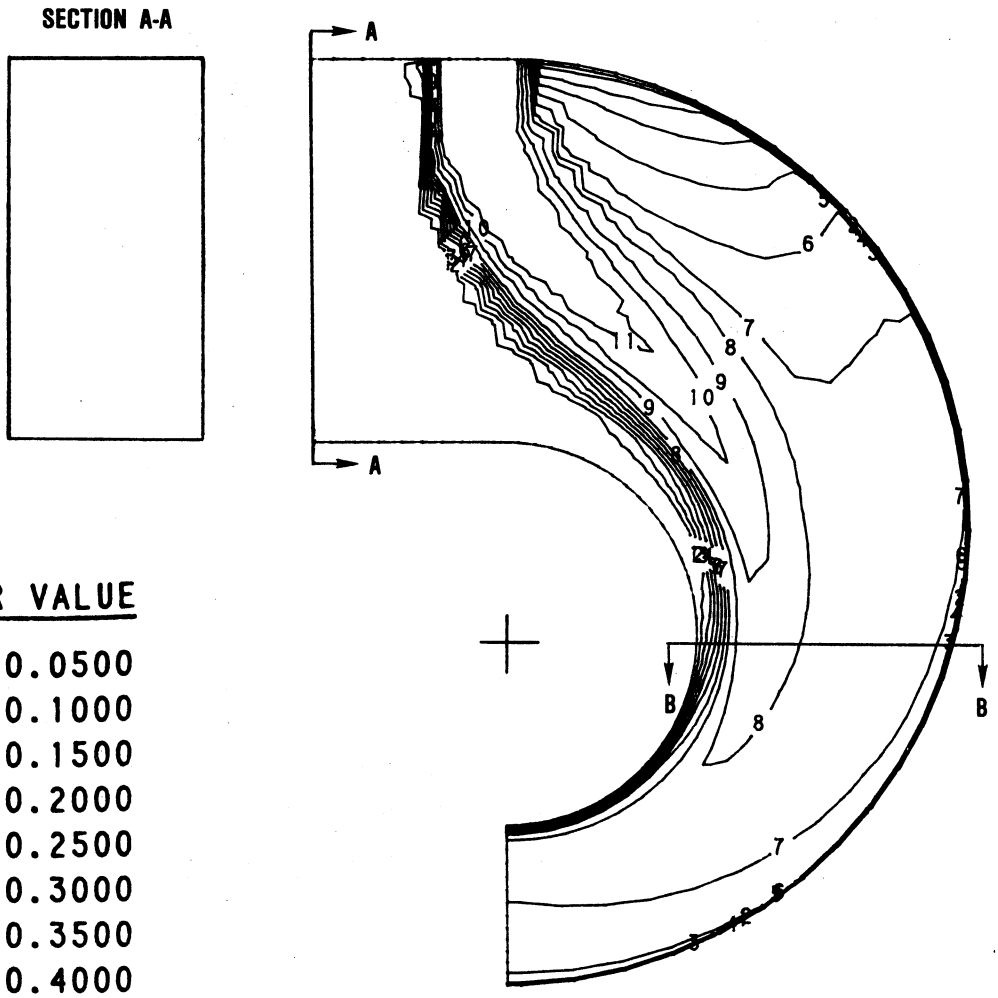

CONTOUR VALUE

1	0.0500
2	0.1000
3	0.1500
4	0.2000
5	0.2500
6	0.3000
7	0.3500
8	0.4000
9	0.5000
10	0.6000
11	0.7000

Figure 5-8a. Streamwise Theta Contours for Case 5.

J = 26.4
S/H0 = .5
H0/D = 4
Rci/H0 = .5
RADIAL CONVERGENCE

CONTOUR	VALUE
1	0.0500
2	0.1000
3	0.1500
4	0.2000
5	0.2500
6	0.3000
7	0.3500
8	0.4000
9	0.5000
10	0.6000
11	0.7000

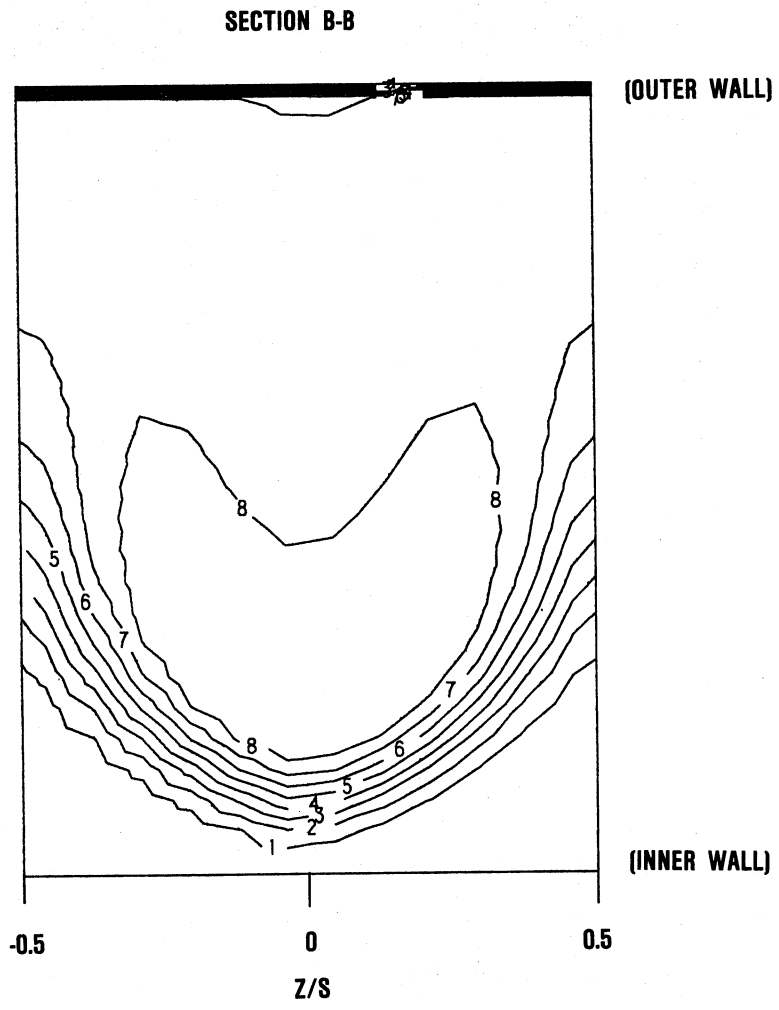

Figure 5-8b. Cross-Stream Theta Contours at Phi=90 Degrees for Case 5.

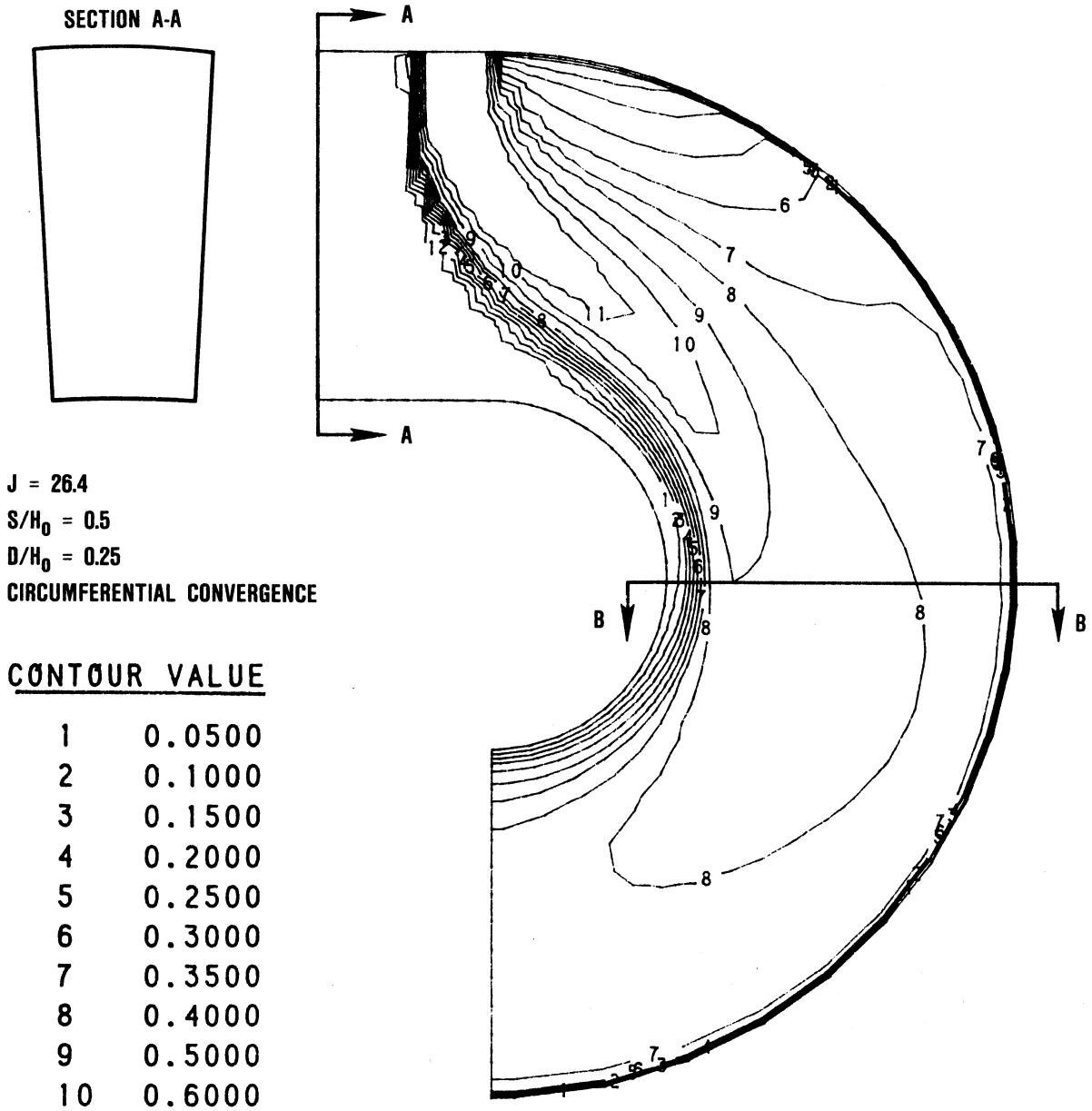

Figure 5-9a. Streamwise Theta Contours for Case 6.

J = 26.4
S/Ho = .5
Ho/D = 4
Rei/Ho = .5
CIRCUMFERENTIAL CONVERGENCE

CONTOUR	VALUE
1	0.0500
2	0.1000
3	0.1500
4	0.2000
5	0.2500
6	0.3000
7	0.3500
8	0.4000
9	0.5000
10	0.6000
11	0.7000

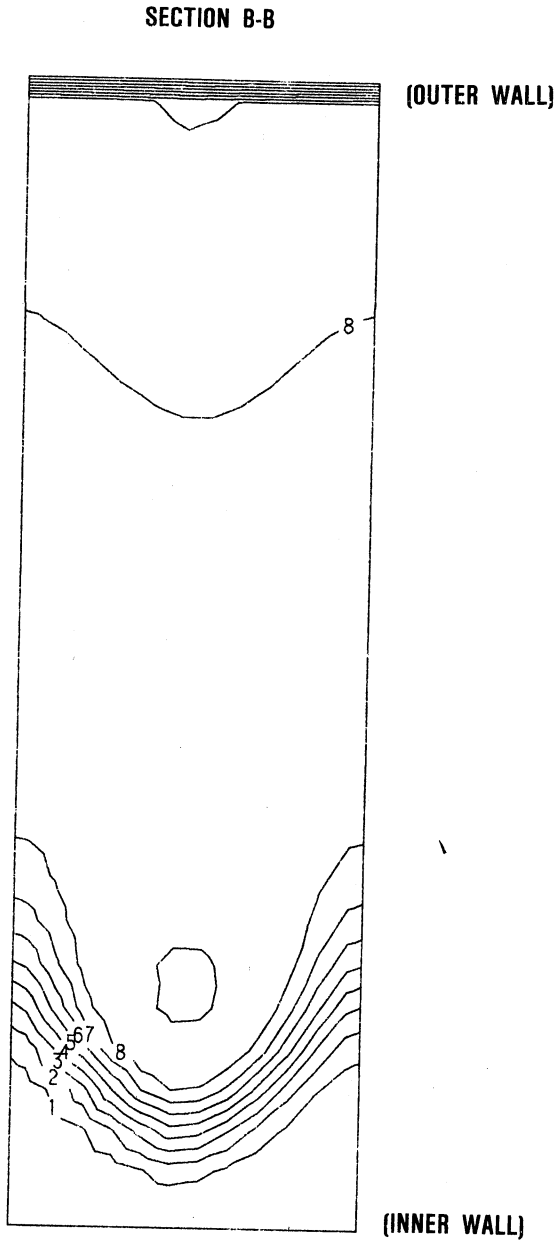

Figure 5-9b. Cross-Stream Theta Contours at Phi=90 Degrees for Case 6.

CONTOUR	VALUE
1	0.0500
2	0.1000
3	0.1500
4	0.2000
5	0.2500
6	0.3000
7	0.3500
8	0.4000
9	0.5000
10	0.6000
11	0.7000

J = 6.6

S/H_0 = 0.5

D/H_0 = 0.25

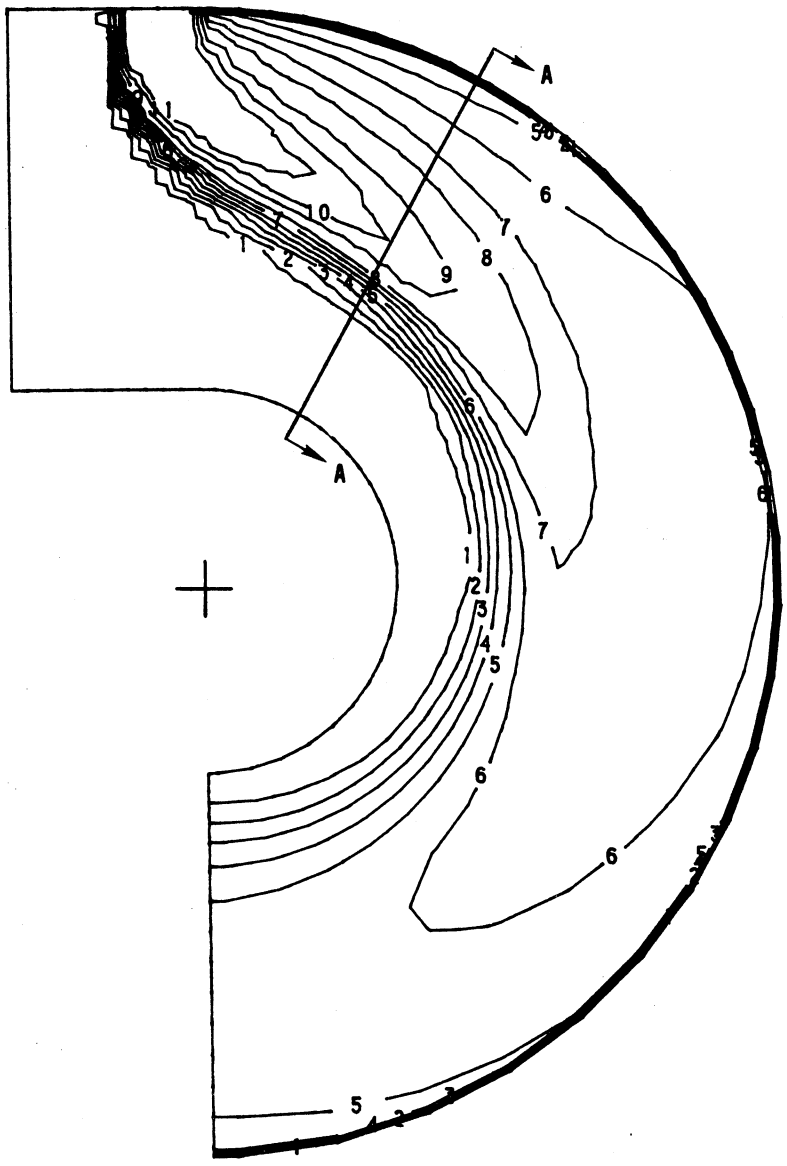

Figure 5-10a. Streamwise Theta Contours for Case 7.

J = 6.6
S/Ho = .5
Ho/D = 4

CONTOUR	VALUE
1	0.0500
2	0.1000
3	0.1500
4	0.2000
5	0.2500
6	0.3000
7	0.3500
8	0.4000
9	0.5000
10	0.6000
11	0.7000

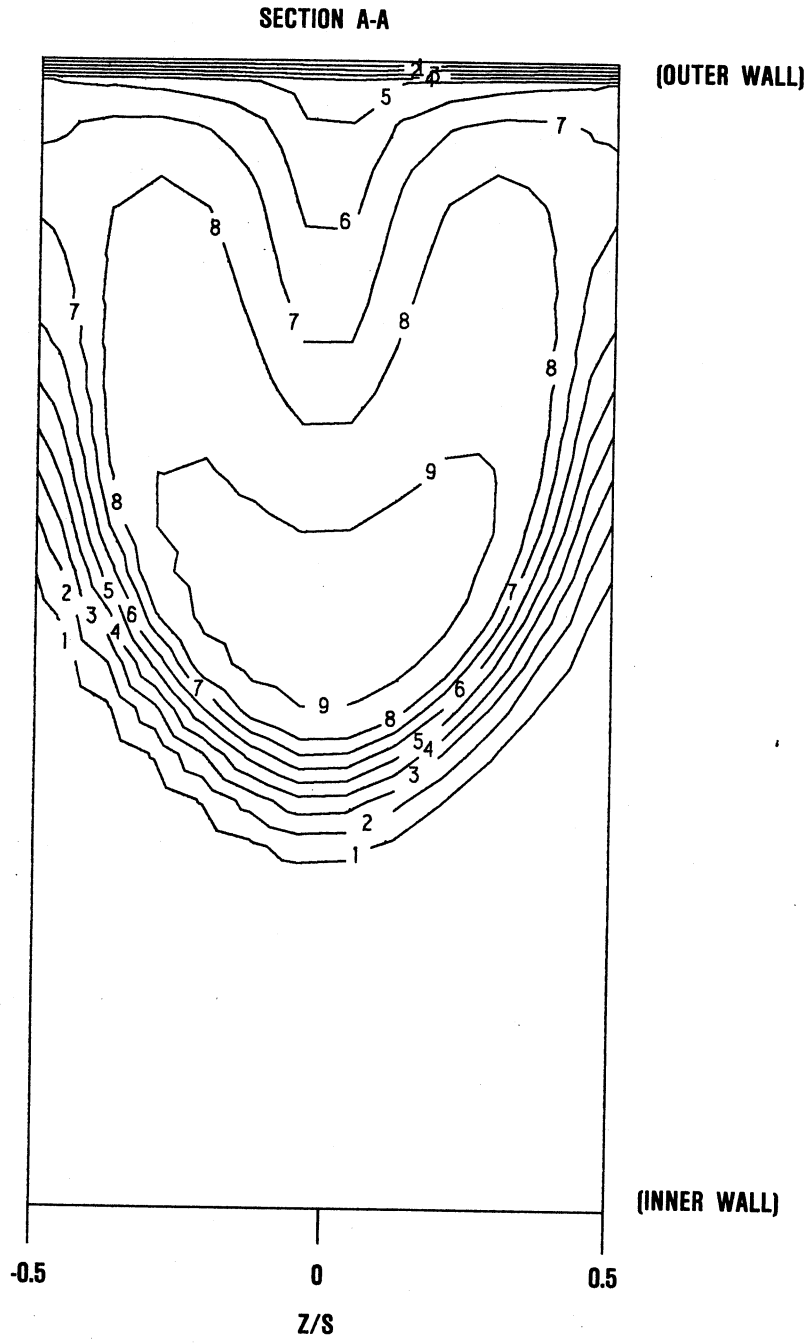

Figure 5-10b. Cross-Stream Theta Contours at Phi=30 Degrees for Case 7.

CONTOUR	VALUE
1	0.0500
2	0.1000
3	0.1500
4	0.2000
5	0.2500
6	0.3000
7	0.3500
8	0.4000
9	0.5000
10	0.6000
11	0.7000

J = 6.6

S/H_0 = 0.5

D/H_0 = 0.25

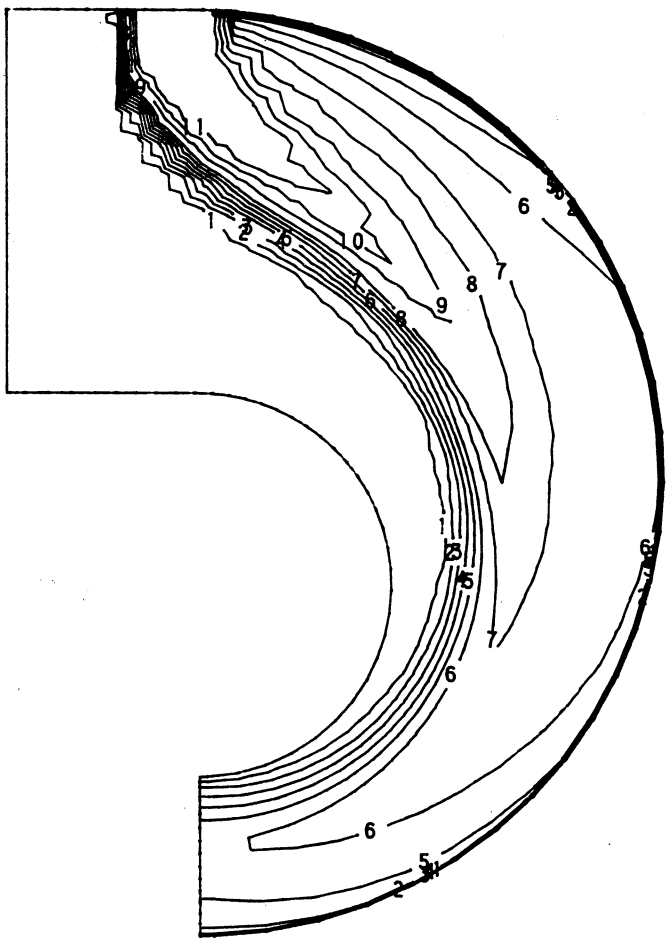

Figure 5-11. Streamwise Theta Contours for Case 8.

J = 6.6
S/Ho = .5
Ho/D = 4
Rci/Ho = .5
RADIAL CONVERGENCE

CONTOUR	VALUE
1	0.0500
2	0.1000
3	0.1500
4	0.2000
5	0.2500
6	0.3000
7	0.3500
8	0.4000
9	0.5000
10	0.6000
11	0.7000

$J = 26.4$

$S/H_0 = 0.5$

$D/H_0 = 0.25$

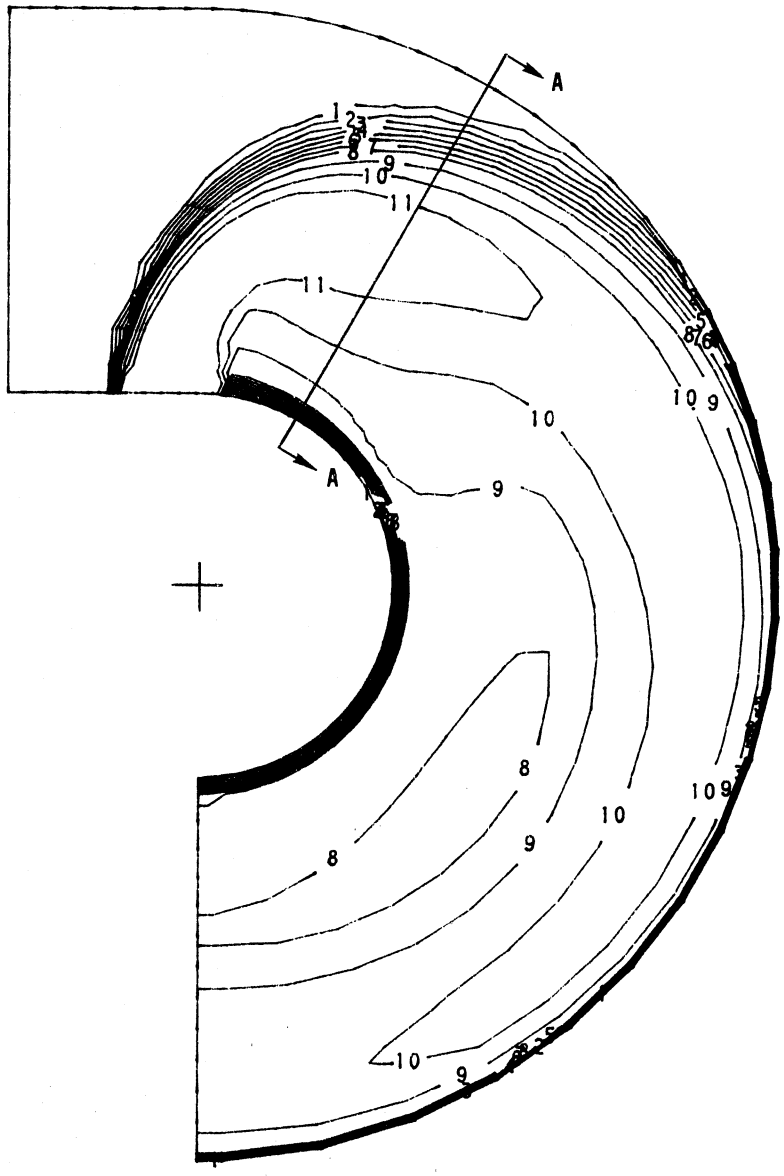

Figure 5-12a. Streamwise Theta Contours for Case 9.

$J = 26.4$
$S/H_0 = .5$
$H_0/D = 4$
$R_{ci}/H_0 = .5$

CONTOUR	VALUE
1	0.0500
2	0.1000
3	0.1500
4	0.2000
5	0.2500
6	0.3000
7	0.3500
8	0.4000
9	0.5000
10	0.6000
11	0.7000

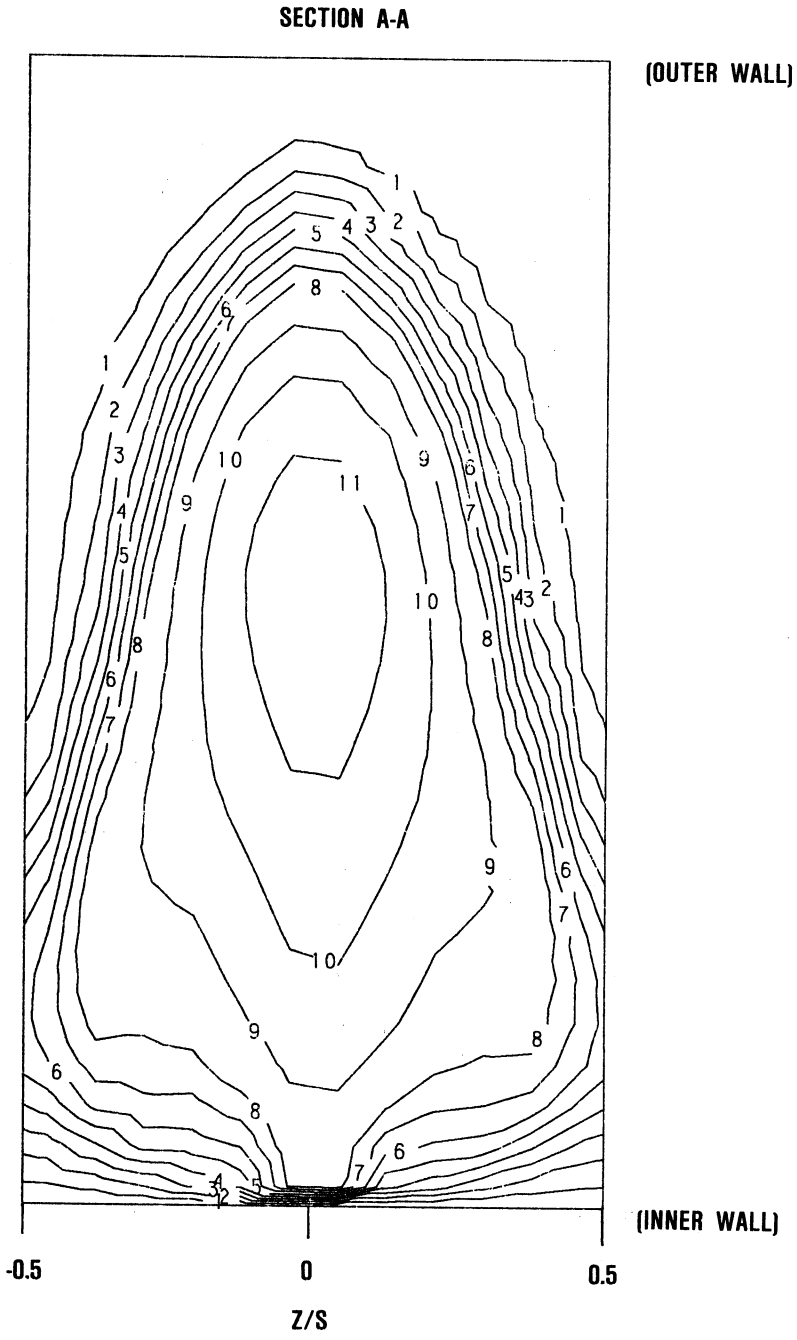

Figure 5-12b. Cross-Stream Theta Contours at Phi=30 Degrees for Case 9.

CONTOUR	VALUE
1	0.0500
2	0.1000
3	0.1500
4	0.2000
5	0.2500
6	0.3000
7	0.3500
8	0.4000
9	0.5000
10	0.6000
11	0.7000

$J = 6.6$

$S/H_0 = 0.5$

$D/H_0 = 0.25$

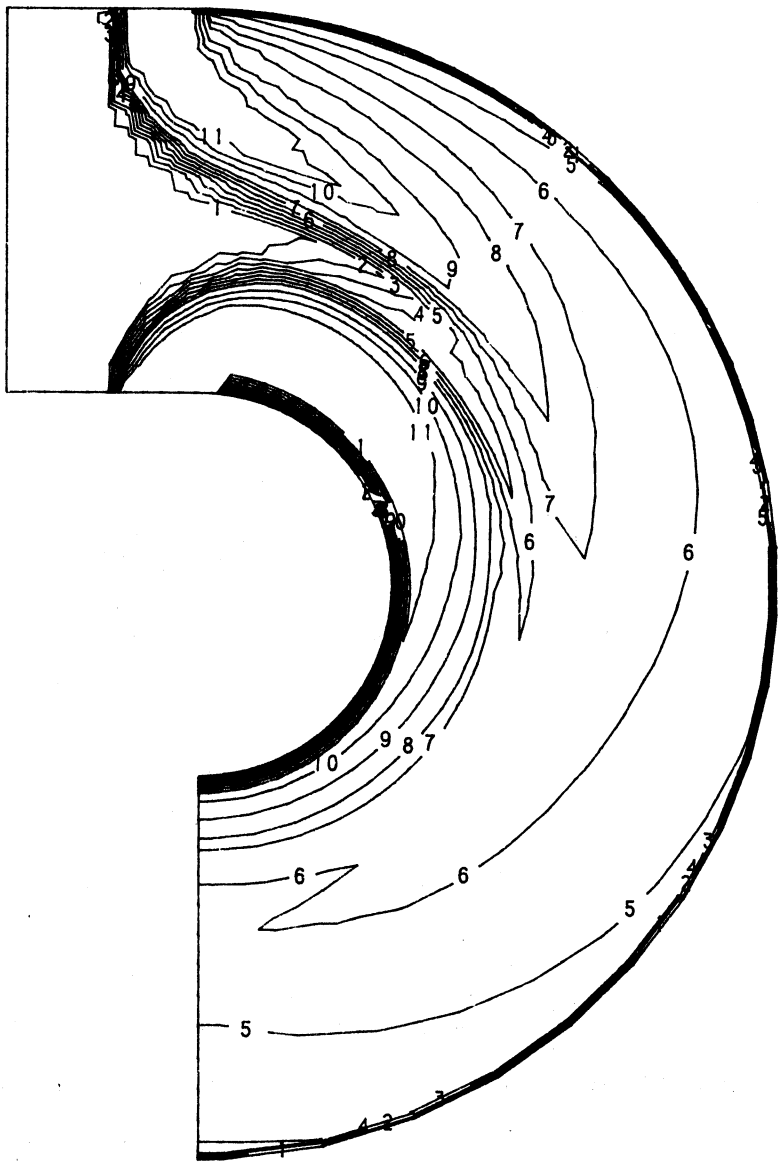

Figure 5-13. Streamwise Theta Contours for Case 10.

J = 6.4
S/Ho = .5
Ho/D = 4
Rci/Ho = .5

CONTOUR	VALUE
1	0.0500
2	0.1000
3	0.1500
4	0.2000
5	0.2500
6	0.3000
7	0.3500
8	0.4000
9	0.5000
10	0.6000
11	0.7000

J = 6.6

S/H_0 = 0.5

D/H_0 = 0.25

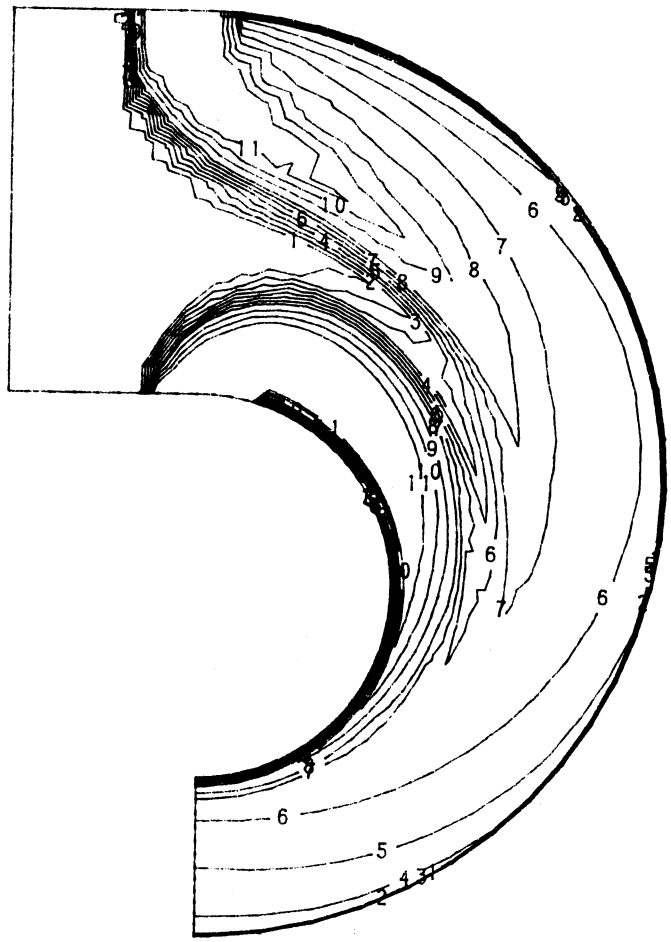

Figure 5-14. Streamwise Theta Contours for Case 11.

J = 6.6
S/Ho = .5
Ho/D = 4
Ri/Ho = .5
RADIAL CONVERGENCE

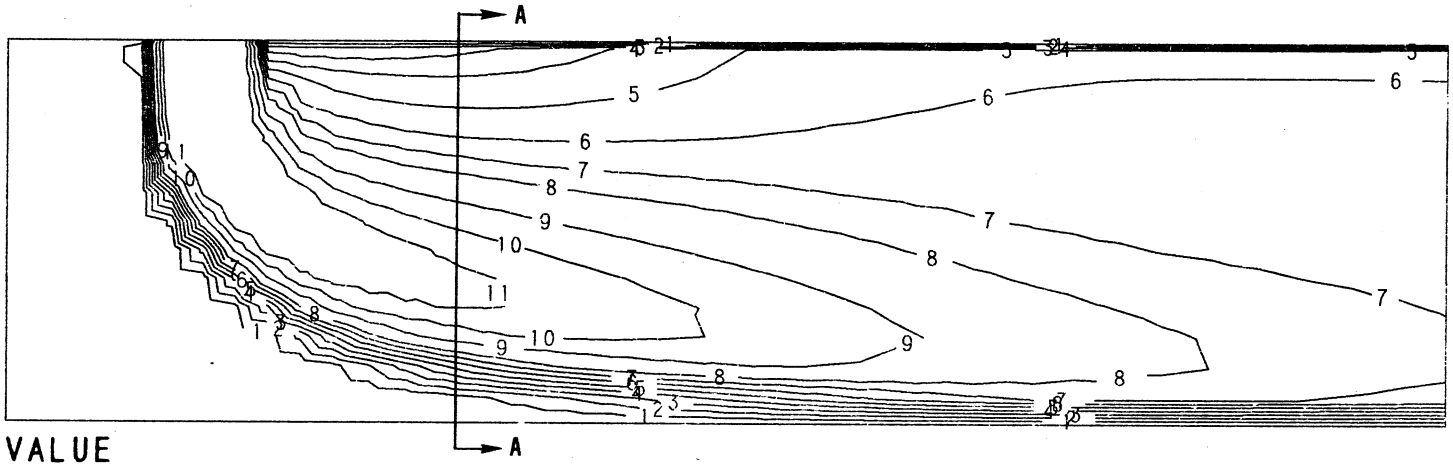

CONTOUR	VALUE
1	0.0500
2	0.1000
3	0.1500
4	0.2000
5	0.2500
6	0.3000
7	0.3500
8	0.4000
9	0.5000
10	0.6000
11	0.7000

J = 26.4
S/H_0 = 0.5
D/H_0 = 0.25

Figure 5-15a. Streamwise Theta Contours for Case 12.

J = 26.4
S/Ho = .5
Ho/D = 4

CONTOUR	VALUE
1	0.0500
2	0.1000
3	0.1500
4	0.2000
5	0.2500
6	0.3000
7	0.3500
8	0.4000
9	0.5000
10	0.6000
11	0.7000

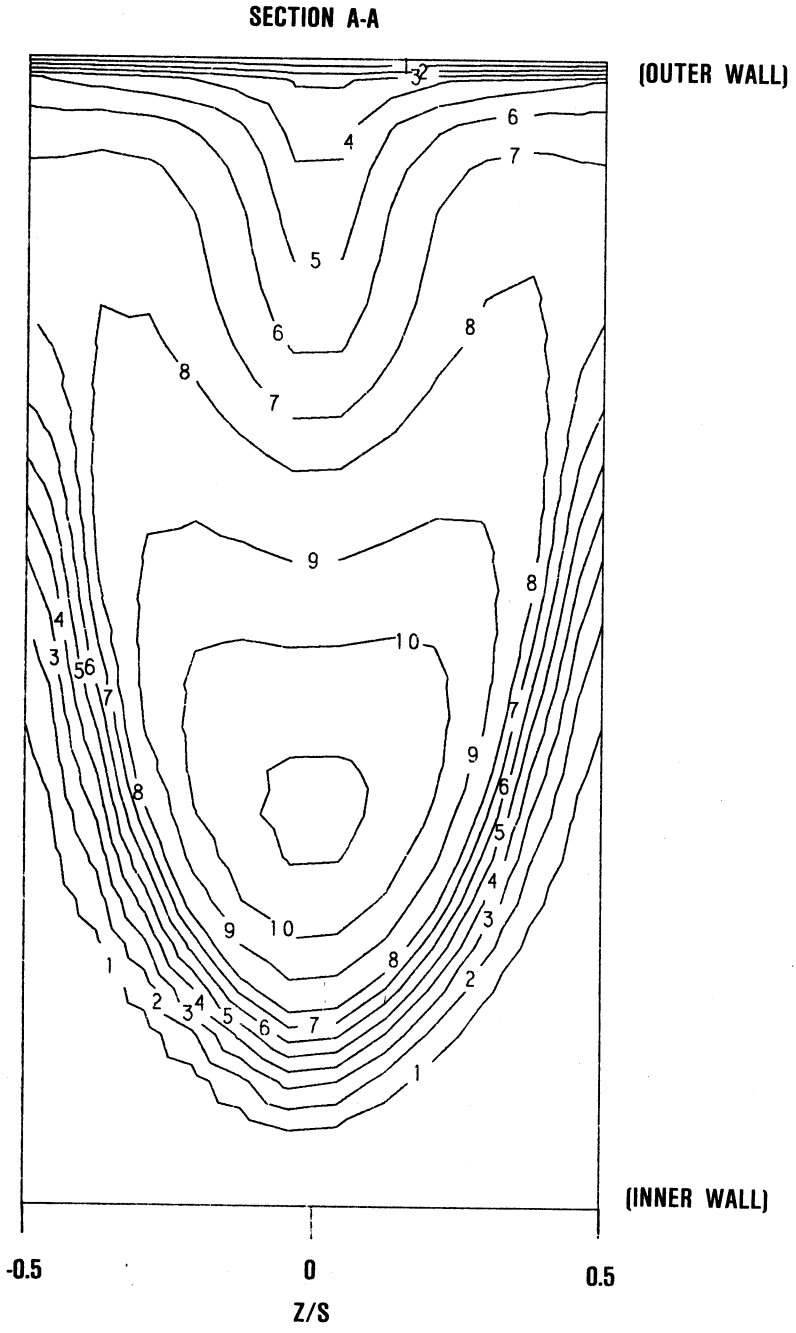

Figure 5-15b. Cross-Stream Theta Contours at X/H=0.75 for Case 12.

CONTOUR	VALUE
1	0.0500
2	0.1000
3	0.1500
4	0.2000
5	0.2500
6	0.3000
7	0.3500
8	0.4000
9	0.5000
10	0.6000
11	0.7000

J = 26.4

S/H_0 = 0.5

D/H_0 = 0.25

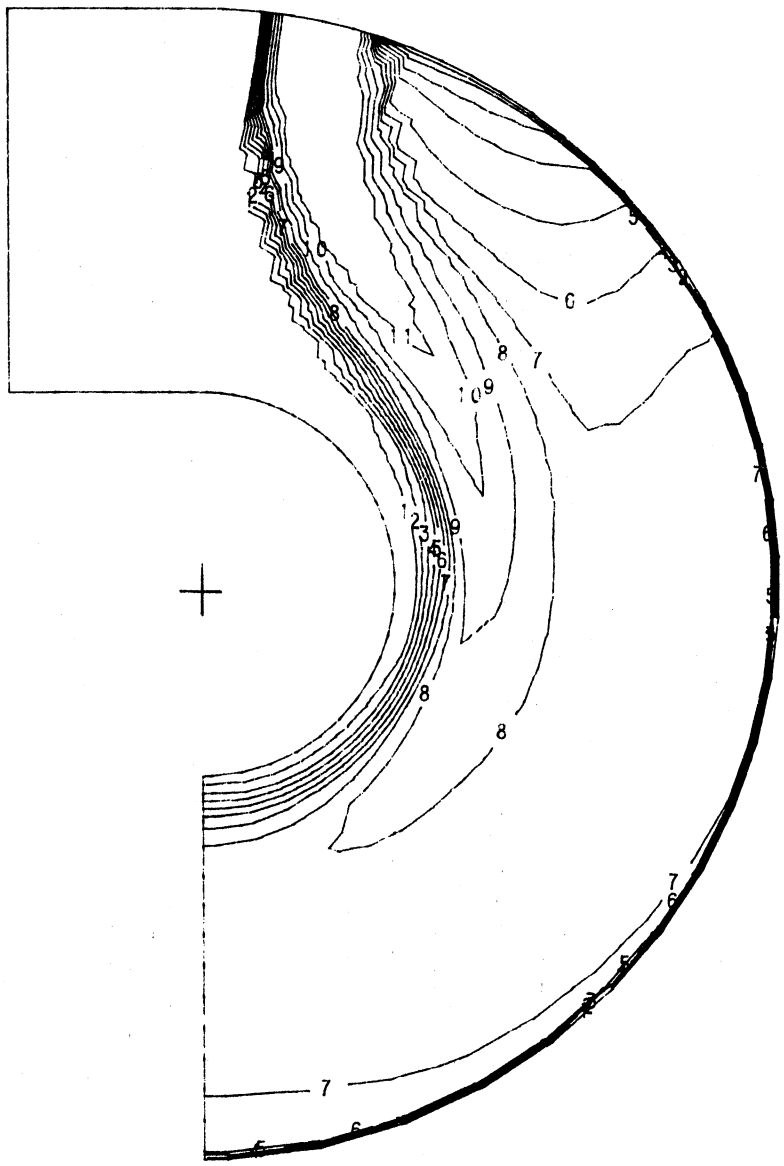

Figure 5-16. Streamwise Theta Contours for Case 13.

CONTOUR	VALUE
1	0.0500
2	0.1000
3	0.1500
4	0.2000
5	0.2500
6	0.3000
7	0.3500
8	0.4000
9	0.5000
10	0.6000
11	0.7000

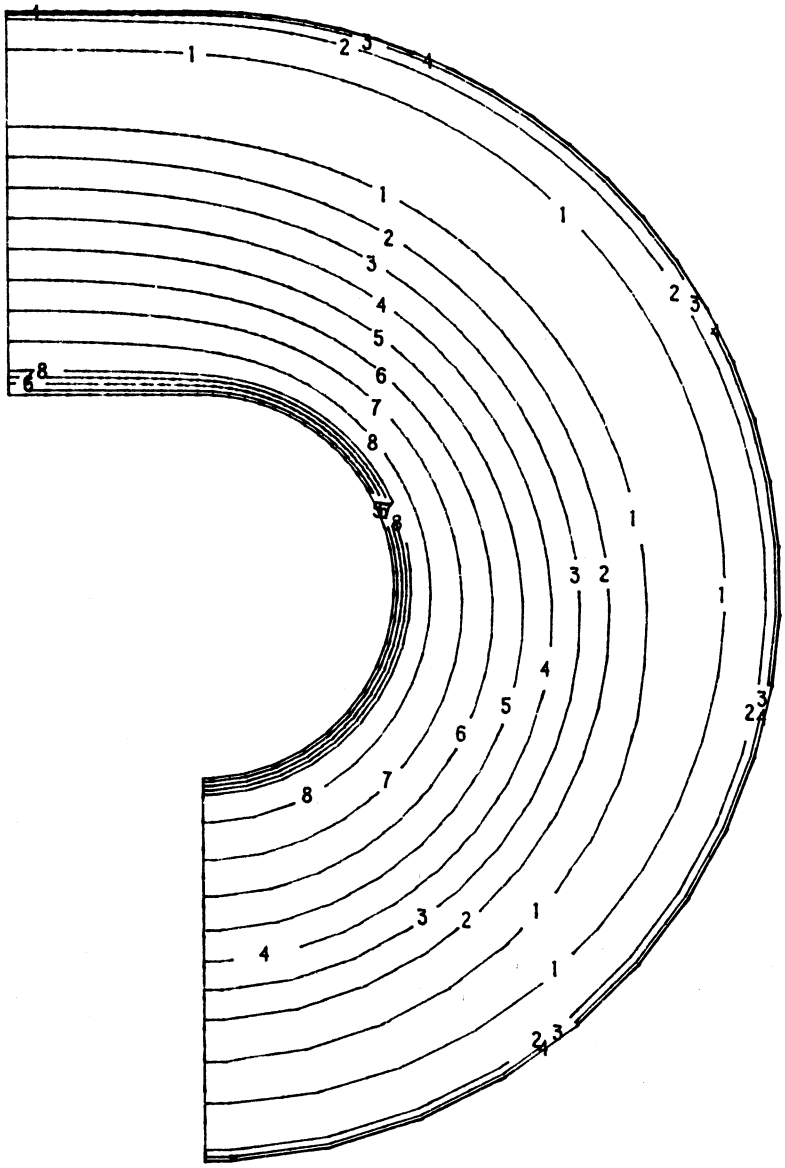

Figure 5-17a. Streamwise Theta Contours for Case 14.

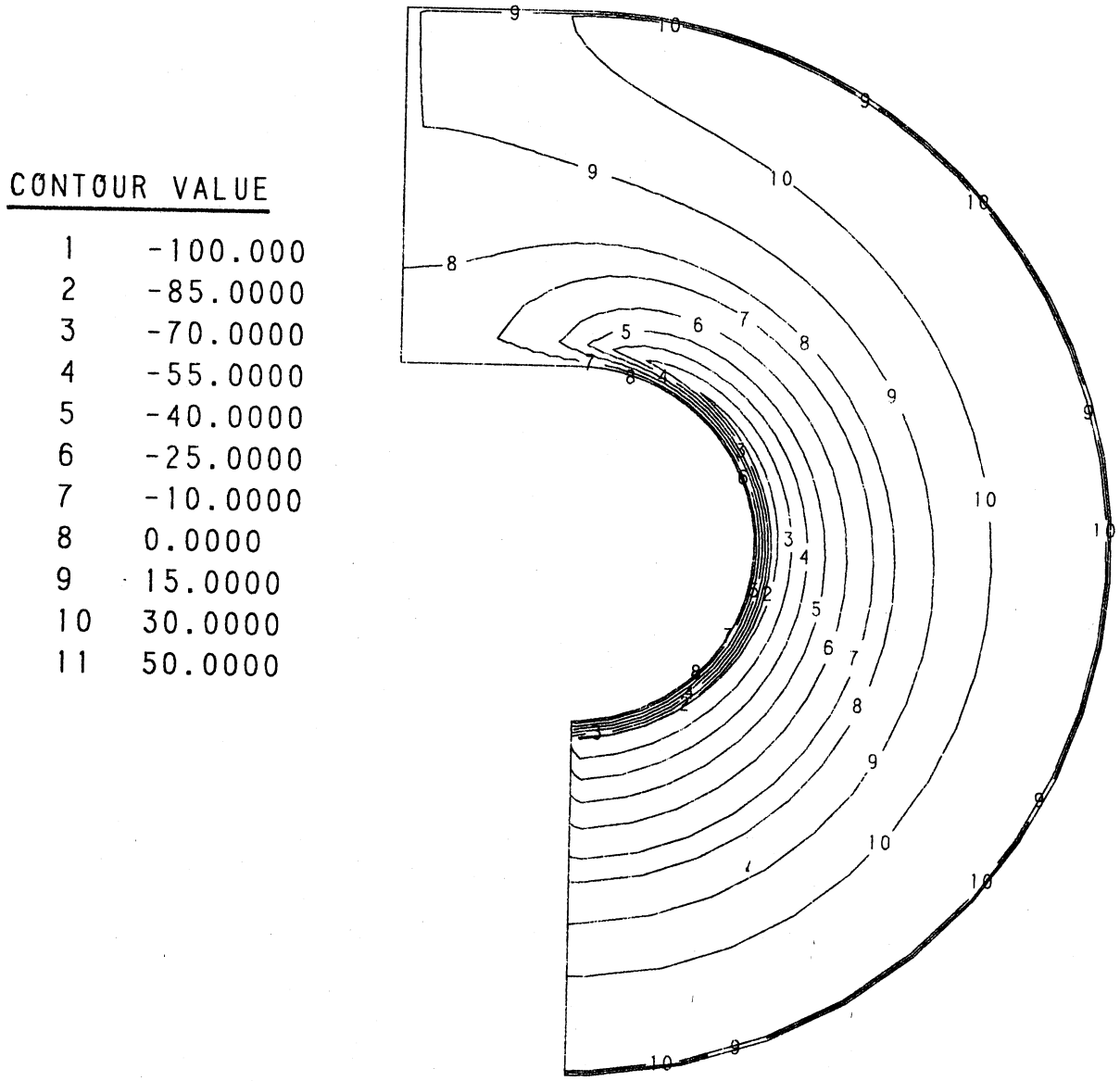

Figure 5-17b. Streamwise Relative Pressure Contours for Case 14.

CONTOUR	VALUE
1	0.0500
2	0.1000
3	0.1500
4	0.2000
5	0.2500
6	0.3000
7	0.3500
8	0.4000
9	0.5000
10	0.6000
11	0.7000

$J = 6.6$

$S/H_0 = 0.5$

$D/H_0 = 0.25$

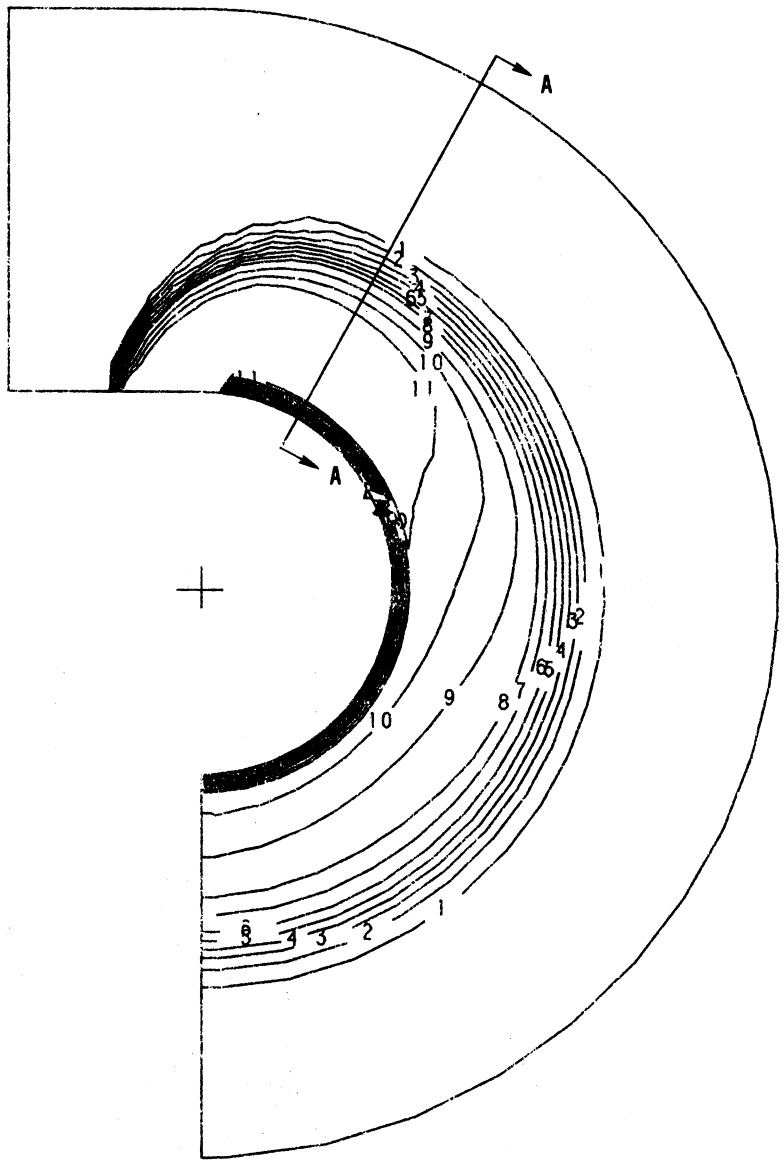

Figure 5-18a. Streamwise Theta Contours for Case 15.

CONTOUR	VALUE
1	0.0500
2	0.1000
3	0.1500
4	0.2000
5	0.2500
6	0.3000
7	0.3500
8	0.4000
9	0.5000
10	0.6000
11	0.7000

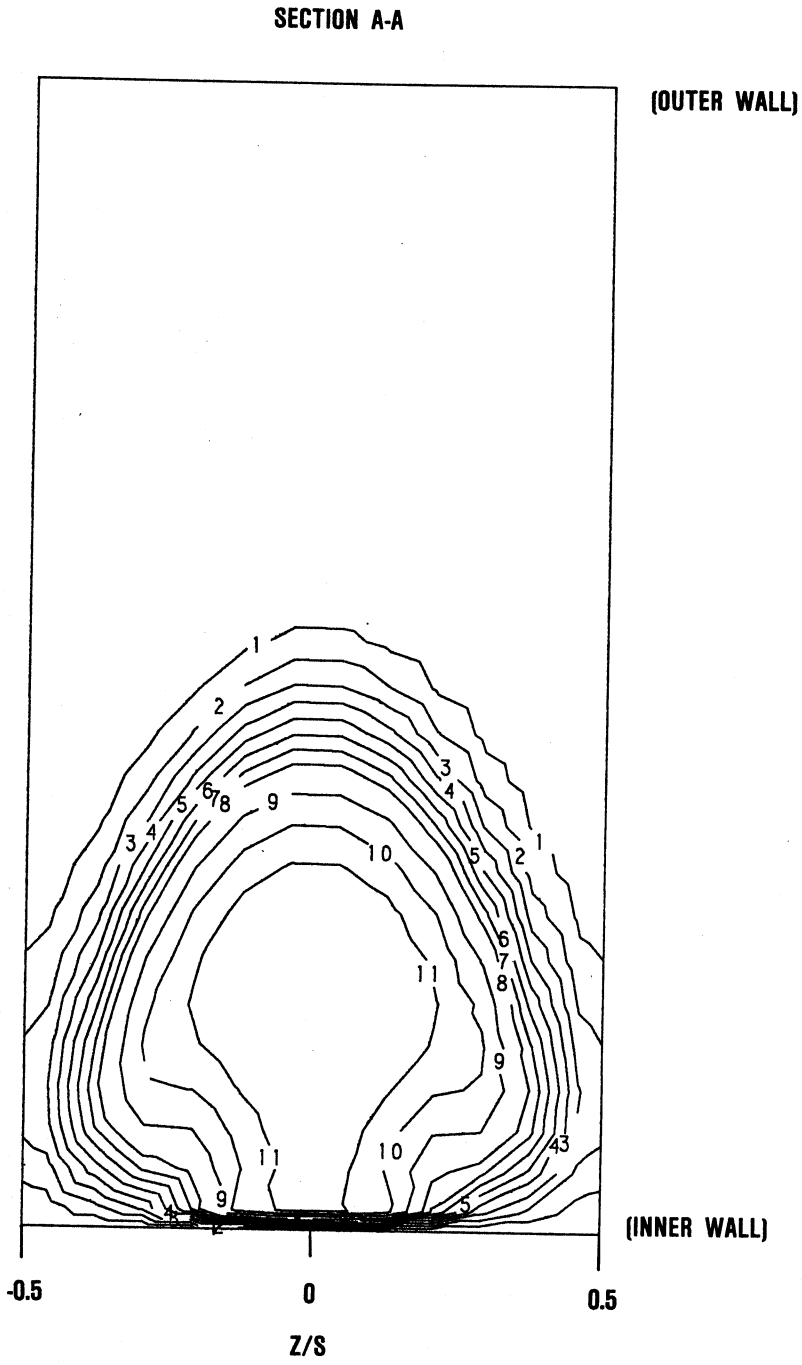

Figure 5-18b. Cross-Stream Theta Contours at Phi=30 Degrees for Case 15.

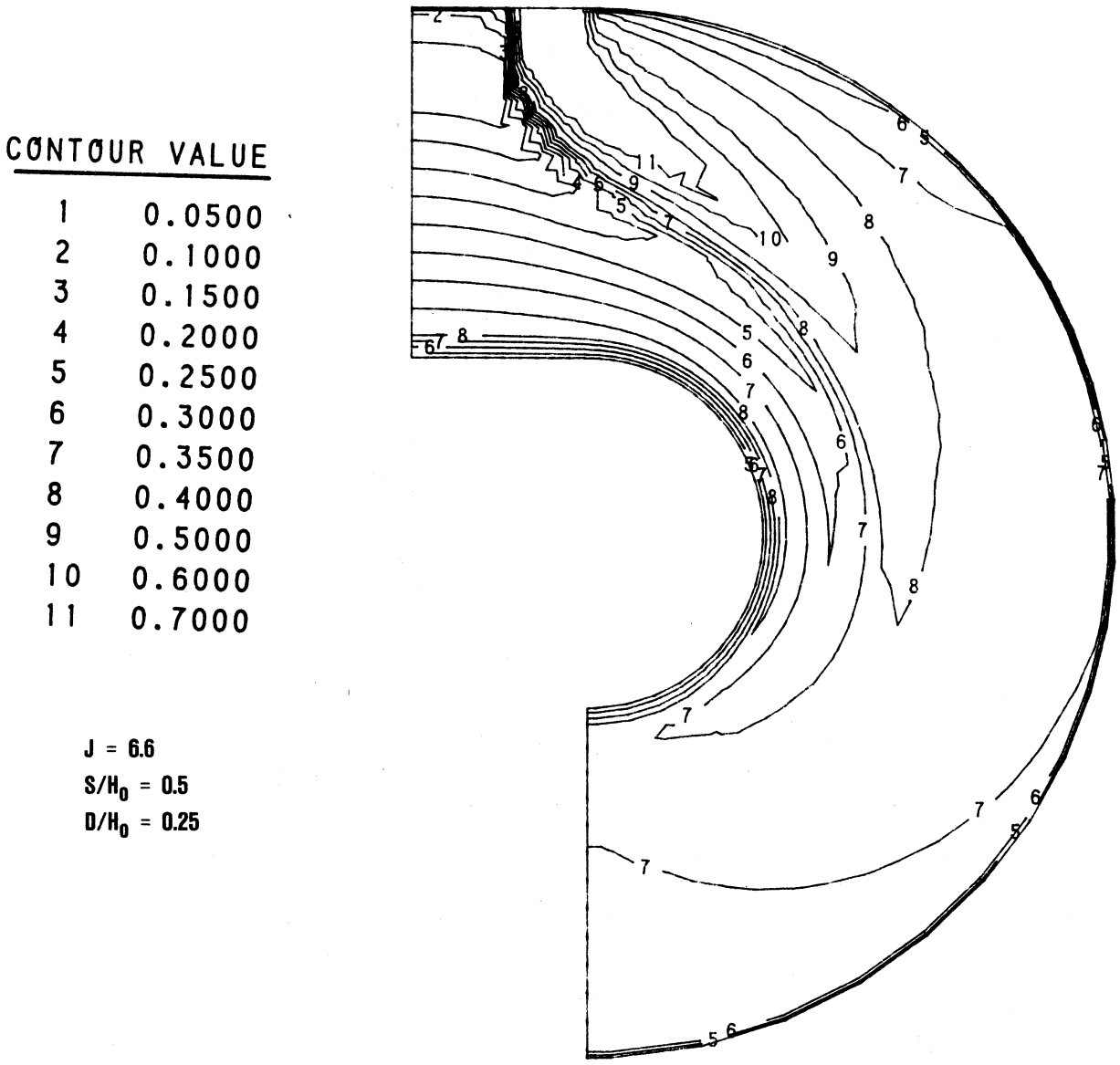

Figure 5-19. Streamwise Theta Contours for Case 16.

CONTOUR	VALUE
1	0.0500
2	0.1000
3	0.1500
4	0.2000
5	0.2500
6	0.3000
7	0.3500
8	0.4000
9	0.5000
10	0.6000
11	0.7000

J = 26.4

S/H_0 = 0.5

D/H_0 = 0.177

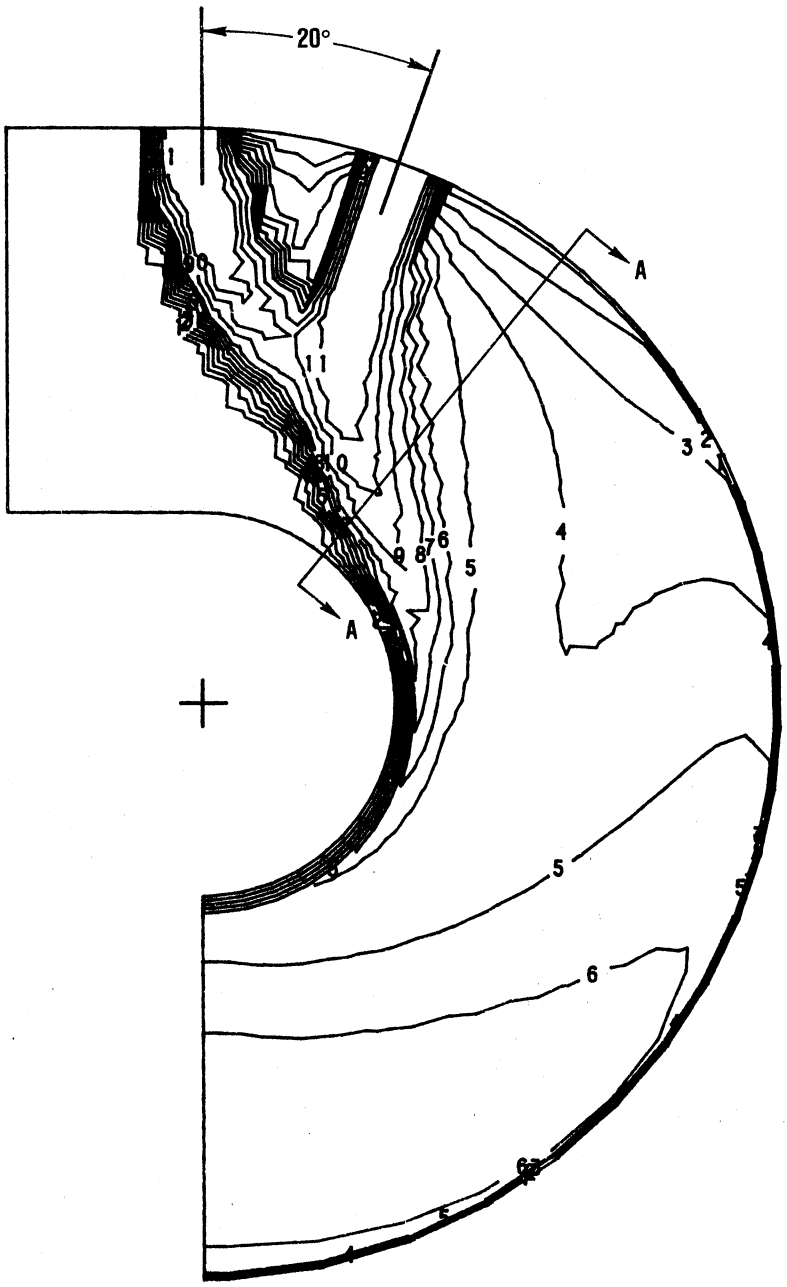

Figure 5-20a. Streamwise Theta Contours for Case 17.

CONTOUR	VALUE
1	0.0500
2	0.1000
3	0.1500
4	0.2000
5	0.2500
6	0.3000
7	0.3500
8	0.4000
9	0.5000
10	0.6000
11	0.7000

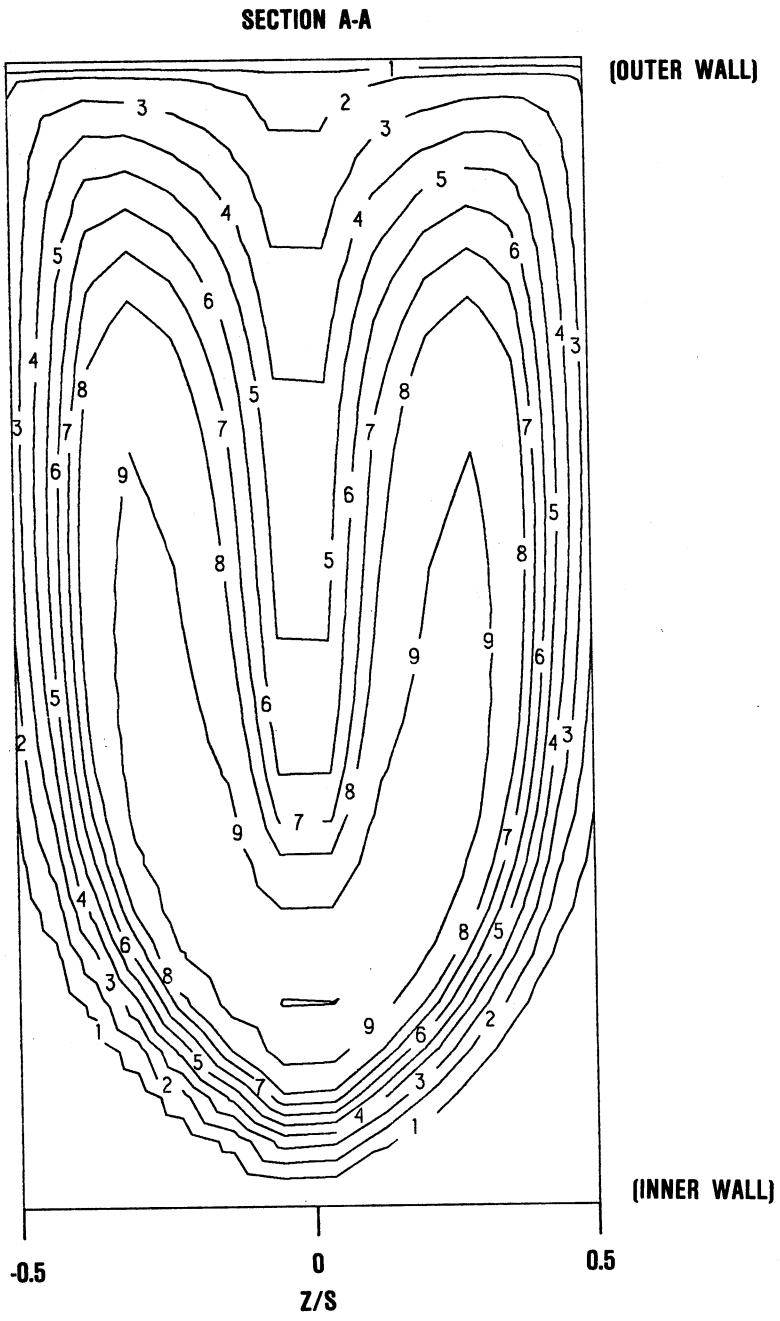

Figure 5-20b. Cross-Stream Theta Contours at Phi=40 Degrees for Case 17.

CONTOUR	VALUE
1	0.0500
2	0.1000
3	0.1500
4	0.2000
5	0.2500
6	0.3000
7	0.3500
8	0.4000
9	0.5000
10	0.6000
11	0.7000

J = 26.4
S/H_0 = 1.0
D/H_0 = 0.25

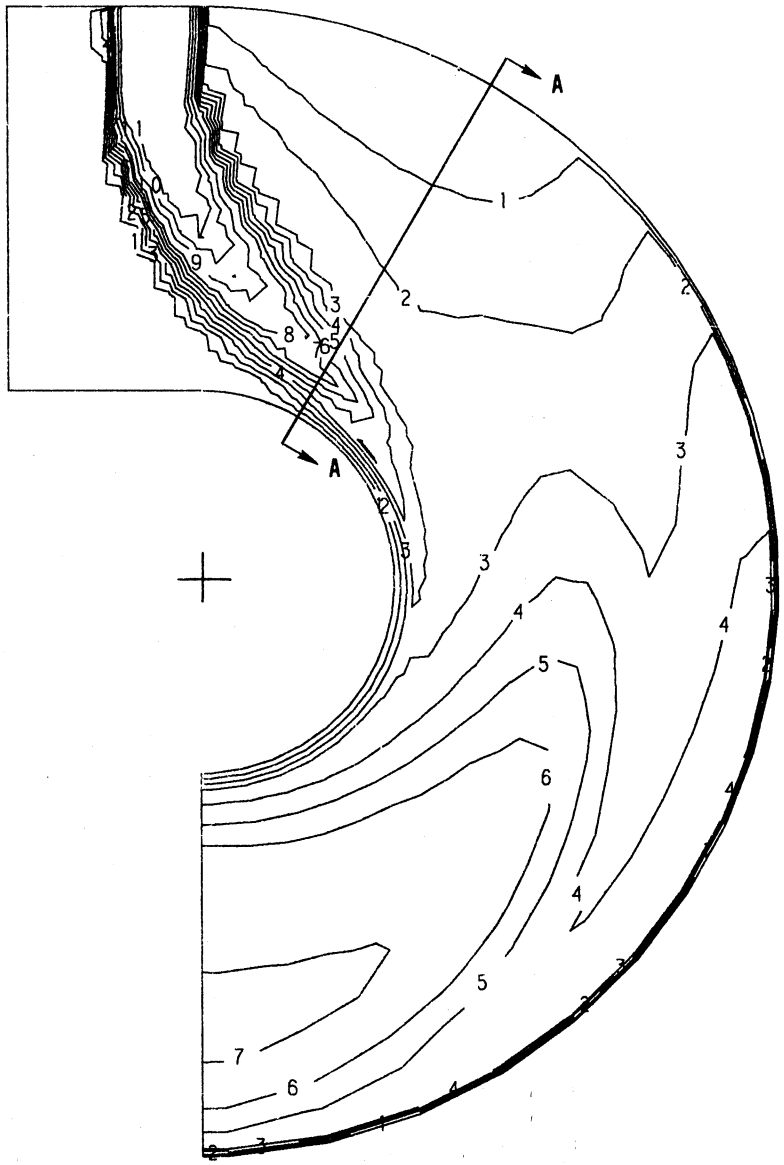

Figure 5-21a. Streamwise Theta Contours for Case 18, OD Jet.

CONTOUR	VALUE
1	0.0500
2	0.1000
3	0.1500
4	0.2000
5	0.2500
6	0.3000
7	0.3500
8	0.4000
9	0.5000
10	0.6000
11	0.7000

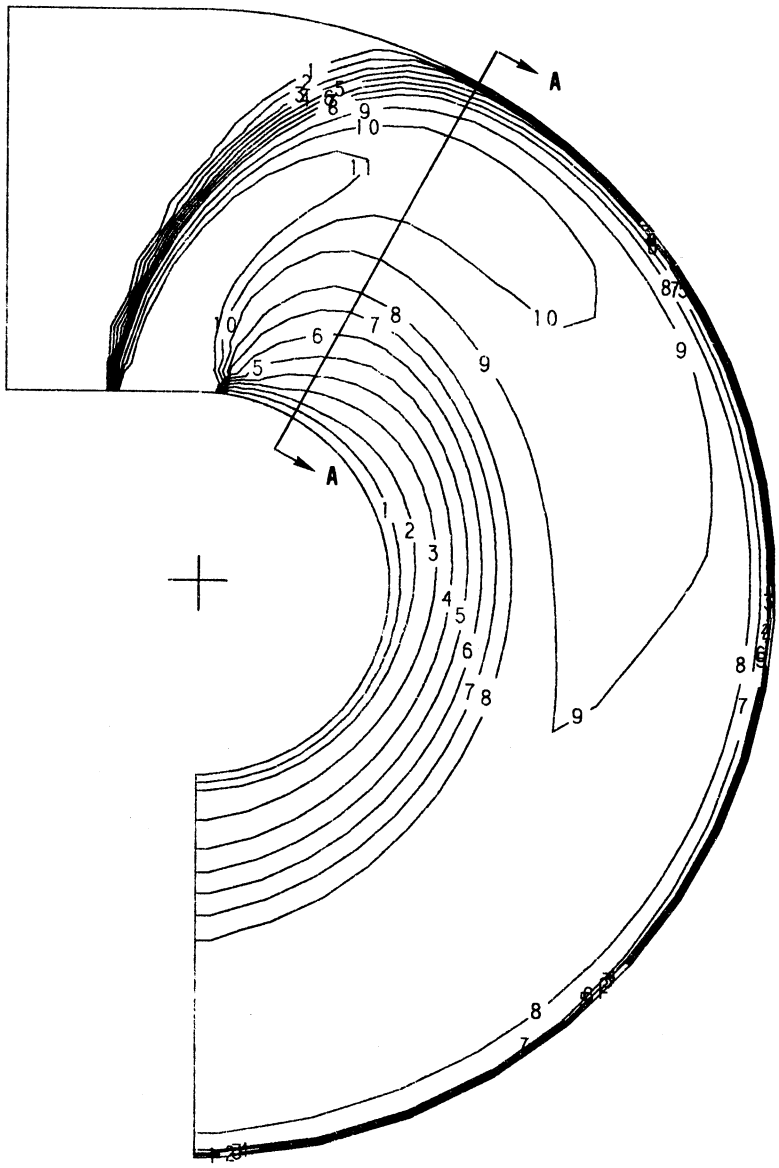

Figure 5-21b. Streamwise Theta Contours for Case 18, ID Jet.

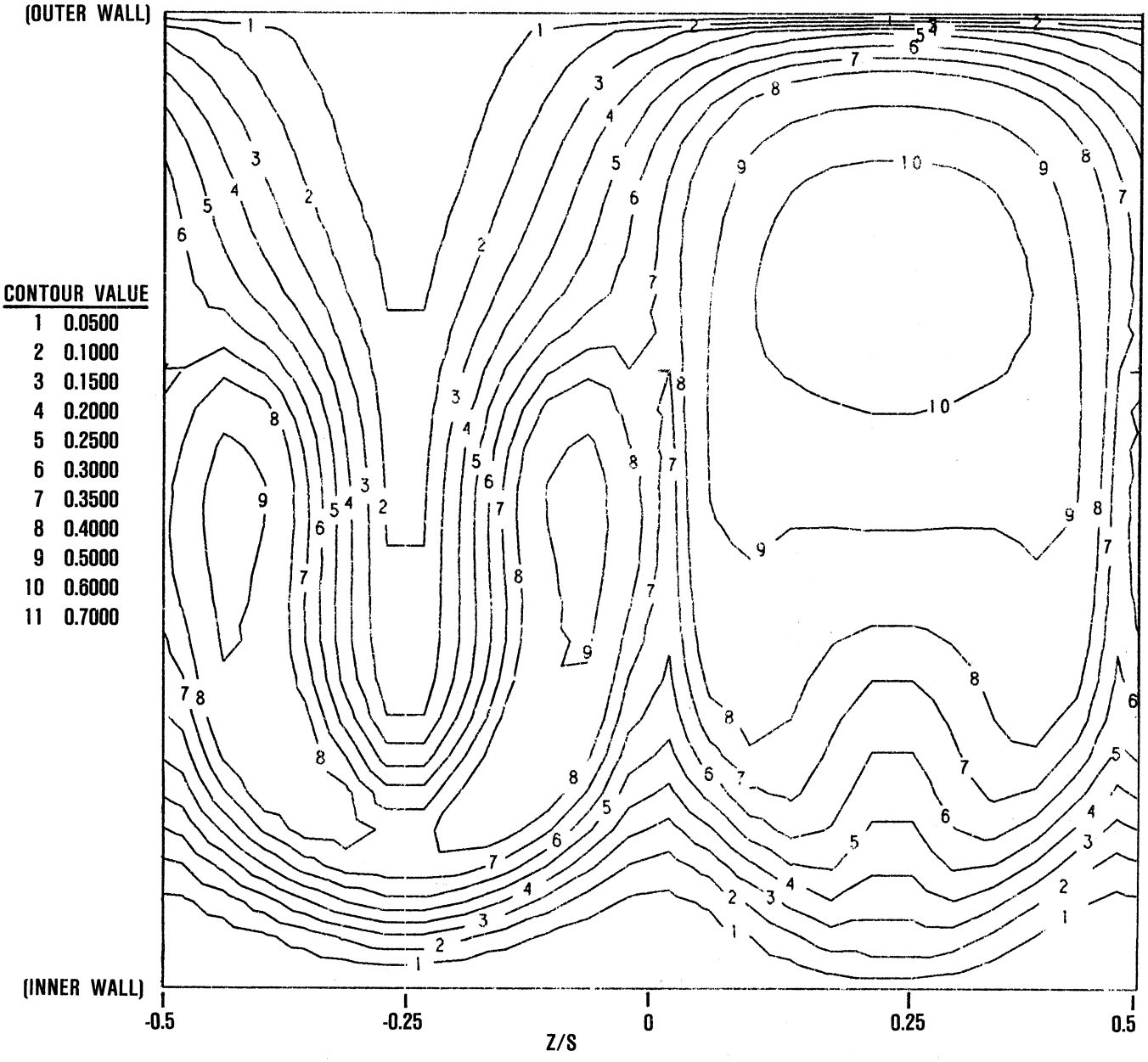

Figure 5-21c. Cross-Stream Theta Contours at Phi=30 Degrees for Case 18.

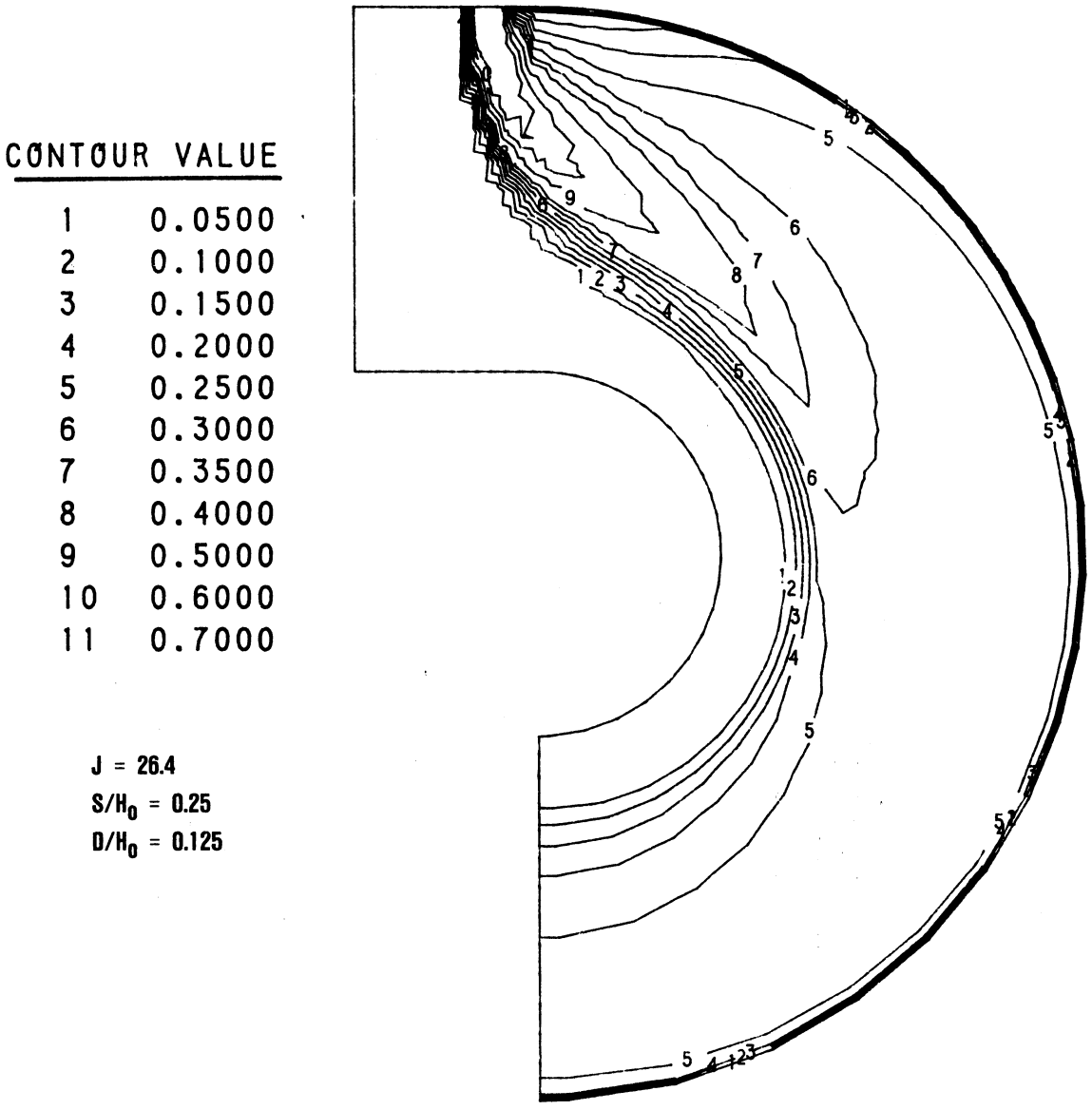

Figure 5-22. Streamwise Theta Contours for Case 19.

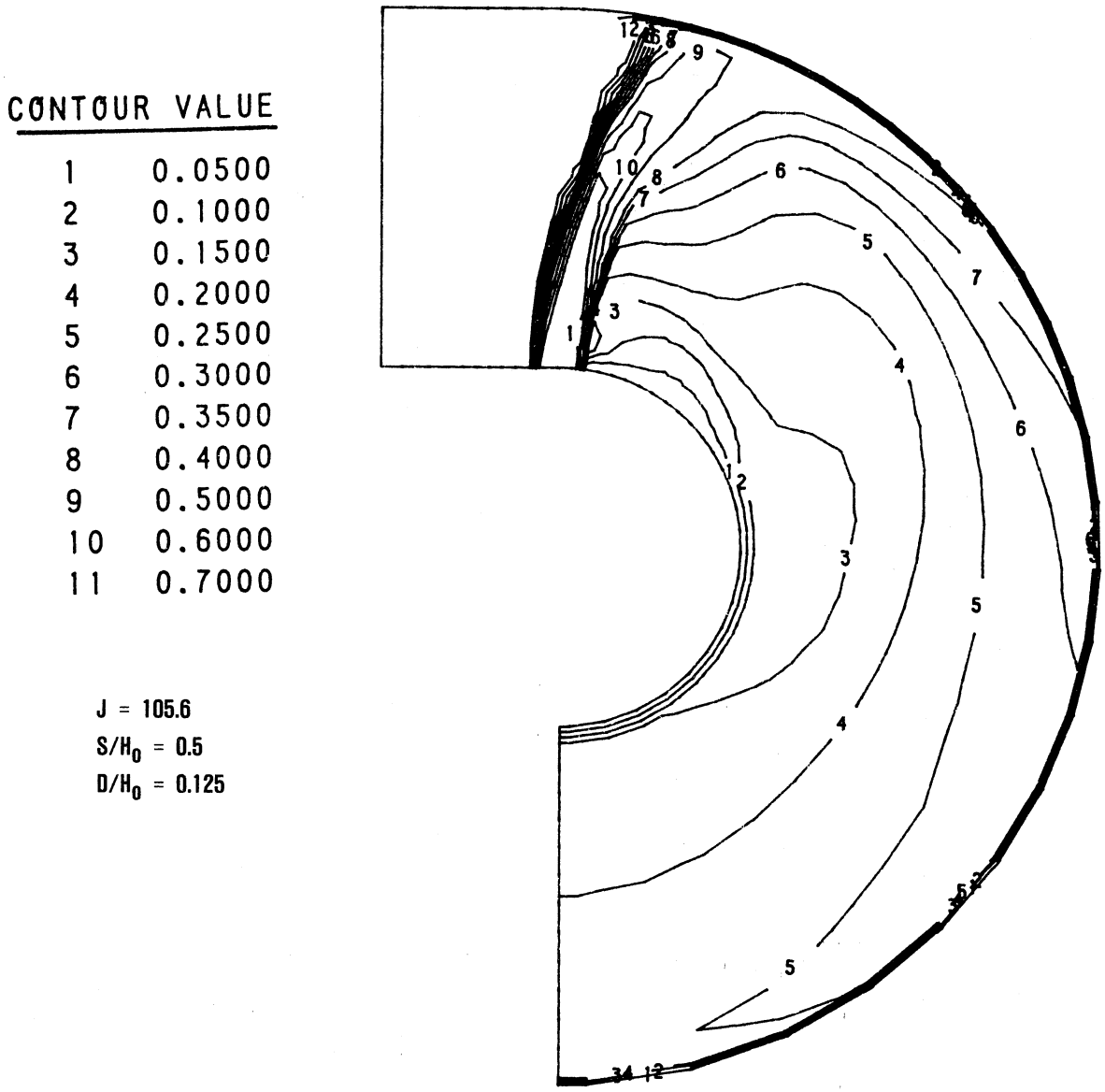

Figure 5-23. Streamwise Theta Contours for Case 20.

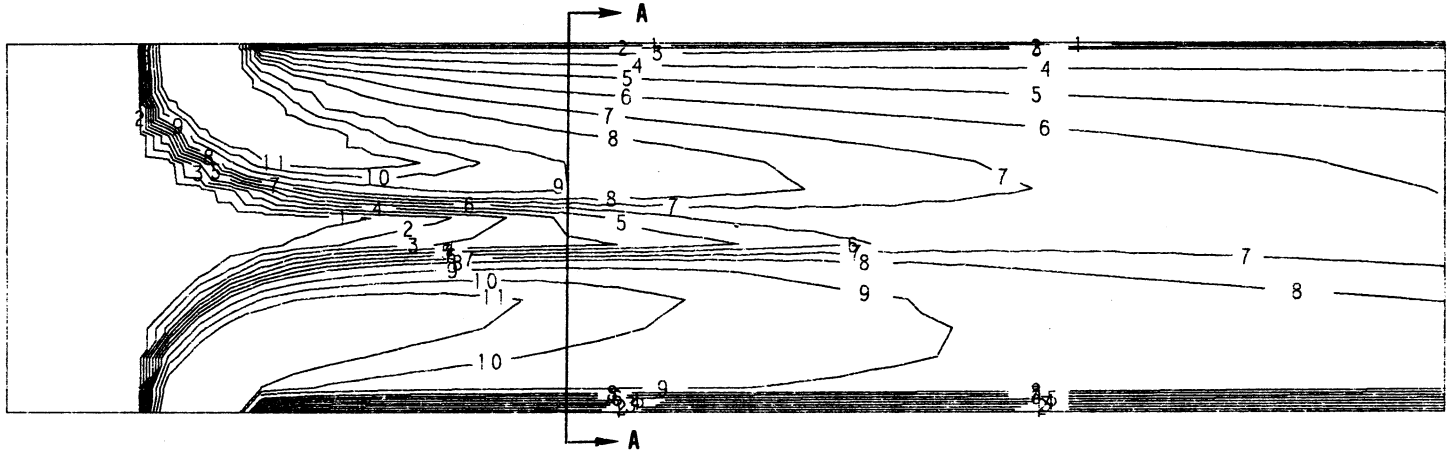

CONTOUR	VALUE
1	0.0500
2	0.1000
3	0.1500
4	0.2000
5	0.2500
6	0.3000
7	0.3500
8	0.4000
9	0.5000
10	0.6000
11	0.7000

J = 6.6
S/H_0 = 0.5
D/H_0 = 0.25

Figure 5-24a. Streamwise Theta Contours for Case 21.

SECTION A-A

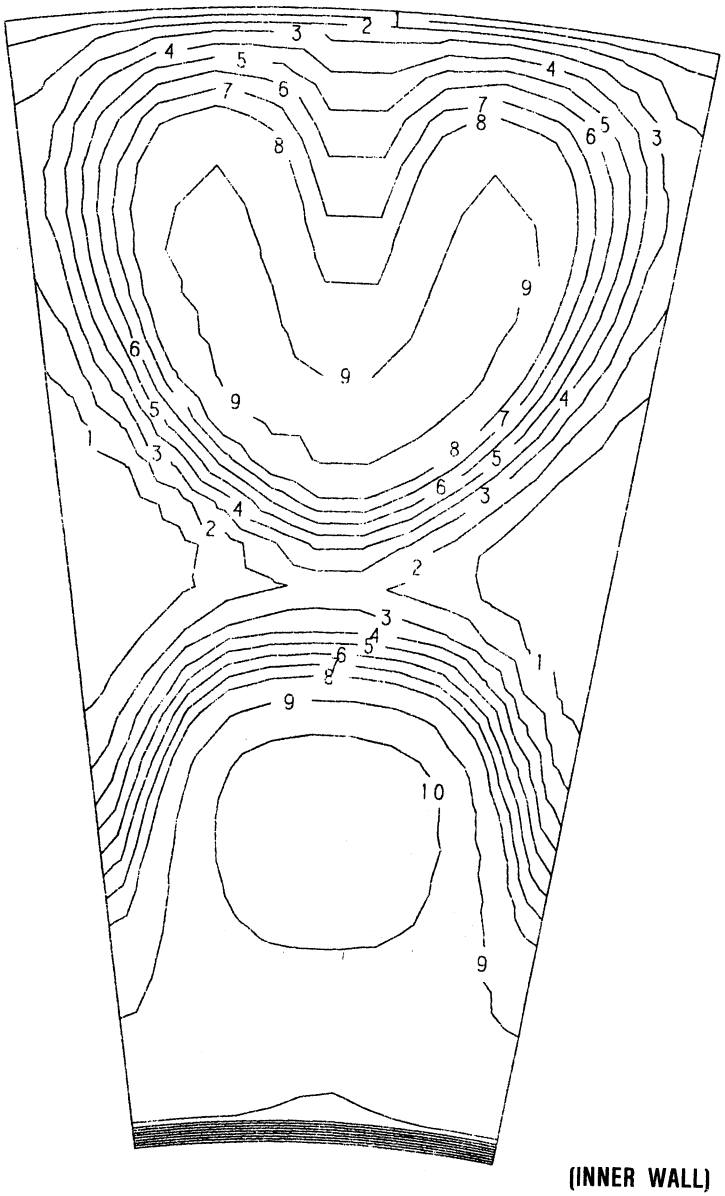

CONTOUR	VALUE
1	0.0500
2	0.1000
3	0.1500
4	0.2000
5	0.2500
6	0.3000
7	0.3500
8	0.4000
9	0.5000
10	0.6000
11	0.7000

Figure 5-24b. Cross-Stream Theta Contours at X/H=1.0 for Case 21.

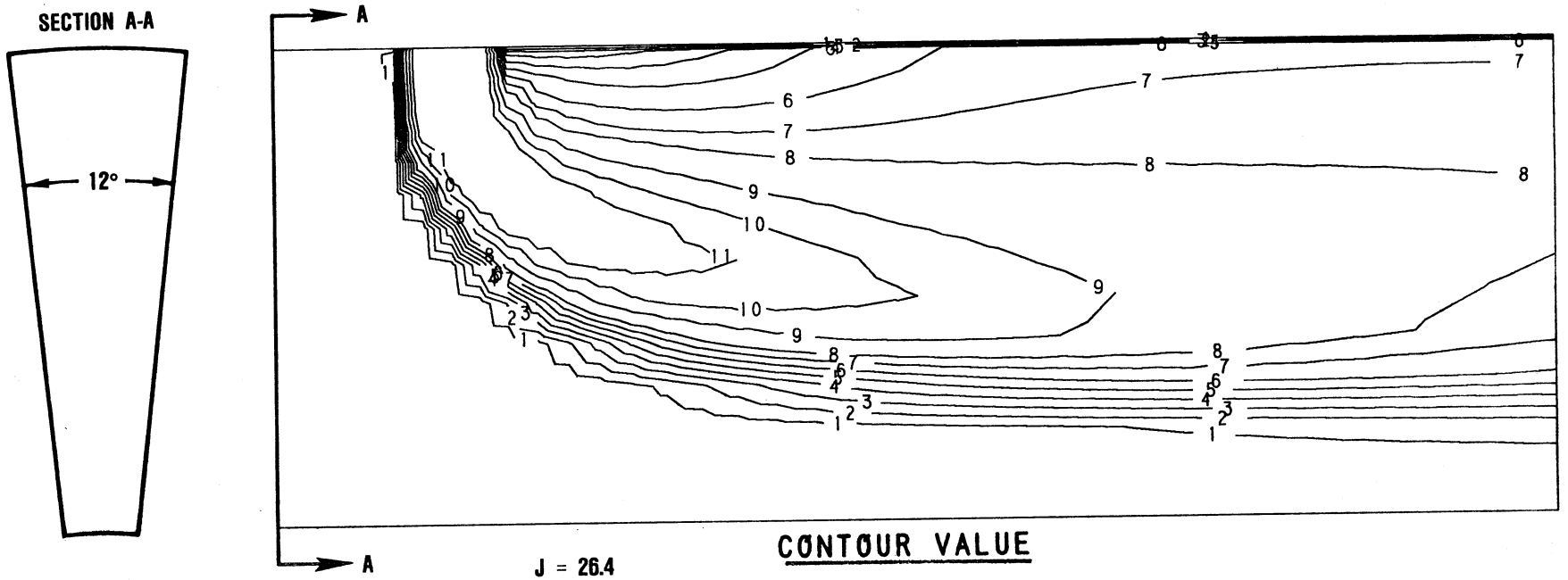

J = 26.4

S/H_0 = 0.3535

D/H_0 = 0.177

CONTOUR	VALUE
1	0.0500
2	0.1000
3	0.1500
4	0.2000
5	0.2500
6	0.3000
7	0.3500
8	0.4000
9	0.5000
10	0.6000
11	0.7000

Figure 5-25. Streamwise Theta Contours for Case 22.

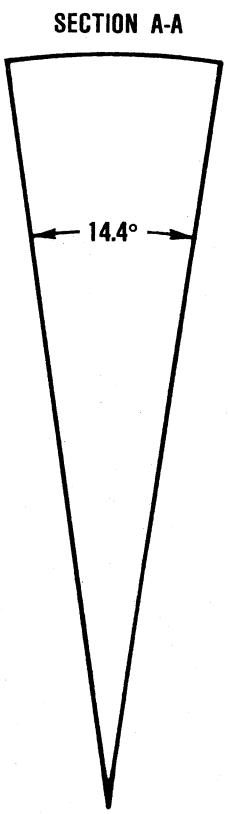

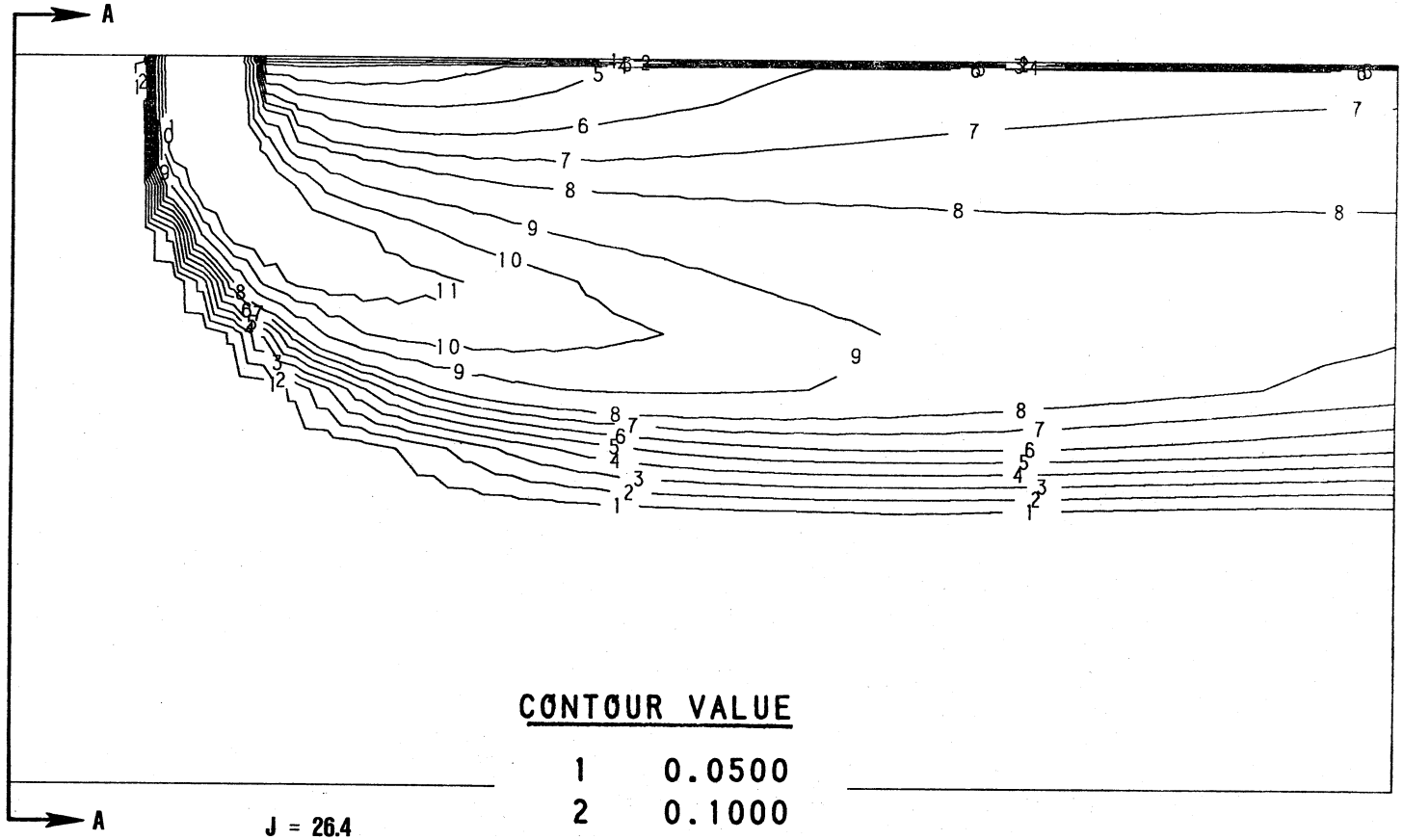

J = 26.4
S/H_0 = 0.25
D/H_0 = 0.125

CONTOUR	VALUE
1	0.0500
2	0.1000
3	0.1500
4	0.2000
5	0.2500
6	0.3000
7	0.3500
8	0.4000
9	0.5000
10	0.6000
11	0.7000

Figure 5-26. Streamwise Theta Contours for Case 23.

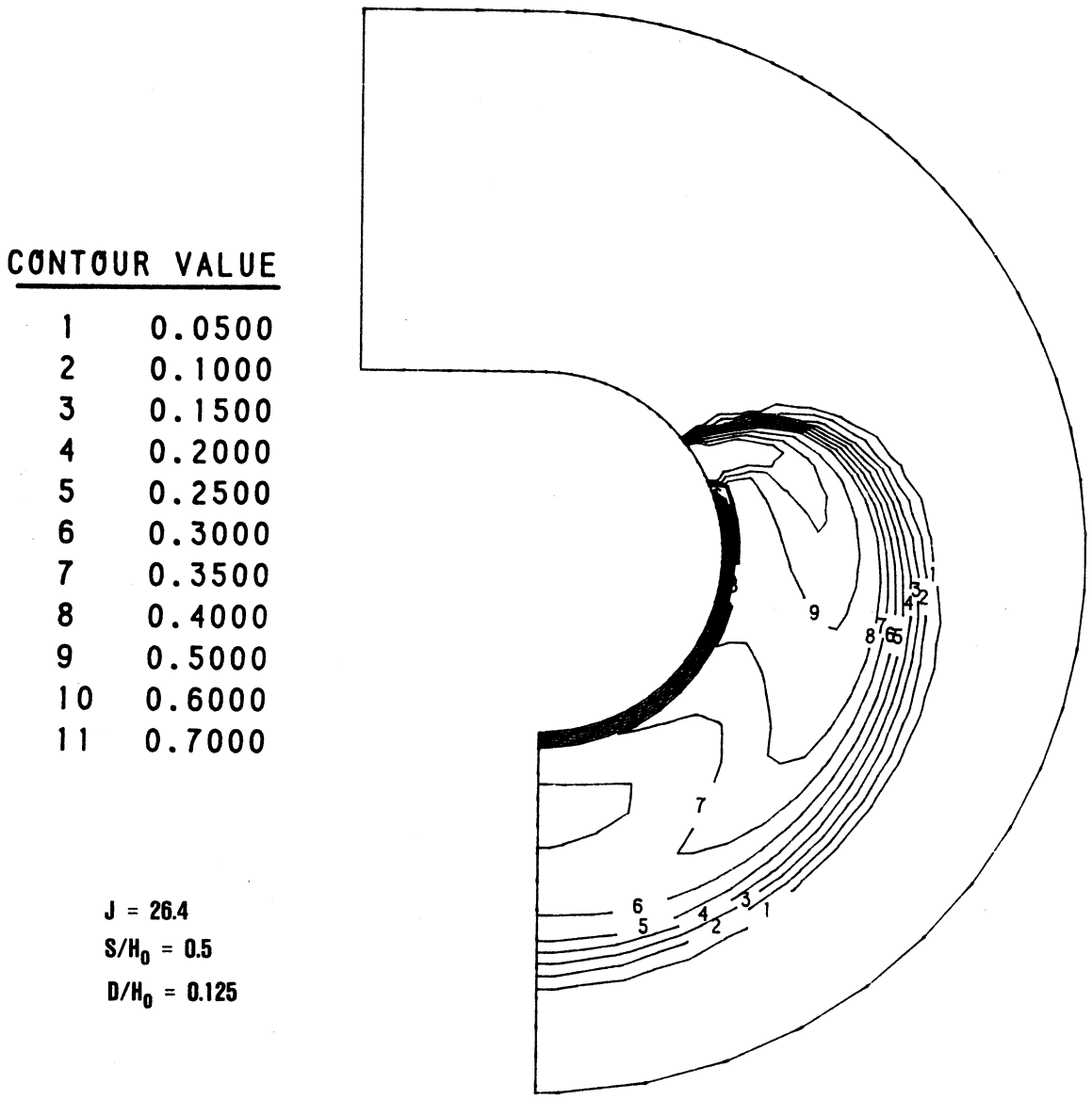

Figure 5-27. Streamwise Theta Contours for Case 24.

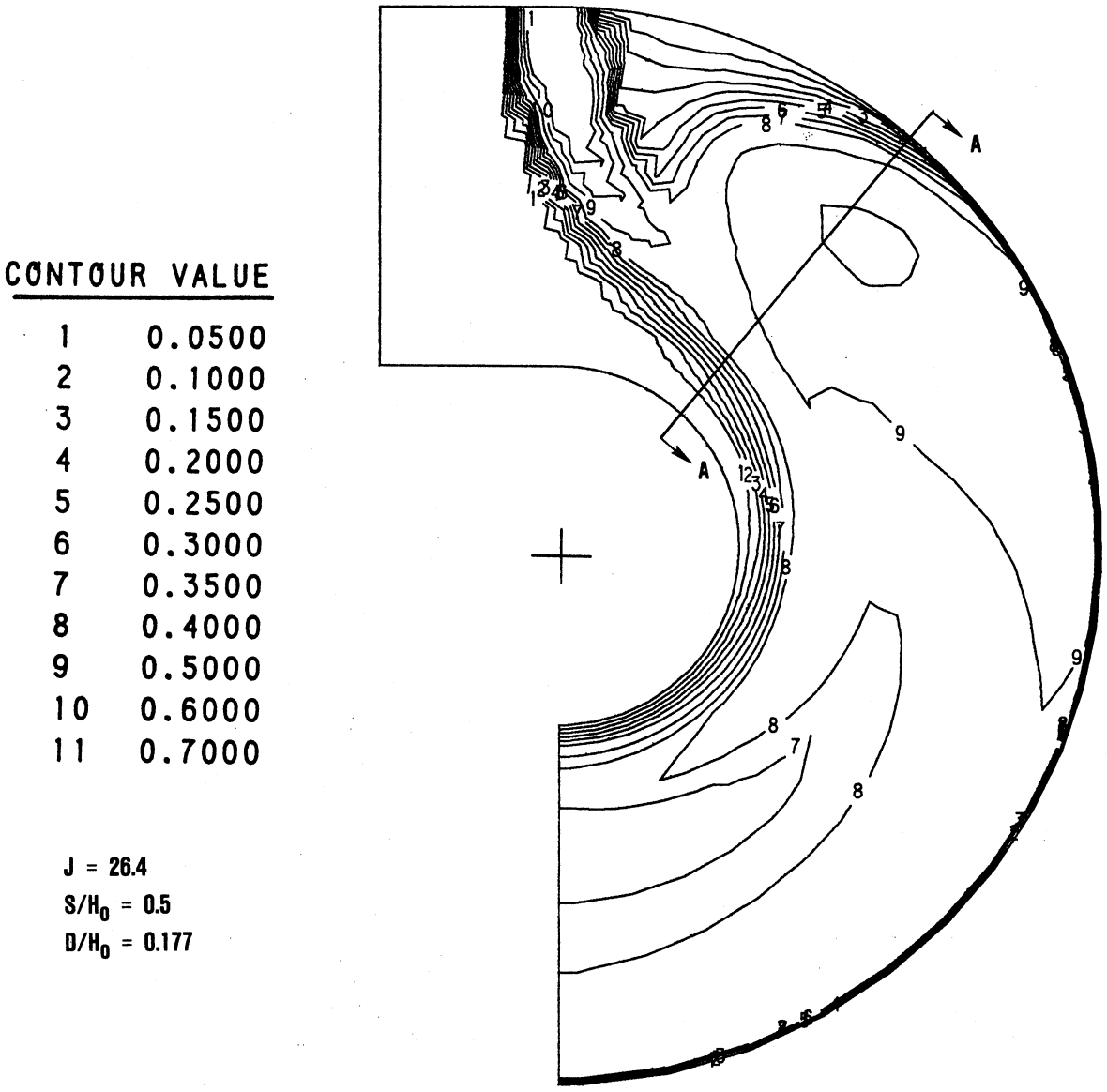

Figure 5-28a. Streamwise Theta Contours for Case 25, Leading Row.

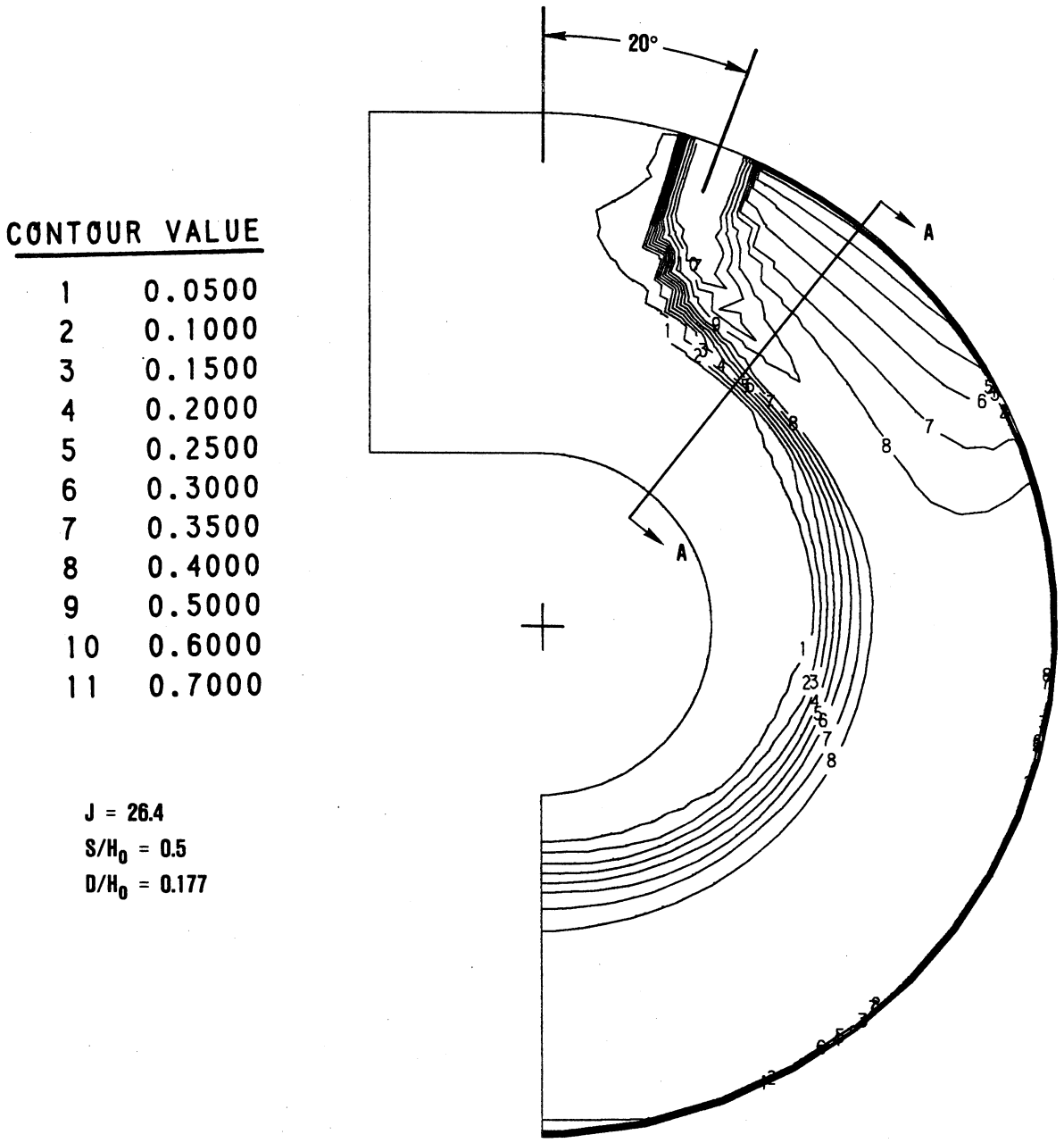

Figure 5-28b. Streamwise Theta Contours for Case 25, Trailing Row.

SECTION A-A

CONTOUR	VALUE
1	0.0500
2	0.1000
3	0.1500
4	0.2000
5	0.2500
6	0.3000
7	0.3500
8	0.4000
9	0.5000
10	0.6000
11	0.7000

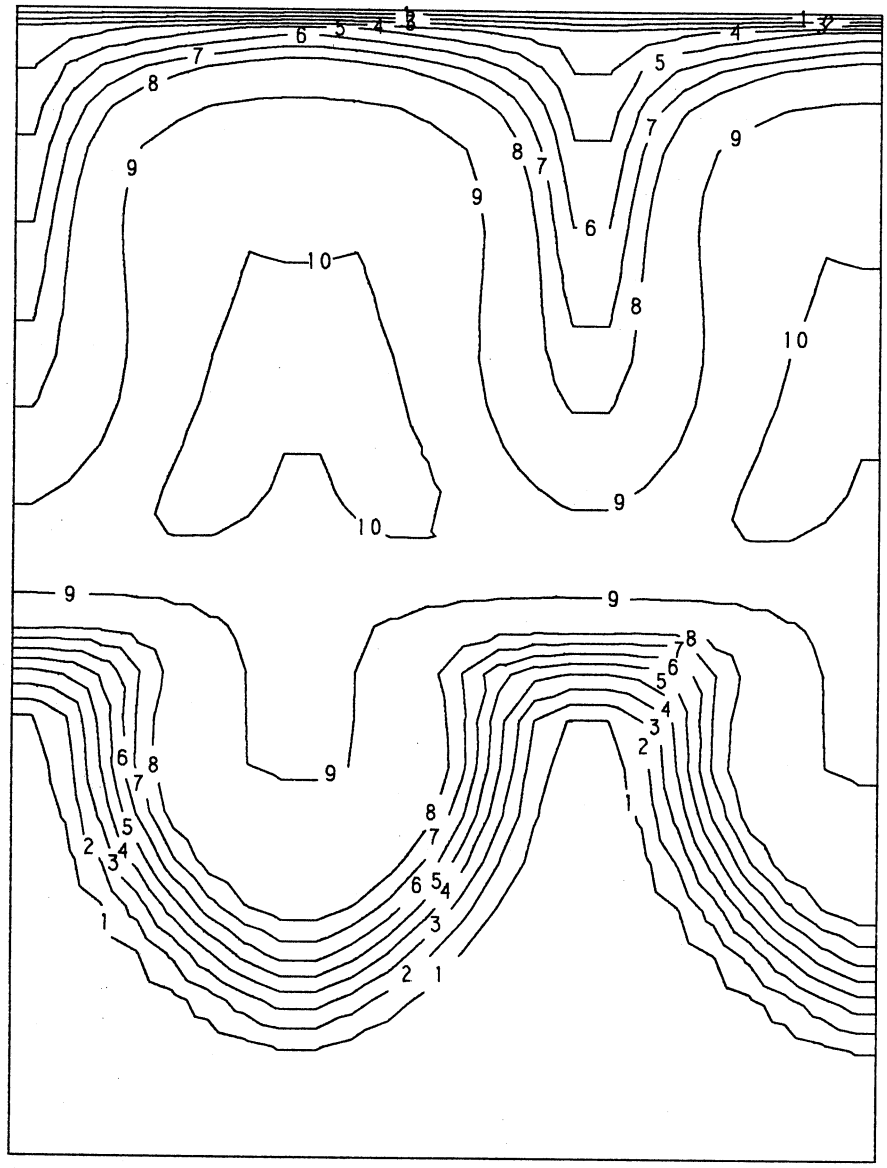

Figure 5-28c. Cross-Stream Theta Contours at Phi=40 Degrees for Case 25.

CONTOUR	VALUE
1	0.0500
2	0.1000
3	0.1500
4	0.2000
5	0.2500
6	0.3000
7	0.3500
8	0.4000
9	0.5000
10	0.6000
11	0.7000

$J = 26.4$

$S/H_0 = 0.5$

$D/H_0 = 0.25$

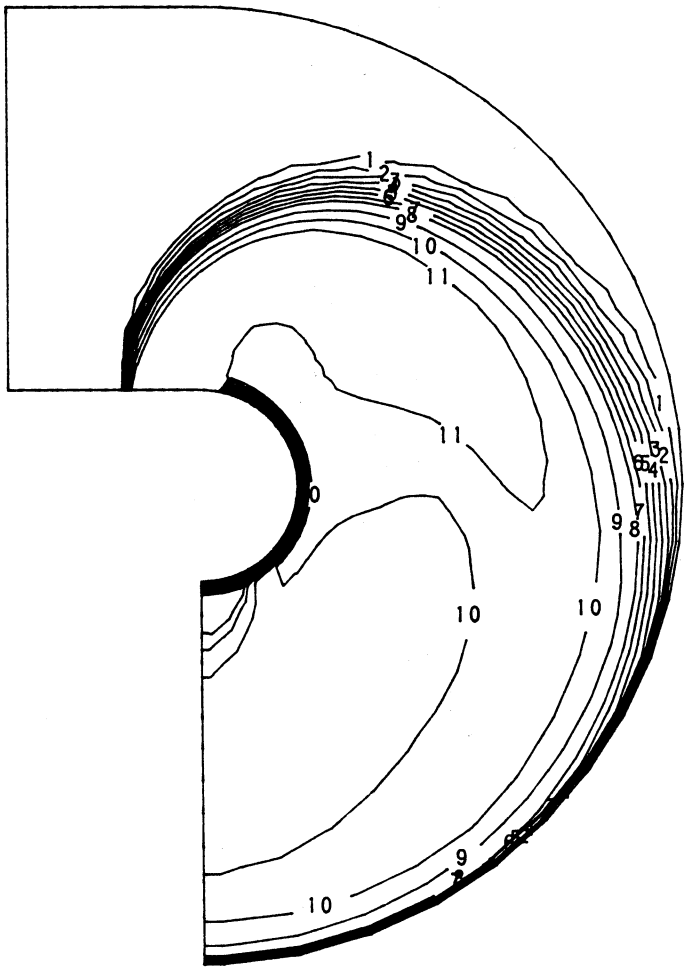

Figure 5-29. Streamwise Theta Contours for Case 26.

CONTOUR	VALUE
1	0.0500
2	0.1000
3	0.1500
4	0.2000
5	0.2500
6	0.3000
7	0.3500
8	0.4000
9	0.5000
10	0.6000
11	0.7000

$J = 6.6$

$S/H_0 = 0.5$

$D/H_0 = 0.25$

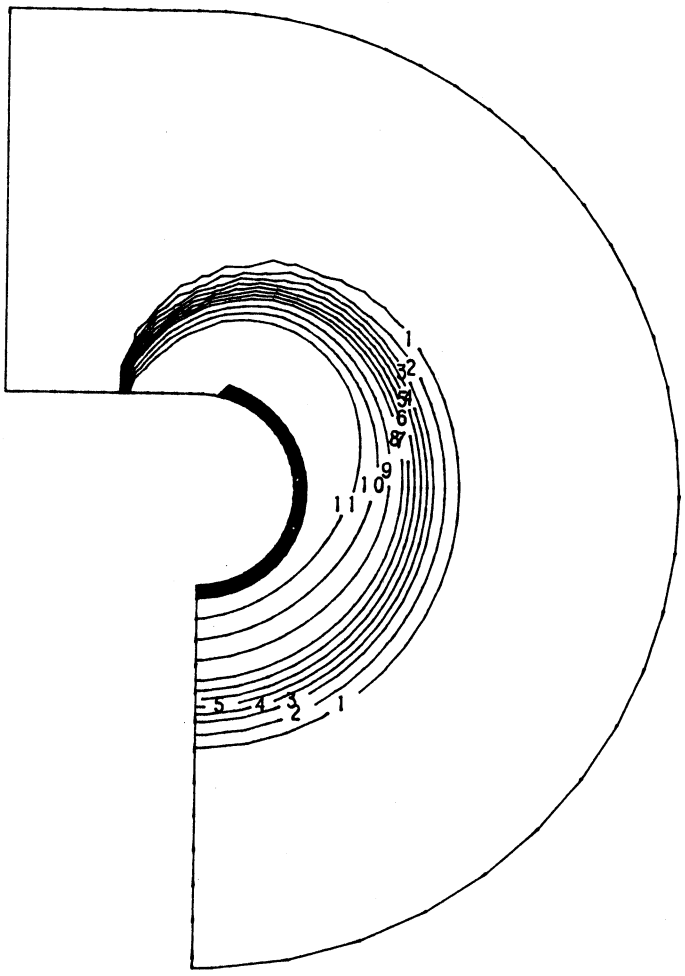

Figure 5-30. Streamwise Theta Contours for Case 27.

CONTOUR	VALUE
1	0.0500
2	0.1000
3	0.1500
4	0.2000
5	0.2500
6	0.3000
7	0.3500
8	0.4000
9	0.5000
10	0.6000
11	0.7000

$J = 6.6$

$S/H_0 = 0.5$

$D/H_0 = 0.25$

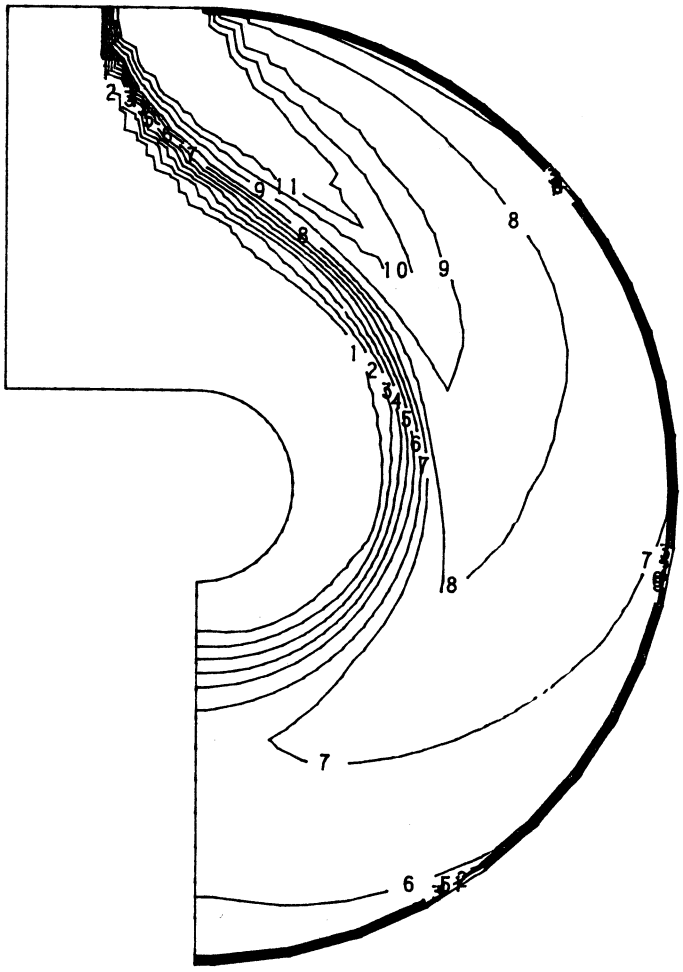

Figure 5-31. Streamwise Theta Contours for Case 28.

CONTOUR	VALUE
1	0.0500
2	0.1000
3	0.1500
4	0.2000
5	0.2500
6	0.3000
7	0.3500
8	0.4000
9	0.5000
10	0.6000
11	0.7000

J = 6.6

S/H_0 = 0.5

D/H_0 = 0.25

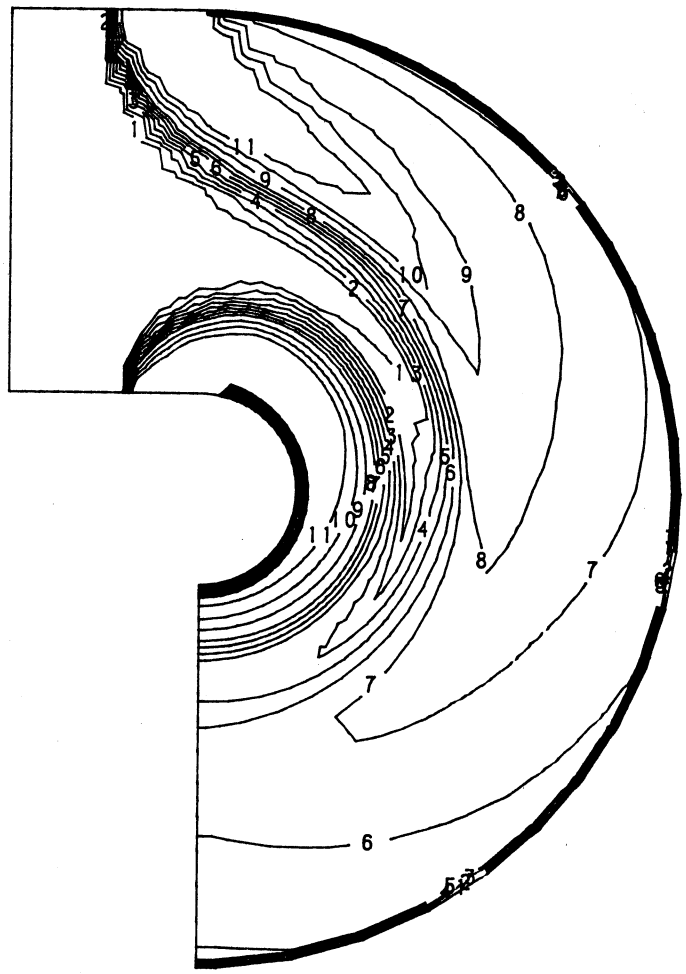

Figure 5-32. Streamwise Theta Contours for Case 29.

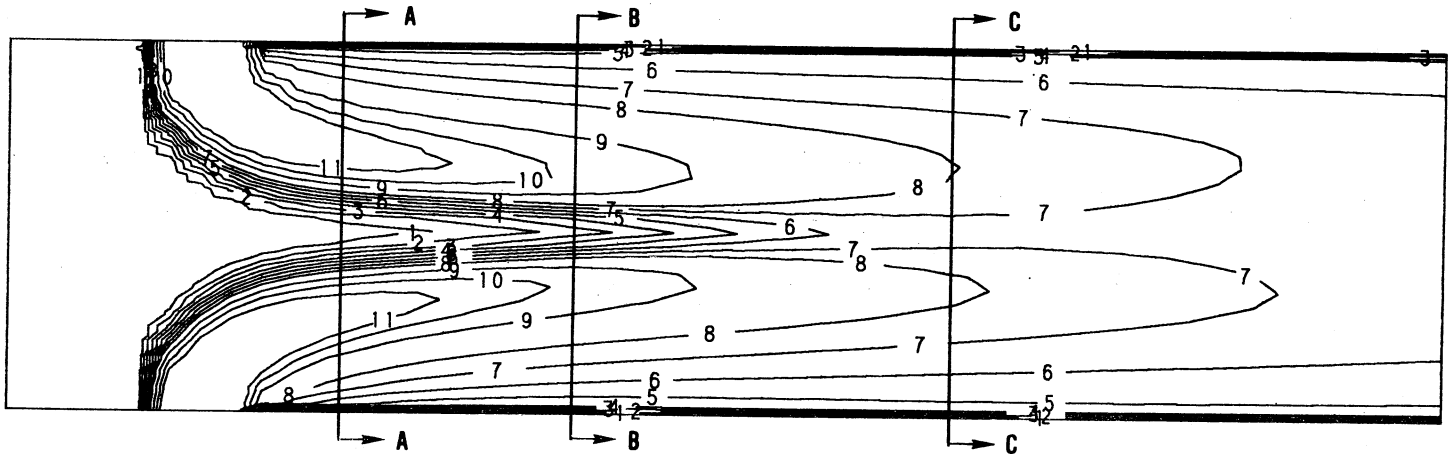

CONTOUR	VALUE
1	0.0500
2	0.1000
3	0.1500
4	0.2000
5	0.2500
6	0.3000
7	0.3500
8	0.4000
9	0.5000
10	0.6000
11	0.7000

J = 6.6

S/H_0 = 0.5

D/H_0 = 0.25

Figure 5-33a. Streamwise Theta Contours for Case 30.

CONTOUR	VALUE
1	0.0500
2	0.1000
3	0.1500
4	0.2000
5	0.2500
6	0.3000
7	0.3500
8	0.4000
9	0.5000
10	0.6000
11	0.7000

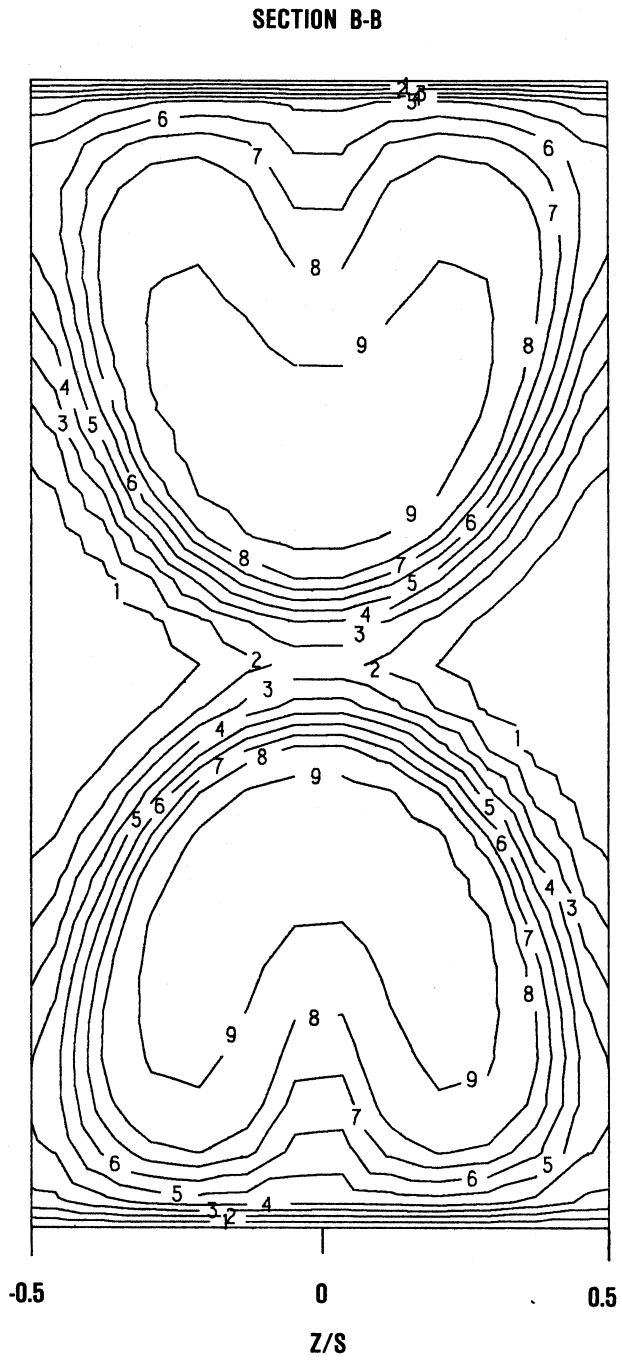

Figure 5-33b. Cross-Stream Theta Contours at X/H=1.0 for Case 30.

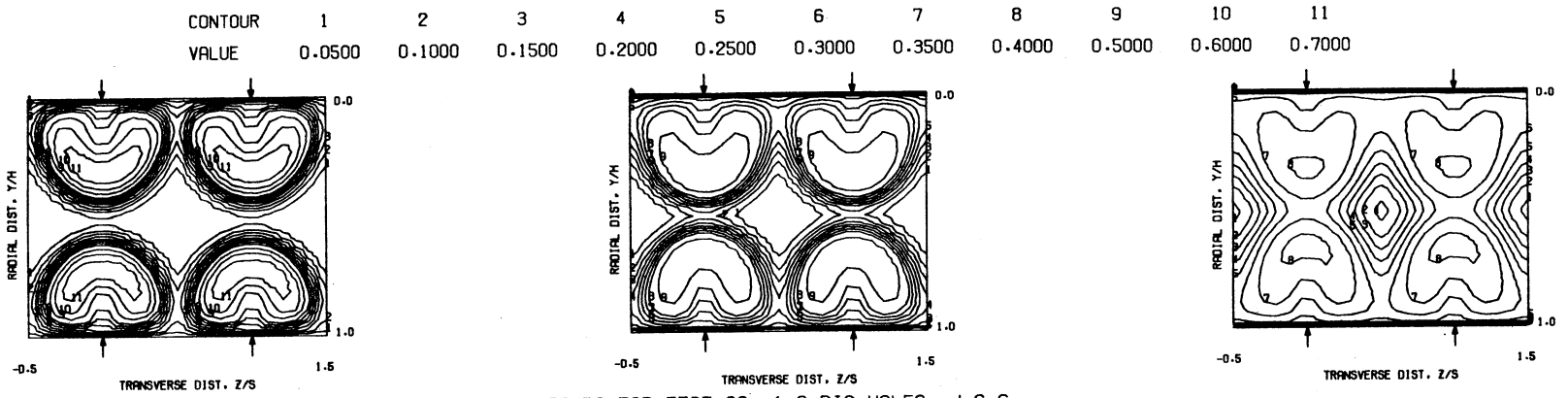

CALCULATED THETA CONTOURS FOR TEST-30, 1.0 DIA HOLES, J=6.6

SECTION A-A **SECTION B-B** **SECTION C-C**

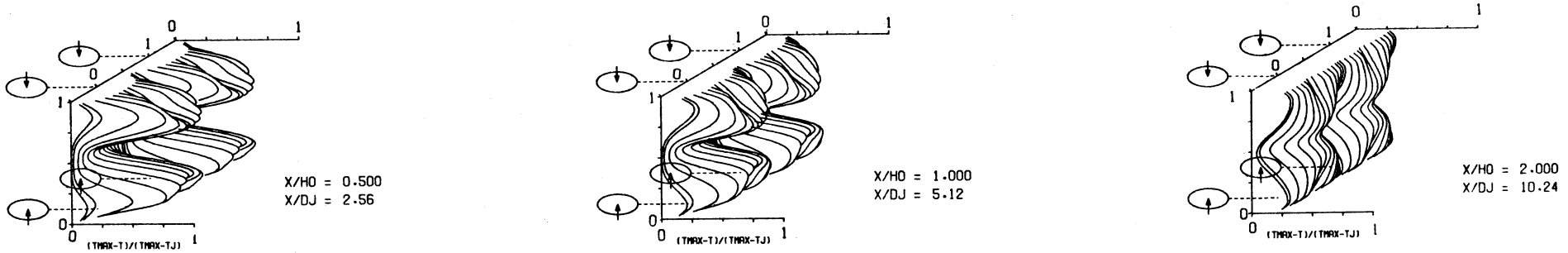

Figure 5-33c. Cross-Stream and Oblique Theta Contours for Case 30.

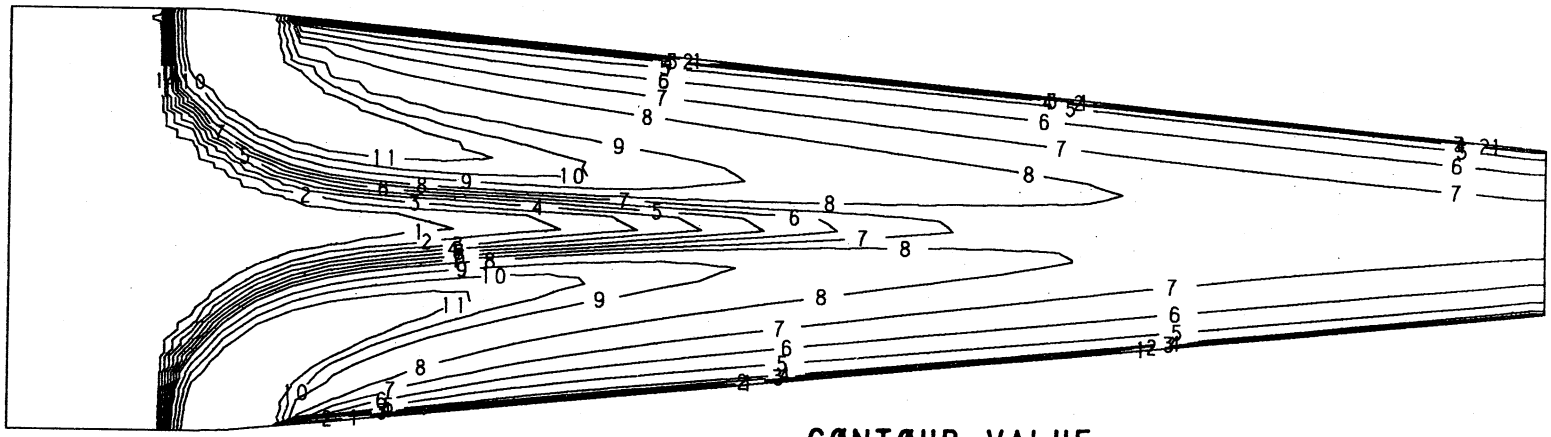

J = 26.4
S/H_0 = 0.5
D/H_0 = 0.25

CONTOUR	VALUE
1	0.0500
2	0.1000
3	0.1500
4	0.2000
5	0.2500
6	0.3000
7	0.3500
8	0.4000
9	0.5000
10	0.6000
11	0.7000

Figure 5-34. Streamwise Theta Contours for Case 31.

CONTOUR	VALUE
1	0.0500
2	0.1000
3	0.1500
4	0.2000
5	0.2500
6	0.3000
7	0.3500
8	0.4000
9	0.5000
10	0.6000
11	0.7000

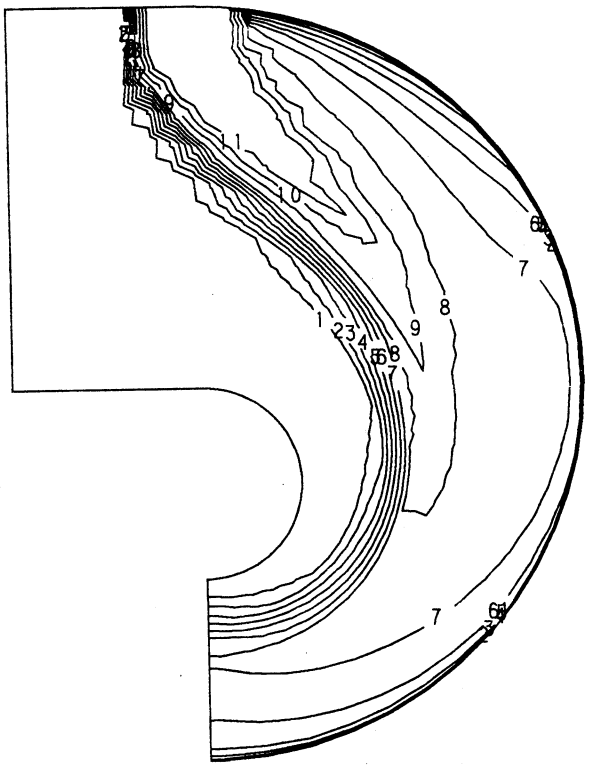

J = 6.6
S/H_0 = 0.5
D/H_0 = 0.25

Figure 5-35. Streamwise Theta Contours for Case 32.

CONTOUR	VALUE
1	0.0500
2	0.1000
3	0.1500
4	0.2000
5	0.2500
6	0.3000
7	0.3500
8	0.4000
9	0.5000
10	0.6000
11	0.7000

$J = 6.6$

$S/H_0 = 0.5$

$D/H_0 = 0.25$

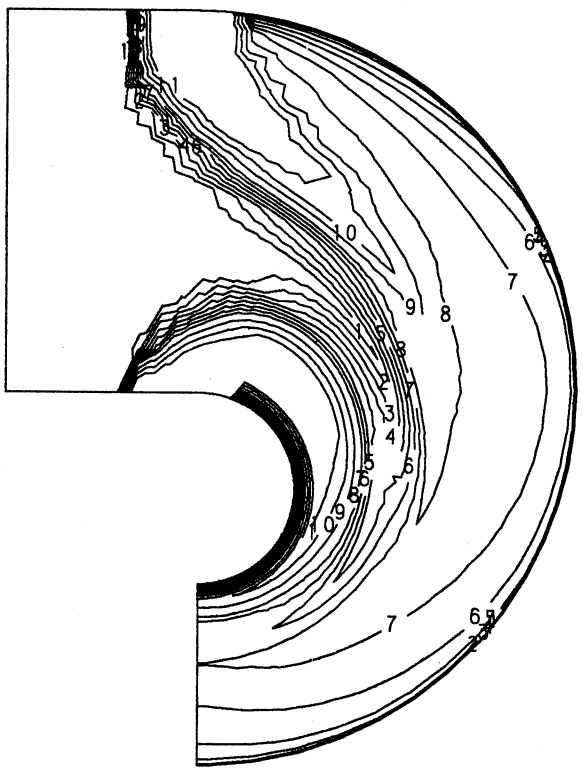

Figure 5-36. Streamwise Theta Contours for Case 33.

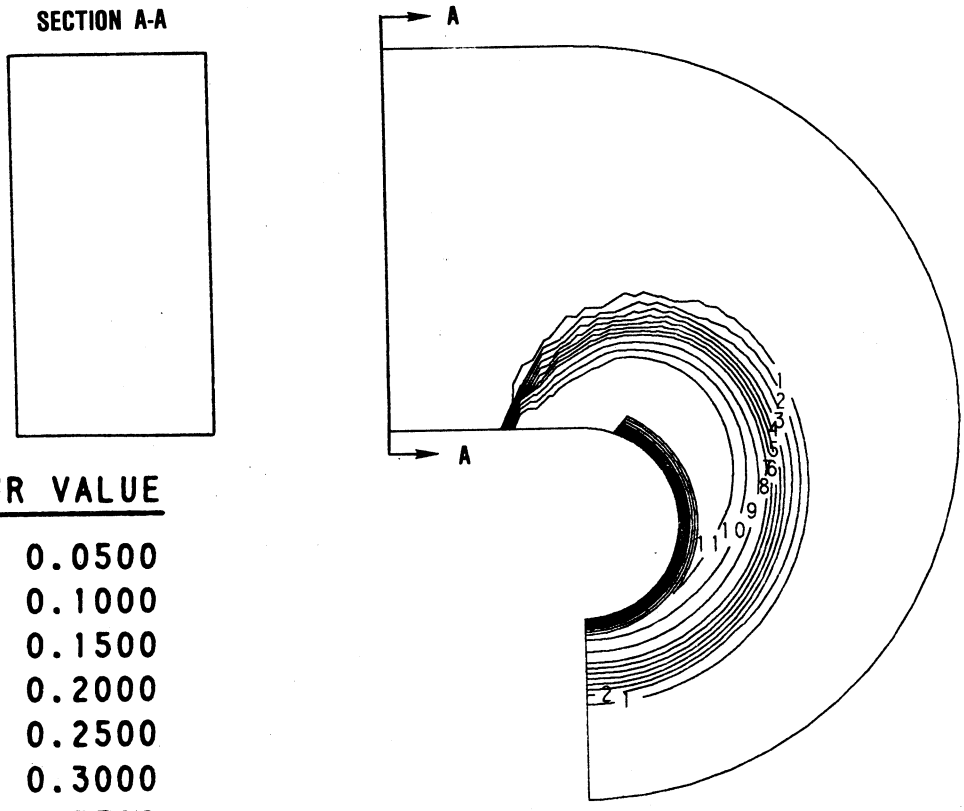

CONTOUR	VALUE
1	0.0500
2	0.1000
3	0.1500
4	0.2000
5	0.2500
6	0.3000
7	0.3500
8	0.4000
9	0.5000
10	0.6000
11	0.7000

Figure 5-37. Streamwise Theta Contours for Case 34.

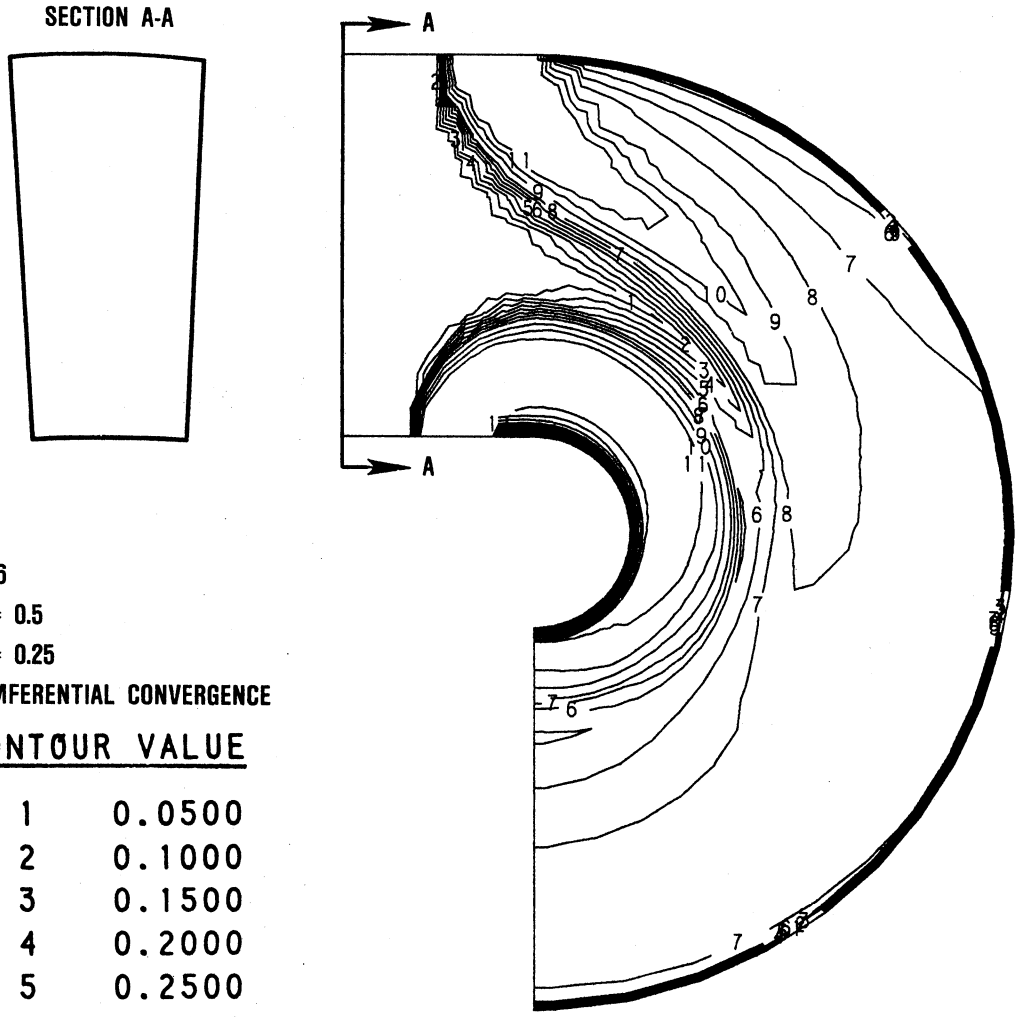

J = 6.6
S/H_0 = 0.5
D/H_0 = 0.25
CIRCUMFERENTIAL CONVERGENCE

CONTOUR	VALUE
1	0.0500
2	0.1000
3	0.1500
4	0.2000
5	0.2500
6	0.3000
7	0.3500
8	0.4000
9	0.5000
10	0.6000
11	0.7000

Figure 5-38. Streamwise Theta Contours for Case 35.

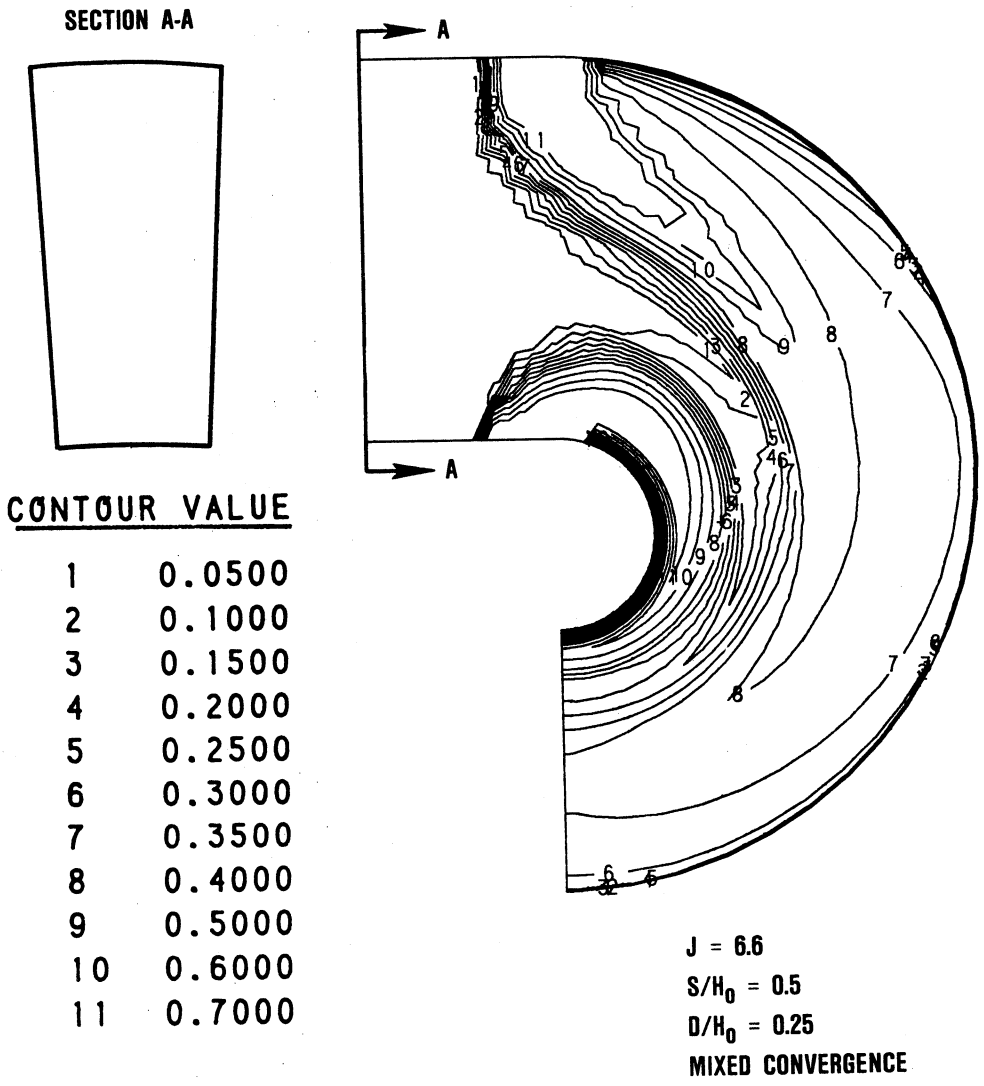

Figure 5-39. Streamwise Theta Contours for Case 36.

CONTOUR	VALUE
1	0.0500
2	0.1000
3	0.1500
4	0.2000
5	0.2500
6	0.3000
7	0.3500
8	0.4000
9	0.5000
10	0.6000
11	0.7000

J = 26.4

S/H_0 = 0.25

D/H_0 = 0.125

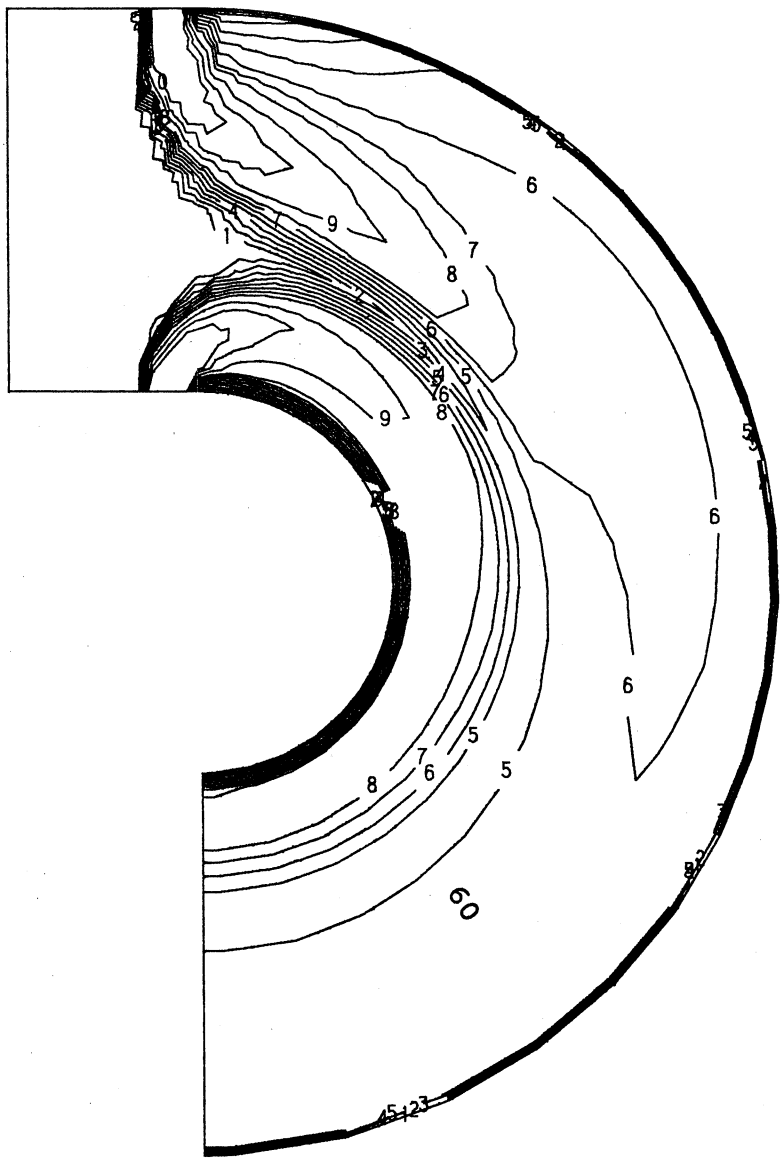

Figure 5-40. Streamwise Theta Contours for Case 37.

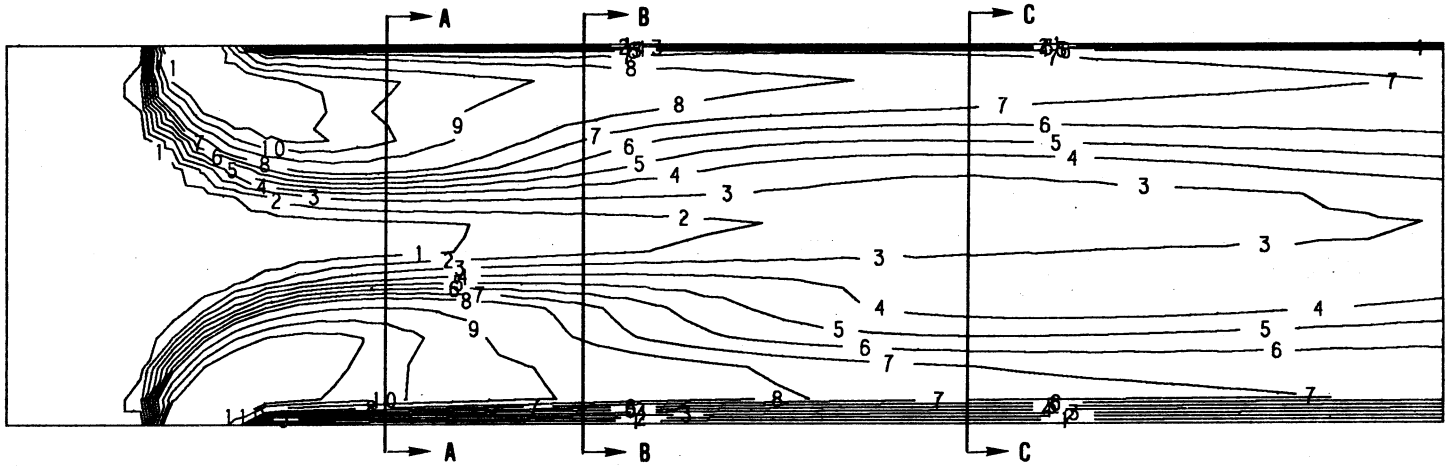

CONTOUR	VALUE
1	0.0500
2	0.1000
3	0.1500
4	0.2000
5	0.2500
6	0.3000
7	0.3500
8	0.4000
9	0.5000
10	0.6000
11	0.7000

J = 6.6

S/H_0 = 0.5

D/H_0 = 0.25

ALIGNED SLOTS

Figure 5-41a. Streamwise Theta Contours for Case 38.

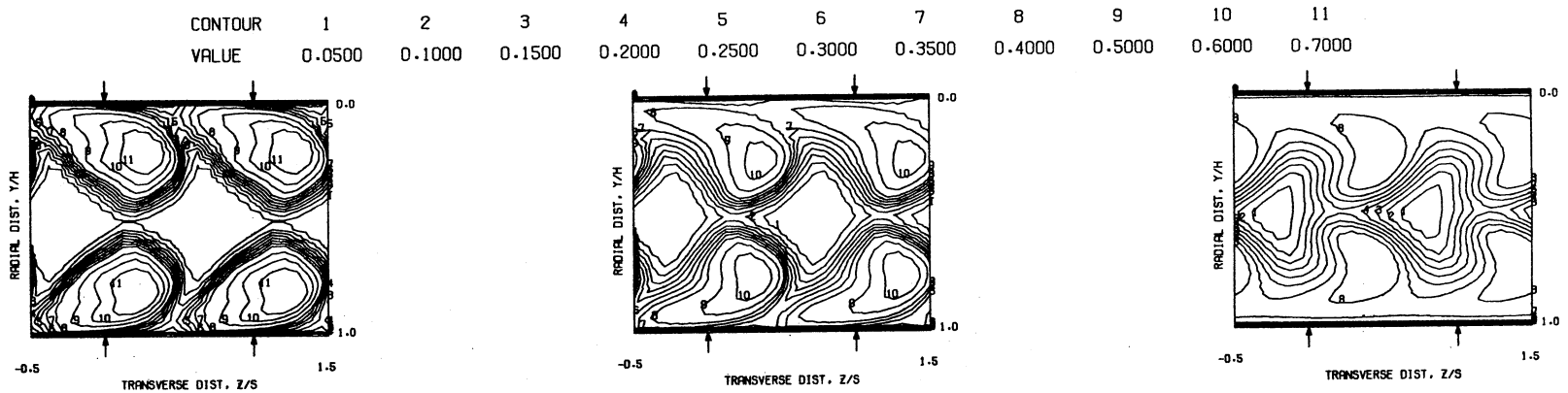

CALCULATED THETA CONTOURS FOR TEST-38, ALIGNED SLOTS, J=6.6

SECTION A-A **SECTION B-B** **SECTION C-C**

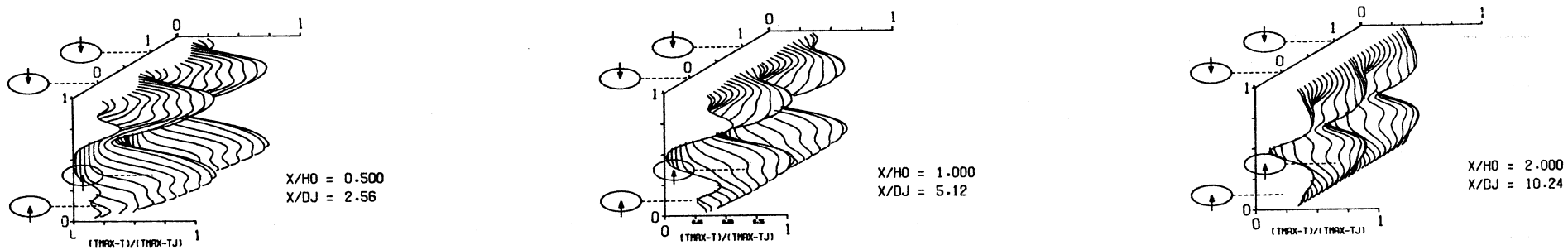

Figure 5-41b. Cross-Stream and Oblique Theta Contours for Case 38.

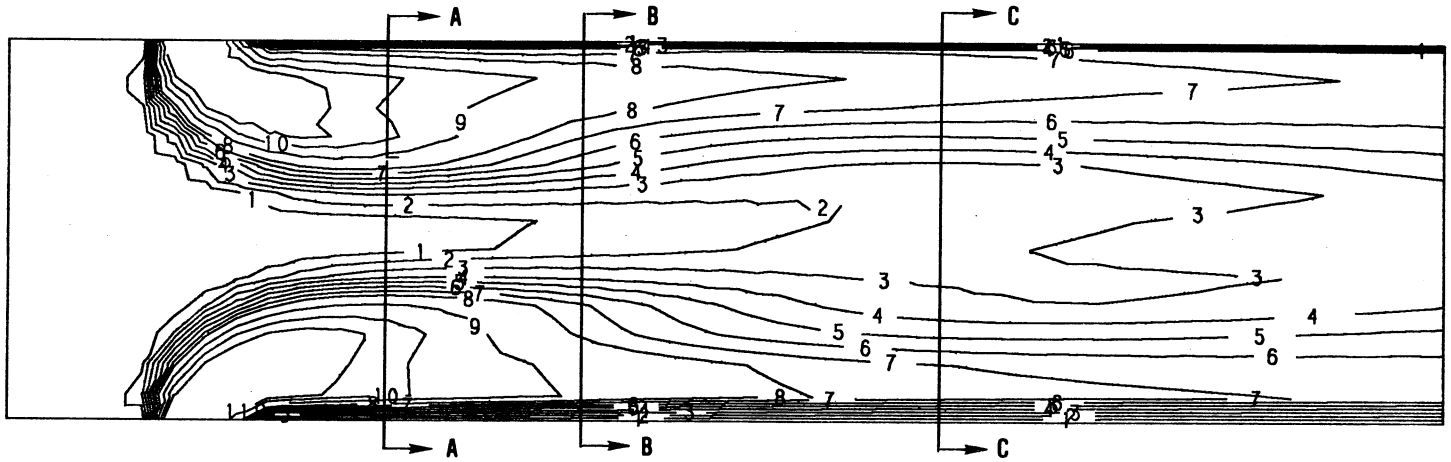

CONTOUR	VALUE
1	0.0500
2	0.1000
3	0.1500
4	0.2000
5	0.2500
6	0.3000
7	0.3500
8	0.4000
9	0.5000
10	0.6000
11	0.7000

J = 6.6
S/H_0 = 0.5
D/H_0 = 0.25
CROSSED SLOTS

Figure 5-42a. Streamwise Theta Contours for Case 39.

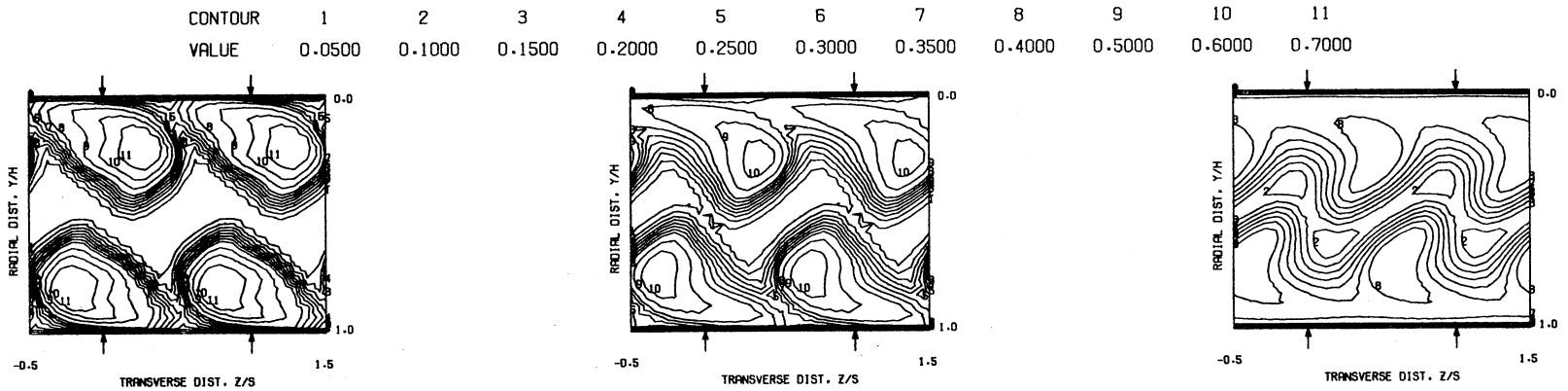

CALCULATED THETA CONTOURS FOR TEST-39, CROSSED SLOTS, J=6.6

SECTION A-A **SECTION B-B** **SECTION C-C**

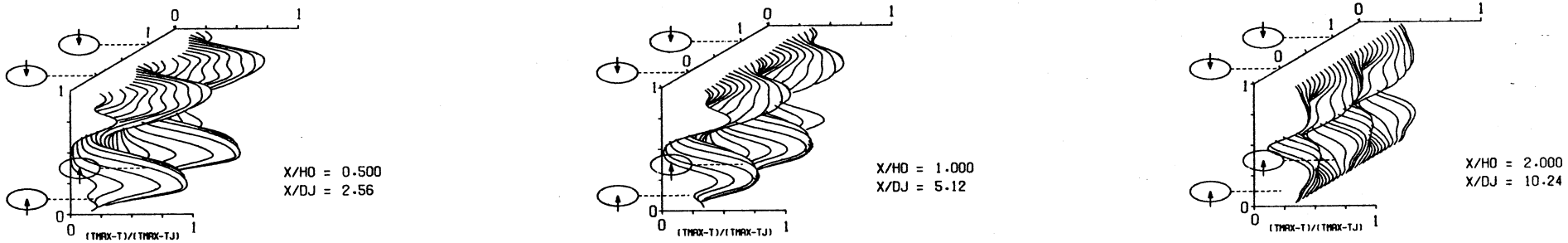

Figure 5-42b. Cross-Stream and Oblique Theta Contours for Case 39.

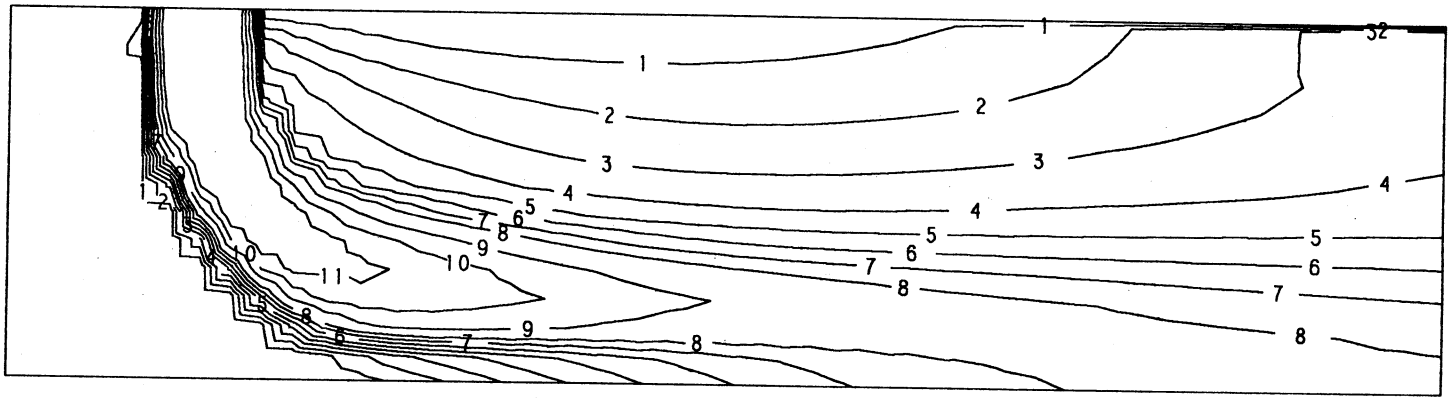

$J = 26.4$

$S/H_0 = 1.0$

$D/H_0 = 0.25$

$(S/H_0 = 0.5$ AT $R/H_0 = 0.5)$

CONTOUR	VALUE
1	0.0500
2	0.1000
3	0.1500
4	0.2000
5	0.2500
6	0.3000
7	0.3500
8	0.4000
9	0.5000
10	0.6000
11	0.7000

Figure 5-43. Streamwise Theta Contours for Case 40.

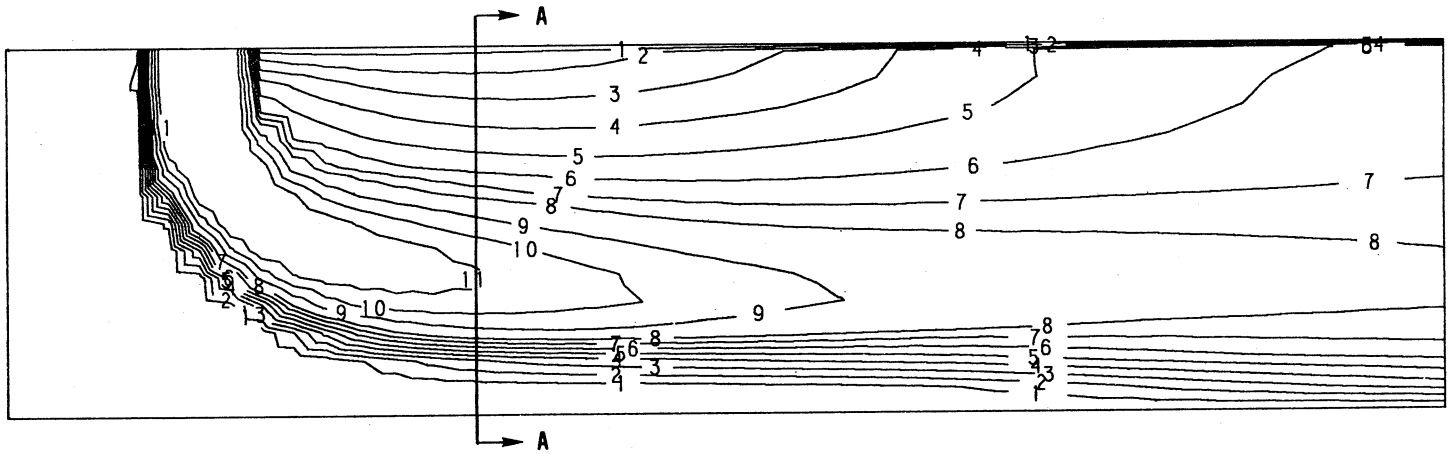

J = 26.4

S/H_0 = 0.707

D/H_0 = 0.25

(S/H_0 = 0.5 AT $R/H_0 = \sqrt{2}/2$)

CONTOUR	VALUE
1	0.0500
2	0.1000
3	0.1500
4	0.2000
5	0.2500
6	0.3000
7	0.3500
8	0.4000
9	0.5000
10	0.6000
11	0.7000

Figure 5-44a. Streamwise Theta Contours for Case 41.

CONTOUR	VALUE
1	0.0500
2	0.1000
3	0.1500
4	0.2000
5	0.2500
6	0.3000
7	0.3500
8	0.4000
9	0.5000
10	0.6000
11	0.7000

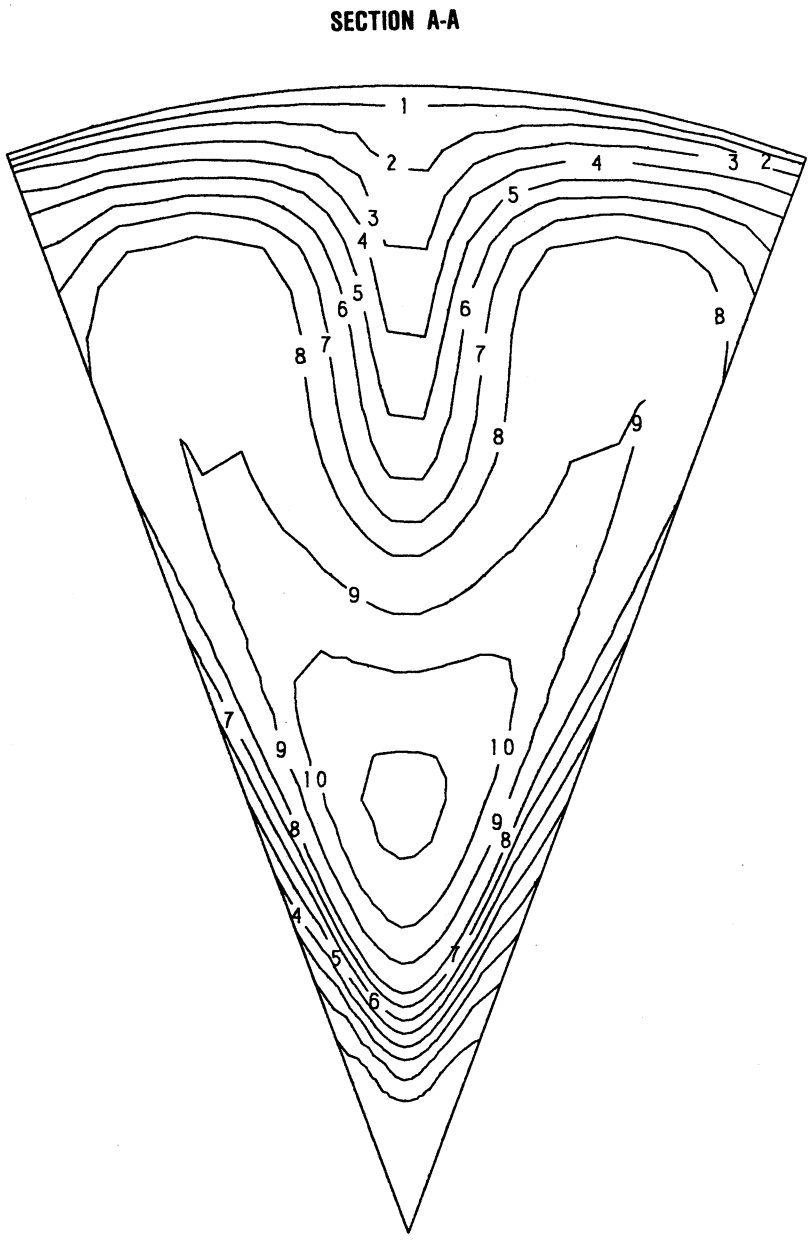

Figure 5-44b. Cross-Stream Theta Contours at X/H=0.75 for Case 41.

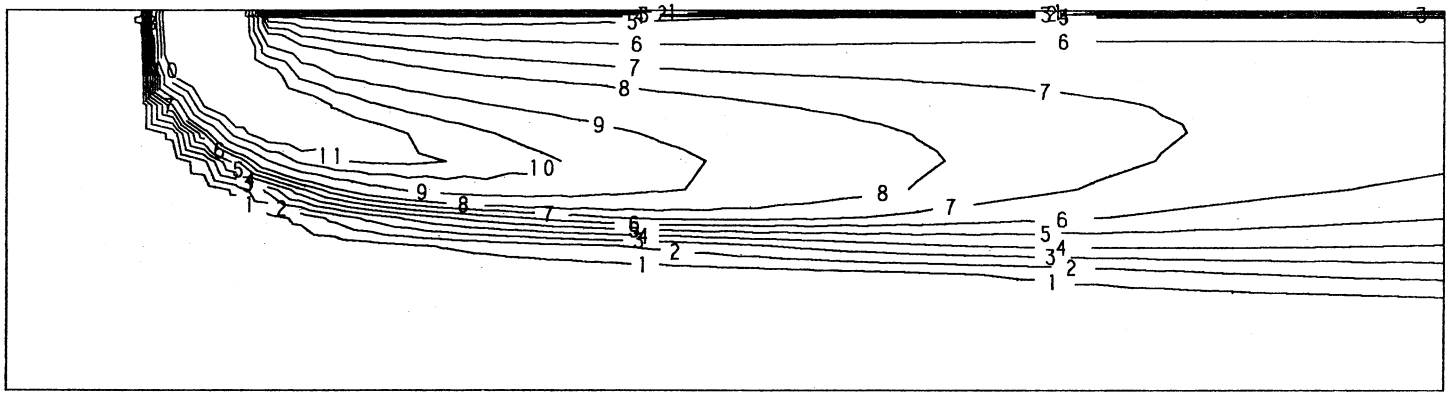

$J = 6.6$

$S/H_0 = 0.5$

$D/H_0 = 0.25$

CONTOUR	VALUE
1	0.0500
2	0.1000
3	0.1500
4	0.2000
5	0.2500
6	0.3000
7	0.3500
8	0.4000
9	0.5000
10	0.6000
11	0.7000

Figure 5-45. Streamwise Theta Contours for Case 42.

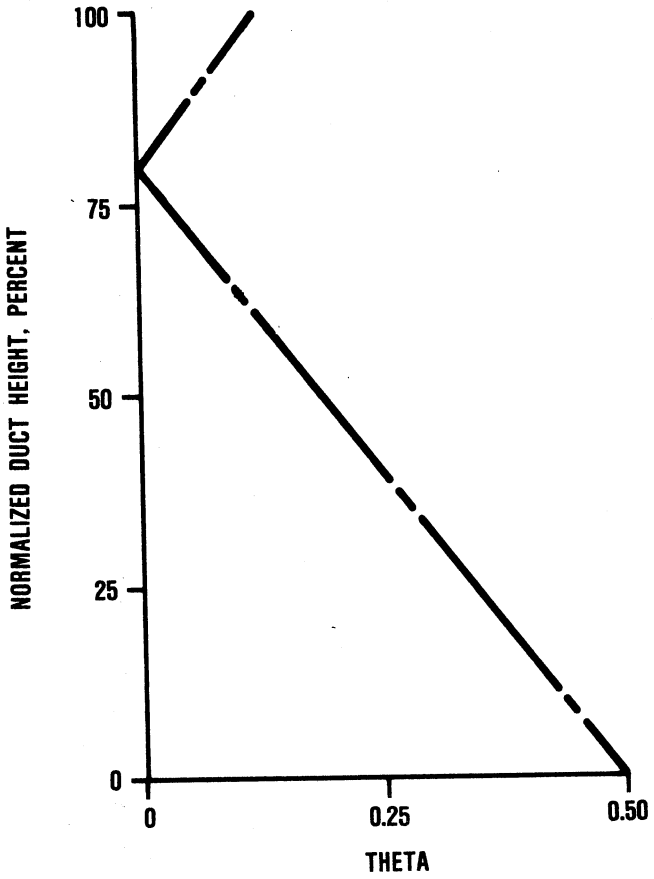

Figure 5-46. Inlet Theta Profile for Case 14 and Case 16.

CONTOUR	VALUE
1	0.0500
2	0.1000
3	0.1500
4	0.2000
5	0.2500
6	0.3000
7	0.3500
8	0.4000
9	0.5000
10	0.6000
11	0.7000

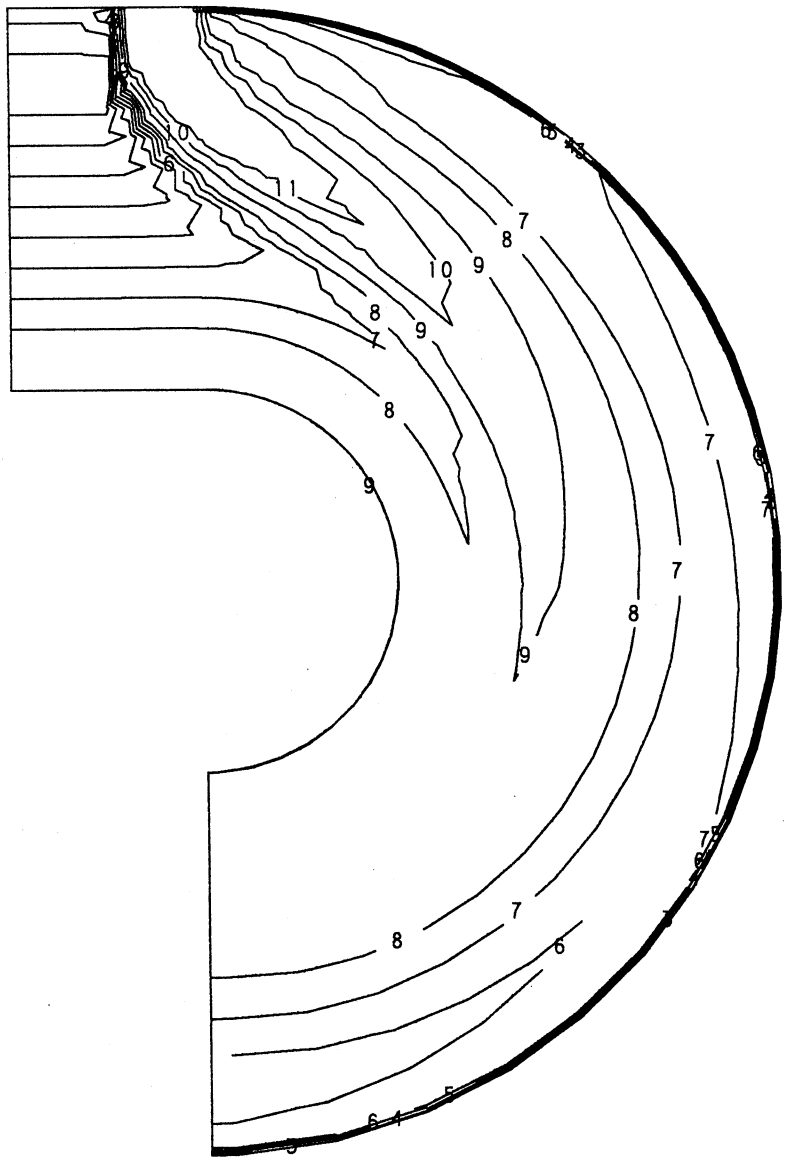

Figure 5-47. Streamwise Theta Contours for Superposition of Case 7 and Case 14.

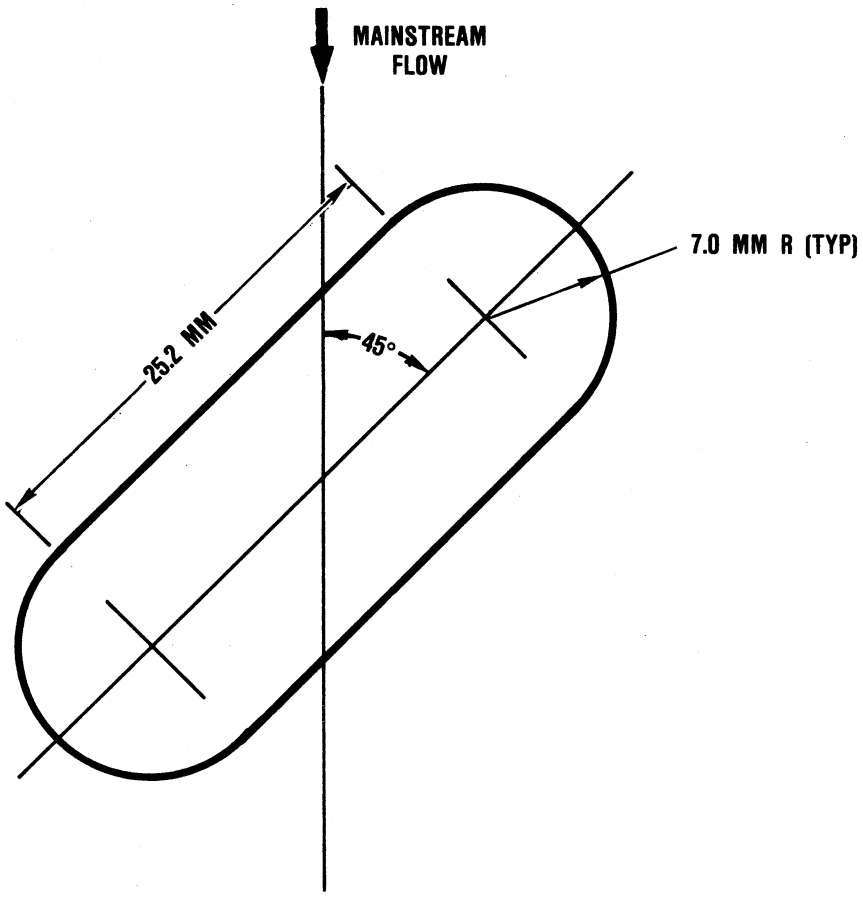

Figure 5-48. Slot Geometry for Case 38 and Case 39.

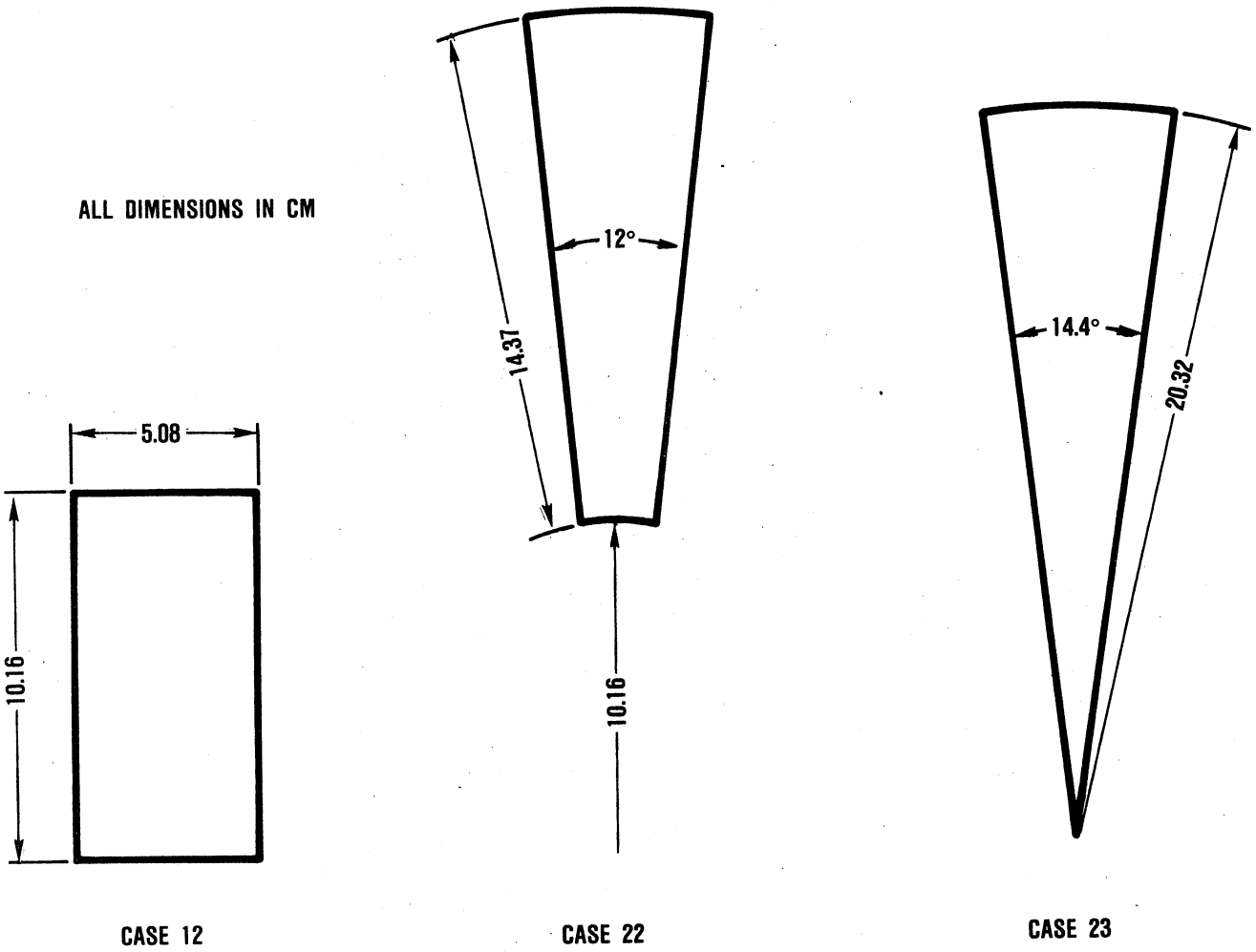

Figure 5-49. Cross-Stream Domains for Cases 12, 22 and 23.

6.0 CONCLUSIONS AND RECOMMENDATIONS

The TMM has been assembled from existing codes and physical submodels and has shown no operational difficulties. The model has been used to analyze a number of flow situations which possess some or all of the characteristics found in transition liner flows. The flow field predictions have been compared with available experimental data and based on that comparison and general observations while running the program, the following conclusions can be made.

- The good agreement for the laminar case indicates that the basic numerical procedure is operating correctly.
- The SIMPLER algorithm reduces the execution time required to achieve a specified level of convergence.
- The ARSM computes Reynolds stress levels which are reasonable when compared to the measured data for turning duct flows.
- The predicted mixing rate using the k-ε model for dilution jet flow situations is considerably less than that indicated by the measurements.
- The ARSM enhances the mixing rate but not to the degree indicated by the data.
- The DFR model has demonstrated improved accuracy over the typical six-flux model; however the geometrical complexity incurred in extending the model to 3 dimensions is significant and the model is not recommended for use without further accurate radiation measurements and detailed validation of the DFR model.
- The slight improvement in the predicted velocity profiles when using the ARSM does not justify the added computation and memory requirements.
- In the current form, the TMM is capable of predicting trends and qualitative results for transition liner flows.

Since it appears that the turbulence model contains deficiencies, it is recommended that additional effort be directed at formulating models which can predict the levels of cross stream mixing exhibited by the experimental data. Although not addressed in this study, it is also suspected that numerical effects contribute to some of the measurement-

prediction discrepencies and therefore additional effort is required in this area.

The TMM has also been used to perform a numerical experiment to illustrate the effect of transition liner curvature on the mixing process of dilution jets and hot mainstream gas. The following conclusions can be made from the analysis of the results:

- Transition liner curvature causes a drift of the jet trajectories toward the inner wall that must be accounted for in any jet mixing correlations.

- The radial pressure gradient induced by the curvature opposes the entrainment of the cross-flow caused by the vortices in the wake region of jets injected from transition liner inner walls and enhances the entrainment for jets injected from outer walls. This produces very different characteristics for the two types of injection resulting in slower mixing for ID jets than those located on the OD.

- Jet trajectories in a pipe are similar to that in a rectangular duct if the same orifice momentum flux ratios and spacing-to-height (or radius) ratios are used. However, the spacing ratio for the pipe must be computed using the arc length at the radius given by $Rm/\sqrt{2}$, where Rm is the maximum pipe radius. Thus jet mixing correlations derived for rectangular ducts can also be used for pipes.

- The use of angled slots is approximately equivalent to round holes of the same open area.

REFERENCES

1. T.W. Bruce, H.C. Mongia, and R.S. Reynolds, "Combustor Design Criteria Validation," USARTL-TR-78-55 (A,B,C), February 1979 [Garrett Report 75-211682(38)].

2. M.A. Habib and J.H. Whitelaw, "The Calculation of Turbulent Flow in Wide-Angle Diffusers," Numerical Heat Transfer, Vol. 15, pp 145-164, (1982).

3. W.F. Hughes and E.W. Gaylord, Basic Equations of Engineering Sciences, McGraw-Hill Book Company, New York, New York, (1964).

4. D.B. Spalding, "A Novel Finite-Difference Formulation for Differential Expressions Involving Both First and Second Derivatives," Int. J. Numer. Meth. Eng., Vol. 4, P 551, (1972).

5. S.V. Patankar, Numerical Heat Transfer and Fluid Flow, McGraw-Hill - Hemisphere, (1980).

6. S.V. Patankar, and D.B. Spalding, "A Calculation Procedure for Heat, Mass and Momentum Transfer in Three-Dimensional Parabolic Flows," Int. J. Heat and Mass Transfer, Vol. 15 (1972).

7. B.E. Launder, G.J. Reece and W. Rodi, "Progress in the Development of Reynolds Stress Turbulence Closure," Journal of Fluid Mechanics, 68:3, 537ff, (1975).

8. F.C. Lockwood and N.G. Shah, "A New Radiation Solution Method for Incorporation in General Combustion Prediction Procedures," presented at the Eighteenth Symposium on Combustion, London, (1980).

9. M.K. Denham, and M.A. Patrick, "Laminar Flow Over a Downstream-Facing Step in a Two-Dimensional Flow Channel," Trans. Instn. Chem. Engrs., Vol. 52, (1974).

10. J. Kim, S.J. Kline and J.P. Johnston, "Investigation of Separation and Reattachment of a Turbulent Shear Layer: Flow Over a Backward-Facing Step," Report MD-37, (Dept. of Mech. Engr., ThermoSciences Division, Stanford University, 1978).

11. J.A. Humphrey, A.M. Taylor and J.H. Whitelaw, "Laminar Flow in a Square Duct of Strong Curvature," Journal of Fluid Mechanics, Vol. 83, p 509, (1977).

12. S.M. Chang, J.A.C. Humphrey and A. Modavi, "Turbulent Flow in a Strongly Curved U-Bend and Downstream Tangent of Square Cross-Sections," Report FM-82-1, (Dept. of Mech. Engr., Berkeley, Calif., November 1982).

13. J.A. Humphrey, J.H. Whitelaw and G.E. Yee, "Turbulent Flow in a Square Duct with Strong Curvature," Journal of Fluid Mechanics, Vol. 103, pp 443-463, (1981).

14. R. Srinivasan, A. Berenfeld and H.C. Mongia, "Dilution Jet Mixing Program, Phase II Report," NASA CR-168031, November (1982).

15. R. Srinivasan, E. Coleman and K. Johnson, "Dilution Jet Mixing Program, Phase II Report," NASA CR-174624, June (1984).

16. A. Lipshitz and I. Greber "Dilution Jets in Accelerated Cross Flows," NASA CR-174714, June (1984).

17. J. Zizelman, "Dilution Jet Experiments in Compact Combustor Configurations," M.S. Thesis, Case Western University, 1983.

18. R. Srinivasan, G. Myers, E. Coleman, and C. White, "Dilution Jet Mixing Program, Phase III Report," NASA CR-174884, September (1985).

REPORT DOCUMENTATION PAGE

Form Approved
OMB No. 0704-0188

1. AGENCY USE ONLY (*Leave blank*)	2. REPORT DATE	3. REPORT TYPE AND DATES COVERED
	October 1986	Final Contractor Report

4. TITLE AND SUBTITLE

Transition Mixing Study Final Report

5. FUNDING NUMBERS

WU–None
NAS3–24340

6. AUTHOR(S)

R. Reynolds and C. White

7. PERFORMING ORGANIZATION NAME(S) AND ADDRESS(ES)

Garrett Turbine Engine Company
P.O. Box 5217
Phoenix, Arizona 85010

8. PERFORMING ORGANIZATION REPORT NUMBER

E–None

9. SPONSORING/MONITORING AGENCY NAME(S) AND ADDRESS(ES)

National Aeronautics and Space Administration
Washington, DC 20546–0001

10. SPONSORING/MONITORING AGENCY REPORT NUMBER

NASA CR–175062
Garrett 21–5723

11. SUPPLEMENTARY NOTES

Project Manager, James D. Holdeman, NASA Lewis Research Center, Cleveland, Ohio 44135. Final 7–84 through 9–86.

12a. DISTRIBUTION/AVAILABILITY STATEMENT

Unclassified - Unlimited
Subject Category: 00

Available electronically at http://gltrs.grc.nasa.gov

This publication is available from the NASA Center for AeroSpace Information, 301–621–0390.

12b. DISTRIBUTION CODE

13. ABSTRACT ***(Maximum 200 words)***

An analytic program has been conducted to develop a computer model capable of analyzing the flow field in the transition liner of small gas turbine engines. A Fortran code has been assembled from existing codes and physical submodels and used to predict the flow in several test geometries which contain characteristics similar to transition liners, and for which experimental data was available. Comparisons between the predictions and measurements indicate that the code produces qualitative results but that the turbulence models, both K-E and algebraic Reynolds Stress, underestimate the cross-stream diffusion. The code has also been used to perform a numerical experiment that examined the effect of a variety of parameters on the mixing process in transition liners. Comparisons between the different analyzed cases have illustrated that geometries with significant curvature show a drift of the jet trajectory toward the convex wall and weaker wake region vortices and decreased penetration for jets located on the convex wall of the liner, when compared to jets located on concave walls. Also shown were the approximate equivalency of angled slots and round holes and a technique by which jet mixing correlations developed for rectangular channels can be used for geometries.

14. SUBJECT TERMS

Combustor; Transition-mixing; Computer model

15. NUMBER OF PAGES

188

16. PRICE CODE

17. SECURITY CLASSIFICATION OF REPORT	18. SECURITY CLASSIFICATION OF THIS PAGE	19. SECURITY CLASSIFICATION OF ABSTRACT	20. LIMITATION OF ABSTRACT
Unclassified	Unclassified	Unclassified	